SYNTHESIS, CHARACTERIZATION AND CATALYTIC ACTIVITIES OF ORGANIC–INORGANIC HYBRID MESOPOROUS MATERIALS

A THESIS

SUBMITTED TO THE

UNIVERSITY OF PUNE

FOR THE DEGREE OF

DOCTOR OF PHILOSOPHY

IN

CHEMISTRY

BY

ANIRBAN GHOSH

CATALYSIS DIVISION
NATIONAL CHEMICAL LABORATORY
PUNE 411 008
INDIA

SEPTEMBER 2004

DECLARATION BY RESEARCH GUIDE

Certified that the work incorporated in the thesis entitled: "**Synthesis, characterization and catalytic activities of organic–inorganic hybrid mesoporous materials**", submitted by Mr. Anirban Ghosh, for the Degree of ***Doctor of Philosophy***, was carried out by the candidate under my supervision at Catalysis Division, National Chemical Laboratory, Pune 411 008, India. Such material as has been obtained from other sources has been duly acknowledged in the thesis.

Dr. Rajiv Kumar
(Research Supervisor)

DECLARATION BY RESEARCH SCHOLAR

I hereby declare that the thesis entitled "**Synthesis, characterization and catalytic activities of organic–inorganic hybrid mesoporous materials**", submitted for the Degree of ***Doctor of Philosophy*** to the University of Pune, has been carried out by me at Catalysis Division, National Chemical Laboratory, Pune 411 008, India, under the supervision of Dr. Rajiv Kumar. The work is original and has not been submitted in part or full by me for any other degree or diploma to this or any other University.

Anirban Ghosh

Dedicated

to my

Parents,

Wife &

Brother

ACKNOWLEDGEMENTS

I find it very difficult to write something in short to acknowledge my research guide, Dr Rajiv Kumar. His constant inspiration, invaluable guidance and constructive criticism helped a lot to focus my views in proper perspective. I take this opportunity to express my intense reverence towards him for guiding me in the right direction throughout the course of this work. My deepest personal regards are due for him forever.

I wish to convey my sincere gratitude to Dr. Murali Sastry, who was my mentor in understanding the world of Nanotechnology, Dr. C. V. V. Satyanarayana, Dr. A. Sarkar, Dr. A. Ahmad, Dr. P. R. Rajamohanan, Dr. C. Gopinathan and Mrs. R. Pasricha for helping me in every possible way through fruitful discussions.

I am highly indebted to Dr. A. V. Ramaswamy, former Head, and Dr. S. Sivasanker, Head, Catalysis Division, not only formally for allowing me to use all the available facilities in the division but also personally for many stimulating discussions and valuable guidance throughout the course of this investigation. My heartfelt thanks are due to Dr. A. P. Singh, Dr. (Mrs.) V. Ramaswamy, Dr. C. S. Gopinath, Dr. P. Manikandan, Ms. V. Samuel, and all other scientific and non-scientific staff of the division for their valuable help and cooperation during my tenure as a research scholar. I am also very much thankful to my senior colleagues Dr. Priyabrata Mukherjee, Dr. Subhash Chandra Laha, Dr. Chitta Ranjan Patra and Dr. Deendayal Mandal, and my junior colleagues Satyajyoti Senapati, Mahesh Kadgaonkar, Raina Gupta, Amit Deshmukh, Sonu Ram Sankar and Pranjal Kalita for their helpful hand, sympathetic ears and making the lab feel like a family. Special thanks to Vandana, Venkatesh, Chidambaram, Sachin Shah, Shylesh, Surendran, Shainaz, Shrikant, Sachin Malwadkar, Thomas, Mahesh Bhagwat, Bennur, Shiju and all other research scholars in Catalysis Division for their constant support throughout my stay in NCL.

I would like to express my appreciation to my colleagues and friends, Kausikda, Atashi, Subarnada, Saptarshida, Somnathda, Sujatadi, Arindamda, Mahuadi, Bikashda, Debasisda, Tarunda, Anuradha, Saikat, Debasis Samanta, Prabalda, Annytda, Babuda, Subhoda, Debdut, Kartick, Soumitra, Prabhas, Pradip, Chanchal and Major for the wonderful time I had with them. It gives me great pleasure to thank my old friends Nilanjana, Susmita, Sibali, Bibhas, Amit, Angshuman, Chiradip and Abhijit from whom I have received unfailing support and encouragement during many years of studies, that they have shown to me in their own special way. I also take this golden opportunity to convey my earnest respect to my schoolteachers Mr. Baneshwar Chakraborty and Mr. Diptiman Dutta, my graduation tutors Dr. Shyamal Gangopadhyay and Dr. Shaktipada Basak, and the professors of Department

of Chemistry, University of Calcutta, for their extraordinary way of teaching that build up my research career in science.

The thesis could not have been completed without the endless love and blessings from my family. Ma and Baba, I should not belittle you by thanking; you taught me how to dream, gave me the skills to chase after those dreams, and encouraged me to reach for the unreachable star. Due adoration to my brother Sayan, and my in-laws (Kaku, Kakima and Didi); their steadfast faith in my capability has always spurred me to go ahead, especially in difficult times. No words of admiration can be adequate to express my feelings towards my dear wife, Silpi, for her love, respect, constant encouragement, prolific scientific discussions, and being the voice of wisdom.

Finally, my thanks are due to Council of Scientific and Industrial Research, Government of India, for awarding the research fellowship, and to Dr. P. Ratnasamy, former Director, Dr. S. Sivaram, Director, and Dr. B. D. Kulkarni, Deputy Director, National Chemical Laboratory, to carry out my research work and extending all possible infrastructural facilities, and to submit me this work in the form of a thesis for the award of PhD degree.

September 2004 Anirban Ghosh

CONTENTS

List of Figures

List of Tables

List of Schemes

List of Abbreviations

AAS	Atomic Absorption Spectroscopy
AES	Atomic Emission Spectroscopy
APTS	3-Aminopropyltrimethoxy silane
BE	Binding Energy
BET	Brunauer-Emmett-Teller
BINAP	2,2'-Bis(diphenylphosphino)-1,1'-binaphthyl
BJH	Barrett-Joyner-Halenda
BTME	1,2-Bis(trimethoxysilyl)ethane
BTSE	1,2-Bis(triethoxysilyl)ethane
BTSEY	1,2-Bis(triethoxysilyl)ethylene
CMC	Critical Micelle Concentration
CP MAS	Cross Polarization Magic Angle Spinning
CPTS	3-Chloropropyltrimethoxy silane
CTABr	Cetyltrimethylammonium bromide
DCM	Dichloromethane
DDA	Dodecylamine
DNA	Deoxyribonucleic acid
DPEN	1,2-Diphenylethylenediamine
DRUV-Vis	Diffuse Reflectance Ultraviolet-Visible
DTA	Differential Thermal Analysis
ee	Enantiomeric Excess
EN	Ethylenediamine
FSM	Folded Sheet Materials
FTIR	Fourier Transform Infrared
GC	Gas Chromatography
GCMS	Gas Chromatography – Mass Spectroscopy
GHSV	Gram Hourly Space Velocity
HMM	Hybrid Mesoporous Material
HMS	Hexagonal Mesoporous Silica
HRTEM	High Resolution Transmission Electron Microscopy
ICP-AES	Inductively Coupled Plasma – Atomic Emission Spectrometry
KCP	Kinetically Controlled Product

LCT	Liquid Crystal Template
MCM	Mobil's Crystalline Material
MPTS	3-Mercaptopropyltrimethoxy Silane
NMR	Nuclear Magnetic Resonance
NOA	n-Octylamine
ODA	Octadecylamine
PEMFC	Polymer Electrolyte Membrane Fuel Cell
PMO	Periodic Mesoporous Organosilica
PROX	Preferential Oxidation of Carbon Monoxide
SAED	Selected Area Electron Diffraction
SAMS	Self-Assembled Monolayers
SB	(*S*)-BINAP or (*S*)-2,2'-Bis(diphenylphosphino)-1,1'-binaphthyl
SBA	Santa Barbara Amorphous
SDPEN	(*S*,*S*)-DPEN or (*S*,*S*)-1,2-Diphenylethylenediamine
SEM	Scanning Electron Microscopy
SLC	Silicatropic Liquid Crystals
TCP	Thermodynamically Controlled Product
TEM	Transmission Electron Microscopy
TEOS	Tetraethyl orthosilicate
TGA	Thermogravimetric Analysis
THF	Tetrahydrofuran
TOF	Turnover Frequency
TON	Turnover Number
TPD	Temperature Programmed Desorption
TPEN	*N*-[3-(trimethoxysilyl)propyl]-ethylenediamine
UOFMN	Unified Organically Functionalized Mesoporous Network
UV-Vis	Ultraviolet-Visible
XPS	X-Ray Photoelectron Spectroscopy
XRD	X-Ray Diffraction
XRF	X-Ray Fluorescence

ABSTRACT

The surface modification of M41S type mesoporous materials by reactive organic functional groups allows the preparation of multifunctional molecular sieves with desired catalytic properties.[1] The mesoporosity and very high surface area of these surface-functionalized mesoporous materials can be exploited for the immobilization of different catalytically reactive species.[2]

During the past few decades, enantioselective hydrogenation of prochiral carbonyl compounds[3] and chemoselective hydrogenation of α,β-unsaturated carbonyl compounds[4] in homogeneous conditions with transition metal complexes have become more important in the pharmaceutical industry, and consequently in catalytic research as well. Recently, an increased demand has developed for the heterogenization of homogeneous organometallic complex catalysts,[5] the goal of which is to combine the superior activity and selectivity offered by homogeneous catalysts with the ease of separation and recycling of heterogeneous ones.[6] Although, several reports of heterogeneous catalysis by encapsulated materials has been addressed for oxidation, epoxidation and Heck reactions, but attempts to heterogenize some of the industrially relevant homogeneous catalysts for enantioselective as well as chemoselective hydrogenation of carbonyl compounds have been, at best, very limited. Also, a direct comparison of the anchored catalysts with their homogeneous counterparts has not been well investigated with meaningful quantitative data.

Immobilized catalysts reported earlier, suffer either from lower selectivity and activity, or low recyclability and hence, of limited practical applications.[7] Therefore, there is ample opportunity to explore development of new methods of heterogenization, which will be advantageous than the state-of-the-art methods. It is in this context that the covalent grafting of organometallic complex catalysts provides an alternative approach for opening up new outlook for the industrial applications in synthesis of fine chemicals. The principal aim of this

thesis is to investigate the approach of immobilization or anchoring of industrially significant catalysts on surface modified mesoporous materials (MCM-41 or MCM-48) for enantioselective and chemoselective hydrogenation of carbonyl compounds under different reaction conditions. In-depth characterization of these immobilized catalysts will be highlighted to understand the mode of interaction of the metal complex with the silicate network, to evaluate the stability of the composite system, and to explore the origin of catalytic activity.

Metallic gold when deposited on selected metal oxides as ultrafine particles of nanometer size range (~2–3 nm), it is found to be very active in many important reactions for chemical industry and environmental protection.[8] Preparation of supported gold catalysts can be achieved by the following different traditional routes; (i) impregnation, (ii) ion exchange, (iii) coprecipitation (iv) deposition-precipitation (v) chemical vapor deposition, (vi) reduction by borohydride or citrate.[9] In all these methods, the hosts or supports are usually passive and do not participate actively in the reduction of metal ions to form nanoparticles followed by their entrapment in host matrix. Industrial application of anyone these methods can either be hazardous or eco-unfriendly.

The thesis will also focus on the synthesis and simultaneous stabilization of gold nanoparticles by spontaneous reduction of aqueous chloroaurate ions ($AuCl_4^-$) by ordered mesoporous silica materials, such as organically modified MCM-41, and by amorphous silica. Employing this method, we can avoid the use of any external reducing environment other than the host matrix, for the formation of nanoparticles from the metal ion solution. Detailed characterization of these hybrid materials will be demonstrated to understand the physicochemical aspects of the supported gold nanoparticles inside the mesoporous matrices. The catalytic activity of these gold catalysts in oxidation of carbon monoxide and hydrogenation of unsaturated hydrocarbons will also be highlighted.

The specific problems chosen are:

(i) Synthesis of mesoporous MCM-41 and MCM-48 materials, and their surface-modification by different approaches.

(ii) Synthesis of novel heterogeneous catalysts containing encapsulated Ruthenium-biphosphine-diamine complexes in surface modified MCM-41 and MCM-48 for chemoselective hydrogenation of α,β-unsaturated aldehydes and enantioselective hydrogenation of prochiral ketones.

(iii) Synthesis and simultaneous stabilization of gold nanoparticles on organo-functionalized MCM-41, and application of these nanocomposites for oxidation of carbon monoxide and hydrogenation of unsaturated hydrocarbons.

(iv) Detailed characterization of all these newer organic–inorganic hybrid materials.

The thesis is divided into **FIVE** chapters, a brief summary of which is given below.

Chapter 1. Introduction

Chapter 1 presents a general introduction about various physicochemical aspects of mesoporous molecular sieve materials. The different characteristic properties of these materials, their synthesis parameters, different approaches for surface-functionalization, characterization techniques, and application as supports for different catalytically active transition metal complexes and nanoparticles are discussed in brief. Based on these reviews, the scope and objective of the present work have been outlined.

Chapter 2. Synthesis, surface modification and characterization of mesoporous silica

Chapter 2 presents experimental results on synthesis of M41S type molecular sieves and their surface modification by reactive organic functional groups by different approaches. The merits and demerits of these approaches by extensive characterization (XRD, N_2 adsorption,

CP MAS NMR, SEM, TEM, TG-DTA and microanalyses) of these parent and organically modified materials are highlighted.

Chapter 3. Immobilization of transition metal complexes for selective reduction

Chapter 3 deals with a novel heterogeneous catalyst system containing immobilized Ru-biphosphine-diamine complexes in mesoporous supports like MCM-41 and MCM-48 for enantioselective hydrogenation of prochiral ketones and chemoselective hydrogenation of α,β-unsaturated aldehydes. The synthesis methods for immobilization and characterization of these heterogeneous catalysts by XRD, N_2 adsorption, FTIR, ^{31}P CP MAS NMR, TEM and XPS are discussed in detail. ICP-AES analyses of the catalysts before and after the reactions and that of the reaction mixtures were performed to investigate the leaching of Ru under reaction conditions. Results of catalytic hydrogenation of different olefins, enantioselective hydrogenation of prochiral ketones, and chemoselective hydrogenation of α,β-unsaturated aldehydes under different reaction conditions are discussed with intrinsic details.

Chapter 4. Formation and stabilization of metal nanoparticles

Chapter 4 focuses on a novel method for the synthesis and simultaneous stabilization of gold nanoparticles by spontaneous reduction of aqueous chloroaurate ions ($AuCl_4^-$) by organically modified mesoporous silica materials, such as propylamine- and propylthiol-functionalized MCM-41. The probable mechanism of the formation of gold nanoparticles has been supported by similar experiments with amorphous silica. These nanocomposites have been characterized by UV-Vis, XRD, N_2 adsorption, XRF, XPS, TEM and TG-DTA. The catalytic activity of these gold catalysts in preferential oxidation of carbon monoxide and in hydrogenation of unsaturated hydrocarbons under different reaction conditions is discussed in detail.

Chapter 5. Summary and conclusions

The summary of the results obtained and the basic findings of the present work are presented in this chapter. The scope for future work is also discussed at the end of this chapter.

References

1. A. Stein, B. J. Melde, R. C. Schroden, *Adv. Mater.* **2000**, *12*, 1403.
2. K. Moller, T. Bein, *Chem. Mater.* **1998**, *10*, 2950.
3. R. Noyori (Nobel Lecture 2001), *Adv. Synth. Catal.* **2003**, *345*, 15.
4. R. L. Augustine, *Heterogeneous Catalysts in Organic Synthesis*, Dekker, New York, **1995**.
5. D. E. De Vos, M. Dams, B. F. Sels, P. A. Jacobs, *Chem Rev.* **2002**, *102*, 3615.
6. C. E. Song, S. Lee, *Chem. Rev.* **2002**, *102*, 3495.
7. A. Zsigmond, K. Bogar, F. Nothiesz, *J. Catal.* **2003**, *213*, 103.
8. M. Haruta, *Catal. Today* **1997**, *36*, 153.
9. G. C. Bond, D. T. Thompson, *Catal. Rev.-Sci. Eng.* **1999**, *41*, 319.

1.1. GENERAL BACKGROUND

Zeolites are classified as crystalline microporous materials consisting of silicon (Si), aluminium (Al) and oxygen (O) as essential elements, in which the Si and Al are tetrahedrally coordinated by O atoms in a three-dimensional network.[1] The crystallographic unit cell of the zeolites can be represented as:

$$M_{x/n}[(AlO_2)_x (SiO_2)_y] ZH_2O$$

where M is a charge compensating cation with valency 'n'. The ratio 'y/x' may have any value ranging from one to infinity. '*Z*' represents the number of water molecules, which can be reversibly adsorbed and desorbed into the zeolite micropores. The presence of trivalent Al atoms in the lattice develops a unit negative charge per Al atom in the framework, whereas the presence of tetravalent Si do not lead to any such residual charge. The negative charge imposed by the presence of Al atoms is compensated either by Group I or Group II metal cations or by quaternary organic cations.

During the past few decades, enormous studies on the synthesis, characterization and applications of different types of zeolites and related microporous materials formed an important part of materials science, inorganic chemistry and heterogeneous catalysis.[2] Different structural features of zeolites and related microporous materials generating different types of shape selectivities, *viz*., product, reactant and transition state shape selectivities,[3] and their relatively high thermal, hydrothermal and chemical stabilities have been well studied, leading to their application as catalysts for oil refining, petrochemistry and organic synthesis in the production of fine and specialty chemicals. Furthermore, microporous zeolitic materials have earned the reputation of environmentally benign catalysts due to several factors like waste minimization, simple operation, easy work-up and recyclability of the catalysts.[4]

However, the main restriction of microporous materials is the pore size constraints of *ca*. 0.75 nm and therefore, they are not suitable for catalytic transformations involving organic molecules having kinetic diameters above 0.75 nm, which are important precursors in synthesis of fine chemicals. Hence, there has been an ever-growing interest in expanding the pore sizes of the zeolitic materials from micropore to mesopore region.[5]

The synthesis of surfactant-templated mesostructures is one of the most exciting discoveries in the field of materials synthesis in the last decade.[6] The discovery of hexagonally ordered mesoporous silicate structures by Mobil Corporation (M41S materials)[6a,b] and by Kuroda *et al*. (FSM-16 materials)[6c,d] pioneered a new era in materials science. These materials possess extremely high surface areas and easily accessible, well-defined mesopores, which broke past the pore size constraint of microporous zeolites. However, a number of limitations were associated with the original mesoporous silicates and aluminosilicates, such as lower hydrothermal stability and lower reactivity than zeolites with equivalent compositions. But, the flexibility to tune these mesoporous structures on nanoscale in a precise manner, by choosing appropriate surfactant templating system or employing some cosolvent, proved to be so important that many of these limitations have been negotiated and overcome by several research groups.[7] New investigations on different aspects of these materials, such as synthesis procedures, synthesis mechanisms, heteroatom insertion, stability, surface modification, physicochemical characterization, adsorption, catalytic applications *etc*., created an explosion in materials research.[5,8]

The M41S type mesoporous materials are classified into three categories: MCM-41, MCM-48 and MCM-50, with hexagonal 'honeycomb', cubic 'gyroid' and lamellar structures, respectively.[5,6a,b] The synthesis of these materials opens new possibilities for preparing catalysts with uniform pores in the mesoporous region, which will allow the access to relatively larger organic molecules for catalytic transformations.[9]

1.2. SYNTHESIS AND MECHANISM OF FORMATION OF MESOPOROUS SILICA

The M41S family of mesoporous materials are synthesized using a silica source and different organic structure directing agents, *e.g*., cationic surfactants containing long alkyl chain quaternary ammonium compounds containing 10–20 carbons, often followed with addition of cosurfactants. The dependence of surfactant/silica molar ratio in a ternary synthesis system containing tetraethylorthosilicate (TEOS, silica source), water and cetyltrimethylammonium ($C_{16}TMA^+$) cations (surfactant) at 100 °C on appearance of different phases of M41S family is summarized in Table 1.1.[10]

Table 1.1. Effect of surfactant/silica molar ratio on emergence of different mesophases

Surfactant/silica	Different phases of M41S type materials
< 1.0	Hexagonal (*p6mm*, MCM-41)
1.0 – 1.5	Cubic (*Ia3d*, MCM-48)
1.2 – 2.0	Thermally unstable materials
2.0	Cubic octamer $[(C_{16}TMA)SiO_{2.5}]_8$

A number of models have been proposed to rationalize the mechanism of formation of mesoporous materials by various synthesis routes. All these models are based on the role of surfactants in solution to direct the formation of silicate mesostructure. In solution, the surfactants have a hydrophilic head group and a long chain hydrophobic tail group within the same molecule, which will aggregate and self-organize in such a way so as to minimize the contact between the incompatible ends. Different types of interaction between the surfactant and the inorganic precursor under different synthesis conditions leads to different postulates for the mechanism of formation of mesoporous materials, which will be discussed briefly in this section.

1.2.1. Liquid Crystal Templating (LCT) Mechanism

The researchers of Mobil Corporation proposed a 'liquid crystal templating (LCT) mechanism' to explain the formation of M41S type mesoporous materials.[6a,b] The mesostructure formation depends on the hydrocarbon chain length of the surfactant tail group,[11] the effect of variation of the surfactant concentration and the additional organic swelling agents. The lowest concentration at which surfactant molecules aggregate to form spherical isotropic micelles is called critical micelle concentration (CMC_1). Further increase in the surfactant concentration initiates aggregation of spherical into cylindrical or rod-like micelles (CMC_2). There are three main liquid crystalline phases with hexagonal, cubic and lamellar structures. The hexagonal phase is the result of hexagonal packing of cylindrical micelles, the lamellar phase corresponds to the formation of surfactant bilayers and the cubic phase may be regarded as a bicontinuous structure.

The Mobil researchers proposed two synthesis mechanisms.[6a,b] In the first route, the $C_nH_{2n+1}(CH_3)_3N^+$ surfactant species organize into lyotropic liquid crystal phase, which can serve as template for the formation of hexagonal MCM-41 structure. Firstly the surfactant micelles aggregate into a hexagonal array of rods, followed by interaction of silicate or aluminate anions present in the reaction mixture with the surfactant cationic head groups. Thereafter condensation of the silicate species occurs, leading to the formation of an inorganic polymeric species. After combusting off the surfactant template by calcination, hexagonally arranged inorganic hollow cylinders are produced (Scheme 1.1). However, the drawbacks of this synthesis pathway was pointed out by Cheng *et al.*,[12] according to whom the hexagonal liquid-crystal phase does not form below 40% of surfactant concentration. It is known that MCM-41 may be formed at low surfactant concentrations (1 wt %) with respect to water content, and *in situ* ^{15}N NMR spectra indicated that the hexagonal liquid-crystalline phase was not present anytime during formation of MCM-41.[13]

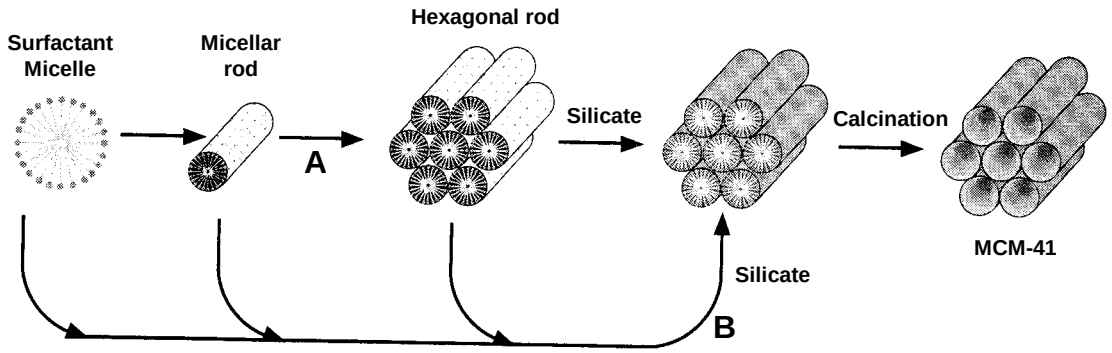

Scheme 1.1. Liquid crystal templating (LCT) mechanism proposed for the formation of MCM-41; (A) liquid crystal phase initiated and (B) silicate anion initiated. [Source: Ref. 6b]

In the second route, the hexagonal ordering is initiated by the presence of silicate species in the reaction mixture.[6a,b] Chen *et al*. explained that randomly distributed surfactant micelles with rod-like morphology form initially, and their interaction with silicate oligomers generate randomly oriented surfactant micelles surrounded by two or three silica monolayers.[13] The presence of rod-like micelles in solution was supported by isotropic *in situ* ^{14}N NMR.[13] Further condensation between silicate species on adjacent rods occurs on heating, initiating the long-range hexagonal ordering (Scheme 1.2).

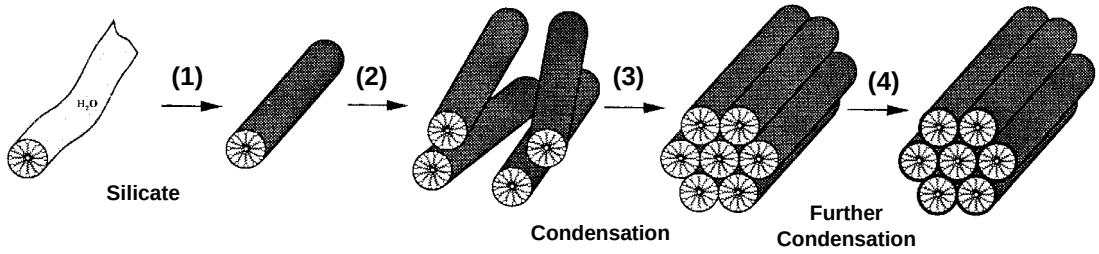

Scheme 1.2. Silicate rod assembly proposed for the formation of MCM-41; (1) and (2) random ordering of rod-like micelles and interaction with silicate species, (3) spontaneous packing of the rods, and (4) remaining condensation of silicate species on further heating. [Source: Ref. 13]

1.2.2. Charge Density Matching

The 'charge density matching' model proposed by Stucky *et al*. suggested that condensation occurs between initially formed silicate species by the electrostatic interaction between the anionic silicates and the cationic surfactant head groups.[14] This eventually reduces the charge density and therefore, curvature was introduced into the layers to maintain the charge density balance with the surfactant head groups, which leads to transformation of the lamellar mesostructure into the hexagonal one (Scheme 1.3.A). Although this silica-initiated synthesis mechanism has been widely accepted, the presence of an intermediate lamellar species has been disputed.

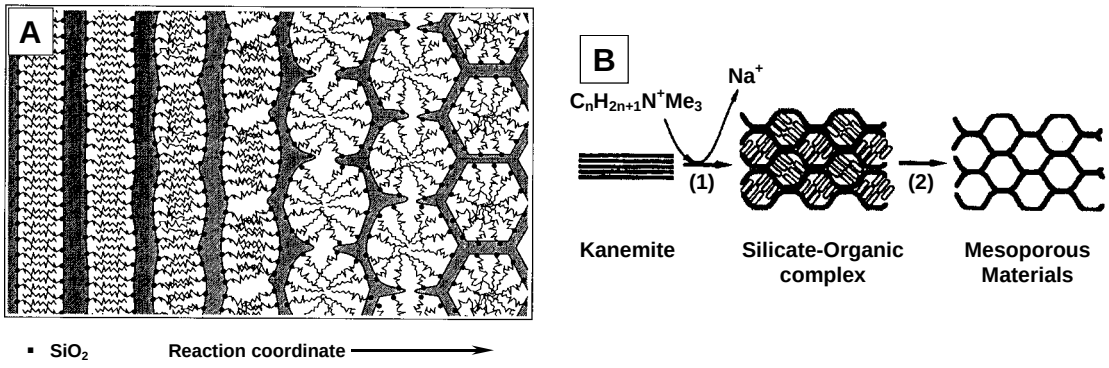

Scheme 1.3. Transformation of surfactant-silicate systems from lamellar to hexagonal mesophases; (A) hexagonal mesophase obtained by charge density matching, and (B) folding of kanemite silicate sheets around intercalated surfactant molecules. [Source: Refs. 14 and 6d]

1.2.3. Folded Sheet Mechanism

The 'folded-sheet mechanism' postulated by Inagaki *et al*. indicated the presence of intercalated silicate phases in the synthesis medium of the reaction products (Scheme 1.3.B).[6d] The flexible silicate layers of kanemite fold around the surfactant cations, and cross-linking of the interlayer occurs by condensation of silanol groups on adjacent silicate sheets. On increase of pH, the amount of occluded $C_nH_{2n+1}(CH_3)_3N^+$ cations in kanemite

increases resulting in expansion of the kanemite interlayers to form another class of regular hexagonal structure called FSM-16.

.

1.2.4. Silicatropic Liquid Crystals

Firouzi *et al*. have developed a model based on cooperative organization of inorganic and organic molecular species into 3D structured arrays.[15] According to this model, the physicochemical properties of a particular system were not determined by the organic arrays having long-range preorganized order, but by the dynamic interplay among ion-pair inorganic and organic species, so that different phases can readily be obtained through small variation of controllable synthesis parameters. The exchange of silicate anions with the surfactant halide counter ions formed the 'silicatropic liquid crystal' (SLC) phase (Scheme 1.4), which exhibited very similar behavior to that of typical lyotropic systems and finally condensed irreversibly into MCM-41.

1.2.5. Generalized Liquid Crystal Templating Mechanism

1.2.5.1. Ionic Route (Electrostatic Interaction)

Huo *et al*. proposed a generalized mechanism for the formation of mesostructures, which was based on specific types of electrostatic interaction between an inorganic precursor (I) and a surfactant head group (S).[16] In this concept, four different approaches were proposed to synthesize transition metal oxide mesostructures.[16a] The first route involves the charge density matching between surfactant cations and inorganic anions (will be referred to as S^+I^- hereafter). The second route deals with the charge-reversed situation, *i.e.*, anionic surfactant and cationic inorganic species (S^-I^+). Both the third and fourth routes are counterion-mediated pathways. The third one demonstrates the assembly of cationic species *via* halide ions ($S^-X^+I^-$), while the fourth one depicts the assembly of anionic

species *via* alkali metal ions ($S^+X^-I^+$). These synthesis strategies are acceptable for the formation of a wide variety of lamellar, hexagonal or cubic mesophases. However, a general problem negotiated very often is the poor stability of the inorganic framework, which frequently collapses after removal of the surfactant.

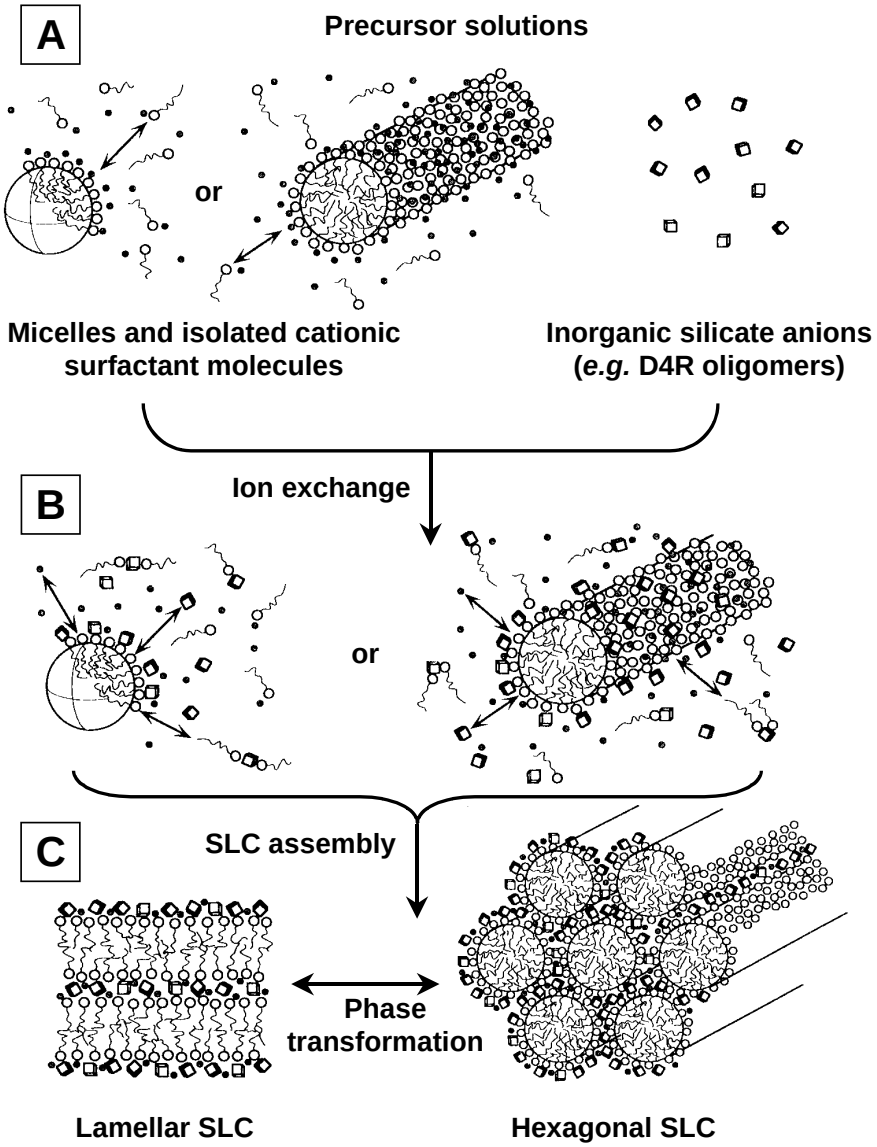

Scheme 1.4. Cooperative organization for the formation of silicatropic liquid crystal phase / silicate-surfactant mesophases; (A) organic and inorganic precursor solutions, (B) preliminary interaction of the two precursor solutions after mixing, and (C) multidentate interaction of the oligomeric silicate units with the surfactant molecules. [Source: Ref. 15]

1.2.5.2. Neutral Templating Route (Hydrogen Bonding Interaction)

Tanev and Pinnavaia proposed another route to synthesize hexagonal mesoporous silicas (HMS) having thicker pore walls, high thermal stability and smaller crystallite size but, having higher amounts of interparticle mesoporosity and lower degree of long-range ordering of pores than MCM-41 materials.[7b,17] This route is essentially based on hydrogen bonding between neutral primary amines (S^0) and neutral inorganic precursors (I^0), wherein hydrolysis of tetraethyl orthosilicate (TEOS) in an aqueous solution of dodecylamine yields neutral inorganic precursor. Using the same approach, porous lamellar silicas with vesicular particle morphology have been synthesized with the aid of double headed alkylamines linked by a hydrophobic alkyl chain (α,ω-dialkylamine).[17b]

1.2.5.3. Ligand-Assisted Templating Route (Covalent Interaction)

Antonelli and Ying have proposed a ligand-assisted templating mechanism for the synthesis of hexagonally packed mesoporous metal oxide completely stable to surfactant removal.[18] In a typical synthesis, the surfactant was dissolved in the metal alkoxide precursor before addition of water to allow nitrogen–metal covalent bond formation between the surfactant head group and the metal alkoxide precursor. The existence of this covalent interaction was confirmed by ^{15}N NMR spectroscopic studies. In this approach, the structure of the mesophases could be controlled by adjustment of the metal/surfactant ratio, which led to a new class of mesoporous transition metal oxides analogous to M41S family.

1.3. CONTROL OF CRYSTAL SIZES, PORE SIZES AND MORPHOLOGY

The past decade saw extensive research to control the crystal size, pore dimensions and pore sizes of ordered mesoporous materials, particularly for MCM-41 with

unidirectional channels. The control of crystal size is of immense importance when these materials are to be used in catalytic processes. The length of the pores must be decreased as much as possible to overcome diffusion limitations, which is normally done by decreasing crystallite size. Wu *et al*. have synthesized thermally stable hexagonal mesoporous materials of smaller crystal sizes (~100 nm) by microwave heating of precursor gels at 150 ºC for not more than 1 h.[19] The fast and homogeneous condensation reactions occurring during microwave synthesis leads to smaller crystal sizes and high thermal stability.

The characteristic feature of the M41S type molecular sieves is the flexibility to synthesize these materials with different pore diameters ranging from 2–10 nm. This can be achieved by the following ways: (i) variation of the chain length of the hydrophobic alkyl group (8 to 22 carbon atoms) in the surfactant molecules,[6b] (ii) addition of organic swelling agents such as 1,3,5-trimethylbenzene,[6b] or alkanes of different chain length,[20] which will increase the micellar size by solvation of the added hydrophobic molecules in the hydrophobic region of the micelles, and (iii) by adjusting the composition of the gel and the crystallization variables.[21] Sun and Ying have demonstrated the tailoring of pore sizes between 0.5 and 2 nm employing short-chain alkylamines as supramolecular templates, *via* the "ligand-assisted templating" route.[18,22]

The morphology of the mesoporous materials obtained by Beck *et al*. consisted of aggregates and loose agglomerates of small particles.[6a,b] However, well-defined morphologies like fibers, thin films, spheres, monoliths *etc*. of these mesoporous materials are required for a wide range of applications such as membranes for large molecule catalysis, separation, optical sensors, slow drug release systems, templates for the assembly of nanostructures, masks for high-resolution lithography, low dielectric constant films for microelectronics and other interface-controlled processes. Huo *et al*.[16a] and Yang *et al*.[23] have synthesized mesoporous silica with highly curved morphologies (toroidal, disk-like,

spiral and spheroidal shapes) in acidic medium *via* the $S^+X^-I^+$ route. Mesoporous fibers (length 50–1000 μm) have been prepared in oil-in-water emulsions[24] and in aqueous phase[25] under acidic conditions ($S^+X^-I^+$). Highly oriented mesoporous free-standing films (diameter ≤10 cm, thickness ~10–500 mm) have been synthesized at the air-water[26] and oil-water[24] interfaces, on both mica[27] and the graphite[28] surfaces and by using dip- or spin-coating[29] methods. The syntheses of hollow (diameter 1–100 μm)[24] as well as hard (diameter 0.1–2 mm)[30] mesoporous silica spheres were achieved through emulsion biphasic chemistry, whereas monolithic periodic mesoporous silica (diameter 150–500 nm, interparticle pores on the order of particle size) was prepared by different systems using ionic[31] and neutral surfactants.[32] Another morphology with vesicle like hierarchical structures, consisting of one or more undulated silica sheets (thickness 3 nm, mesopore diameter 2.7–4.0 nm) running both parallel and orthogonal to the silica sheets, was prepared by Kim *et al*. using neutral gemini surfactants.[7d]

1.4. SURFACE MODIFICATION OF MESOPOROUS SILICA

The application of pure mesoporous silicates or aluminosilicates as catalysts is rather limited because of the limitations in the nature of their active sites, leading to limited scope of the reactions they could accomplish. To utilize these mesoporous materials for several specific applications including catalysis and also sorption, ion exchange, sensing *etc*., the introduction of reactive organic functional groups by modifying the inner surfaces of these materials, to form inorganic–organic hybrid materials, is essential.[33] The inorganic components of these inorganic–organic hybrid materials can provide mechanical, thermal or structural stability, while the organic components can introduce flexibility into the framework and can more readily be modified for specific applications.[34] The presence of large amount of silanol groups in the surfaces of M41S materials could be exploited for

anchoring of desired organic functional groups by condensation with necessary alkoxysilane precursors.[35] These parent organic functional groups, with or without further modification, can facilitate anchoring of different types of catalytically reactive metal particles or organometallic complexes inside the mesoporous network.[36] Different methods for organic modification of mesoporous surfaces will be briefly highlighted in this section.

1.4.1. Grafting Methods

Grafting refers to post synthesis modification of the inner surface of mesoporous silica, where the organic functional groups are introduced as the terminal groups of an organic monolayer.[37] The large concentration of surface silanol [$(–SiO)_3Si–OH$)] groups present in mesoporous silica can be utilized as convenient moieties for anchoring of organic functional groups.[38] The surface modification with organic functional groups is generally carried out by silylation, as depicted in Scheme 1.5.

The surfactant molecules from the mesopores are usually removed either by calcination or by extraction with appropriate solvents. At typical calcinations temperatures (~500 °C) several surface silanol groups are lost after condensation of unreacted silanol groups. However, it is necessary to maintain a large concentration of surface silanol groups after calcination, if a high coverage of organic functional groups on the surfaces is desired. This can be achieved by treatment of calcined mesoporous silica with boiling water[39] or steam,[40] or by acid hydrolysis.[41] Solvent-extraction processes reduce the possibility of loss of surface silanol groups, although thermal treatments after extraction can increase the surface reactivity towards silylation.

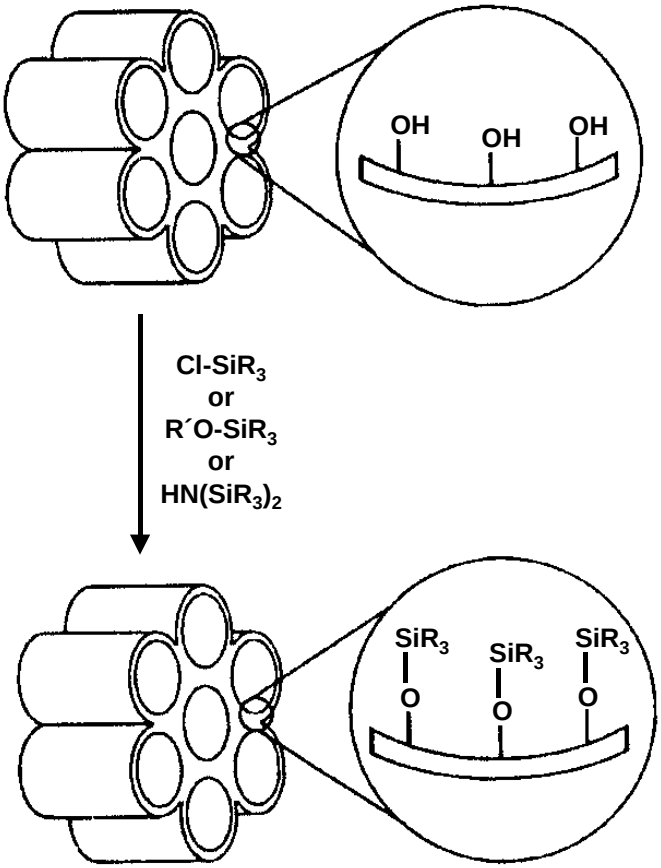

Scheme 1.5. Functionalization of inner walls of mesoporous silicates by grafting. [Source: Ref. 33]

1.4.1.1. Grafting with Passive Surface Groups

Organic functional groups with lower reactivity such as alkyl or phenyl groups could be grafted to alter the accessible pore volume of mesoporous silica, thereby enhancing the hydrophobicity of the surface and protecting towards hydrolysis. The pore diameters of ordered mesoporous materials could be adjusted by varying the alkyl chain length of the silylating agent or the quantity of the silylating agent.[42] The most commonly used surface modifying agents containing lower reactive functional groups are trimethylchlorosilane (Me_3SiCl),[6d,43] and hexamethyldisilazane [$(Me_3Si)_2NH$].[44]

1.4.1.2. Grafting with Reactive Surface Groups

Grafting of the mesopore surfaces with reactive functional groups like olefin, cyanide, thiol, amine, halide, epoxide *etc*. permits further functionalization of the surface. Further functionalization includes hydroboration[45] and bromination[44] of olefins (vinyl groups), hydrolysis of cyanides to carboxylic acids,[46] oxidation of thiols to sulfonic acids,[47] alkylation and nucleophilic substitution of amines,[48] and nucleophilic substitution of halides.[49] After the desired modification of the reactive functional groups, a rational design for anchoring of catalytically active transition metal complexes onto mesoporous network could be made.[50]

1.4.1.3. Site-Selective Grafting

For grafting of organic functional groups, the external surface of the mesoporous materials is kinetically more accessible than the internal surface and is functionalized predominantly.[51] To minimize the grafting on the external surface, it is necessary to passivate the silanol groups on the external surface before functionalizing those on the internal surface. Shephard *et al*. have carried out the passivation of external surface with dichlorodiphenylsilane (Ph_2SiCl_2) first, and functionalization of internal surface with 3-aminopropyltrimethoxysilane [$(MeO)_3Si(CH_2)_3NH_2$] thereafter.[52] The existence of the amine functional groups almost entirely on the internal surface was confirmed by high-resolution transmission electron microscopy (HRTEM).

In a different approach, grafting of the external surface by Me_3SiCl was carried out on the as-prepared mesoporous material without the surfactant being removed from the mesopores.[53] Grafting occurred mainly on the external surface due to steric constraint of the surfactant. After solvent extraction of the surfactant the internal surface was functionalized with the desired organic group. An alternate pathway by Antochshuk and Jaroniec describes

simultaneous grafting of Me_3SiCl and extraction of surfactant template, by refluxing as-synthesized MCM-41 material with neat Me_3SiCl.[54] Since the calcination step is not required in these two processes, larger number of surface silanol groups is likely to be present inside the mesopores.

1.4.2. Co-condensation Reactions

In the grafting methods, incorporation of organic groups is done by attachment of the organosiloxane precursor with surface Si atoms through Si–O–Si–C covalent bond formation (Scheme 1.5). Then Si–O can be cleaved at some reaction conditions as experienced by Price *et al*.[37] Therefore, in some cases it would be desirable to have direct formation of a C–Si (surface) covalent bond. Thus, the "one-pot" co-condensation method, where condensation occurs between a tetraalkoxysilane and one or more trialkoxyorganosilanes through sol-gel chemistry, seems to have distinct advantages over the grafting methods (Scheme 1.6).[55] Several research groups have employed this method to prepare inorganic–organic hybrid mesoporous materials under a wide range of synthesis conditions.[45,56] Usually the solvent extraction technique is used to remove the surfactant from the resultant materials. The co-condensation reactions proceed through different pathways, which will be discussed briefly in this section.

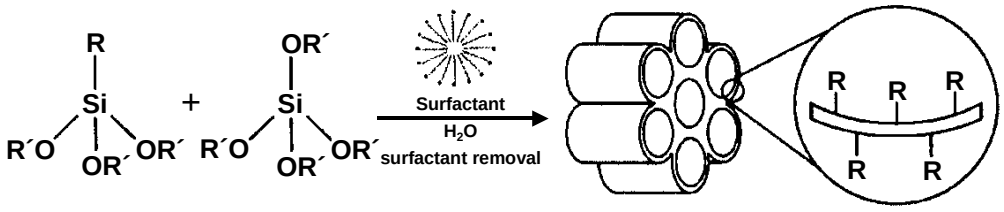

Scheme 1.6. Synthesis of organo-functionalized mesoporous silicates by co-condensation. [Source: Ref. 33]

1.4.2.1. S^+I^- Pathway

This pathway refers to condensation between anionic silica precursors (I^-), obtained under basic conditions, initiated by cationic surfactant (S^+) micelles. The surfactants are normally extracted with acid-alcohol mixtures.[13,44] It has been observed that the d_{100} spacing and the pore size of the channels are significantly reduced as the concentration of the trialkoxyorganosilane increases, even when the same surfactant is used.[51,56b] Simultaneously, an increase in wall thickness has been observed, probably because of protrusion of organic groups into the channels. The decrease in cell dimensions may be attributed to the interaction between nonpolar organic groups and the surfactant tails, which drag the organic precursor further into the micelles.

Functionalization with two or more organic groups is also possible in this pathway.[57] However, the functional groups are randomly distributed in the resultant material, and their location cannot be controlled as precisely as done by the grafting processes mentioned earlier.

1.4.2.2. $S^+X^-I^+$ Pathway

In this pathway interaction of cationic silicate precursors (I^+), obtained under acidic conditions, occurs with the S^+X^- pair, where S^+ represents cationic surfactant species and X^- denotes anions generated from the acid.[56d,58] Unlike the S^+I^- pathway, a simple extraction technique using pure solvent can be used to remove the surfactant.

1.4.2.3. S^0I^0 Pathway

This mechanism deals with a weak interaction between a neutral silica precursor (I^0) and neutral surfactant micelles (S^0).[56c,59] In this case also, surfactant removal can be achieved by extraction with pure solvent. The pore volume and surface area do not vary

systematically with increasing concentration of the organosilane, but smaller pore sizes have been obtained with increasing the same.[59b]

1.4.2.4. N^0I^0 Pathway

In this pathway, non-ionic surfactants (N^0) like alkylpoly(ethyleneoxide) are used as the template, and the syntheses are carried out at neutral pH.[60] Worm-like channel structures have been obtained in this method. The cell dimensions usually get reduced with higher loading of organic functional groups.[60a]

1.4.2.5. Inorganic–Organic Hybrids with Organic Moiety in the Framework

The co-condensation method has recently been employed to create organic–inorganic hybrid materials lacking long-range ordering and containing the organic moiety as component of the solid network.[61] The templates used in the syntheses of these materials consist of two trialkoxysilyl groups connected by an aliphatic chain (Scheme 1.7). Inagaki *et al*. have first reported the synthesis of "periodic mesoporous organosilica" (PMO) with organic functional groups uniformly incorporated in the mesoporous walls, using 1,2-bis(trimethoxysilyl)ethane (BTME) as the framework precursor and octadecyltrimethylammonium chloride as the surfactant.[61a,b] By varying the synthesis conditions, three highly ordered mesoporous structures have been obtained: (a) a 2D hexagonal mesophase (hexagonal rod-like morphology), denoted as HMM-1; (b) a 3D hexagonal mesophase (spherical morphology), denoted as HMM-2; and (c) a cubic mesophase (decaoctahedral morphology), denoted as HMM-3.

Asefa *et al*.[61c] and Melde *et al*.[61d] have studied the co-condensation of either 1,2-bis(triethoxysilyl)ethane (BTSE) or 1,2-bis(triethoxysilyl)ethylene BTSEY with silica precursors to synthesize hexagonal hybrid framework materials under basic reaction

conditions. Melde *et al*. have designated their materials as "unified organically functionalized mesoporous networks" (UOFMN), having worm-like channel systems and lacking long-range ordering.[61d] Both of the materials synthesized by Asefa *et al*. and Melde *et al*. have higher hydrothermal stability than M41S materials synthesized under identical conditions.

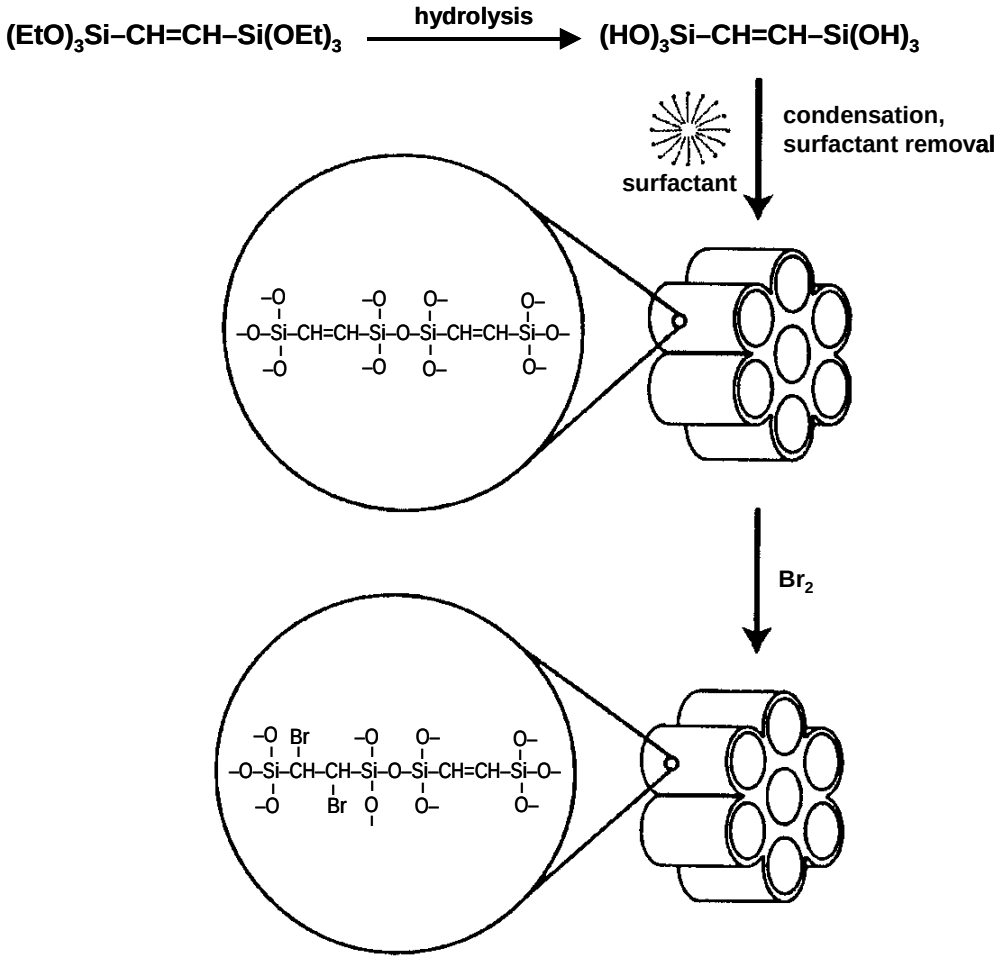

Scheme 1.7. Synthesis of mesoporous materials with reactive organic functional groups on the solid framework. [Source: Ref. 33]

1.5. MESOPOROUS SILICA AS SUPPORT OR HOST

The ordered hexagonal MCM-41 and cubic MCM-48 materials possess narrow and controlled pore size distribution and large pore openings, which has stimulated fundamental

research in inclusion of metal,[62] metal oxide[63] and semiconductor nanoclusters,[64] and metal complexes[2g,9] inside the mesoporous channels. The reactivity of the internal surfaces of mesoporous silica has been widely exploited by anchoring of several organic functional groups on the channel walls, as discussed in the previous section. These functional groups can act as ligands to form bulky metal complexes,[2g] and also can act as capping agents for nanoclusters in order to stabilize them inside the network.[62e]

1.5.1. Immobilization of Transition Metal Coordination Compounds

Since the mesoporous surfaces are inert towards abrasion and biodegradation, several strategies were developed for the incorporation of metal complexes into the mesoporous channels. An outline of these will be discussed in this section.

1.5.1.1. Adsorption

Ligands containing a sulfonic acid functional group can be adsorbed onto silica surfaces through hydrogen bonding interactions with the surface silanol groups (Scheme 1.8). Following this strategy, Bianchini *et al*. have immobilized rhodium(I)–norbornadiene (Rh^I-nbd) complexes through a sulfonate-functionalized chiral diphosphine ligand hydrogen-bonded to silica surface.[65] In a different approach, De Rege *et al*. have immobilized a Rh^I-diphosphine complex containing a trifluoromethanesulfonate (triflate) counterion, which can be hydrogen-bonded to the silanol groups.[66] Several research groups have reported adsorption of complexes of platinum grouped metals onto hexagonal mesoporous silica surfaces functionalized with propylamine moiety (Scheme 1.9).[67] The adsorption methodologies are comparatively easier than the other strategies (to be discussed next), but are likely to produce less stable composite materials.

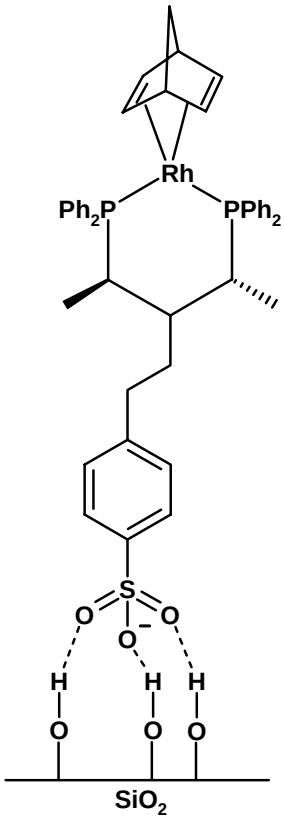

Scheme 1.8. Immobilization of $Rh^{I}[(R,R)\text{-BDPBzPSO}_3]^-$ complex on mesoporous silica by hydrogen bonding interactions. [Source: Ref. 65]

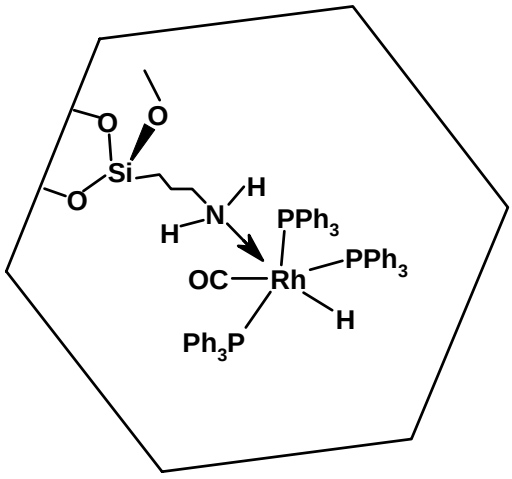

Scheme 1.9. Adsorption of Wilkinson's hydroformylation catalyst on mesoporous silica. [Source: Ref. 67c]

1.5.1.2. Covalent Tethering

The covalent tethering techniques are the most favored ones to design stable hybrid materials. Ligands containing –OH, $–NH_2$ groups can be grafted directly onto the silica surface, prefunctionalized with a propylhalide group, through a nucleophilic substitution mechanism (Scheme 1.10).[49] Using this approach, several ligands such as amino alcohols[68] or diamines[69] were anchored into the surfaces of chloropropyl-functionalized MCM-41 before complexation with the desired metal ion. Few metal–salen complexes were also immobilized on aminopropyl-functionalized MCM-41 following similar strategy, as demonstrated by Baleizao *et al*.[70] and Kim and Park.[71] Complexes containing ligands like bisoxazoline,[72] ferrocenyl[73] *etc*., or the Sharpless catalyst system[74] can be modified by trialkoxysilane moieties, so that they can be grafted *via* condensation with the surface silanol groups (Scheme 1.11).

1.5.1.3. Ion Exchange (Electrostatic Interaction)

A large number of metal complex cations can be immobilized through electrostatic interactions utilizing the existence of extraframework cations on ordered mesoporous silica materials. This ion exchange method is conceptually simple and has been observed to produce stable hybrid materials. Copper pyridine $[Cu(py)_4]^{2+}$ complexes were the first to be incorporated inside the mesoporous network by ion exchange.[75] Later on, a series of cationic diphosphine[76] and bisoxazoline[77] chelate complexes were ion-exchanged inside the porous network.

1.5.1.4. Direct Synthesis

This is the only process that does not require any interaction between the metal complex and the silica support. Other methods, by some means, resulted in changes in the

complex, which may influence the conformation and electronic properties of the ligand. Hoppe *et al*. were the first to introduce metal phthalocyanine complexes directly into the mesoporous hosts by adding into the synthesis gel and hydrothermal treatment thereafter.[78] The hexagonal structure of MCM-41 was formed under inclusion of the phthalocyanine complex in the surfactant micelles.

Macrocyclic compounds like 5-dodecyl-12,17-dimethyl-1,5,9,12,17-pentaazobicyclo [7.5.5]nonadecane (C_{12}CESTO) can coordinate with metal ions as well as can form micelles with the template of MCM-41. Poppl *et al*. have employed this cage compound for immobilization of cuprous ions (Cu^{2+}) into the MCM-41 pores.[79]

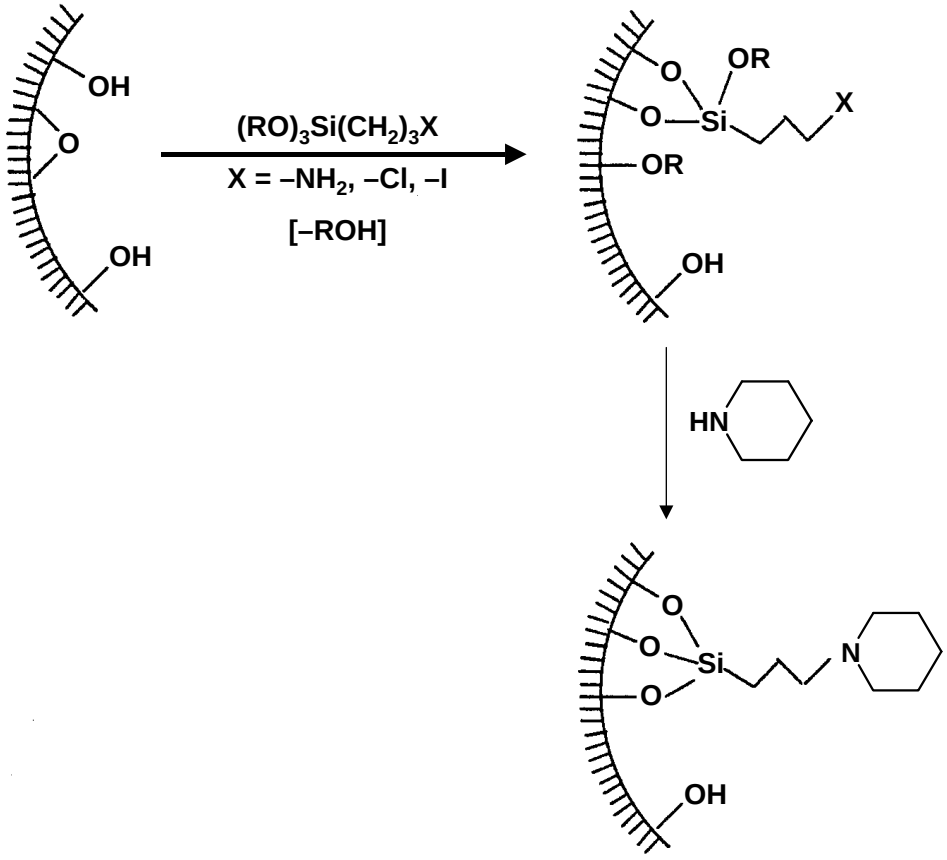

Scheme 1.10. Anchoring of piperidine moiety on inner surfaces of mesoporous silica by nucleophilic substitution. [Source: Ref. 49]

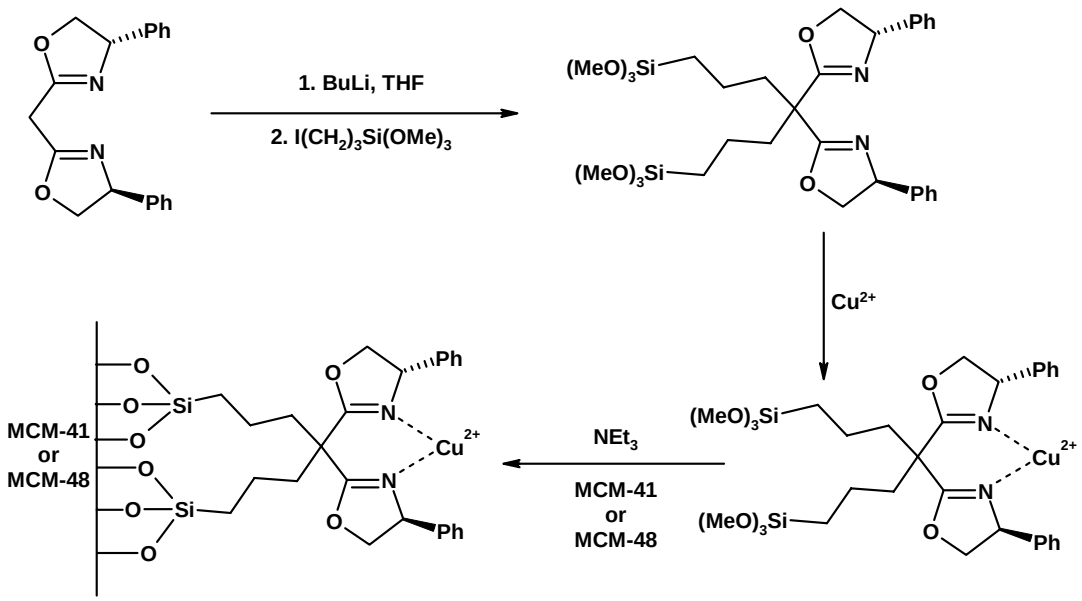

Scheme 1.11. Covalent immobilization of Cu^{II}-bisoxazoline complex on mesoporous silica through sulfonation followed by condensation. [Source: Ref. 72b]

1.5.2. Stabilization of Transition Metal Nanoparticles

During the last few decades a substantial amount of research has been aimed towards the synthesis and size-dependent physicochemical properties of nanoparticles because of their enormous importance in a variety of applications, *viz*., catalysis,[80] optoelectronics,[81] biomineralization,[82] as electron microscopy markers,[83] in DNA sequence determination,[84] to mention just a few. Ryoo *et al*. have prepared platinum (Pt) nanoclusters and nanowires inside the channels of mesoporous silica through consecutive ion exchange, impregnation and thermal reduction of Pt^{II}.[85] Schuth *et al*. have synthesized monodispersed palladium (Pd) nanoclusters by reduction Pd^{II} in presence of phenanthroline stabilizers, followed by incipient wetness impregnation into the mesoporous host.[62b] Several other transition metal[62c,d] and bimetallic nanoparticles[86] were introduced into the channels of mesoporous silicates and the resultant nanocomposites were employed in various applications.[87]

Colloidal nanoparticle solutions are also being known for a long time[88] and a large number of methods for their synthesis are also available in literature.[89] These nanoparticles have a tendency to agglomerate slowly depending on synthesis conditions. To prevent this agglomeration, Brust *et al*. have stabilized gold (Au) nanoparticles using surfactant molecules containing polar head groups like thiol (–SH).[90] Later on, formation of self-assembled monolayers (SAMS) of long aliphatic chain alkylamine molecules on metal nanoparticle surfaces was also established.[91] These surfactant molecules through their –SH or $–NH_2$ head groups bind to the surface of the nanoparticles through covalent linkage and prevent further growth beyond the initial stage of nucleation.[92]

Mesoporous silica materials with their inner surfaces functionalized with propylamine and propylthiol groups are particularly important in this regard since they have the necessary polar head groups generally required to stabilize the nanoparticles.[62e,93] Further, they provide a solid support of well-defined pores to the nanoclusters. These inorganic–organic nanohybrid materials can be envisaged as a three-layered entity (Scheme 1.12), which are excellent materials for studying non-linear optical properties[94] and 'host-guest' interactions.[95]

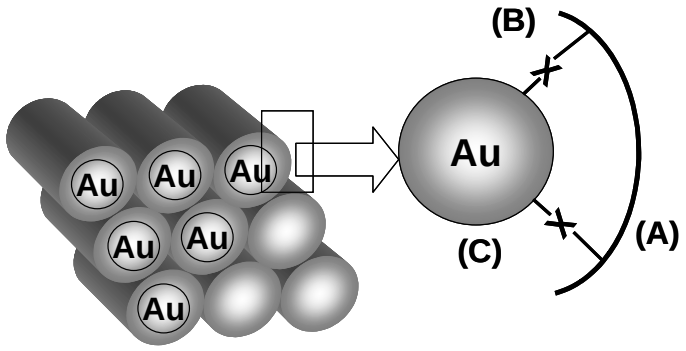

Scheme 1.12. Schematic representation of a three-layered nanocomposite; (A) mesoporous silicate matrix (outer layer), (B) organic functional group –X attached to the inner surface of mesoporous silica (mid layer), and (C) Au nanoparticles hooked to the polar head groups of the organic moiety (inner layer). [Source: Ref. 93a]

1.6. PHYSICOCHEMICAL CHARACTERIZATION

The inorganic–organic hybrid mesostructured materials can be characterized by various techniques, which provide important information about different physicochemical features. The most extensively used techniques can be categorized into the following.

1. Spectroscopic techniques:

(a) Powder X-ray diffraction (XRD), (b) Ultraviolet-visible (UV-Vis) spectroscopy, (c) Fourier transform infrared (FTIR) spectroscopy, (d) Solid state nuclear magnetic resonance (NMR) spectroscopy, (e) X-ray photoelectron spectroscopy (XPS), (f) X-ray fluorescence (XRF) spectrometry, (g) Atomic absorption and emission spectrometry (AAS and AES).

2. Microscopic techniques:

(a) Scanning electron microscopy (SEM), (b) Transmission electron microscopy (TEM).

3. Volumetric techniques:

(a) Porosity measurements by nitrogen (N_2) adsorption (BET method), (b) Acidity measurements by pyridine or ammonia (NH_3) adsorption.

4. Gravimetric techniques:

(a) Thermogravimetric analyses (TGA), (b) Differential thermal analysis (DTA).

1.6.1. X-Ray Diffraction

It is well recognized that X-ray diffraction, based on wide-angle elastic scattering of X-rays, has been the single most important tool to determine the structure of the materials characterized by long-range ordering. The X-ray diffraction patterns are obtained by measurement of the angles at which an X-ray beam is diffracted by the sample. Bragg's equation relates the distance between two *hkl* planes (d) and the angle of diffraction (2θ) as: $n\lambda = 2d\sin\theta$, where λ = wavelength of X-rays, n = an integer known as the order of reflection (h, k and l represent Miller indices of the respective planes).[96] From the

diffraction patterns, the uniqueness of mesoporous structure,[97] phase purity,[98] degree of crystallinity[98] and unit cell parameters[97] of the semicrystalline hybrid materials can be determined.

The identification of phase is based on the comparison of the set of reflections of the sample with that of pure reference phases distributed by International Center for Diffraction Data (ICDD). Unit cell parameter (a_0) of a cubic lattice can be determined by the following equation: $a_0 = d_{hkl}\sqrt{(h^2 + k^2 + l^2)}$, where d = distance between two consecutive parallel lattice planes having Miller indices h, k and l.[96]

X-ray diffraction broadening analysis has been widely used to characterize supported metal crystallites in the nanoscale. The average size of the nanoparticles can be estimated using the Debye-Scherrer equation: $D = k\lambda / \beta\cos\theta$, where D = thickness of the nanocrystal, k is a constant, λ = wavelength of X-rays, β = width at half maxima of (111) reflection at Bragg's angle 2θ.[99]

1.6.2. Diffuse Reflectance UV-Vis Spectroscopy

UV-Vis spectroscopy deals with the study of electronic transitions between orbitals or bands of atoms, ions or molecules in gaseous, liquid and solid state. In the case of transition metal ions or atoms, any change in their coordination sphere may affect their optical properties and therefore can be characterized by UV-Vis.[100] For solid substances like transition metal containing mesoporous materials, diffuse reflectance UV-Vis spectroscopy (DRUV-Vis) is applied to determine the ligand field symmetry and oxidation state of the metal inside the solid matrices. Thus DRUV-Vis is a sensitive probe to examine the type of the sites, framework or extra-framework, in which that metal ion or cluster exist.[101]

For a vast period of time metallic nanoparticles have fascinated researchers due to their colorful colloidal solutions.[102] Mie explained the origin of this color theoretically by

solving Maxwell's equation for the absorption and scattering of electromagnetic radiation by small metallic particles.[103] This absorption of electromagnetic radiation by metallic nanoparticles originates from the coherent oscillation of the valence band electrons induced by an interaction with the electromagnetic field. These resonances are known as surface plasmons, which occur only in the case of nanoparticles and not in the case of bulk metallic particles.[104] Hence, DRUV-Vis can be utilized to study the unique optical properties of the hybrid mesoporous materials containing occluded metallic nanoparticles, exploiting the size- and shape-dependent surface plasmon resonance.[105]

1.6.3. Fourier Transform Infrared Spectroscopy

Fourier transform infrared (FTIR) spectroscopy deals with the vibration of chemical bonds in a molecule at various frequencies depending on the elements and types of bonds. After absorbing electromagnetic radiation the frequency of vibration of a bond increases leading to transition between ground state and several excited states. The energy corresponding to these transitions corresponds to the infrared region (4000–400 cm^{-1}) of the electromagnetic spectrum. The term Fourier transform (FT) refers to a recent development in the manner in which the data are collected and converted from an interference pattern to an infrared absorption spectrum that is like a molecular "fingerprint".[106]

In the case of porous silicates, the FTIR spectra in the 400–1300 cm^{-1} region provides information about the structural details including isomorphous substitution in framework, whereas the bands in the 3000–4000 cm^{-1} region allows to determine different Bronsted and Lewis acid sites[107] and silanol groups.[108] Acidic and basic properties as well as their strength can also be estimated using carbon dioxide (CO_2), ammonia (NH_3), pyridine, triphenylphosphine (PPh_3) *etc*. as probe molecules and their quantitative estimation by FTIR.[109]

1.6.4. Cross-Polarization Magic Angle Spinning NMR Spectroscopy

Nuclear magnetic resonance (NMR) spectroscopy is one of the most powerful tools to investigate structure and dynamics of a molecular system in liquid phase. Atomic nuclei consisting of odd number of protons and/or neutrons possessing a nuclear spin $I \neq 0$ and consequently a magnetic moment $\mu = \gamma\hbar I$ (γ = gyromagnetic ratio), when placed in a magnetic field of strength B_0, Zeeman interaction results in quantized orientations of the nuclear magnetic moments.[110] The nucleus can adopt $2I + 1$ Eigen states with energies $E(m) = -m\gamma\hbar B_0$, where m = (I, I–1,…., –I). Transitions between neighboring energy states ($\Delta m = \pm 1$) can be induced by electromagnetic radiation (energy $E = h\nu$) of frequency $\nu_0 = \gamma B_0/2\pi$.

The chemical shift interaction arises from secondary local magnetic fields induced by the interaction of the electrons surrounding the nucleus. The induced local field opposes B_0 and hence shields the nucleus under observation. The shielding is spatially anisotropic due to the nonspherical electron distribution around the nucleus.[111]

With the advent of sophisticated solid-state NMR techniques, it has become possible to obtain NMR spectra of solids with spectral resolution comparable to that of liquids.[112] Modern high-resolution solid-state NMR spectroscopy allows to elucidate the chemical and structural environment of several atoms (*e.g.* ^{13}C, ^{27}Al, ^{29}Si, ^{31}P, ^{51}V *etc.*) in a solid matrix like that of porous materials.[113] The most popular technique to get high-resolution NMR spectra with narrow line width is the magic angle spinning (MAS), where the solid sample is fast rotated about an axis inclined at a "magic" angle $\theta = 54°44'$ to the direction of B_0.[114]

Cross-polarization (CP) technique does not affect the line width of the spectra, but is applied to improve the sensitivity, *i.e.*, the signal to noise ratio (SNR) of the spectra of nuclei with low natural abundance (*e.g.* ^{13}C, ^{29}Si, ^{31}P *etc.*), and to monitor the spatial proximity of nuclei.[114] CP involves indirect excitation of the less abundant nucleus through magnetization transfer from an abundant spin system (*e.g.* ^{1}H).

1.6.5. X-Ray Photoelectron Spectroscopy

X-ray photoelectron spectroscopy (XPS) is widely used for probing the electronic structure of atoms, molecules and condensed matter. When an X-ray photon of energy $h\nu$ is incident on a solid matter, the kinetic energy (E_k) and the binding energy (E_b) of the ejected photoelectrons can be related as follows: $E_k = h\nu - E_b$.

This kinetic energy distribution of the photoelectrons is fabricated by a series of discrete bands, which symbolizes for the electronic structure of the sample.[115] The core level binding energies of all the elements (other than H and He) in all different oxidation states are unique, which provides instant detection of the chemical composition of the sample after a full range scan.[116] However, to account for the multiplet splitting and satellites accompanying the photoemission peaks, the photoelectron spectra should be interpreted in terms of many-electron states of the final ionized state of the sample, rather than the occupied one-electron states of the neutral species.[117]

1.6.6. X-Ray Fluorescence Spectrometry

X-ray fluorescence (XRF) spectrometry is a powerful multielemental and nondestructive analytical technique, which provides accurate analysis of the global chemical composition of a solid sample, in major elements and in trace elements. When a solid substance is bombarded with X-ray photons of appropriate energy, characteristics radiations of same nature are emitted by the chemical elements of the sample. These emitted X-rays are first collimated and then selectively separated on an analyzing crystal by diffraction applying Bragg's law. The number of emerging X-ray photons are measured with a proportional detector. Corrected intensities from inter-element effects are linearly correlated with certified concentrations of reference materials.[118]

1.6.7. Atomic Absorption and Emission Spectrometry

The principle of atomic absorption is based on energy absorbed during transitions between electronic energy levels of an atom. When some sort of energy is provided to an atom in ground state by a source such as a flame (temperature ranging from 2100–2800 °C), outer-shell electrons are promoted to a higher energy excited state. The radiation absorbed as a result of this transition between electronic levels can be used for quantitative analysis of metals and metalloids present in solid matrices, which have to be dissolved by appropriate solvents before analysis. The basis of quantitative analysis depends on measurement of radiation intensity and the assumption that radiation absorbed is proportional to atomic concentration. Analogy of relative intensity values for reference standards is used to determine elemental concentrations.[119]

Atomic emission spectrometry (AES) is similar to atomic absorption spectrometry (AAS). In both the cases the sample must be atomized in order to obtain usable absorption spectra. However, in contrast to AAS, in AES the sample is heated at a very high temperature (8000–10000 °C), where the atoms in the sample are excited to higher energy levels. When the excited atoms are relaxed and fall back to the ground energy level, radiations are emitted. Measurement of the intensities of the emission forms the basis of quantitative determination.[120]

1.6.8. Scanning Electron Microscopy

Scanning electron microscopy (SEM) is an important tool for morphological characterization of mesoporous molecular sieve materials. A scanning electron microscope can generate an electron beam scanning back and forth over a solid sample. The interaction between the beam and the sample produces different types of signals providing detailed information about the surface structure and morphology of the sample. When an electron

from the beam encounters a nucleus in the sample, the resultant Coulombic attraction leads to a deflection in the electron's path, known as Rutherford elastic scattering. A fraction of these electrons will be completely backscattered, reemerging from the incident surface of the sample. Since the scattering angle depends on the atomic number of the nucleus, the primary electrons arriving at a given detector position can be used to produce images containing topological and compositional information.[121]

The high-energy incident electrons can also interact with the loosely bound conduction band electrons in the sample. However, the amount of energy given to these secondary electrons as a result of the interactions is small, and so they have a very limited range in the sample. Hence, only those secondary electrons that are produced within a very short distance from the surface are able to escape from the sample. As a result, high-resolution topographical images can be obtained in this detection mode.[122]

1.6.9. Transmission Electron Microscopy

Transmission electron microscopy (TEM) is typically used for high resolution imaging of thin films of a solid sample for microstructural and compositional analysis. The technique involves: (i) irradiation of a very thin sample by a high-energy electron beam, which is diffracted by the lattices of a crystalline or semicrystalline material and propagated along different directions, (ii) imaging and angular distribution analysis of the forward-scattered electrons (unlike SEM where backscattered electrons are detected), and (iii) energy analysis of the emitted X-rays.[123] The topographic information obtained by TEM in the vicinity of atomic resolution can be utilized for structural characterization and identification of various phases of mesoporous materials, *viz*., hexagonal, cubic or lamellar.[124] TEM also provides real space image on the atomic distribution in the bulk and surface of a nanocrystal.[125]

1.6.10. Porosity Measurements by N_2 Adsorption

Despite of some theoretical limitations, the Brunauer-Emmett-Teller (BET) method continues to be the most widely used method for the evaluation of surface area, pore volumes and pore size distributions of porous solids from N_2 physisorption isotherm data. The BET equation can be represented as follows: $\frac{p}{v(p_0 - p)} = \frac{1}{v_m c} + \frac{c-1}{v_m c}\frac{p}{p_0}$, where v = volume of N_2 adsorbed by the sample under pressure p, p_0 = saturated vapor pressure at the same temperature, v_m = volume of N_2 adsorbed when the surface is covered with a unimolecular layer, and c = constant for a given adsorbate.[126]

The equation suggests that the plot of $\frac{p}{v(p_0 - p)}$ versus $\frac{p}{p_0}$ should be linear, and from the intercept $\frac{1}{v_m c}$ and slope $\frac{c-1}{v_m c}$, the values of v_m and c can be determined as follows: $v_m = (\text{slope} + \text{intercept})^{-1}$.

Thus the specific surface area (S) of a sample can be determined as follows: $S = \frac{N_0 v_m A}{22414 m}$, where N_0 = Avogadro number, m = amount of solid adsorbent, A = cross-section of the gas molecules (16.2 $Å^2$ for N_2), and S is expressed in $cm^2\ g^{-1}$ unit.

Several computational procedures are available for the derivation of pore size distribution of mesoporous samples from physisorption isotherms. Most popular among them is the Barrett-Joyner-Halenda (BJH) model, which is based on speculative emptying of the pores by a stepwise reduction of p/p_0, and allowance being made for the contraction of the multilayer in those pores already emptied by the condensate.[127] The mesopores size distribution is usually expressed as a plot of $\Delta V_p/\Delta r_p$ versus r_p, where V_p = mesopore volume, and r_p = pore radius. It is assumed that the mesopores volume is completely filled at high p/p_0.

1.6.11. Thermal Analyses

The thermoanalytical techniques, *viz*., thermogravimetric analysis (TGA) and differential thermal analysis (DTA) have been widely used to establish the thermal stability of ordered mesoporous silica. Both TGA and DTA provide important information about the following: (i) temperature programmed desorption (TPD) and removal of physisorbed water below 150 °C, (ii) oxidative decomposition of the occluded organic materials, accompanied by one or several exotherms within 150 °C and 600 °C, and (iii) dehydroxylation occurring from condensation of adjacent silanol groups to form siloxane bonds at or above 600 °C.[128] Further, DTA can also detect any phase transitions if occur.

1.7. CATALYTIC APPLICATIONS AND PROSPECTS

The commercialization of quite a few homogeneous catalytic systems consisting of transition metal complexes is difficult due to some inherent shortcomings, *viz*., (i) complicated work-up of the reaction mixture, (ii) preparation of the pure products not contaminated with catalysts or constituents thereof, (ii) isolation of the valuable catalyst or its constituents, which can be achieved only with high technical complexity and expenditure.[129] The most feasible way to circumvent this problem is to "*heterogenize*" the homogeneous catalyst, by means of immobilization, anchoring, or encapsulation on an inorganic (zeolites or mesoporous materials)[36] or organic (polymeric)[130] solid support.

The concept of heterogenization provides the prospective for extending the benefits of heterogeneous catalysis to homogeneous systems. These benefits include easier separation of catalyst and reaction products leading to shorter work up times, improved process efficiency, the potential for reactivation and reuse of the supported catalyst comprising of expensive ligands. However, the prime requirement of the heterogenization approach is to maintain the stability of the heterogenized complex, such that it does not

decompose or leach out from the solid matrix to the liquid phase during the course of reaction, and at the same time retains high activity, selectivity and original configuration.

The synthesis of enantiomerically pure chiral compounds has fascinated researchers owing to its immense importance in the fine chemical industry.[131] Among the several strategies developed to produce the desired enantiomer of an optically active compound, asymmetric catalysis offers exclusive and enormous advantages.[132] To date, a number of reports are available in literature, where heterogeneous catalysis by immobilized transition metal complexes on mesoporous silica have been addressed for enantioselective reactions.[133] In this section we will review the catalytic applications and prospects of the "transition metal complex–mesoporous silica" composite materials in chemo- and enantioselective hydrogenation reactions.

Transition metal nanoparticles, when deposited on certain metal oxides exhibits surprisingly high catalytic activity in a variety of reactions, *viz*., selective and complete oxidation of hydrocarbons, hydrogenation of hydrocarbons, oxidation and hydrogenation of carbon monoxide *etc*.[134] Hence, nanoparticle-containing hybrid mesoporous materials can be ideal materials for catalyzing similar kind of reactions. In this section, the potential of those nanocomposites in selective oxidation reactions will also be highlighted.

1.7.1. Selective Hydrogenation by Immobilized Transition Metal Complexes on Mesoporous Supports

For hydrogenation reactions in the heterogeneous phase, it is quite challenging to surpass the commercial success of Raney nickel (RaNi), palladium on carbon (Pd/C), platinum on alumina (Pt/Al_2O_3) catalysts. Numerous reports concerning hydrogenation of alkenes by Au nanoparticles supported on metal oxides are also available in the literature, where catalytic activity depends on size of nanoparticle and nature of support.[135] But when

factors like catalyst poisoning and product selectivity come into play, heterogenized homogeneous catalysts become distinctly and significantly beneficial.[136]

Enantioselective hydrogenation of functionalized C=C and C=O groups, involving molecular dihydrogen (H_2) and catalytic amount of transition metal complexes, is one of the most fundamental molecular transformations.[137] Hydrogenation of C=C bond is facile than that of C=O bond due to both thermodynamic and kinetic reasons. However, the industrial demand for hydrogenation of prochiral carbonyl compounds to produce optically active alcohols has been amplified in the past few decades.[138]

So far, extensive efforts have been made to heterogenize relevant homogeneous catalysts on mesoporous materials for asymmetric hydrogenation of C=C bonds present in prochiral alkenes,[139] unsaturated alcohols,[140] unsaturated carboxylic acids,[141] unsaturated esters,[65] unsaturated amino acids[142] *etc*. But, there are limited reports in the literature where hydrogenation of prochiral carbonyl groups was performed using heterogenized homogeneous catalysts on mesoporous matrices.[143] Some of these reports are summarized in Table 1.2.

Another long-standing problem in the chemical industries is the chemoselective hydrogenation of the C=O bond in α,β-unsaturated aldehydes to form allylic alcohols, which are important intermediates in pharmaceuticals and cosmetics industry.[144] Conventional hydrogenation catalysts (Pt, Ru, Ni *etc*. supported on oxides) produce predominantly the saturated aldehyde or the saturated alcohol from the consecutive hydrogenation.[145] Several attempts have been made to develop suitable heterogeneous catalysts for the chemoselective hydrogenation of the C=O group in α,β-unsaturated aldehydes,[146] few of which are summarized in Table 1.3. It is evident from the table that all of the catalysts consist of a metal or alloy supported on an oxide support.

Table 1.2. Literature survey on asymmetric hydrogenation by heterogeneous catalysts

Catalyst[a]	Support	Substrate	Product	ee[b]	Ref.
Rh–NBD–DPPE	Catalyst copolymerized with ethylene glycol dimethacrylate	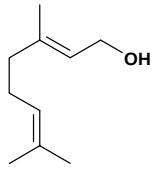	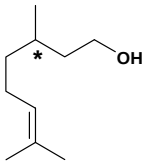	n.g.[c]	140
Ru–(BINAP-4SO_3^-)	Catalyst and ethylene glycol (hydrophilic liquid phase) on controlled-pore glass (CPG-240)	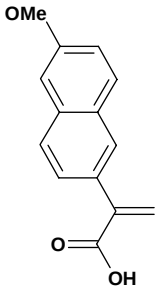	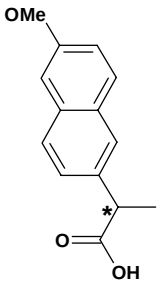	96	141
Rh–NBD–(BDPBz-4SO_3^-)	Silica, MCM-41	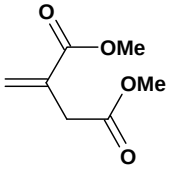	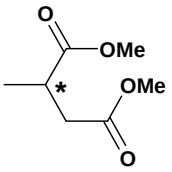	53	65
Rh–COD–(*L*)-prolinamide	Silica, USY[d]	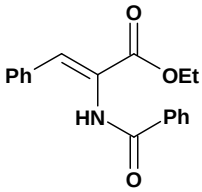	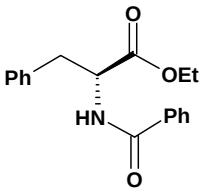	99	142
Ru–(*R*)-BINAP–(*R*,*R*)-DPEN	Mesoporous zirconium phosphonate	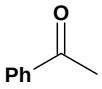	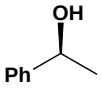	96	143b
Rh–NBD–AEP	Silica, MCM-41	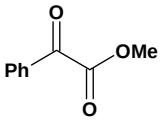	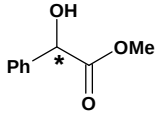	99	143d
Ru–(*R*,*R*)-TsDPEN	MCM-41, SBA-15	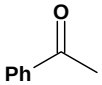	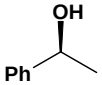	97	143e

[a]NBD = 2,5-norbornadiene, DPPE = 1,2-bis(diphenylphosphino)ethane, BINAP = 2,2'-bis(diphenylphosphino)-1,1'-binaphthyl, COD = 1,5-cyclooctadiene, BDPBz = 3-benzyl-2,4-bis(diphenylphosphino)pentane, DPEN = 1,2-diphenylethylenediamine, AEP = 2-amino methyl-1-ethyl-pyrrolidine, TsDPEN = [*N*-(*p*-toluenesulfonyl)-1,2-diphenylethylene diamine.
[b]Enantiomeric excess.
[c]Not given.
[d]Ultrastable Y zeolite.

Table 1.3. Literature survey on chemoselective hydrogenation of α,β-unsaturated aldehydes by heterogeneous catalysts

Catalyst	Support	Substrate	Product	C=O Selectivity	Ref.
Ag(111)	Silica	$CH_3CH=CHCHO$	$CH_3CH=CHCH_2OH$	63	145
Rh-Sn alloy	Silica	$CH_3CH=CHCHO$	$CH_3CH=CHCH_2OH$	66	145
Au(111)	Zirconia	$CH_2=CHCHO$	$CH_2=CHCH_2OH$	43	146b
Au(111)	Titania	$CH_2=CHCHO$	$CH_2=CHCH_2OH$	23	146b
Pt(111)	Silica	$(CH_3)_2C=CHCHO$	$(CH_3)_2CH=CHCH_2OH$	62	146c
Pt-Sn alloy	Silica	$(CH_3)_2C=CHCHO$	$(CH_3)_2CH=CHCH_2OH$	77.5	146d

1.7.2. Selective Oxidation by Supported Nanoparticles

It is well recognized that nanosized gold particles when deposited on certain oxides exhibits surprisingly high catalytic activity in oxidation of carbon monoxide (CO) at or below ambient temperatures.[147] Supported gold nanoparticles can also catalyze partial and complete oxidation of hydrocarbons,[148] and hydrogenation of unsaturated hydrocarbons.[149] The remarkably high catalytic activity of gold arises from formation of very small and highly dispersed particles. The principal factors for attaining high catalytic activity are (i) smaller particle size and (ii) nature of support.

To obtain superior catalytic efficiency, the optimum size for Au nanoparticles on both oxide and molecular sieve supports is *ca*. 2–5 nm.[150] By decreasing the size of the nanoparticle from 20 nm to 5 nm, a sharp increase in turnover frequency (TOF) in the oxidation of CO was observed by Okumura *et al*.[151]

Generally the cations of the first transition series elements, and a few pre- or post-transition series elements, which can form hydroxides or hydrated oxides in presence of an alkali, are used as support precursors. The interaction between the support and the nanoparticles has significant influence on catalytic activity. For oxidation of CO, Au

supported on titania (TiO_2), alumina (Al_2O_3) or zirconia (ZrO_2) is more active than that supported on silica (SiO_2).[152]

The oxidation of CO has many important applications, a few of which are as follows: (i) removal of CO from air to produce high purity nitrogen (N_2) and oxygen (O_2);[153] (ii) selective removal of CO from streams containing an excess of H_2 and significant amounts of CO_2 and H_2O, especially for preparation of H_2 suitable for polymer electrolyte membrane fuel cells (PEMFC);[154] (iii) CO_2 regeneration catalysts for sealed and unheated CO_2 lasers[155] *etc*.

Au nanoparticles supported on titanium containing molecular sieves like Titanosilicalite-1 (TS-1),[156] Ti-MCM-41[157] or Ti-MCM-48[158] are highly active catalysts of partial oxidation of hydrocarbons. Nijhuis *et al*.[156] and Uphade *et al*.[157,158] have performed vapor-phase epoxidation of propylene to propylene oxide (PO) using these catalysts with ~3% conversion of propylene and as high as 99% selectivity towards PO. Supported Au catalysts can also catalyze complete oxidation of hydrocarbon fuels like methane and propane,[159] or oxidation (decomposition) of odorous compounds like trimethylamine.[160]

1.8. SCOPE AND OBJECTIVES OF THE THESIS

The surface modification of M41S type mesoporous materials by reactive organic functional groups allows the preparation of multifunctional molecular sieves with desired catalytic properties.[33] The mesoporosity and very high surface area of these surface-functionalized mesoporous materials can be exploited for the immobilization of different catalytically reactive species.[36]

During the past few decades, enantioselective hydrogenation of prochiral carbonyl compounds and chemoselective hydrogenation of α,β-unsaturated carbonyl compounds in homogeneous conditions with transition metal complexes have become more important in

the pharmaceutical industry, and consequently in catalytic research as well.[138,144] Recently, an increased demand has developed for the heterogenization of homogeneous organometallic complex catalysts, the goal of which is to combine the superior activity and selectivity offered by homogeneous catalysts with the ease of separation and recycling of heterogeneous ones.[133] Although, several reports of heterogeneous catalysis by encapsulated materials has been addressed for oxidation, epoxidation and Heck reactions,[36] but attempts to heterogenize some of the industrially relevant homogeneous catalysts for enantioselective as well as chemoselective hydrogenation of carbonyl compounds have been, at best, very limited.[143] Also, a direct comparison of the anchored catalysts with their homogeneous counterparts has not been well investigated with meaningful quantitative data.

Immobilized catalysts reported earlier, suffer either from lower selectivity and activity, or low recyclability and hence, of limited practical applications. Therefore, there is ample opportunity to explore development of new methods of heterogenization, which will be advantageous than the state-of-the-art methods.[161] In this context, the covalent grafting of organometallic complex catalysts provides an alternative approach for opening up new outlook for the industrial applications in synthesis of fine chemicals.[162] The principal aim of this thesis was to investigate the approach of immobilization or anchoring of industrially significant catalysts on surface modified mesoporous materials (MCM-41 or MCM-48) for enantioselective and chemoselective hydrogenation of carbonyl compounds under different reaction conditions. In-depth characterization of these immobilized catalysts will be highlighted to understand the mode of interaction of the metal complex with the silicate network, to evaluate the stability of the composite system, and to explore the origin of catalytic activity.

Metallic gold when deposited on selected metal oxides as ultrafine particles of nanometer size range (~2–3 nm), it is found to be very active in many important reactions

for chemical industry and environmental protection.[134] Preparation of supported gold catalysts can be achieved by the following different traditional routes; (i) impregnation, (ii) ion exchange, (iii) coprecipitation (iv) deposition-precipitation (v) chemical vapor deposition, (vi) reduction by borohydride or citrate.[105a,135] In all these methods, the hosts or supports are usually passive and do not participate actively in the reduction of metal ions to form nanoparticles followed by their entrapment in host matrix. Industrial application of anyone these methods can either be hazardous or eco-unfriendly.

The thesis will also focus on the synthesis and simultaneous stabilization of gold nanoparticles by spontaneous reduction of aqueous chloroaurate ions ($AuCl_4^-$) by ordered mesoporous silica materials, such as organically modified MCM-41, and by amorphous silica. Employing this method, we can avoid the use of any external reducing environment other than the host matrix, for the formation of nanoparticles from the metal ion solution. Detailed characterization of these hybrid materials will be demonstrated to understand the physicochemical aspects of the supported gold nanoparticles inside the mesoporous matrices. The catalytic activity of these gold catalysts in oxidation of carbon monoxide and hydrogenation of unsaturated hydrocarbons will also be highlighted.

The specific problems chosen are:

(i) Synthesis of mesoporous MCM-41 and MCM-48 materials, and their surface-modification by organic functional groups *via* different routes.

(ii) Synthesis of novel heterogeneous catalysts containing immobilized Ruthenium-biphosphine-diamine complexes on surface modified MCM-41 and MCM-48 materials, and application of these composite materials in chemoselective hydrogenation of α,β-unsaturated aldehydes and enantioselective hydrogenation of prochiral ketones.

(iii) Synthesis and simultaneous stabilization of gold nanoparticles on organo-functionalized MCM-41, and application of these nanocomposites in oxidation of carbon monoxide and hydrogenation of unsaturated hydrocarbons.

(iv) Detailed characterization of all these newer organic–inorganic hybrid materials.

1.9. OUTLINE OF THE THESIS

The thesis will be presented in **FIVE** chapters, a brief summary of which is given below.

Chapter 1 presents a general introduction about various physicochemical aspects of mesoporous molecular sieve materials. The different characteristic properties of these materials, their synthesis parameters, different approaches for surface-functionalization, characterization techniques, and application as supports for different catalytically active transition metal complexes and nanoparticles are discussed in brief. Based on these reviews, the scope and objective of the present work have been outlined.

Chapter 2 presents experimental results on synthesis of M41S type molecular sieves and their surface modification by reactive organic functional groups through different approaches. The merits and demerits of these approaches by extensive characterization (XRD, N_2 adsorption, ^{13}C and ^{29}Si CP MAS NMR, SEM, TEM, TG-DTA and microanalyses) of these parent and organically modified materials are highlighted.

Chapter 3 deals with a novel heterogeneous catalyst system containing immobilized Ru-biphosphine-diamine complexes in mesoporous supports like MCM-41 and MCM-48 for enantioselective hydrogenation of prochiral ketones and chemoselective hydrogenation of α,β-unsaturated aldehydes. The synthesis methods for immobilization and characterization of these heterogeneous catalysts by XRD, N_2 adsorption, FTIR, ^{31}P CP MAS NMR, TEM and XPS are described. Results of catalytic hydrogenation of different

olefins, enantioselective hydrogenation of prochiral ketones, and chemoselective hydrogenation α,β-unsaturated aldehydes under different reaction conditions are discussed with intrinsic details. ICP-AES analyses of the catalysts before and after the reactions and that of the reaction mixtures are highlighted to emphasize the recyclability of the heterogeneous catalysts.

Chapter 4 focuses on a novel method for the synthesis and simultaneous stabilization of gold nanoparticles by spontaneous reduction of aqueous chloroaurate ions ($AuCl_4^-$) by organically modified mesoporous silica materials, such as propylamine- and propylthiol-functionalized MCM-41. The probable mechanism of the formation of gold nanoparticles has been supported by similar experiments with amorphous silica. These nanocomposites have been characterized by UV-Vis, XRD, N_2 adsorption, XRF, XPS, TEM and TG-DTA. The catalytic activity of these gold catalysts in selective oxidation of carbon monoxide and in hydrogenation of unsaturated hydrocarbons under different reaction conditions is discussed in detail.

Chapter 5 summarizes the results obtained and the basic findings of the present work. The scope for future work is also discussed at the end of this chapter.

1.10. REFERENCES

1. D. W. Breck, Zeolite Molecular Sieves, Wiley, New York, **1974**.

2. (a) R. M. Barrer, *Hydrothermal Chemistry of Zeolites*, Academic Press, New York, **1982**. (b) R. Szostak, *Molecular Sieves: Principles of Synthesis and Identification*, Van Nostrand Reinhold, New York, **1989**. (c) M. E. Davis, *Acc. Chem. Res.* **1993**, *26*, 111. (d) P. G. Schultz, *Angew. Chem. Int. Ed.* **1989**, *28*, 1283. (e) A. Corma, *Chem. Rev.* **1995**, *95*, 559. (f) I. W. C. E. Arends, R. A. Sheldon, M. Wallau, U. Schuchardt, *Angew. Chem. Int. Ed.* **1997**, *36*, 1144. (g) J. M. Thomas, *Angew. Chem. Int. Ed.* **1999**, *38*, 3588.

3. (a) S. M. Csicsery, *Zeolites* **1984**, *4*, 202. (b) S. M. Csicsery, *Pure Appl. Chem.* **1986**, *58*, 841. (c) P. Ratnasamy, R. Kumar, *Stud. Surf. Sci. Catal.* **1995**, *97*, 367.

4. (a) P. -S. E. Dai, *Catal. Today* **1995**, *26*, 3. (b) R. A. Sheldon, *J. Mol. Catal. A: Chem.* **1996**, *107*, 75. (c) J. H. Clark, D. J. Macquarrie, *Chem. Soc. Rev.* **1996**, *25*, 303.

5. A. Corma, *Chem. Rev.* **1997**, *97*, 2373.

6. (a) C. T. Kresge, M. E. Leonowicz, W. J. Roth, J. C. Vartuli, J. S. Beck, *Nature* **1992**, *359*, 710. (b) J. S. Beck, J. C. Vartuli, W. J. Roth, M. E. Leonowicz, C. T. Kresge, K. D. Schmitt, C. T. -W. Chu, D. H. Olson, E. W. Sheppard, S. B. McCullen, J. B. Higgins, J. L. Schlenker, *J. Am. Chem. Soc.* **1992**, *114*, 10834. (c) T. Yanagisawa, T. Shimizu, K. Kuroda, *Bull. Chem. Soc. Jpn.* **1990**, *63*, 988. (d) S. Inagaki, Y. Fukushima, K. Kuroda, *J. Chem. Soc., Chem. Commun.* **1993**, 680.

7. (a) R. Ryoo, S. Jun, *J. Phys. Chem. B* **1997**, *101*, 317. (b) P. T. Tanev, T. J. Pinnavaia, *Science* **1995**, *267*, 865. (c) Q. Huo, R. Leon, P. M. Petroff, G. D. Stucky, *Science* **1995**, *268*, 1324. (d) S. S. Kim, W. Zhang, T. J. Pinnavaia, *Science* **1998**, *282*, 1302. (e) D. Zhao, J. Feng, Q. Huo, N. Melosh, G. H. Fredrickson, B. F. Chmelka, G. D. Stucky, *Science* **1998**, *279*, 548.

8. (a) A. Sayari, *Chem. Mater.* **1996**, *8*, 1840. (b) G. D. Stucky, Q. Huo, A. Firouzi, B. F. Chmelka, S. Schacht, I. G. V. Martin, F. Schuth, *Stud. Surf. Sci. Catal.* **1997**, *105*, 3. (c) J. Y. Ying, C. P. Mehnert, M. S. Wong, *Angew. Chem. Int. Ed.* **1999**, *38*, 56.

9. K. Moller, T. Bein, *Chem. Mater.* **1998**, *10*, 2950.

10. J. C. Vartuli, K. D. Schmitt, C. T. Kresge, *Chem. Mater.* **1994**, *6*, 2317.

11. J. S. Beck, J. C. Vartuli, G. J. Kennedy, C. T. Kresge, W. J. Roth, S. E. Schramm, *Chem. Mater.* **1994**, *6*, 1816.

12. C. F. Cheng, H. He, W. Zhou, J. Klinowski, *Chem. Phys. Lett.* **1995**, *244*, 117.

13. C. -Y. Chen, S. L. Burkett, H. -X. Li, M. E. Davis, *Microporous Mater.* **1993**, *2*, 27.

14. (a) A. Monnier, F. Schuth, Q. Huo, D. Kumar, D. I. Margolese, R. S. Maxwell, G. D. Stucky, M. Krishnamurthy, P. Petroff, A. Firouzi, M. Janicke, B. F. Chmelka, *Science* **1993**, *261*, 1299. (b) G. D. Stucky, A. Monnier, F. Schuth, Q. Huo, D. I. Margolese, D. Kumar, M. Krishnamurthy, P. Petroff, A. Firouzi, M. Janicke, B. F. Chmelka, *Mol. Cryst. Liq. Cryst.* **1994**, *240*, 187.

15. (a) A. Firouzi, D. Kumar, L. M. Bull, T. Besier, P. Sieger, Q. Huo, S. A. Walker, J. A. Zasadzinski, C. Glinka, J. Nicol, D. I. Margolese, G. D. Stucky, B. F. Chmelka, *Science* **1995**, *267*, 1138. (b) A. Firouzi, F. Atef, A. G. Oertli, G. D. Stucky, B. F. Chmelka, *J. Am. Chem. Soc.* **1997**, *119*, 3596.

16. (a) Q. Huo, D. I. Margolese, U. Ciesla, P. Feng, P. Sieger, R. Leon, P. Petroff, F. Schuth, G. D. Stucky, *Nature* **1994**, *368*, 317. (b) Q. Huo, D. I. Margolese, U. Ciesla, D. G. Demuth, P. Feng, T. E. Gier, P. Sieger, A. Firouzi, B. F. Chmelka, F. Schuth, G. D. Stucky, *Chem. Mater.* **1994**, *6*, 1176.

17. (a) P. T. Tanev, T. J. Pinnavaia, *Chem. Mater.* **1996**, *8*, 2068. (b) P. T. Tanev, T. J. Pinnavaia, *Science* **1996**, *271*, 1267.

18. D. M. Antonelli, J. Y. Ying, *Angew. Chem. Int. Ed.* **1996**, *35*, 426.

19. C. G. Wu, T. Bein, *J. Chem. Soc., Chem. Commun.* **1995**, 925.

20. N. Ulagappan, C. N. R. Rao, *Chem. Commun.* **1996**, 2759.

21. D. Khushalani, A. Kuperman, G. A. Ozin, K. Tanaka, J. Garces, M. M. Olken, A. Kuperman, *Adv. Mater.* **1996**, *7*, 842.

22. T. Sun, J. Y. Ying, *Nature* **1997**, *389*, 704.

23. H. Yang, N. Coombs, G. A. Ozin, *Nature* **1997**, *386*, 692.

24. S. Schacht, Q. Huo, I. G. V. Martin, G. D. Stucky, F. Schuth, *Science* **1996**, *273*, 768.

25. Q. Huo, D. Zhao, J. Feng, K. Weston, S. K. Burratto, G. D. Stucky, S. Schacht, F. Schuth, *Adv. Mater.* **1997**, *9*, 974.

26. H. Yang, N. Coombs, I. Sokolov, G. A. Ozin, *Nature* **1996**, *381*, 589.

27. H. Yang, A. Kuperman, N. Coombs, S. M. Afara, G. A. Ozin, *Nature* **1996**, *379*, 703.

28. I. A. Aksay, M. Trau, S. Manne, I. Honma, N. Yao, L. Zhou, P. Fenter, P. M. Eisenberger, S. M. Gruner, *Science* **1996**, *273*, 892.

29. M. Ogawa, *Chem. Commun.* **1996**, 1149.

30. Q. Huo, J. Feng, F. Schuth, G. D. Stucky, *Chem. Mater.* **1997**, *9*, 14.

31. G. S. Attard, J. C. Glyde, C. G. Goltner, *Nature* **1995**, *378*, 366.

32. M. T. Anderson, J. E. Martin, J. G. Odinek, P. P. Newcomer, J. P. Wilcoxon, *Microporous Mater.* **1997**, *10*, 13.

33. A. Stein, B. J. Melde, R. C. Schroden, *Adv. Mater.* **2000**, *12*, 1403.

34. A. P. Wight, M. E. Davis, *Chem. Rev.* **2002**, *102*, 3589.

35. X. Feng, G. E. Fryxell, L. -Q. Wang, A. Y. Kim, J. Liu, K. M. Kemner, *Science* **1997**, *276*, 923.

36. D. E. De Vos, M. Dams, B. F. Sels, P. A. Jacobs, *Chem. Rev.* **2002**, *102*, 3615.

37. P. M. Price, J. H. Clark, D. J. Macquarrie, *J. Chem. Soc., Dalton Trans.* **2000**, 101.

38. K. Moller, T. Bein, *Stud. Surf. Sci. Catal.* **1998**, *117*, 53.

39. J. Liu, X. Feng, G. E. Fryxell, L. -Q. Wang, A. Y. Kim, M. Gong, *Adv. Mater.* **1998**, *10*, 161.

40. K. K. Unger, *Porous Silica – Its Properties and Use as Support in Column Liquid Chromatography*, *Vol. 16*, Elsevier, Amsterdam, **1979**.

41. L. Mercier, T. J. Pinnavaia, *Environ. Sci. Tech.* **1998**, *32*, 2749.

42. T. Kimura, S. Saeki, Y. Sugahara, K. Kuroda, *Langmuir* **1999**, *15*, 2794.

43. J. S. Beck, D. C. Calabro, S. B. McCullen, B. P. Pelrine, K. D. Schmitt, J. C. Vartuli, *Method for Functionalizing Synthetic Mesoporous Crystalline Material*, Mobil Oil Corporation, USA, **1992**.

44. R. Anwander, I. Nagl, M. Widenmeyer, G. Engelhardt, O. Groeger, C. Palm, T. Roser, *J. Phys. Chem. B* **2000**, *104*, 3532.

45. M. H. Lim, C. F. Blanford, A. Stein, *J. Am. Chem. Soc.* **1997**, *119*, 4090.

46. M. H. Lim, C. F. Blanford, A. Stein, *Chem. Mater.* **1998**, *10*, 467.

47. W. M. van Rhijn, D. E. De Vos, B. F. Sels, W. D. Bosaert, P. A. Jacobs, *Chem. Commun.* **1998**, 317.

48. J. H. Clark, D. J. Macquarrie, *Chem. Commun.* **1998**, 853.

49. D. Brunel, *Microporous Mesoporous Mater.* **1999**, *27*, 329.

50. (a) P. Sutra, D. Brunel, *Chem. Commun.* **1996**, 2485. (b) Y. V. Subba Rao, D. E. De Vos, P. A. Jacobs, *Angew. Chem. Int. Ed.* **1997**, *36*, 2661. (c) J. F. Diaz, K. J. Balkus Jr., F. Bedioui, V. Kurshev, L. Kevan, *Chem. Mater.* **1997**, *9*, 61.

51. M. H. Lim, A. Stein, *Chem. Mater.* **1999**, *11*, 3285.

52. D. S. Shephard, W. Zhou, T. Maschmeyer, J. M. Matters, C. L. Roper, S. Parsons, B. F. G. Johnson, M. J. Duer, *Angew. Chem. Int. Ed.* **1998**, *37*, 2719.

53. F. De Juan, E. Ruiz-Hitzky, *Adv. Mater.* **2000**, *12*, 430.

54. V. Antochshuk, M. Jaroniec, *Chem. Commun.* **1999**, 2373.

55. C. Sanchez, F. Ribot, *New. J. Chem.* **1994**, *18*, 1007.

56. (a) S. L. Burkett, S. D. Sims, S. Mann, *Chem. Commun.* **1996**, 1367. (b) S. D. Sims, S. L. Burkett, S. Mann, *Mater. Res. Soc. Symp. Proc.* **1996**, *8*, 1147. (c) D. J. Macquarrie, *Chem. Commun.* **1996**, 1961. (d) Q. Huo, D. I. Margolese, G. D. Stucky, *Chem. Mater.* **1996**, *8*, 1147.

57. (a) P. Mukherjee, S. Laha, D. Mandal, R. Kumar, *Stud. Surf. Sci. Catal.* **2000**, *129*, 283. (b) S. R. Hall, C. E. Fowler, B. Lebeau, S. Mann, *Chem. Commun.* **1999**, 201.

58. (a) F. Babonneau, L. Leite, S. Fontlupt, *J. Mater. Chem.* **1999**, *9*, 175. (b) V. Goletto, V. Dagry, F. Babonneau, *Mater. Res. Soc. Symp. Proc.* **1999**, *576*, 229.

59. (a) L. Mercier, T. J. Pinnavaia, *Chem. Mater.* **2000**, *12*, 188. (b) M. Koya, H. Nakajima, *Stud. Surf. Sci. Catal.* **1998**, *117*, 243.

60. (a) R. Richer, L. Mercier, *Chem. Commun.* **1998**, 1775. (b) J. Brown, R. Richer, L. Mercier, *Microporous Mesoporous Mater.* **2000**, *37*, 41.

61. (a) S. Inagaki, S. Guan, Y. Fukushima, T. Ohsuma, O. Terasaki, *J. Am. Chem. Soc.* **1999**, *121*, 9611. (b) S. Guan, S. Inagaki, T. Ohsuma, O. Terasaki, *J. Am. Chem. Soc.* **2000**, *122*, 5660. (c) T. Asefa, M. J. McLachlan, N. Coombs, G. A. Ozin, *Nature* **1999**, *402*, 867. (d) B. J. Melde, B. T. Holland, C. F. Blanford, A. Stein, *Chem. Mater.* **1999**, *11*, 3302.

62. (a) R. Ryoo, C. H. Ko, J. M. Kim, R. Howe, *Catal. Lett.* **1996**, *37*, 29. (b) U. Junges, F. Schuth, G. Schmid, Y. Uchida, R. Schogl, *Ber. Bunsen-Ges. Phys. Chem.* **1997**, *101*, 1631. (c) A. Jentys, N. H. Pham, H. Vinek, M. Englisch, J. A. Lercher, *Microporous Mater.* **1996**, *6*, 13. (d) C. T. Fishel, R. J. Davis, J. M. Garces, *J. Catal.* **1996**, *163*, 148. (e) P. Mukherjee, M. Sastry, R. Kumar, *PhysChemComm* **2000**, *3*, 15.

63. (a) X. He, D. Antonelli, *Angew. Chem. Int. Ed.* **2002**, *41*, 214. (b) B. J. Aronson, C. F. Blanford, A. Stein, *Chem. Mater.* **1997**, *9*, 2842.

64. (a) R. Leon, D. Margolese, G. Stucky, P. M. Petroff, *Phys. Rev. B* **1995**, *52*, r2285. (b) T. Hirai, H. Okubo, I. Komasawa, *J. Phys. Chem. B.* **1999**, *103*, 4228.

65. C. Bianchini, P. Barbaro, V. Dal Santo, R. Gobetto, A. Meli, W. Oberhauser, R. Psaro, F. Vizza, *Adv. Synth. Catal.* **2001**, *343*, 41.

66. F. M. De Rege, D. K. Morita, K. C. Ott, W. Tumas, R. D. Broene, *Chem. Commun.* **2000**, 1797.

67. (a) K. Mukhopadhyay, B. R. Sarkar, R. V. Chaudhari, *J. Am. Chem. Soc.* **2002**, *124*, 9692. (b) J. Jamis, J. R. Anderson, R. S. Dickson, E. M. Campi, W. R. Jackson, *J. Organomet. Chem.* **2001**, *627*, 37. (c) K. Mukhopadhyay, A. B. Mandale, R. V. Chaudhari, *Chem. Mater.* **2003**, *15*, 1766.

68. S. Abramson, N. Bellocq, M. Lasperas, *Top. Catal.* **2000**, *13*, 339.

69. A. Ghosh, R. Kumar, *J. Catal.* **2004**, (in press).

70. C. Baleizao, B. Gigante, M. J. Sabatier, H. Garcia, A. Corma, *Appl. Catal. A* **2002**, *288*, 279.

71. G. -J. Kim, D. -W. Park, *Catal. Today* **2000**, *63*, 537.

72. (a) D. Rechavi, M. Lemaire, *J. Mol. Catal. A: Chem.* **2002**, *182–183*, 239. (b) R. J. Clarke, I. J. Shannon, *Chem. Commun.* **2001**, 1936.

73. S. A. Raynor, J. M. Thomas, R. Raja, B. F. G. Johnson, R. G. Bell, M. D. Mantle, *Chem. Commun.* **2000**, 1925.

74. S. Xiang, Y. Zhang, Q. Xin, C. Li, *Angew. Chem. Int. Ed.* **2002**, *41*, 821.

75. W. Bohlmann, K. Schandert, A. Poppl, H. C. Semmelhack, *Zeolites* **1997**, *19*, 297.

76. R. Selke, M. Capka, *J. Mol. Catal.* **1990**, *63*, 319.

77. S. Taylor, J. Gullick, P. McMorn, D. Bethell, P. C. Bullman Page, F. E. Hancock, F. King, G. J. Hutchings, *J. Chem. Soc., Perkin 2* **2001**, 1714.

78. R. Hoppe, A. Ortlam, J. Rathousky, G. Schulz-Ekloff, A. Zukal, *Microporous Mater.* **1997**, *8*, 267.

79. A. Poppl, P. Baglioni, L. Kevan, *J. Phys. Chem.* **1995**, *99*, 14156.

80. (a) A. T. Bell, *Science* **2003**, *299*, 1688. (b) J. M. Thomas, R. Raja, *Chem. Record* **2001**, *1*, 448.

81. (a) G. Markovich, C. P. Collier, S. E. Henrichs, F. Remacle, R. D. Levine, J. R. Heath, *Acc. Chem. Res.* **1999**, *32*, 415. (b) M. L. Brongersma, J. W. Hartman, H. A. Atwater, *Phys. Rev. B* **2000**, *62*, 16356.

82. J. Kunther, R. Seshadri, G. Nelles, W. Assenmacher, H. -J. Butt, W. Mader, W. Tremel, *Chem. Mater.* **1999**, *11*, 1317.

83. W. Baschong, N. G. Wrigley, *J. Electron Microsc. Technique* **1990**, *14*, 313.

84. (a) R. Elghanian, J. J. Storhoff, R. C. Mucic, R. L. Letsinger, C. A. Mirkin, *Science* **1997**, *277*, 1078. (b) G. W. Hacker, C. Hauser-Kronberger, I. Zehbe, H. Su, A. Schiechl, O. Dietze, R. Tubbs, *Cell Vision* **1997**, *4*, 54.

85. C. H. Ko, R. Ryoo, *Chem. Commun.* **1996**, 2467.

86. D. S. Shephard, T. Maschmeyer, B. F. G. Johnson, J. M. Thomas, G. Sankar, D. Ozkaya, W. Zhou, R. D. Oldroyd, R. G. Bell, *Angew. Chem. Int. Ed.* **1997**, *36*, 2242.

87. J. M. Thomas, B. F. G. Johnson, R. Raja, G. Sankar, P. A. Midgley, *Acc. Chem. Res.* **2003**, *36*, 20.

88. J. W. Mellor, *A Comprehensive Treatise on Inorganic and Theoretical Chemistry*, *Vol. 3*, Longmans, Green and Co., London, **1923**, p. 554.

89. (a) P. P. Edwards, *Mater. Res. Soc. Symp. Proc.* **1992**, *272*, 311. (b) J. M. Thomas, *Pure Appl. Chem.* **1988**, *60*, 1517.

90. M. Brust, M. Walker, D. Bethell, D. J. Schiffrin, R. Whyman, *J. Chem. Soc., Chem. Commun.* **1994**, 801.

91. D. V. Leff, L. Brandt, J. R. Heath, *Langmuir* **1996**, *12*, 4723.

92. (a) M. D. Porter, T. B. Bright, D. L. Allara, C. E. D. Chidsey, *J. Am. Chem. Soc.* **1987**, *109*, 3559. (b) P. Mukherjee, C. R. Patra, A. Ghosh, R. Kumar, M. Sastry, *Chem. Mater.* **2002**, *14*, 1678.

93. (a) P. Mukherjee, C. R. Patra, R. Kumar, M. Sastry, *PhysChemComm* **2001**, *4*, 24. (b) C. R. Patra, A. Ghosh, P. Mukherjee, M. Sastry, R. Kumar, *Stud. Surf. Sci. Catal.* **2002**, *141*, 641.

94. D. H. Gracias, J. Tien, T. L. Breen, C. Hsu, G. M. Whitesides, *Science* **2000**, *289*, 1170.

95. S. Stepanow, M. Lingenfelder, A. Dmitriev, H. Spillmann, E. Delvigne, N. Lin, X. Deng, C. Cai, J. V. Barth, K. Kern, *Nature Mater.* **2004**, *3*, 229.

96. W. H. Bragg, W. L. Bragg, *The Crystalline State*, *Vol. 1*, McMillan, New York, **1949**.

97. S. Biz, M. Occelli, *Catal. Rev. -Sci. Eng.* **1998**, *40*, 329.

98. G. Bergeret, in: *Handbook of Heterogeneous Catalysis*, *Vol. 2*, Eds: G. Ertl, H. Knozinger, J. Weitkamp, Wiley-VCH, Weinheim, **1997**, pp. 464–475.

99. R. C. Rau, in: *Advances in X-Ray Analysis*, *Vol. 5*, Ed: W. M. Mueller, Sir Isaac Pitman and Sons Ltd., London, **1962**, pp. 104–116.

100. C. K. Jorgensen, *Absorption Spectra and Chemical Bonding in Complexes*, Pergamon, New York, **1962**.

101. G. Kortum, *Reflectance Spectroscopy*, Springer, Berlin, **1969**.

102. M. Faraday, *Philos. Trans.* **1857**, *147*, 145.

103. G. Mie, *Ann. Physik* **1908**, *25*, 377.

104. G. C. Papavassiliou, *Prog. Solid State Chem.* **1980**, *12*, 185.

105. (a) S. Link, M. A. El-Sayed, *J. Phys. Chem. B* **1999**, *103*, 4212. (b) C. Burda, T. Green, C. Landes, S. Link, R. Little, J. Petroski, M. A. El-Sayed, in: *Characterization of*

Nanophase Materials, Ed: Z. L. Wang, Wiley-VCH, Weinheim, **2000**, Chapter 7, pp. 197–241.

106. P. R. Griffiths, J. A. De Haseth, *Fourier Transform Infrared Spectrometry*, John Wiley and Sons Inc., New York,**1986**.

107. C. C. Freyhardt, M. Tsapatsis, R. F. Lobo, K. J. Balkus, M. E. Davis, *Nature* **1996**, *381*, 295.

108. P. A. Jacobs, W. Y. Martier, *Zeolites* **1982**, *2*, 226.

109. J. Ryczkowski, *Catal. Today* **2001**, *68*, 263.

110. F. A. Rushworth, D. P. Tunstall, *Nuclear Magnetic Resonance*, Gordon and Breach Science Publishers Ltd., London, **1973**.

111. W. W. Paudler, *Nuclear Magnetic Resonance: General Concepts and Applications*, John Wiley and Sons Inc., New York, **1987**.

112. M. Mehring, *High Resolution NMR Spectroscopy in Solids*, Springer-Verlag, Berlin, **1976**.

113. G. Engelhardt, D. Michel, *High-Resolution Solid-State NMR of Silicates and Zeolites*, John Wiley and Sons Ltd., Chichester, **1987**.

114. G. Engelhardt, in: *Handbook of Heterogeneous Catalysis*, *Vol. 2*, Eds: G. Ertl, H. Knozinger, J. Weitkamp, Wiley-VCH, Weinheim, **1997**, pp. 525–539.

115. C. S. Fadley, in: *Electron Spectroscopy: Theory, Techniques and Applications*, *Vol. 2*, Eds: C. R. Brundle, A. D. Baker, Academic Press, New York, **1978**, pp. 1–156.

116. W. N. Delgass, T. R. Hughes, C. S. Fadley, *Catal. Rev.* **1970**, *4*, 179.

117. W. F. Egelhoff Jr., *Surf. Sci. Rep.* **1987**, *6*, 253.

118. R. O. Muller, *Spectrochemical Analysis by X-ray Fluorescence*, Plenum Press, New York, **1972**.

119. J. W. Robinson, *Atomic Absorption Spectroscopy*, Marcel Dekker, New York, **1975**.

120. G. L. Moore, *Introduction to Inductively Coupled Plasma Atomic Emission Spectrometry*, Elsevier, Amsterdam, **1988**.

121. G. Lawes, *Scanning Electron Microscopy And X-Ray Microanalysis*, John Wiley and Sons Ltd., Chichester, **1987**.

122. D. E. Newbury, D. C. Joy, P. Echlin, C. E. Fiori, J. I. Goldstein, *Advanced Scanning Electron Microscopy and X-Ray Microanalysis*, Plenum Press, New York, **1986**.

123. J. R. Fryer, *Chemical Applications of Transmission Electron Microscopy*, Academic Press, San Diego, **1979**.

124. (a) J. M. Thomas, O. Terasaki, P. L. Gai, W. Zhou, J. Gonzalez-Calbet, *Acc. Chem. Res.* **2001**, *34*, 583. (b) V. Alfredsson, M. Keung, A. Monnier, G. D. Stucky, K. K. Unger, F. Schuth, *J. Chem. Soc., Chem. Commun.* **1994**, 921.

125. Z. L. Wang, in: *Characterization of Nanophase Materials*, Ed: Z. L. Wang, Wiley-VCH, Weinheim, **2000**, Chapter 3, pp. 37–80.

126. S. Brunauer, P. H. Emmett, E. Teller, *J. Am. Chem. Soc.* **1938**, *60*, 309.

127. E. P. Barrett, L. G. Joyner, P. P. Halenda, *J. Am. Chem. Soc.* **1951**, *73*, 373.

128. C. -Y. Chen, H. -X. Li, M. E. Davis, *Microporous Mater.* **1993**, *2*, 17.

129. J. Manassen, in: *Catalysis, Progress in Research*, Eds: F. Basolo, R. E. Burwell Jr., Plenum Press, New York, **1973**, p. 177.

130. P. Ermert, in: *Solid-Supported Combinatorial and Parallel Synthesis of Small-Molecular-Weight Compound Libraries*, Eds: D. Obrecht, J. M. Villalgordo, Elsevier, Oxford, **1998**, pp. 44–84.

131. A. N. Collins, G. N. Sheldrake, J. Crosby (Eds), *Chirality in Industry: The Commercial Manufacture and Applications of Optically Active Compounds*, Wiley, New York, **1997**.

132. I. Ojima (Ed), *Catalytic Asymmetric Synthesis*, *2nd ed*., Wiley, New York, **2000**.

133. C. E. Song, S. Lee, *Chem Rev.* **2002**, *102*, 3495.

134. G. C. Bond, D. T. Thompson, *Catal. Rev. -Sci. Eng.* **1999**, *41*, 319.

135. M. Haruta, *Catal. Today* **1997**, *36*, 153.

136. A. Kinting, H. Krause, M. Capka, *J. Catal.* **1985**, *25*, 152.

137. (a) R. Noyori, *Adv. Synth. Catal.* **2003**, *345*, 15. (b) J. Halpern, *Science* **1982**, *217*, 401.

138. R. Noyori, *Asymmetric Catalysis in Organic Synthesis*, Wiley, New York, **1994**, pp. 17–94.

139. A. Zsigmond, K. Bogar, F. Nothiesz, *J. Catal.* **2003**, *213*, 103

140. R. A. Taylor, B. P. Santora, M. R. Gagne, *Org. Lett.* **2000**, *2*, 1781.

141. (a) K. T. Wan, M. E. Davis, *Nature* **1994**, *370*, 449. (b) K. T. Wan, M. E. Davis, *J. Catal.* **1995**, *152*, 25.

142. A. Corma, M. Iglesias, C. Del Pino, F. Sanchez, *J. Chem. Soc., Chem. Commun.* **1991**, 1253.

143. (a) A. Hu, H. L. Ngo, W. Lin, *Angew. Chem. Int. Ed.* **2003**, *42*, 6000. (b) A. Hu, H. L. Ngo, W. Lin, *J. Am. Chem. Soc.* **2003**, *125*, 11490. (c) R. Raja, J. M. Thomas, M. D. Jones, B. F. G. Johnson, D. E. W. Vaughan, *J. Am. Chem. Soc.* **2003**, *125*, 14982. (d) M. D. Jones, R. Raja, J. M. Thomas, B. F. G. Johnson, D. W. Lewis, J. Rouzaud, K. D. M. Harris, *Angew. Chem. Int. Ed.* **2003**, *42*, 4326. (e) P. N. Liu, P. M. Gu, F. Wang, Y. Q. Tu, *Org. Lett.* **2004**, *6*, 169.

144. R. L. Augustine, *Heterogeneous Catalysts in Organic Synthesis*, Dekker, New York, **1995**.

145. P. Claus, *Top. Catal.* **1998**, *5*, 51.

146. (a) V. Ponec, *Appl. Catal. A* **1997**, *149*, 27. (b) P. Claus, A. Bruckner, C. Mohr, H. Hofmeister, *J. Am. Chem. Soc.* **2000**, *122*, 11430. (c) F. Delbecq, P. Sautet, *J. Catal.* **2002**, *211*, 398. (d) F. Delbecq, P. Sautet, *J. Catal.* **2003**, *220*, 115.

147. M. Valden, X. Lai, D. W. Goodman, *Science* **1998**, *281*, 1647.

148. M. Haruta, M. Date, *Appl. Catal. A* **2001**, *222*, 427.

149. P. A. Sermon, G. C. Bond, P. B. Wells, *J. Chem. Soc., Faraday Trans. I* **1979**, *75*, 385.

150. M. Okumura, K. Tanaka, A. Ueda, M. Haruta, *Solid State Ionics* **1997**, *95*, 143.

151. M. Okumura, S. Nakamura, S. Tsubota, T. Nakamura, M. Azuma, M. Haruta, *Catal. Lett.* **1998**, *51*, 53.

152. S. Galvagno, G. Parravano, *Ber. Bunsen-Ges. Phys. Chem.* **1979**, *83*, 894.

153. M. Haruta, T. Takase, T. Kobayashi, S. Tsubota, in: *Catalytic Science and Technology*, *Vol. 1*, Ed: S. Yoshida, N. Takezawa, T. Ono, Kodansha, Tokyo, **1991**, pp. 331–334.

154. D. L. Trimm, Z. Ilsen Onsan, *Catal. Rev. -Sci. Eng.* **2001**, *43*, 31.

155. S. D. Gardner, G. B. Hoflund, B. T. Upchurch, D. R. Schryer, E. J. Kielin, J. Schryer, *J. Catal.* **1991**, *129*, 114.

156. T. A. Nijhuis, B. J. Huizinga, M. Makkee, J. A. Moulijn, *Ind. Eng. Chem. Res.* **1999**, *38*, 884.

157. B. S. Uphade, Y. Yamada, T. Akita, T. Nakamura, M. Haruta, *Appl. Catal. A* **2001**, *215*, 137.

158. B. S. Uphade, T. Akita, T. Nakamura, M. Haruta, *J. Catal*. **2002**, *209*, 331.

159. R. D. Waters, J. J. Weimer, J. E. Smith, *Catal. Lett.* **1995**, *30*, 181.

160. A. Ueda, M. Haruta, *Shigen Kankyo Taisaku* **1992**, *28*, 1035.

161. P. McMorn, G. J. Hutchings, *Chem. Soc. Rev.* **2004**, *33*, 108.

162. C. Bianchini, P. Barbaro, *Top. Catal.* **2002**, *19*, 17.

2.1. INTRODUCTION

The syntheses of mesoporous silicate materials *via* liquid crystal templates have opened up new possibilities for preparing heterogeneous catalysts containing uniform pores in the mesoporous regime.[1-3] This new family of materials, termed as M41S, is broadly classified into three categories: hexagonal (MCM-41), cubic (MCM-48) and lamellar (MCM-50).

In recent years, surface modification of M41S type mesoporous silicates by reactive organic functional groups have been investigated extensively.[4] This surface modification allows tailoring of the surface properties for quite a lot of potential applications, *viz*., catalysis, immobilization of catalytically reactive species, chemical sensing, fabrication of nanomaterials, to mention just a few.[5,6] The inorganic part (polymeric silicate framework) of the surface modified hybrid mesoporous materials provides structural, thermal and mechanical stability; whereas the pendant organic species permit flexible control of interfacial and bulk properties, such as porosity or hydrophobicity.

Organo-functionalization of the internal surfaces of mesoporous silicates can be achieved either by covalent grafting of various organic species onto the channel walls or by incorporating functionalities directly during the synthesis.[4,5] The grafting process has been widely applied to anchor desired organic functional groups *via* condensation with surface silanol groups of the mesoporous silicate. However, it is somewhat difficult to control the concentration and distribution of organic moieties in the silicate surface mainly due to non-uniform presence of silanol groups in different mesoporous samples.[7] Another phenomenon to be taken into consideration is the greater accessibility of the silanol groups of the external surface towards functionalization.[7] This grafting on the external surface can be minimized by passivating the external silanol groups before functionalization of those on the internal surface.[8]

The direct synthesis approach is based on the co-condensation of one tetraalkoxysilane with one or more trialkoxyorganosilane precursors in a templating environment. The tetraalkoxysilane precursor acts as a building block to create the mesoporous silicate framework, whereas the trialkoxyorganosilanes function as both framework silicate units and pendant organic functional groups.[9] The most frequently encountered problem in this method is the relatively faster hydrolysis of the organosilane precursor and its self-condensation. However, this problem can easily be circumvented by using a suitable solvent in the synthesis gel to reduce and control the faster hydrolysis.[10] This one step synthesis procedure can produce mesoporous silicates with high loading and homogeneous surface coverage of organic functional groups.[7]

In the preceding chapter, the different synthesis mechanisms, and surface modification of mesoporous materials by different routes have been reviewed. This chapter will present the experimental data regarding (i) the synthesis of siliceous mesoporous MCM-41 and MCM-48 materials, (ii) surface modification of these materials by different organic functional groups, *viz*., amine ($-NH_2$), thiol (–SH), chloro (–Cl), and ethylenediamine ($-NHCH_2CH_2NH_2$) through grafting and co-condensation routes, and (iii) comparison of the products obtained from both methods with respect to different physicochemical characteristics. In this context, an efficient room temperature grafting process will also be discussed.

2.2. EXPERIMENTAL

2.2.1. Materials

Fumed silica (Surface area = 384 $m^2\ g^{-1}$), tetraethyl orthosilicate (TEOS), 3-aminopropyltrimethoxy silane (APTS), 3-mercaptopropyltrimethoxy silane (MPTS), 3-chloropropyltrimethoxy silane (CPTS), *N*-[3-(trimethoxysilyl)propyl]-ethylenediamine

(TPEN) and dichlorodiphenylsilane (Ph_2SiCl_2) were purchased from Aldrich; cetyltrimethylammonium bromide (CTABr) was purchased from Loba Chemie, India, and were used as received without further purification.

2.2.2. Synthesis of Siliceous MCM-41 and MCM-48

The syntheses of pure siliceous MCM-41 and MCM-48 were carried out applying a published procedure[11] using the following initial molar gel compositions: SiO_2–0.32NaOH–0.2CTABr–125H_2O and SiO_2–0.4NaOH–0.21CTABr–120H_2O, respectively.

In a typical synthesis of MCM-41, fumed silica (3 g) was added to a solution of 0.64 g NaOH in 25 mL H_2O and stirred for 45 min. To this mixture, a solution of 3.64 g CTABr in 50 mL H_2O was added dropwise and stirred for another 45 min. Finally 37 mL of H_2O was added to the synthesis gel, stirred further for 30 min and autoclaved at 100 °C for 16 h. The product thus obtained after hydrothermal synthesis was filtered, washed thoroughly with distilled water and acetone, and dried at ambient temperature under vacuum.

In a typical synthesis of MCM-48, fumed silica (3 g) was added to a solution of 0.8 g NaOH in 25 mL H_2O and stirred for 1 h. A solution of 3.82 g of CTABr in 50 mL H_2O was added dropwise to the above mixture and stirring was continued for 1 h. Finally 33 mL of H_2O was added to the synthesis gel, stirred for another 30 min and autoclaved at 150 °C for 36 h. The solid product thus obtained was filtered, washed repeatedly with distilled water and acetone, and dried *in vacuo* at room temperature. All the as-synthesized mesoporous samples were air-calcined at 540 °C for 10 h.

2.2.3. Surface Modification of MCM-41 and MCM-48 by Post-Synthesis Grafting

The calcined MCM-41 or MCM-48 materials were first treated with dichlorodiphenylsilane (Ph_2SiCl_2) to passivate the silanol groups on external surface by

silylation.[8] By this method the tethering of desired organic functional groups is expected to occur predominantly inside the channels, as has been demonstrated by Shephard *et al*.[8]

1 g of calcined MCM-41 or MCM-48 was suspended in 30 mL of dry dichloromethane (DCM), and to this 0.03 mL of Ph_2SiCl_2 was added and stirred for 1 h at room temperature under inert conditions. The contents were then cooled to –78 °C, and 1 mL of the desired trialkoxyorganosilane was added dropwise to this slurry. Thereafter, the contents were slowly warmed to ambient temperature and the reaction mixture was further stirred for 24 h under inert atmosphere, filtered, washed several times with dry DCM and dried under vacuum.

The grafting process was also carried out on other dry solvents such as methanol (MeOH), toluene and tetrahydrofuran (THF). The following trialkoxyorganosilanes, *viz*., 3-aminopropyltrimethoxy silane (APTS), 3-mercaptopropyltrimethoxy silane (MPTS), *N*-[3-(trimethoxysilyl)propyl]-ethylenediamine (TPEN) and 3-chloropropyltrimethoxy silane (CPTS) were used in this study.

Another set of samples was prepared, where the step involving addition of Ph_2SiCl_2 was omitted. In this approach, the grafting of organic functional groups is expected to occur on the exterior as well as on the interior walls.

2.2.4. Synthesis of Organo-Functionalized MCM-41 and MCM-48 by "One-Pot" Co-condensation

In the co-condensation method, the organo-functionalized MCM-41 and MCM-48 materials were synthesized using the following initial gel composition: 1.0TEOS–0.4XPTS–0.21CTABr–0.32NaOH–75H_2O–16MeOH, where XPTS = APTS / MPTS / CPTS / TPEN. Methanol was used in the initial gel mixture to reduce and control the relatively faster hydrolysis of XPTS.

In a typical synthesis, 7.654 g of CTABr was added to a solution consisting of 1.28 g NaOH in 35 mL of water and 32 mL of MeOH, and homogenized by stirring. To this solution, another solution containing 20.83 g of TEOS and requisite amount of XPTS in 32 mL of MeOH was added dropwise and the stirring was continued for another 2 h. Thereafter, 100 mL of water was added dropwise to this synthesis mixture, and the stirring was continued for another 12 h to remove MeOH. Finally the synthesis gel was autoclaved at 100 °C for 36 h (for MCM-41) and at 150 °C for 72 h (for MCM-48) to obtain surface-functionalized mesoporous materials. The products obtained were filtered, washed several times with distilled water and acetone, and then dried at room temperature under vacuum.

The surfactant from the organo-functionalized MCM-41 and MCM-48 was removed by a solvent extraction method, where 1 g of each of the materials was treated with a mixture of 85 mL of MeOH and 2 mL of concentrated hydrochloric acid (HCl) under reflux conditions for 24 h.

The designations of all the surface modified mesoporous samples synthesized either by grafting or by co-condensation are summarized in Table 2.1.

2.2.5. Instruments for Characterization

Powder X-ray diffraction (XRD) patterns were recorded at room temperature on a Rigaku MiniFlex instrument using Cu K_α radiation (l = 1.5404 Å), in the 2θ range 1.5–10° at a scan rate of 1°/min. The specific surface areas of the samples were determined by the BET method[12] from N_2 adsorption isotherms at 77 K using an Omnisorb CX-100 Coulter instrument. Prior to the adsorption experiments, the samples were activated at 150 °C for 6 h at 1.333×10^{-2} Pa. Pore size distributions of the samples were computed by the Barrett-Joyner-Halenda (BJH) model.[13]

Table 2.1. Designation of various organically modified MCM-41 and MCM-48 materials

Functional Group	Precursor of Functional Group	Support	Functionalization Process	Designation
$–NH_2$	APTS	MCM-41	Grafting	NH_2-MCM-41-G
–SH	MPTS	MCM-41	Grafting	SH-MCM-41-G
–Cl	CPTS	MCM-41	Grafting	Cl-MCM-41-G
$–NH(CH_2)_2NH_2$	TPEN	MCM-41	Grafting	TPEN-MCM-41-G
$–NH_2$	APTS	MCM-48	Grafting	NH_2-MCM-48-G
–SH	MPTS	MCM-48	Grafting	SH-MCM-48-G
–Cl	CPTS	MCM-48	Grafting	Cl-MCM-48-G
$–NH(CH_2)_2NH_2$	TPEN	MCM-48	Grafting	TPEN-MCM-48-G
$–NH_2$	APTS	MCM-41	Co-condensation[a]	NH_2-MCM-41-C
–SH	MPTS	MCM-41	Co-condensation[a]	SH-MCM-41-C
–Cl	CPTS	MCM-41	Co-condensation[a]	Cl-MCM-41-C
$–NH(CH_2)_2NH_2$	TPEN	MCM-41	Co-condensation[a]	TPEN-MCM-41-C
$–NH_2$	APTS	MCM-48	Co-condensation[a]	NH_2-MCM-48-C
–SH	MPTS	MCM-48	Co-condensation[a]	SH-MCM-48-C
–Cl	CPTS	MCM-48	Co-condensation[a]	Cl-MCM-48-C
$–NH(CH_2)_2NH_2$	TPEN	MCM-48	Co-condensation[a]	TPEN-MCM-48-C

[a]All the samples were considered after removal of the surfactant template.

The samples were dispersed on Holey carbon grids and transmission electron microscopic (TEM) images were scanned on a Jeol Model 1200 EX instrument operated at an accelerating voltage of 100 kV. The scanning electron microscopic (SEM) images were recorded on a Philips Model XL 30 instrument.

^{13}C and ^{29}Si cross-polarization magic angle spinning nuclear magnetic resonance (CP MAS NMR) spectra were recorded in a Bruker DRX-500 FT NMR spectrophotometer. The finely powdered samples were spun at 7–8 kHz in a 7 mm zirconia rotor. The chemical

shifts were referred with respect to adamantane (δ = 28.7 ppm from TMS) and tetraethyl orthosilicate (δ = –82.4 ppm from TMS), respectively.

The samples were subjected to thermogravimetric (TGA) and differential thermal analyses (DTA) performed on a Seiko Instruments model TG/DTA 32 at a heating rate of 10 °C/min. Elemental analyses of the organo-functionalized mesoporous materials after template removal were carried out on a Carlo Erba EA 1108 elemental analyzer.

2.3. CHARACTERIZATION

2.3.1. Powder X-Ray Diffraction

The uniqueness of mesoporous structure, phase purity, degree of orderedness and unit cell parameters of all the siliceous and surface modified mesoporous materials were determined by powder X-ray diffraction (XRD). Figure 2.1 shows representative powder XRD patterns of the calcined MCM-41 and MCM-48 samples. The XRD pattern of siliceous MCM-41 shows characteristic four distinct low angle reflections [strong 100 reflection and feeble (110), (200) and (210) reflections] at 2θ = 2.1°, 3.7°, 4.3° and 5.6°, respectively, and a d_{100} spacing value of ~4.3 nm. Similarly, the XRD pattern of Si-MCM-48 reveals eight distinct reflections, *viz*., sharp (211) and (220) reflections and weak (321), (400), (420), (322), (422) and (431) reflections at 2θ = 2.4°, 2.7°, 3.6°, 3.9°, 4.4°, 4.6°, 4.8° and 4.9°, respectively, with d_{211} spacing value of ~3.9 nm. These XRD patterns indicate high degree of orderedness amongst the hexagonal (*p6mm*) and cubic (*Ia3d*) mesophases of Si-MCM-41 and Si-MCM-48 materials, respectively.[1,14,15]

Figure 2.2.A represents XRD patterns of the organically modified MCM-41 samples, synthesized by grafting of the following functional groups: (a) $–NH_2$, (b) –SH, (c) –Cl, and (d) $–NH(CH_2)_2NH_2$, using dry DCM solvent, and after treatment with Ph_2SiCl_2. Fig. 2.2.B represents XRD patterns of similar materials synthesized by post-synthesis

grafting without treatment with Ph_2SiCl_2. As evident from the figure, the XRD patterns of the samples synthesized after treatment with Ph_2SiCl_2 (Fig. 2.2.A) are almost the similar to the parent MCM-41 sample (Fig. 2.1), whereas those of the samples synthesized without Ph_2SiCl_2 treatment (Fig. 2.2.B) are quite broad, less in overall intensity and the 110, 200 and 210 reflections are diminished. An analogous trend was also observed in the case of surface modified MCM-48 samples (Figure 2.3) synthesized by grafting of the following functional groups: (a) $–NH_2$, (b) –SH, (c) –Cl, and (d) $–NH(CH_2)_2NH_2$, using dry DCM solvent, after treatment with Ph_2SiCl_2 (Fig. 2.3.A), and without Ph_2SiCl_2 treatment (Fig. 2.3.B).

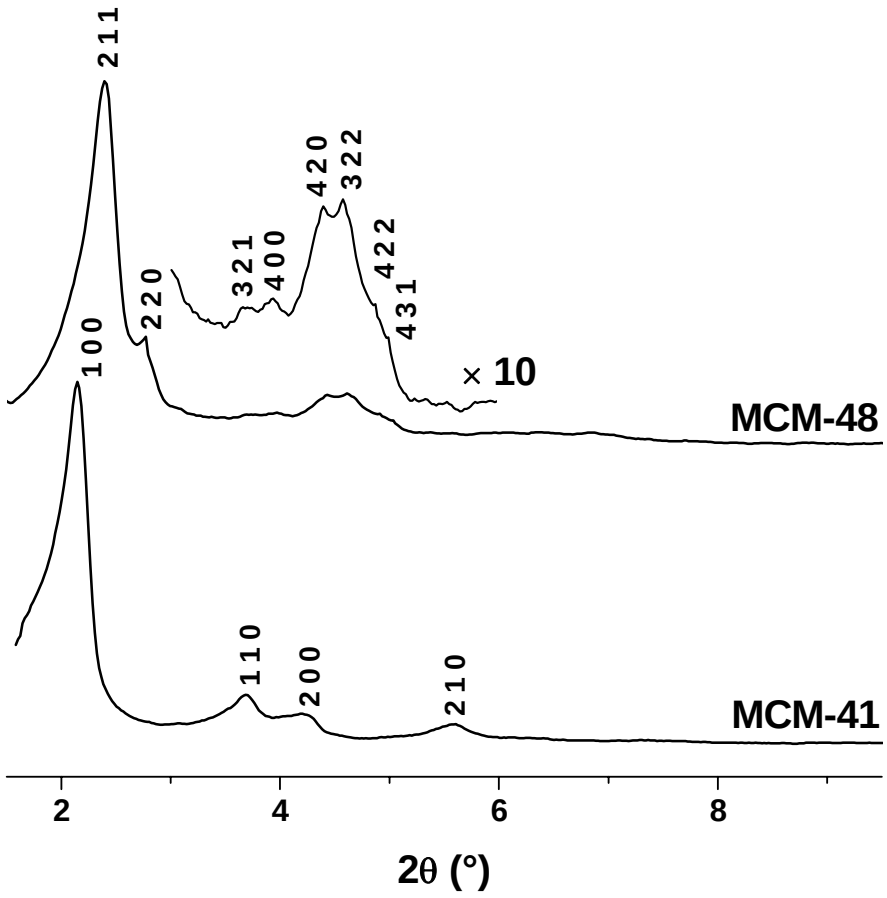

Figure 2.1. Powder XRD patterns recorded from pure siliceous MCM-41 and MCM-48 materials.

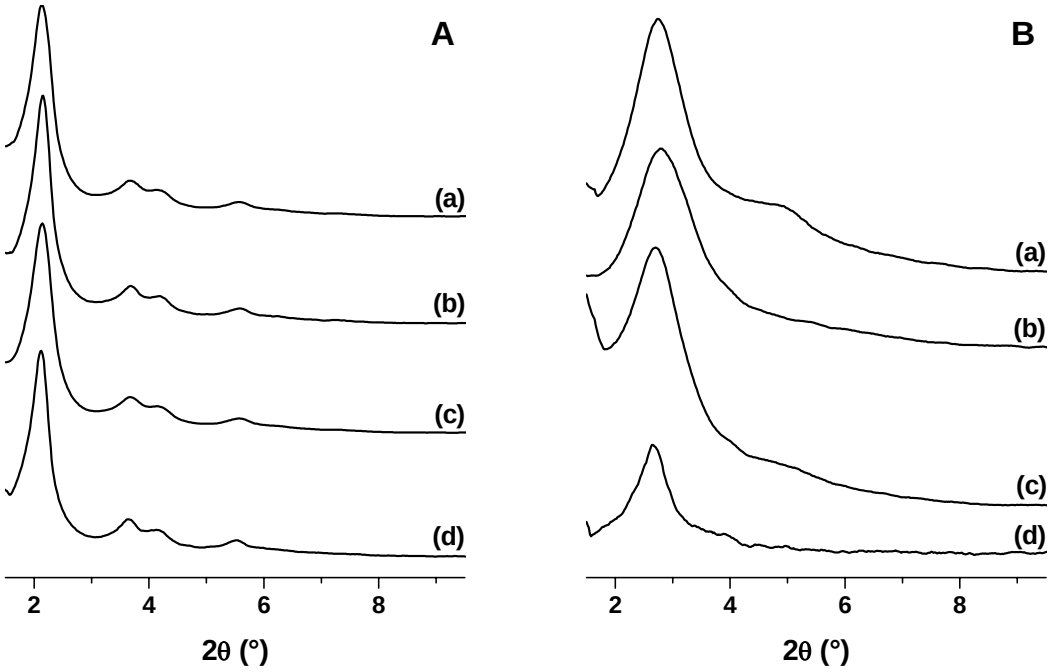

Figure 2.2. Powder XRD patterns: Attempts to synthesize organically modified MCM-41 by post-synthesis grafting of the following functional groups; (a) $–NH_2$, (b) –SH, (c) –Cl, and (d) $–NH(CH_2)_2NH_2$. The syntheses were carried out (A) after treatment with Ph_2SiCl_2, and (B) without Ph_2SiCl_2 treatment.

It is assumed that the most kinetically accessible Si–OH groups exists on the external walls of the mesoporous silica particles. After treatment with Ph_2SiCl_2, these external silanol groups will be silylated and deactivated for further reaction. Therefore, the purpose of using Ph_2SiCl_2 in the grafting process was to ensure that the anchoring of the desired trialkoxyorganosilane occurs predominantly within the internal walls of MCM-41 and MCM-48. If not treated with Ph_2SiCl_2, grafting will occur uncontrollably on the external and internal surfaces of mesoporous silica, which will certainly weaken the orderedness of the materials. This was indeed confirmed from the XRD patterns of the organo-functionalized MCM-41 (Fig. 2.2.B) and MCM-48 (Fig. 2.3.B) samples synthesized without Ph_2SiCl_2 treatment. Henceforth, the organic-group-grafted MCM-41 and MCM-48

materials mentioned in this chapter will be considered as those synthesized after Ph_2SiCl_2 treatment.

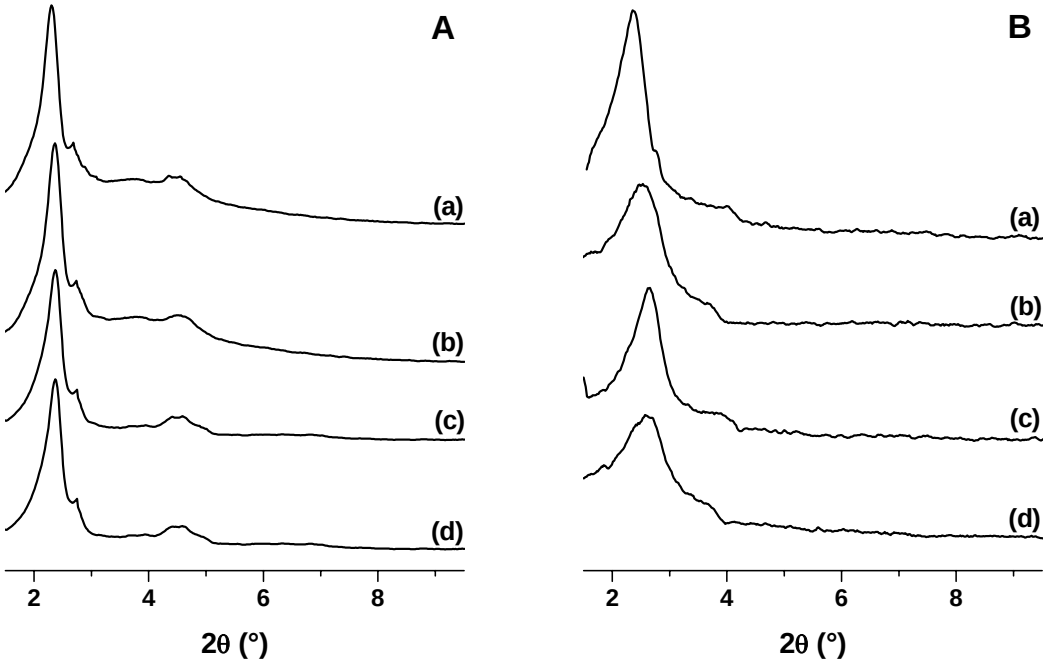

Figure 2.3. Powder XRD patterns: Attempts to synthesize surface modified MCM-48 by post-synthesis grafting of the following functional groups; (a) $–NH_2$, (b) –SH, (c) –Cl, and (d) $–NH(CH_2)_2NH_2$. The syntheses were carried out (A) after treatment with Ph_2SiCl_2, and (B) without Ph_2SiCl_2 treatment.

Figure 2.4 shows the XRD patterns of the amine-functionalized (A) MCM-41 and (B) MCM-48 samples, synthesized by post-synthesis grafting at room temperature using the following dry solvents: (a) DCM, (b) toluene, (c) THF, and (d) MeOH. It was observed that the mesoporous structure was completely collapsed when THF or MeOH were used as solvent (Fig. 2.4.A and 2.4.B, curves c and d). Using toluene as the solvent, comparatively better XRD patterns were obtained (Fig. 2.4.A and 2.4.B, curve b). However, the best ordered structure was obtained when DCM solvent was used (Fig. 2.4.A and 2.4.B, curve a). Therefore, the majority of the grafting experiments were carried out at room temperature using DCM as the solvent.

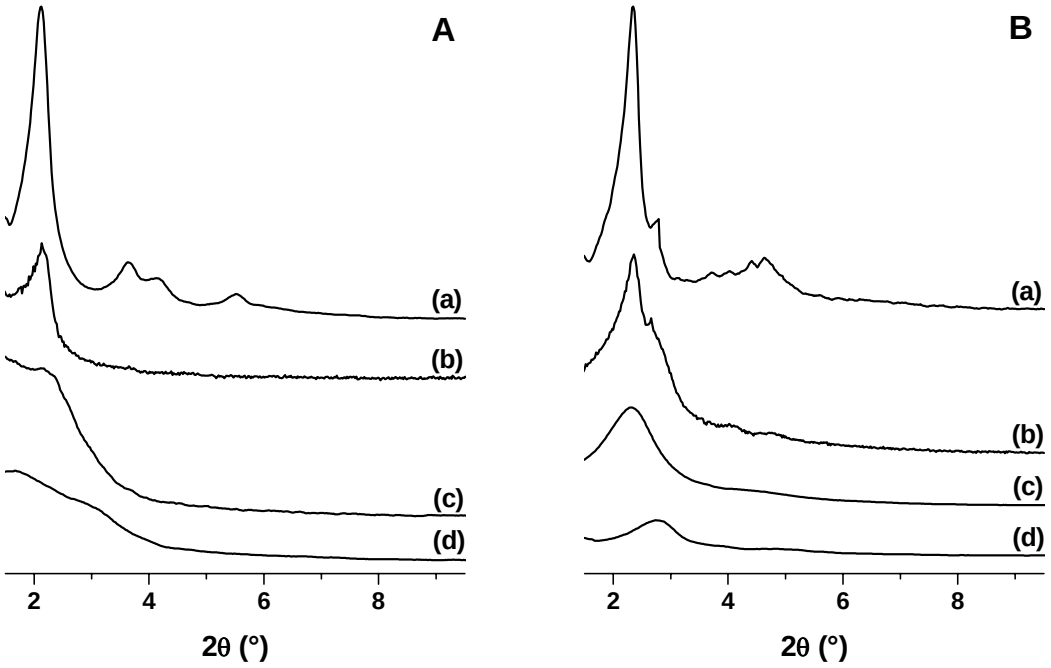

Figure 2.4. Powder XRD patterns: Attempts to synthesize NH_2-functionalized (A) MCM-41 and (B) MCM-48, by post-synthesis grafting, using the following solvents: (a) DCM, (b) toluene, (c) THF, and (d) MeOH.

Figure 2.5 represents the XRD patterns of the surface-functionalized (A) MCM-41 and (B) MCM-48 materials synthesized by the co-condensation process. The MCM-41 samples show characteristic hexagonal ordering (Fig. 2.5.A), as evident from the 100, 110, 200 and 210 reflections. However, the typical cubic pattern of MCM-48 was not achieved at all by the co-condensation method. On the contrary, the XRD patterns (Fig. 2.5.B) resemble with those of the hexagonal mesoporous silica (HMS) materials.[16] Even by increasing the hydrothermal synthesis time upto 120 h, the cubic structure was not obtained. Hence, it can be concluded that organically modified MCM-48 materials cannot be synthesized by the one-pot co-condensation method.

The *d*-spacings and unit cell parameter (a_0) values of all the siliceous and surface modified MCM-41 and MCM-48 materials, calculated from XRD patterns, are summarized in Table 2.2.

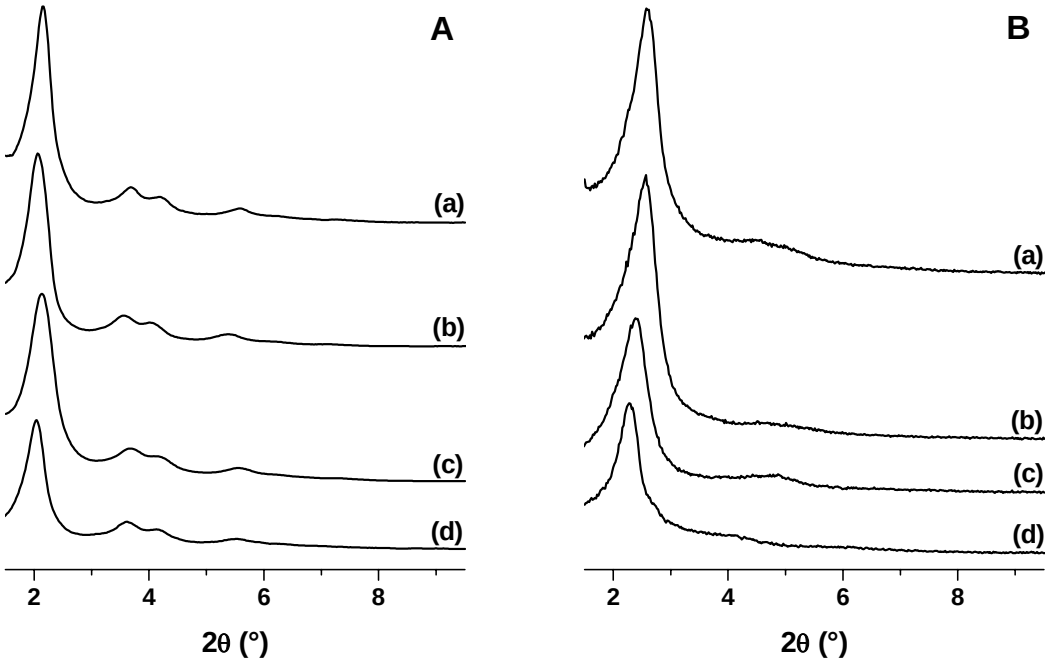

Figure 2.5. Powder XRD patterns: Attempts to synthesize surface-functionalized (A) MCM-41 and (B) MCM-48, by co-condensation method, with the following functional groups: (a) $–NH_2$, (b) –SH, (c) –Cl, and (d) $–NH(CH_2)_2NH_2$.

2.3.2. Porosity Measurements

The specific surface areas of the siliceous as well as organo-functionalized MCM-41 and MCM-48 materials were determined from N_2 adsorption isotherms. Figure 2.6 shows the typical N_2 adsorption-desorption isotherms for the (A) Si-MCM-41, (B) NH_2-MCM-41-G, (C) Si-MCM-48, and (D) NH_2-MCM-48-G samples. All the samples showed isotherms of type IV in the IUPAC classification[17] having a sharp capillary condensation step at P/P_0 = 0.3–0.45 region, which is characteristic of M41S type ordered mesoporous materials.[14] The position of the inflection point depends on the diameter of the mesopores, and its sharpness indicates the uniformity of the narrow pore size distribution. The isotherms of the Si-MCM-41 (Fig. 2.6.A) and Si-MCM-48 (Fig. 2.6.C) samples exhibited virtually no hysteresis loops at $P/P_0 < 0.4$. On the contrary, the NH_2-MCM-41-G (Fig. 2.6.B) and NH_2-MCM-48-G (Fig. 2.6.D) samples display complementary textural and framework-confined

mesoporosity, as evidenced by the presence of a well-defined hysteresis loop in the P/P_0 = 0.25–0.4 region.[18]

Table 2.2. Physical characteristics of various surface modified MCM-41 and MCM-48 materials

Sample	d_{hkl} (Å)[a]	a_0 (Å)[b]	Pore Diameter (Å)	Pore Volume ($cm^3\ g^{-1}$)	Surface Area ($m^2\ g^{-1}$)
Si-MCM-41	42.64 (100)	49.24	39.61	1.19	1322
NH_2-MCM-41-G	41.24 (100)	47.62	30.76	1.12	1047
SH-MCM-41-G	41.15 (100)	47.52	30.25	1.09	1026
Cl-MCM-41-G	40.11 (100)	46.31	29.79	1.08	1031
TPEN-MCM-41-G	41.05 (100)	47.40	28.43	1.06	993
Si-MCM-48	39.13 (211)	95.85	30.40	1.40	1932
NH_2-MCM-48-G	38.30 (211)	93.81	27.69	1.28	1623
SH-MCM-48-G	38.45 (211)	94.18	27.14	1.25	1575
Cl-MCM-48-G	38.92 (211)	95.33	26.93	1.23	1510
TPEN-MCM-48-G	38.12 (211)	93.37	25.40	1.19	1336
NH_2-MCM-41-C	42.03 (100)	48.53	38.77	1.06	947
SH-MCM-41-C	40.11 (100)	46.31	36.79	1.01	883
Cl-MCM-41-C	41.23 (100)	47.61	36.64	1.03	906
TPEN-MCM-41-C	40.84 (100)	47.16	35.52	0.98	796

[a]Calculated from XRD patterns ($n\lambda = 2d\sin\theta$, where $n = 1$ and $\lambda = 1.5404$ Å). Values in parentheses indicate respective principal Miller indices.

[b]$a_0 = d_{100} \times 2/\sqrt{3}$ (for MCM-41); $a_0 = d_{211} \times \sqrt{6}$ (for MCM-48).

The insets of Fig. 2.6 represent the corresponding pore size distribution curves, computed from the BJH model. It was observed that the pore size distribution of the MCM-48 samples is quite narrow than the analogous MCM-41 samples, indicating uniformity of the cubic structure rather than its hexagonal counterpart.

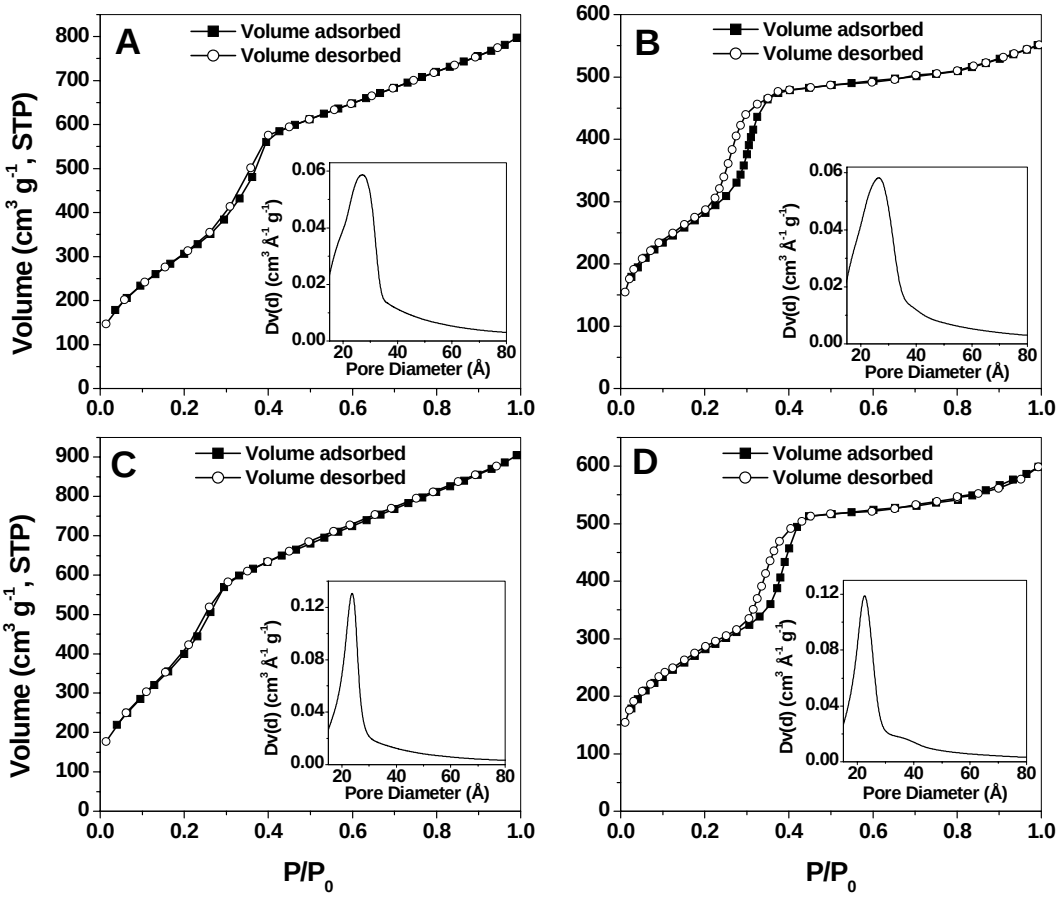

Figure 2.6. N_2 adsorption-desorption isotherms and corresponding pore size distribution curves (insets) for (A) Si-MCM-41, (B) NH_2-MCM-41-G, (C) Si-MCM-48, and (D) NH_2-MCM-48-G samples.

The pore volumes, average pore diameters and BET surface area values of all the siliceous and organo-functionalized MCM-41 and MCM-48 samples are summarized in Table 2.2. After grafting of the $–NH_2$, –SH, –Cl and $–NH(CH_2)_2NH_2$ functional groups, it was observed that surface areas of the MCM-41 materials were decreased by *ca*. 20–25%, pore volumes were decreased by *ca*. 6–11%, and pore diameters were decreased by *ca*. 22–28%. Analogous decreases of surface areas (*ca*. 16–31%), pore volumes (*ca*. 9–15%), and pore diameters (*ca*. 9–16%) were observed in the case of the MCM-48 materials also. All these results strongly indicate that the organic functional groups are located inside the channels.

The surface areas, pore volumes, and pore diameters of the surface-functionalized MCM-41 samples synthesized by co-condensation method were less than those of the Si-MCM-41 sample by *ca*. 28–40%, *ca*. 11–18%, and *ca*. 2–11%, respectively. However, a striking difference in the average pore diameter values was observed in the organo-functionalized MCM-41-G (*ca*. 3 nm) and MCM-41-C (*ca*. 3.7 nm) samples. This estimation of pore diameters was quite important since the pore sizes determine the accessibility of guest species with different dimensions. Thus, the MCM-41-C materials can be widely exploited for size-selective incorporation of chemical entities (such as nanoparticles) having dimensions in the range of 3–3.6 nm.

2.3.3. Scanning Electron Microscopy

The particle size and morphology of different Si-MCM-41, Si-MCM-48, and organo-functionalized MCM-41 and MCM-48 samples have been determined by scanning electron microscopy (SEM). Figure 2.7 represents the SEM micrographs of (A) Si-MCM-41, (B) NH_2-MCM-41-G, (C) NH_2-MCM-41-C, (D) Si-MCM-48, (E) NH_2-MCM-48-G, and (F) NH_2-MCM-48-C samples. Whilst the SEM images of the siliceous (Fig. 2.7.A) as well as organo-functionalized MCM-41 (Fig. 2.7.B and 2.7.C) samples revealed well-distributed hexagonal and spheroidal particles of *ca*. 1 μm dimension, those of the Si-MCM-48 (Fig. 2.7.D) and NH_2-MCM-48-G (Fig. 2.7.E) samples disclosed spheroidal and cuboidal particles of dimensions ranging from 0.5–1.2 μm. Interestingly, the SEM micrograph of the NH_2-MCM-48-C sample (Fig. 2.7.F) shows relatively bigger (*ca*. 2 μm size) hexagonal particles, indicating formation of hexagonal mesoporous silica (HMS) structure, which was earlier predicted from powder XRD patterns (Fig. 2.5.B).

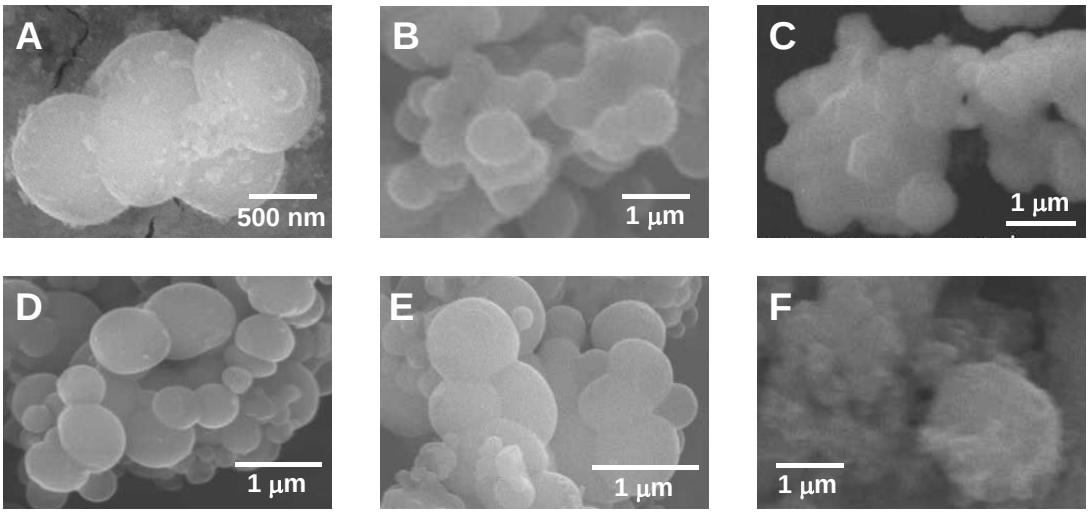

Figure 2.7. SEM images of (A) Si-MCM-41, (B) NH_2-MCM-41-G, (C) NH_2-MCM-41-C, (D) Si-MCM-48, (E) NH_2-MCM-48-G, and (F) NH_2-MCM-48-C samples.

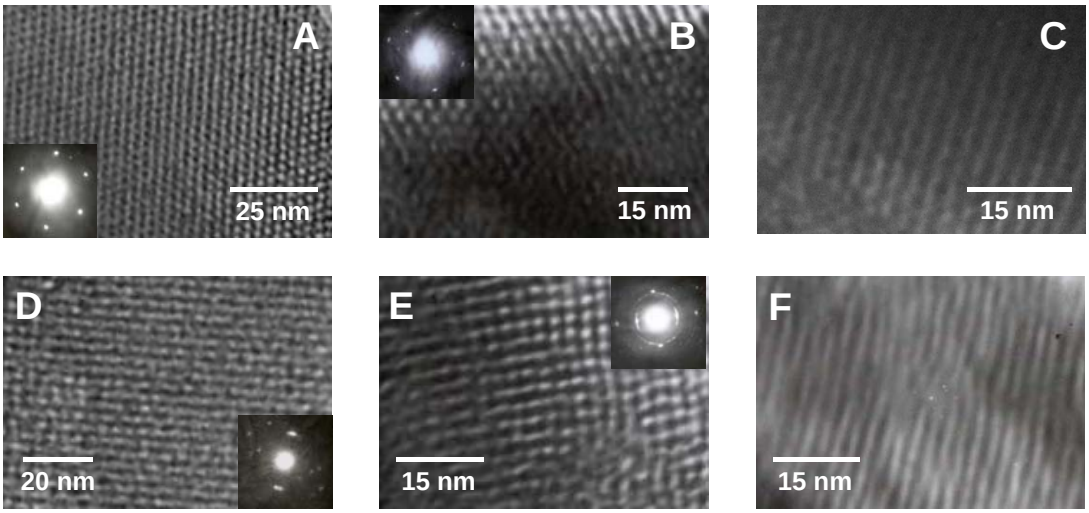

Figure 2.8. TEM images of (A) Si-MCM-41, (B) NH_2-MCM-41-G, (C) NH_2-MCM-41-C, (D) Si-MCM-48, (E) NH_2-MCM-48-G, and (F) NH_2-MCM-48-C samples. Insets show respective selected area electron diffraction patterns.

2.3.4. Transmission Electron Microscopy

Transmission electron microscopy (TEM) has been used to obtain topographic information about the mesoporous matrices at near atomic resolution. Figure 2.8 shows the TEM images of (A) Si-MCM-41, (B) NH_2-MCM-41-G, (C) NH_2-MCM-41-C, (D) Si-MCM-48, (E) NH_2-MCM-48-G, and (F) NH_2-MCM-48-C samples. Insets show the

corresponding selected area electron diffraction (SAED) patterns. The TEM micrographs of the MCM-41 samples (Fig. 2.8.A–C), seen along the pore direction, revealed regular hexagonal array of uniform channels. The respective SAED patterns are also well consistent with the hexagonal mesophase. Similarly, the TEM images and SAED patterns of the Si-MCM-48 (Fig. 2.8.D) and NH_2-MCM-48-G (Fig. 2.8.E) samples exposed well defined cubic patterns of a uniform channel system. Nevertheless, the TEM image of the NH_2-MCM-48-C sample (Fig. 2.8.F) represents parallel fringes corresponding to side-on view of the long pores. The equidistant parallel fringes illustrate exclusive feature of separate layers, the addition of which forms a bunch of layers. This characteristic of hexagonal mesoporous silica (HMS) structure further supports the XRD (Fig. 2.5.B) and SEM (Fig. 2.7.F) results presented earlier.

2.3.5. Elemental Microanalyses

The results of microanalyses alongwith the theoretical values (for C, H, N and S) of all the surface-functionalized mesoporous materials are summarized in Table 2.3. In the case of the samples prepared by post-synthesis grafting, the theoretical values were calculated assuming formal weights (FW) of both Si-MCM-41 and Si-MCM-48 equal to 60, *i.e.*, that of pure SiO_2. For the samples prepared by co-condensation, the theoretical values were calculated according to the initial molar ratio of the synthesis gel. The results give indirect proof towards incorporation of respective organic functional groups.

2.3.6. Solid State NMR

Unambiguous direct proof of organic functional group incorporation on the MCM-41 and MCM-48 samples was obtained from solid state NMR experiments. ^{13}C and ^{29}Si CP MAS NMR spectra of all the samples were recorded in order to confirm the existence of

different chemical environments around carbon and silicon atoms in the mesoporous matrices (Scheme 2.1), and the degree of organic group functionalization.

Table 2.3. Theoretical and observed organic composition of various organo-functionalized MCM-41 and MCM-48 materials

Sample	Theoretical (wt %)				Experimental (wt %)			
	C	H	N	S	C	H	N	S
NH_2-MCM-41-G	13.74	3.06	5.35	-	12.63	2.91	4.81	-
SH-MCM-41-G	12.41	2.42	-	11.03	11.43	2.36	-	10.17
Cl-MCM-41-G	12.42	2.07	-	-	11.51	1.95	-	-
TPEN-MCM-41-G	17.18	3.72	8.02	-	15.36	3.39	7.19	-
NH_2-MCM-48-G	13.74	3.06	5.35	-	12.16	2.85	4.66	-
SH-MCM-48-G	12.41	2.42	-	11.03	10.88	2.22	-	9.57
Cl-MCM-48-G	12.42	2.07	-	-	11.05	1.94	-	-
TPEN-MCM-48-G	17.18	3.72	8.02	-	14.75	3.31	6.89	-
NH_2-MCM-41-C	15.25	3.39	5.93	-	14.32	3.27	5.52	-
SH-MCM-41-C	14.23	2.77	-	12.65	13.19	2.69	-	11.70
Cl-MCM-41-C	14.09	2.35	-	-	13.11	2.24	-	-
TPEN-MCM-41-C	21.50	4.66	10.04	-	20.27	4.45	9.45	-

2.3.6.1. ^{13}C CP MAS NMR Spectra

Figure 2.9 represents the ^{1}H–^{13}C coupled CP MAS NMR spectra of (a) NH_2-MCM-41-G, (b) SH-MCM-41-G, (c) Cl-MCM-41-G, and (d) TPEN-MCM-41-G samples. In all the spectra, a doublet centered at $\delta \approx 133$ ppm was observed, which might occur due to the aromatic carbon atoms of the externally grafted Ph_2SiCl_2. The spectra of the NH_2-MCM-41-G (Fig. 2.9, curve a), Cl-MCM-41-G (Fig. 2.9, curve c) samples reveal three distinct ^{13}C signals at $\delta \approx 11$, 29 and 50 ppm, which can be assigned to C_1, C_2 and C_3 atoms, respectively, of the propyl chain (Scheme 2.1).

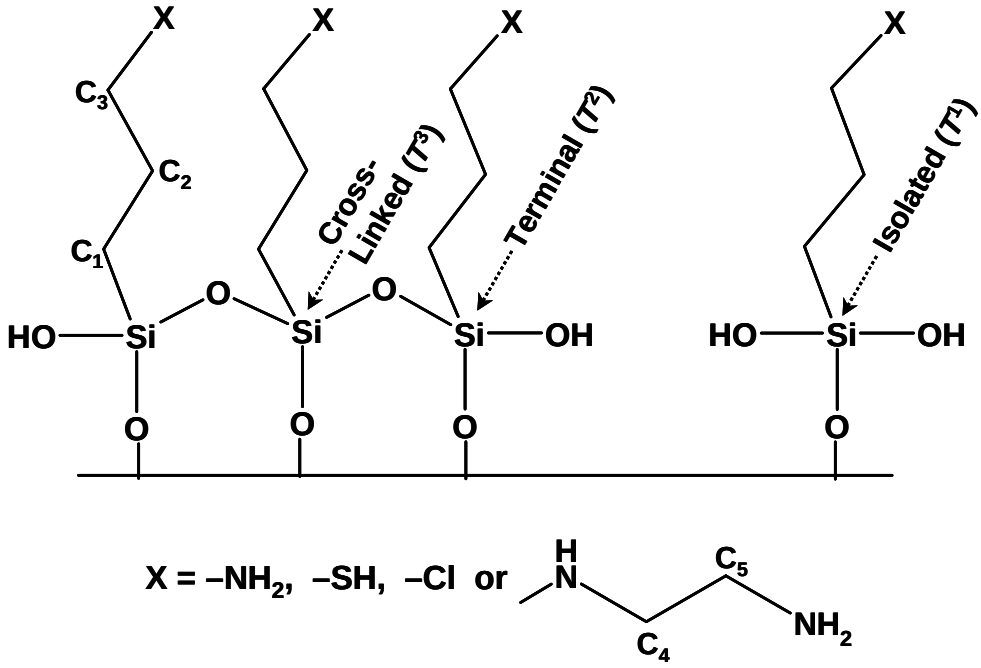

Scheme 2.1. Schematic representation of different chemical environments of carbon (C) and silicon (Si) atoms.

The spectrum of the SH-MCM-41-G material (Fig. 2.9, curve b) shows the presence of the most prominent peak at $\delta = 21$ ppm for both the C_2 and C_3 atoms. The signal at $\delta = 9$ ppm arises from the C_1 atom.

In the spectrum of the TPEN-MCM-41-G sample (Fig. 2.9, curve d), four resonances at $\delta = 14$, 25, 41 and 53 ppm were observed. The peaks at 14 and 25 ppm are assigned to the C_1 and C_2 atoms. The signal at 52 ppm is a broader one, which arises from both of the C_3 and C_4 atoms, *i.e.*, the two carbon atoms bonded to the imine (–NH–) moiety (Scheme 2.1). The signal for the C_5 atom, adjacent to the $–NH_2$ group (Scheme 2.1), comes at 41 ppm.

Figure 2.10 shows the $^{1}H–^{13}C$ coupled CP MAS NMR spectra of (a) NH_2-MCM-48-G, (b) SH-MCM-48-G, (c) Cl-MCM-48-G, and (d) TPEN-MCM-48-G materials. The spectra of these materials were similar to those of the corresponding organic-group-grafted MCM-41 materials (Fig. 2.9). For instance, a doublet centered at $\delta \approx 133$ ppm was observed

in all the spectra, which was attributed to the aromatic carbon atoms of the externally grafted Ph_2SiCl_2. The spectra of the NH_2-MCM-48-G (Fig. 2.10, curve a) and Cl-MCM-48-G (Fig. 2.10, curve c) samples also reveal three strong signals at $\delta \approx 12$, 29 and 49 ppm, which can be assigned to C_1, C_2 and C_3 atoms, respectively (Scheme 2.1).

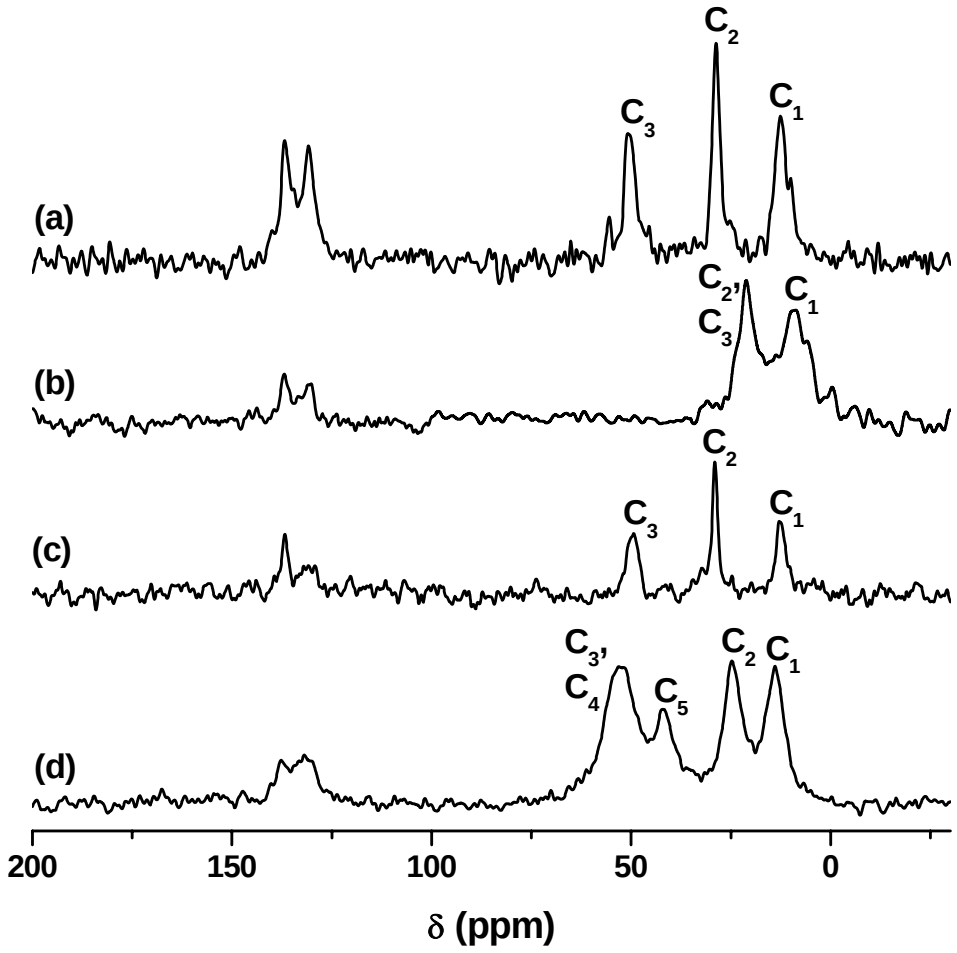

Figure 2.9. The ^{1}H–^{13}C coupled CP MAS NMR spectra of (A) (a) NH_2-MCM-41-G, (b) SH-MCM-41-G, (c) Cl-MCM-41-G, and (d) TPEN-MCM-41-G materials.

The spectrum of the SH-MCM-48-G material (Fig. 2.10, curve b) shows one strong peak at $\delta = 29$ ppm arising from both the C_2 and C_3 atoms, and another peak at $\delta = 12$ ppm arising from the C_1 atom. The spectrum of the TPEN-MCM-48-G sample (Fig. 2.10, curve d) shows three strong resonances at $\delta = 14$, 24 and 41 ppm, attributed to C_1, C_2 and C_5

atoms, respectively, and a not-so-well-resolved doublet centered at δ = 52 ppm, attributed to the C_3 and C_4 atoms (Scheme 2.1).

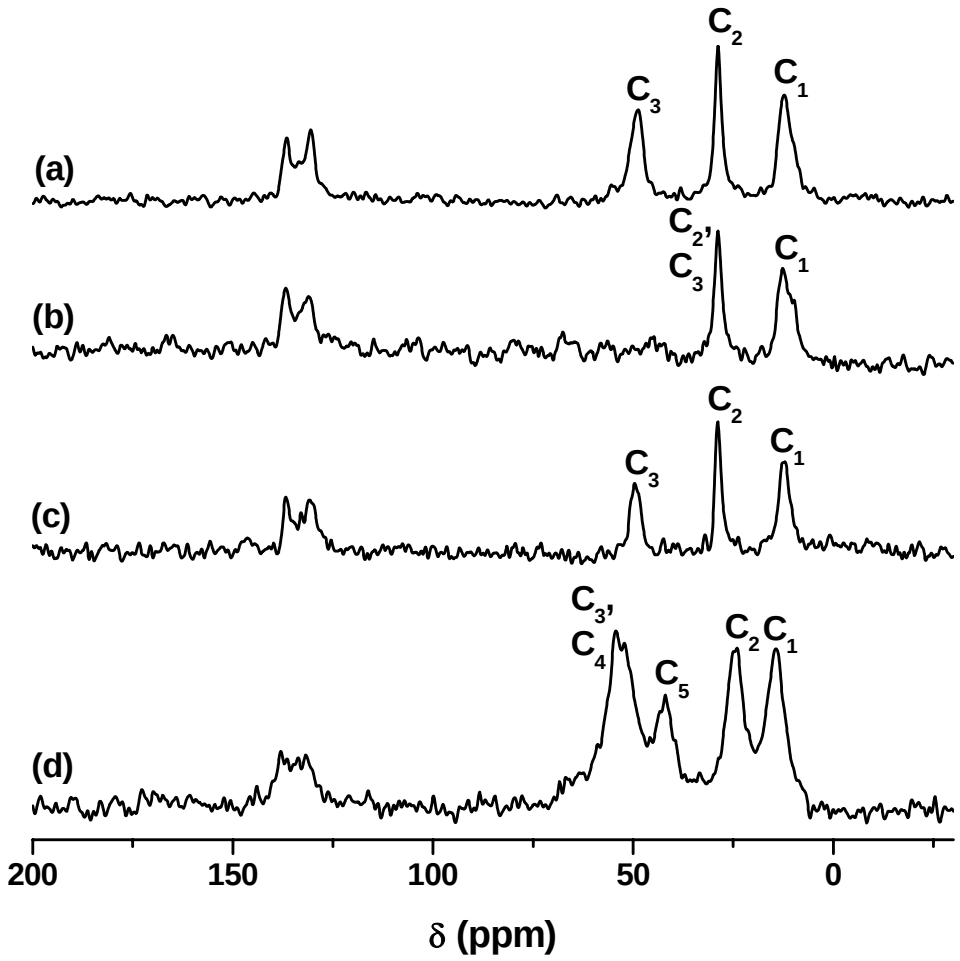

Figure 2.10. The $^{1}H–^{13}C$ coupled CP MAS NMR spectra of (a) NH_2-MCM-48-G, (b) SH-MCM-48-G, (c) Cl-MCM-48-G, and (d) TPEN-MCM-48-G samples.

Figure 2.11 represents the $^{1}H–^{13}C$ coupled CP MAS NMR spectra of (a) NH_2-MCM-41-C, (b) SH-MCM-41-C, (c) Cl-MCM-41-C, and (d) TPEN-MCM-41-C samples. In contrast to the previous spectra of the organo-functionalized MCM-41 (Fig. 2.9) and MCM-48 (Fig. 2.10) samples synthesized by post-synthesis grafting, the doublet at δ ≈ 133 ppm was absent in the spectra of the surface modified MCM-41 materials (Fig. 2.11) synthesized by co-condensation, indicating the absence of Ph_2SiCl_2 in the external surface.

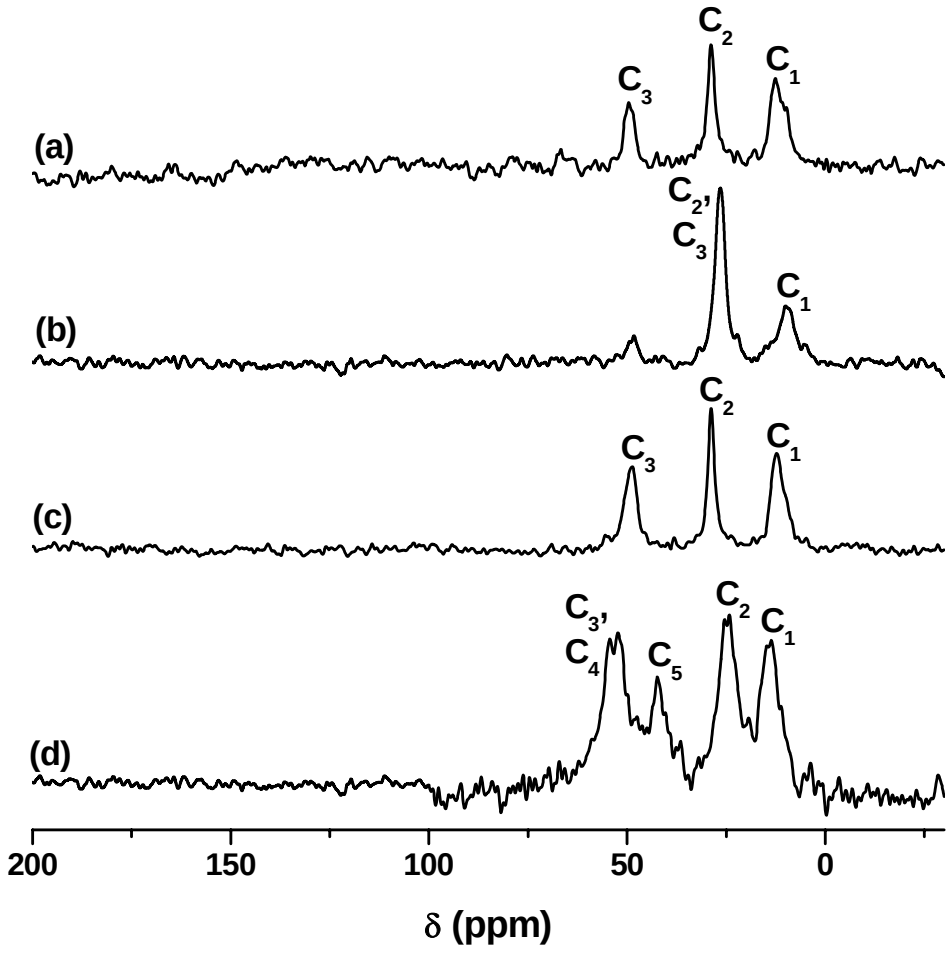

Figure 2.11. The $^{1}H–^{13}C$ coupled CP MAS NMR spectra of (a) NH_2-MCM-41-C, (b) SH-MCM-41-C, (c) Cl-MCM-41-C, and (d) TPEN-MCM-41-C materials.

The spectra of the NH_2-MCM-41-C (Fig. 2.11, curve a) and Cl-MCM-41-C (Fig. 2.11, curve c) samples also show three distinct ^{13}C signals at $\delta \approx 13$, 29 and 49 ppm as usual, which can be assigned to C_1, C_2 and C_3 atoms (Scheme 2.1), respectively.

The spectrum of the SH-MCM-41-C material (Fig. 2.11, curve b) also reveals one prominent peak at $\delta = 27$ ppm for both the C_2 and C_3 atoms, and another signal at $\delta = 10$ ppm for the C_1 atom. One additional weak resonance observed at 50 ppm in the case of the SH-MCM-41-C sample (Fig. 2.11, curve b) can be attributed to residual methanol used in the extraction of surfactants.

The spectrum of the TPEN-MCM-41-C sample (Fig. 2.11, curve d) shows four distinct resonances at δ = 14, 25, 43 and 53 ppm. The peaks at 14 and 25 ppm are assigned to the C_1 and C_2 atoms as usual. The strong signal at 53 ppm is a not-so-well-resolved doublet, which arises from the C_3 and C_4 atoms, *i.e.*, the atoms adjacent to the –NH– moiety (Scheme 2.1). The signal at 41 ppm arises from the C_5 atom, adjacent to the $–NH_2$ group (Scheme 2.1).

2.3.6.2. ^{29}Si CP MAS NMR Spectra

Figure 2.12 shows the ^{29}Si CP MAS NMR spectra of the (a) Si-MCM-41, (b) NH_2-MCM-41-G, (c) NH_2-MCM-41-C, (d) Si-MCM-48, and (e) NH_2-MCM-48-G samples. In all the spectra, the strong resonances at δ ≈ –101 and –110 ppm are attributed to Q^3 [$(SiO)_3$≡Si–OH] and Q^4 [$(SiO)_3$≡Si–O–Si≡] species, respectively, present in the silicate framework of MCM-41 and MCM-48 materials.

The spectra of the NH_2-MCM-41-G (Fig. 2.12, curve b) and NH_2-MCM-48-G (Fig. 2.10, curve e) show evidence for the close-packed conformation of propyl chains in the functionalized materials, as three additional peaks were observed at δ ≈ –49, –57 and –66 ppm, which correspond to three different environments for the siloxane groups in the functionalized monolayers. These peaks are due to the presence of isolated (T^1), terminal (T^2) and cross-linked (T^3) siloxane moieties (Scheme 2.1), respectively. Among the three, the strongest peak comes from the terminal group (T^2).

The presence of close-packed conformation of propyl chains is also manifested from the spectrum of the NH_2-MCM-41-C sample (Fig. 2.12, curve c). The two additional signals at δ ≈ –60 and –67 ppm are assigned to terminal (T^2) and cross-linked (T^3) siloxane groups, respectively, attached with pendant organic groups. The intensity of the signal corresponding to T^3 species is approximately double than that of the T^2 species. Moreover,

the signal for the T^1 species was not at all observed for this sample. These results suggest that in the co-condensation process, the organic functional groups are more tightly bound to the inner walls, than in the case of post-synthesis grafting.

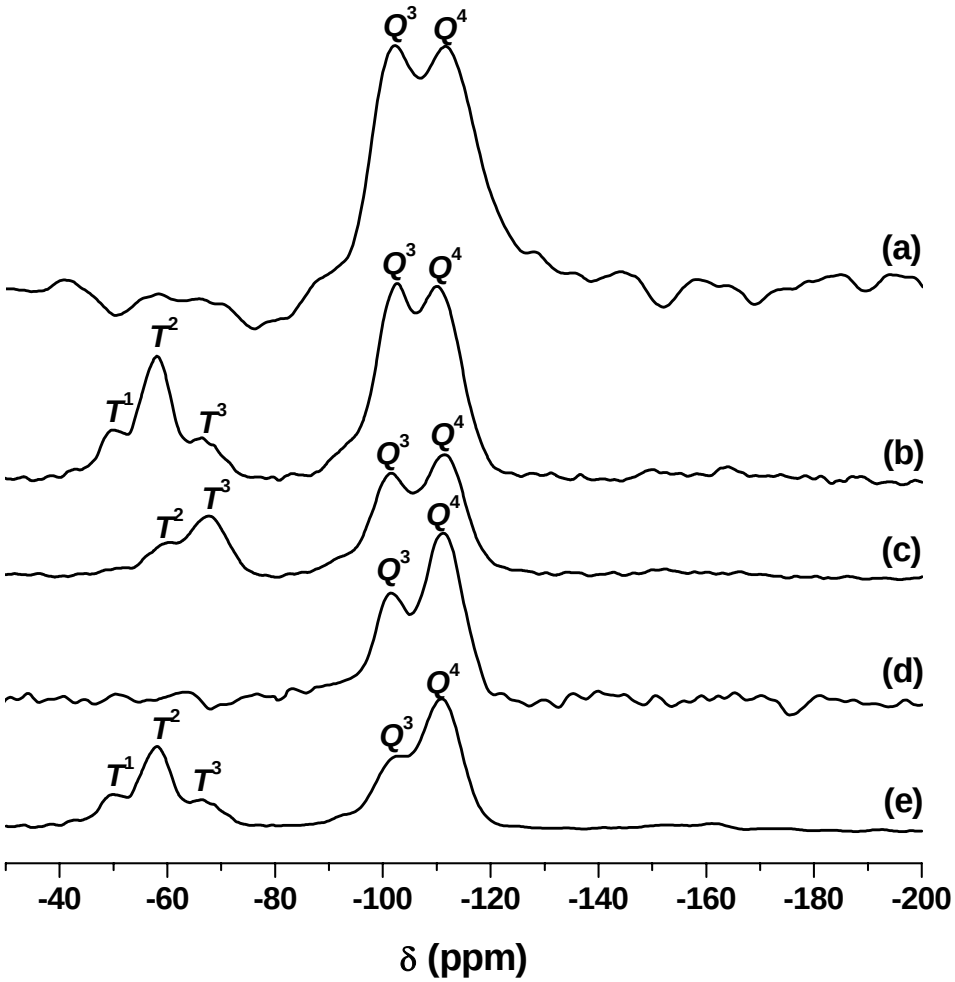

Figure 2.12. ^{29}Si CP MAS NMR spectra of (a) Si-MCM-41, (b) NH_2-MCM-41-G, (c) NH_2-MCM-41-C, (d) Si-MCM-48, and (e) NH_2-MCM-48-G samples.

2.3.7. Thermal Analyses

The thermal stability of the organic functional groups within the mesoporous network was evaluated by thermogravimetry and differential thermal analyses (TG-DTA). Figure 2.13 represents the TGA curves (left axes) and DTA curves (right axes) for (A) NH_2-MCM-41-G, (B) NH_2-MCM-48-G, and (C) NH_2-MCM-41-C samples. An initial weight

loss below 150 °C corresponds to desorption and removal of physisorbed water from the pore system. This loss is significant (*ca*. 10%) in the case of the NH_2-MCM-41-C sample (Fig. 2.13.C), also indicated by an endotherm in the DTA curve. A second weight loss (*ca*. 10–15%), accompanied by several exotherms, occurs between 250 °C and 450 °C and is attributed to oxidative decomposition of the organic content in three or more steps.

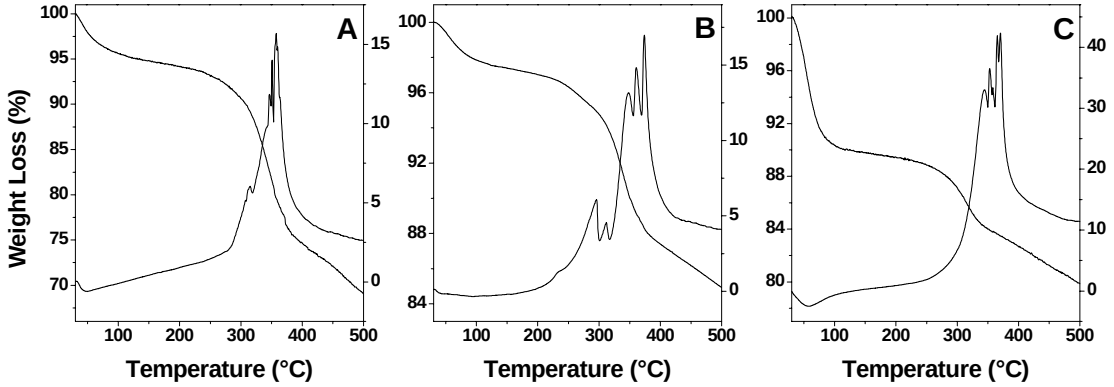

Figure 2.13. TGA (left axes) and DTA curves (right axes) for (A) NH_2-MCM-41-G, (B) NH_2-MCM-48-G, and (C) NH_2-MCM-41-C samples.

In conclusion, a number of surface-functionalized mesoporous MCM-41 and MCM-48 materials were prepared by post-synthesis grafting and direct synthesis (co-condensation) methods, and the products obtained from both methods were assessed *via* thorough characterization. The applications of these inorganic–organic hybrid materials as hosts for different catalytically active species will be demonstrated in the succeeding chapters.

2.4. REFERENCES

1. C. T. Kresge, M. E. Leonowicz, W. J. Roth, J. C. Vartuli, J. S. Beck, *Nature* **1992**, *359*, 710.
2. J. S. Beck, J. C. Vartuli, W. J. Roth, M. E. Leonowicz, C. T. Kresge, K. D. Schmitt, C. T. -W. Chu, D. H. Olson, E. W. Sheppard, S. B. McCullen, J. B. Higgins, J. L. Schlenker, *J. Am. Chem. Soc.* **1992**, *114*, 10834.
3. A. Corma, *Chem. Rev.* **1997**, *97*, 2373.
4. A. Stein, B. J. Melde, R. C. Schroden, *Adv. Mater.* **2000**, *12*, 1403.
5. A. P. Wight, M. E. Davis, *Chem. Rev.* **2002**, *102*, 3589.
6. K. Moller, T. Bein, *Chem. Mater.* **1998**, *10*, 2950.
7. M. H. Lim, A. Stein, *Chem. Mater.* **1999**, *11*, 3285.
8. D. S. Shephard, W. Zhou, T. Maschmeyer, J. M. Matters, C. L. Roper, S. Parsons, B. F. G. Johnson, M. J. Duer, *Angew. Chem. Int. Ed.* **1998**, *37*, 2719.
9. S. L. Burkett, S. D. Sims, S. Mann, *Chem. Commun.* **1996**, 1367.
10. P. Mukherjee, S. Laha, D. Mandal, R. Kumar, *Stud. Surf. Sci. Catal.* **2000**, *129*, 283.
11. K. Mukhopadhyay, A. Ghosh, R. Kumar, *Chem. Commun.* **2002**, 2404.
12. S. Brunauer, P. H. Emmett, E. Teller, *J. Am. Chem. Soc.* **1938**, **60**, 309.
13. E. P. Barrett, L. G. Joyner, P. P. Halenda, *J. Am. Chem. Soc.* **1951**, *73*, 373.
14. C. -Y. Chen, H. -X. Li, M. E. Davis, *Microporous Mater.* **1993**, *2*, 17.
15. J. Xu, Z. Luan, H. He, W. Zhou, L. Kevan, *Chem. Mater.* **1998**, *10*, 3690.
16. P. T. Tanev, T. J. Pinnavaia, *Chem. Mater.* **1996**, *8*, 2068.
17. S. J. Gregg, K. S. W. Sing, *Adsorption, Surface Area and Porosity*, Academic Press, London, **1967**, pp. 121–194.
18. X. Chen, L. Huang, Q. Li, *J. Phys. Chem. B.* **1997**, *101*, 8460.

3.1. INTRODUCTION

The synthesis of enantiomerically pure chiral compounds has fascinated researchers owing to its immense importance in the fine chemical industry, particularly in pharmaceuticals, agrochemicals, fragrance chemicals, to mention just a few.[1] An explosive research in this area has been inspired by the fact that the "wrong" enantiomer of a chiral compound could be a toxin in quite a few biological processes, whose detrimental effects can overshadow the vitalities of a "right" enantiomer.[2] So far, numerous strategies have been developed to produce the desired enantiomer of an optically active compound, amongst which asymmetric catalysis offers exclusive and enormous advantages.[3]

Enantioselective reduction of functionalized C=C and C=O groups, involving molecular dihydrogen and catalytic amount of transition metal complexes, is one of the most fundamental molecular transformations.[4,5] Hydrogenation of C=C bond is relatively easier than that of C=O bond owing to the following reasons: (a) thermodynamics favors hydrogenation of C=C over C=O group by about 35 kJ mol^{-1}, and (b) kinetically the reactivity of the C=C group towards hydrogenation is higher than that of C=O group hydrogenation. However, the industrial demand for hydrogenation of prochiral carbonyl compounds to produce optically active alcohols has been amplified in the past few decades.[6,7]

Chemoselective hydrogenation of α,β-unsaturated aldehydes containing both C=O and C=C functional groups to unsaturated (allylic) alcohols is another industrially important reaction, as unsaturated alcohols are important intermediates in pharmaceuticals and cosmetics industry.[8] Conventional hydrogenation catalysts (Pt, Ru, Ni *etc*. supported on oxides) produce predominantly the saturated aldehyde or the saturated alcohol from the consecutive hydrogenation.[9] However, the saturated aldehyde can easily be produced by an alternate route involving alkene hydroformylation. Studies on these supported metal

catalysts revealed that the selectivity to the unsaturated alcohols increases with increasing substitution on the terminal carbon atom of the C=C group.[10] To date, several attempts have been made to develop suitable heterogeneous catalysts for the chemoselective hydrogenation of the C=O group in α,β-unsaturated aldehydes.[11] But the rational design of heterogenized homogeneous catalysts applied to this preferential hydrogenation of the C=O group to the unsaturated alcohol is not fully understood.

Although, Wilkinson's Ru^{II}-phosphine complexes are well recognized to catalyze hydrogenation of olefins, such catalysts are normally not very active for hydrogenation of carbonyl groups. However, the activity can be remarkably enhanced with the addition of stoichiometric amount of ethylenediamine,[12,13] which decelerates hydrogenation of C=C bond and in turn accelerates C=O hydrogenation by a "*Metal-ligand bifunctional catalysis*" mechanism.[14,15] This concept, established by Noyori *et al*., was successfully applied towards hydrogenation of prochiral ketones by using Ru^{II}–chiral-diphosphine–chiral-diamine species as a soluble catalyst in the organic phase.[4,14-16] Appropriate enantiomers of 2,2'-bis(diphenylphosphino)-1,1'-binaphthyl (BINAP) and 1,2-diphenylethylenediamine (DPEN) as the abovementioned chiral ligands (coordinated to Ru^{II}) are widely used nowadays in the production of various specialty chemicals.[4]

While several attempts have been made to heterogenize the soluble transition metal complex catalysts to extend the benefits of heterogeneous catalysis to homogeneous systems, *viz*., easier separation catalyst and reaction products, and reusability for the supported catalyst,[17] there has been limited success in the case of asymmetric heterogeneous catalysis.[18-26] Moreover, homogeneous catalysts are characterized by high activity and selectivity, which are not generally achieved by the corresponding heterogeneous catalysts.[21-23] Therefore, during heterogenization of homogeneous catalysts, it was a long-held view that any advantages, with regard to work up of the reaction mixture, purity of the

product prepared, catalyst recovery and continuous reaction procedure, can only be realized in conjunction with serious disadvantages with regard to activity and selectivity. However, recent studies have revealed that some heterogenized catalysts indeed can give equivalent or higher selectivity and yields compared to their homogeneous counterparts.[24-26]

Surface-functionalized M41S type molecular sieves can be one of the appropriate choices for immobilization of Ru^{II}–phosphine complexes. But a rational design for grafting of such complexes inside the mesopores of MCM-41 and MCM-48 is indispensable.[18,21,22,25,26] It is in this context; we have synthesized efficient heterogeneous catalytic systems for chemo- and enantioselective hydrogenation of carbonyl compounds, involving anchoring of Ru^{II}-phosphine or Ru^{II}-diphosphine complexes on the inner surfaces of amine- or ethylenediamine–functionalized MCM-41 and MCM-48 materials.[27] In depth characterization of these catalyst systems reveals that the integrity of the mesoporous supports and the Ru^{II}-complexes was retained after the immobilization process. Applying these new heterogeneous catalysts, we have obtained fairly good chemoselectivities in the hydrogenation of C=O bond in α,β-unsaturated aldehydes, and excellent enantioselectivities in the hydrogenation of prochiral ketones.[27] Hydrogenation of unsaturated hydrocarbons was also performed using these catalysts. Acting as a true heterogeneous catalyst, these show comparable activity and selectivity even after four recycles without any leaching of the Ru-complex from the support.

The Ru-complexes were also grafted onto the organically modified surfaces of amorphous (fumed) silica for comparison of activity and selectivity in hydrogenation reactions. Considerable leaching of ruthenium from fumed silica supports was observed after the reactions.

3.2. EXPERIMENTAL

3.2.1. Materials

$RuCl_3.xH_2O$, 1,3-cyclohexadiene, (*S*,*S*)-1,2-diphenylethylenediamine (SDPEN), (*S*)-2,2'-bis(diphenylphosphino)-1,1'-binaphthyl [(*S*)-BINAP], 3-aminopropyltrimethoxy silane (APTS), *N*-[3-(trimethoxysilyl)propyl]-ethylenediamine (TPEN), 3-chloropropyltrimethoxy silane (CPTS), fumed silica, 1-hexene, 1-octene, acrolein, crotonaldehyde, α-methyl-*trans*-cinnamaldehyde, acetophenone, *p*-methylacetophenone, *p*-chloroacetophenone, *p*-methoxyacetophenone, propiophenone, cyclohexylmethylketone, cyclobutylphenylketone were purchased from Aldrich; triethylamine (NEt_3), triphenylphosphine (PPh_3), ethylmethylketone, potassium *tert*-butoxide (^tBuOK), cinnamaldehyde and 2-propanol were purchased from Loba Chemie, India, and were used as received without further purification.

3.2.2. Anchoring of $RuCl_2(PPh_3)_3$ Complex inside Amine-Functionalized MCM-41 and MCM-48

The $RuCl_2(PPh_3)_3$ complex was synthesized applying a published procedure.[28] $RuCl_3.xH_2O$ and PPh_3 were dissolved in 25 mL of dry ethanol in 1:6 molar ratios and refluxed for 4 h under N_2 atmosphere. The resulting brown solid was filtered, thoroughly washed several times with dry methanol, and dried under vacuum.

All the organo-functionalized MCM-41 and MCM-48 materials to be mentioned henceforth in this chapter were synthesized applying the post-synthesis grafting method, as described in Chapter 2.

The $RuCl_2(PPh_3)_3$ complex was anchored to the inner surfaces of amine-functionalized MCM-41 or MCM-48 (NH_2-MCM-41/48) by the following manner (Scheme 3.1). 1 g of NH_2-MCM-41 or NH_2-MCM-48 was added to a solution containing 38 mg (0.04 mmol) of the complex dissolved in 30 mL of dry dichloromethane (DCM), and the mixture

was stirred at room temperature for 12 h under N_2 atmosphere, filtered, washed with DCM, and dried under vacuum. The resultant material was designated as RuP-NH_2-MCM-41/48.

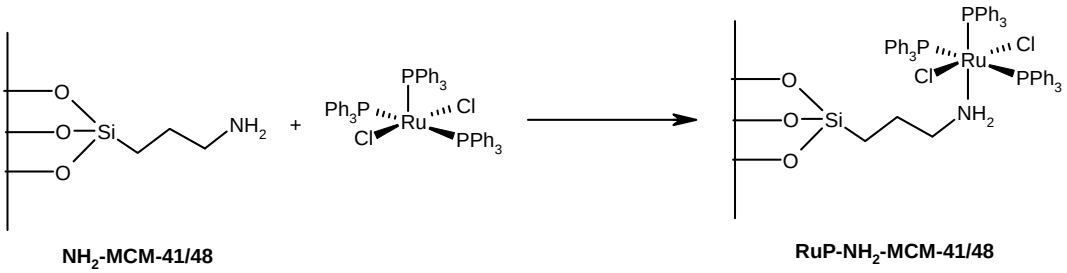

Scheme 3.1. Immobilization of $RuCl_2(PPh_3)_3$ complex on NH_2-functionalized MCM-41 and MCM-48.

3.2.3. Anchoring of $RuCl_2(PPh_3)_3$ Complex inside Ethylenediamine-Functionalized MCM-41 and MCM-48

The $RuCl_2(PPh_3)_3$ complex was anchored to the inner surfaces of ethylenediamine-functionalized MCM-41 or MCM-48 (TPEN-MCM-41/48) by the following method (Scheme 3.2).

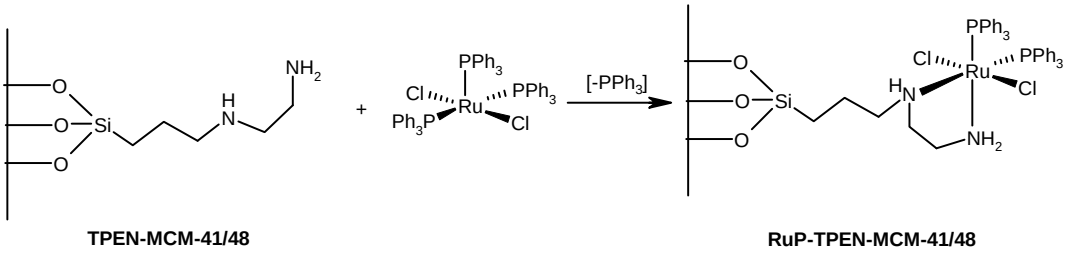

Scheme 3.2. Immobilization of $RuCl_2(PPh_3)_3$ complex onto ethylenediamine-functionalized MCM-41 and MCM-48.

1 g of TPEN-MCM-41 or TPEN-MCM-48 was added to a solution containing 38 mg (0.04 mmol) of the complex dissolved in 30 mL of dry dichloromethane (DCM), and the mixture was stirred at room temperature for 12 h under inert atmosphere, filtered, washed with dry DCM, and dried under vacuum. The resultant material was designated as RuP-TPEN-MCM-41/48.

3.2.4. Anchoring of Ru-(*S*)-BINAP Complex Inside Ethylenediamine-Functionalized MCM-41 and MCM-48

The $[Ru(benzene)Cl_2]_2$ complex was synthesized applying a published procedure.[29] 2.0 g of $RuCl_3.xH_2O$ was dissolved in 100 mL of dry ethanol, and refluxed with 10 mL of 1,3-cyclohexadiene for 4 h under N_2 atmosphere. The brown precipitate was filtered, washed several times with dry methanol and dried under vacuum.

The Ru-(*S*)-BINAP complex was grafted inside the TPEN-functionalized MCM-41 or MCM-48 by the following procedure (Scheme 3.3). 1 g of the TPEN-MCM-41/48 material was treated with 30 mg (0.06 mmol) of $[Ru(benzene)Cl_2]_2$ complex and 75 mg (0.12 mmol) of (*S*)-2,2'-bis(diphenylphosphino)-1,1'-binaphthyl [(*S*)-BINAP or SB] dissolved in 30 mL of dry DCM, and refluxed for 12 h under N_2 atmosphere, filtered, washed with dry DCM, and dried under vacuum. The resultant material was designated as Ru-SB-TPEN-MCM-41/48.

3.2.5. Grafting of (*S*,*S*)-1,2-Diphenylethylenediamine inside Chloro-Functionalized MCM-41 and MCM-48

A chiral diamine moiety was introduced into the inner surfaces of MCM-41 and MCM-48 *via* a nucleophilic substitution mechanism (Scheme 3.4). The chiral diamine compound chosen here was (*S*,*S*)-1,2-diphenylethylenediamine (SDPEN).

1 g of chloro-functionalized MCM-41 or MCM-48 (Cl-MCM-41/48) was added to a solution containing 106 mg (0.5 mmol) of SDPEN and 0.14 mL of triethylamine (NEt_3) in 30 mL of dry methanol, refluxed for 24 h under inert conditions, filtered, washed with methanol-water mixture and then with methanol, and dried under vacuum. The resultant material was designated as SDPEN-MCM-41/48.

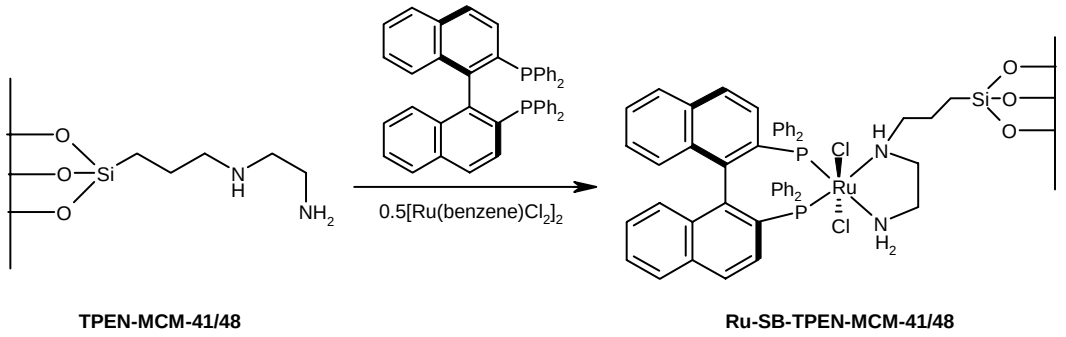

Scheme 3.3. Immobilization of Ru-(*S*)-BINAP complex inside ethylenediamine-functionalized MCM-41 and MCM-48.

3.2.6. Anchoring of Ru-(*S*)-BINAP Complex inside SDPEN-Functionalized MCM-41 and MCM-48

The Ru-(*S*)-BINAP complex was anchored into the SDPEN-MCM-41/48 material applying the following method (Scheme 3.4). 1 g of the SDPEN-MCM-41/48 material was treated with 30 mg (0.06 mmol) of $[Ru(benzene)Cl_2]_2$ complex and 75 mg (0.12 mmol) of (*S*)-BINAP (SB) dissolved in 30 mL of dry DCM, and refluxed for 12 h under N_2 atmosphere, filtered, washed with dry DCM, and dried under vacuum. The resultant material was designated as Ru-SB-SDPEN-MCM-41/48.

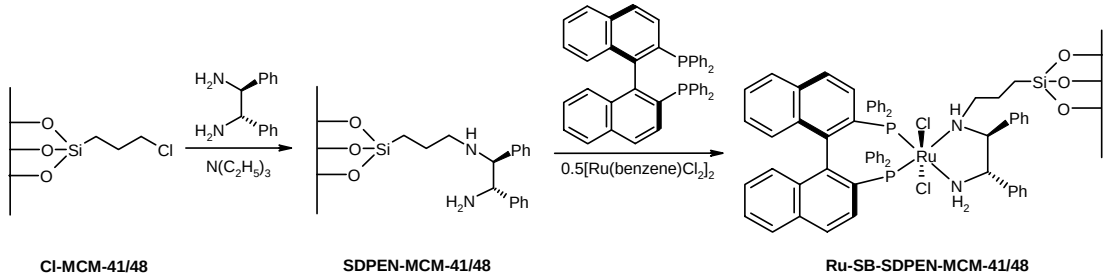

Scheme 3.4. Immobilization of Ru-(*S*)-BINAP complex inside SDPEN-functionalized MCM-41 and MCM-48.

3.2.7. Grafting of the Ru-Complexes on Surfaces of Amorphous Silica

The surfaces of amorphous (fumed) silica were modified by different organic functional groups according to the following procedure. 1 g of fumed silica was suspended in 30 mL of dry DCM, and to this either 1 mL of APTS, or 1 mL of TPEN, or 1 mL of CPTS was added dropwise. The reaction mixture was refluxed for 24 h under inert atmosphere, filtered, washed several times with dry DCM and dried under vacuum to obtain the respective organo-functionalized silica materials designated as NH_2-SiO_2, TPEN-SiO_2 or Cl-SiO_2, respectively.

Further, 1 g of the Cl-SiO_2 material was added to a solution containing 106 mg (0.5 mmol) of SDPEN and 0.14 mL of triethylamine (NEt_3) in 30 mL of dry methanol, refluxed for 24 h under inert conditions, filtered, washed with methanol-water mixture and then with methanol, and dried under vacuum. The resultant material was designated as SDPEN-SiO_2.

The $RuCl_2(PPh_3)_3$ and Ru-(*S*)-BINAP complexes were anchored on NH_2-SiO_2, TPEN-SiO_2 and SDPEN-SiO_2 materials by similar methods as in case of MCM-41 or MCM-48 (Schemes 3.1–3.3). The resultant materials were designated as RuP-NH_2-SiO_2, RuP-TPEN-SiO_2, Ru-SB-TPEN-SiO_2 and Ru-SB-SDPEN-SiO_2, respectively.

3.2.8. Catalytic Hydrogenation Reactions

The catalytic hydrogenation reactions of different olefins, prochiral ketones and α,β-unsaturated aldehydes were performed in a 100 mL high-pressure autoclave at temperatures ranging from 80–120 °C, H_2 pressure ranging from 0.34–2.76 MPa, stirring speed 500 rpm, and for different durations ranging from 1–6 h. 100 mg of the solid catalyst, potassium *tert*-butoxide (^{t}BuOK) as the base and 2-propanol as solvent were used in each reaction. Thereafter, the catalysts were recovered from the hot reaction mixtures by filtration and recycled four times for hydrogenation of the same substrates under same conditions.

3.2.9. Instruments for Characterization

Powder X-ray diffraction (XRD) patterns were recorded at room temperature on a Rigaku MiniFlex instrument using Cu K_α radiation (λ = 1.5404 Å), in the 2θ range 1.5–10° at a scan rate of 1°/min. The specific surface areas of the samples were determined by the BET method from N_2 adsorption isotherms at 77 K using an Omnisorb CX-100 Coulter instrument. Prior to the adsorption experiments, the samples were activated at 150 °C for 6 h at 1.333×10^{-2} Pa. The Fourier transform infrared (FTIR) spectra were recorded at diffuse reflectance mode on a Perkin-Elmer Spectrum One spectrophotometer operated at a resolution of 4 cm^{-1}. ^{31}P cross-polarization magic angle spinning nuclear magnetic resonance (CP MAS NMR) spectra were recorded at 11.7 Tesla and 202.64 MHz in a Bruker DRX-500 FT NMR spectrophotometer. X-ray photoelectron spectra (XPS) of the catalysts before and after hydrogenation reactions were recorded on a VG Microtech ESCA 3000 spectrometer using unmonochromatized Mg K_α radiation (photon energy = 1253.6 eV) at a pressure better than 0.133 μPa, pass energy of 50 eV and electron take-off angle of 60°. Transmission electron microscopic (TEM) images were recorded on a Jeol Model 1200 EX instrument operated at an accelerating voltage of 100 kV.

The reaction mixtures were analyzed by an Agilent 6890 series gas chromatograph (GC) containing chiral capillary column (10% permethylated β-cyclodextrin, 30 m × 0.32 mm × 0.25 μm film thickness) and flame ionization detector. The enantiomeric excess (ee) values were determined quantitatively from integration of peak areas in the chromatogram. The products were also confirmed by GC–Mass spectroscopy (GCMS) on a Shimadzu GCMS-QP 2000A instrument. The absolute configuration of the products was determined after chemical separation of the enantiomers, by measuring optical rotation of the individual enantiomers on a JASCO DIP-1020 digital polarimeter and comparing with literature.[30,31]

Further, the separated enantiomers were also analyzed by GC to confirm about their respective retention time and quantification.

Inductively coupled plasma–atomic emission spectroscopic (ICP-AES) analyses of the catalysts before and after reactions and that of the reaction mixtures after filtration of the catalysts were performed on a Perkin-Elmer 1200 Inductively Coupled Plasma Spectrophotometer.

3.3. CHARACTERIZATION

3.3.1. Powder X-Ray Diffraction

Figure 3.1.A shows the powder X-ray diffraction (XRD) patterns recorded from the (a) NH_2-MCM-41, (b) TPEN-MCM-41, (c) SDPEN-MCM-41, (d) RuP-NH_2-MCM-41, (e) RuP-TPEN-MCM-41, (f) Ru-SB-TPEN-MCM-41, and (g) Ru-SB-SDPEN-MCM-41 materials. The typical hexagonal phase (*p6mm*) of MCM-41 [main (100) peak with weak (110), (200) and (210) reflections] is clearly visible in all the samples.

Figure 3.1.B shows the XRD patterns of the (a) NH_2-MCM-48, (b) TPEN-MCM-48, (c) SDPEN-MCM-48, (d) RuP-NH_2-MCM-48, (e) RuP-TPEN-MCM-48, (f) Ru-SB-TPEN-MCM-48, and (g) Ru-SB-SDPEN-MCM-48 materials, in which the strong (211) and (220) reflections alongwith the weak (321), (400), (420), (322), (422) and (431) reflections are observed in all the materials, characteristic of cubic phase (*Ia3d*) of MCM-48. These results indicate highly ordered mesoporosity even after incorporation of organic functional groups and Ru-complexes. However, a slight decrease in the peak intensities was observed in the case of the Ru-complex loaded samples, which might be due to partial filling of Ru-complexes inside the mesopores.

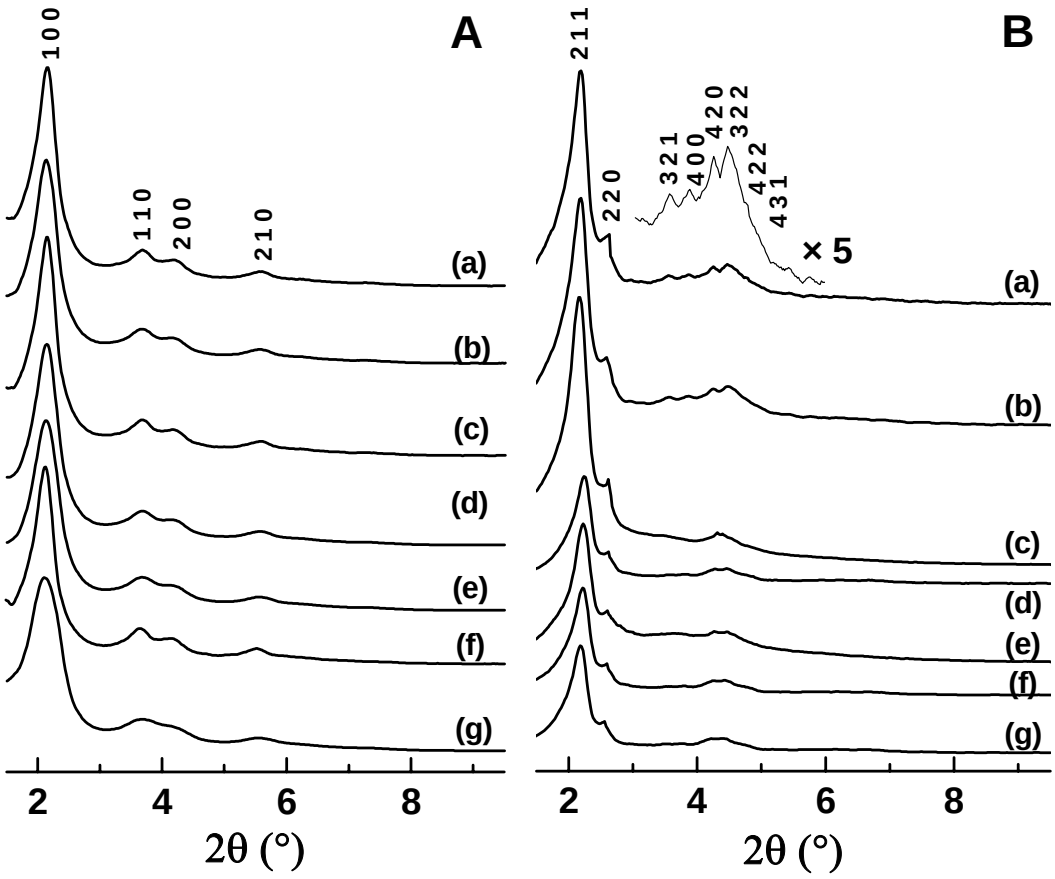

Figure 3.1. Powder XRD patterns recorded from the (A) (a) NH_2-MCM-41, (b) TPEN-MCM-41, (c) SDPEN-MCM-41, (d) RuP-NH_2-MCM-41, (e) RuP-TPEN-MCM-41, (f) Ru-SB-TPEN-MCM-41, and (g) Ru-SB-SDPEN-MCM-41 materials; and (B) (a) NH_2-MCM-48, (b) TPEN-MCM-48, (c) SDPEN-MCM-48, (d) RuP-NH_2-MCM-48, (e) RuP-TPEN-MCM-48, (f) Ru-SB-TPEN-MCM-48, and (g) Ru-SB-SDPEN-MCM-48 materials.

A comparison of the *d*-spacings and unit cell parameter (a_0) values (calculated from XRD patterns) of the functionalized MCM-41 and MCM-48 materials, and those with anchored Ru-complexes has been presented in Table 3.1. The Ru contents in each material (including the Ru-complex–fumed silica composite materials), analyzed by ICP-AES, are also included in the table.

Table 3.1. Physical characteristics of the organo-functionalized MCM-41 and MCM-48 materials before and after anchoring of $RuCl_2(PPh_3)_3$ and Ru-(*S*)-BINAP complexes

Materials	% Ru (w/w)[a]	d_{hkl} (Å)[b]	a_0 (Å)[c]	Pore Diameter (Å)	Pore Volume ($cm^3\ g^{-1}$)	Surface Area ($m^2\ g^{-1}$)
NH_2-MCM-41	-	41.24 (100)	47.62	30.76	1.12	1047
RuP-NH_2-MCM-41	0.321	41.63 (100)	48.07	30.68	1.04	922
TPEN-MCM-41	-	41.05 (100)	47.40	28.43	1.06	993
RuP-TPEN-MCM-41	0.309	41.15 (100)	47.52	28.39	0.90	864
Ru-SB-TPEN-MCM-41	0.329	41.79 (100)	48.25	28.42	0.83	824
Cl-MCM-41	-	40.11 (100)	46.31	29.79	1.08	1031
SDPEN-MCM-41	-	40.49 (100)	46.75	29.82	0.93	877
Ru-SB-SDPEN-MCM-41	0.348	40.83 (100)	47.15	29.75	0.84	828
NH_2-MCM-48	-	38.30 (211)	93.81	27.69	1.28	1623
RuP-NH_2-MCM-48	0.316	38.49 (211)	94.28	27.72	1.15	1411
TPEN-MCM-48	-	38.12 (211)	93.37	25.40	1.19	1336
RuP-TPEN-MCM-48	0.319	38.67 (211)	94.72	25.31	1.07	1176
Ru-SB-TPEN-MCM-48	0.351	38.77 (211)	94.97	25.36	0.98	1122
Cl-MCM-48	-	38.92 (211)	95.33	26.93	1.23	1510
SDPEN-MCM-48	-	39.05 (211)	95.65	26.91	1.06	1268
Ru-SB-SDPEN-MCM-48	0.335	39.09 (211)	95.75	27.01	0.95	1141
RuP-NH_2-SiO_2	0.306	-	-	-	-	n. d.[d]
RuP-TPEN-SiO_2	0.327	-	-	-	-	n. d.
Ru-SB-TPEN-SiO_2	0.345	-	-	-	-	n. d.
Ru-SB-SDPEN-SiO_2	0.329	-	-	-	-	n. d.

[a]Analyzed from ICP-AES.

[b]Calculated from XRD patterns ($n\lambda = 2d\sin\theta$, where $n = 1$ and $\lambda = 1.5404$ Å). Values in parentheses are respective principal Miller indices.

[c]$a_0 = d_{100} \times 2/\sqrt{3}$ (for MCM-41); $a_0 = d_{211} \times \sqrt{6}$ (for MCM-48).

[d]n. d. = Not determined.

3.3.2. Specific Surface Area

The specific surface area, pore volume and pore diameter values (estimated from N_2 adsorption-desorption isotherms) of the organo-functionalized MCM-41 and MCM-48 materials with and without Ru-complexes are represented in Table 3.1. In the case of NH_2-MCM-41 material, *ca*. 12% decrease in surface area values was observed after incorporation of $RuCl_2(PPh_3)_3$ complex. Similar decreases were observed after inclusion of $RuCl_2(PPh_3)_3$ and Ru-(*S*)-BINAP complexes (*ca*. 13% and 17%, respectively) inside TPEN-MCM-41 material, and after anchoring of SDPEN and Ru-(*S*)-BINAP (*ca*. 15% and 20%, respectively) inside Cl-MCM-41 material. Analogous trends were also observed in the surface area values of the MCM-48 materials, and in the pore volumes of the MCM-41 and MCM-48 materials after anchoring of the Ru-complexes. The pore diameter values of these materials, however, did not change considerably after anchoring of the Ru-complexes. All these results indicate that partial filling of the mesopores was occurred by the aforesaid coordination compounds, which are anchored inside of the pore structure.

3.3.3. FTIR Spectra

Figure 3.2 shows the FTIR spectra of the (A) (a) RuP-TPEN-MCM-41 and (b) Ru-SB-SDPEN-MCM-41; and (B) (a) RuP-TPEN-MCM-48 and (b) Ru-SB-SDPEN-MCM-48 materials. Insets show the FTIR spectra of the (A) SDPEN-MCM-41 and (B) SDPEN-MCM-48 materials. The characteristic P–Ph band at *ca*. 1086 cm^{-1} were observed in the spectra[32] of the RuP-TPEN-MCM-41/48 and Ru-SB-SDPEN-MCM-41/48 materials, clearly indicating the incorporation of Ru-phosphine complexes inside the siliceous matrices. In the case of SDPEN-MCM-41 (inset of Fig. 3.2.A) and SDPEN-MCM-48 (inset of Fig. 3.2.B) materials, the characteristic bands of $–NH_2$ at 3303 and 3365 cm^{-1}, and another two bands at 2935 and 2872 cm^{-1} corresponding to asymmetric and symmetric vibrations respectively of

the $–CH_2$ groups of the propyl chain of the silylating agent were observed, indicative of successful anchoring of amine moieties in the mesopores.

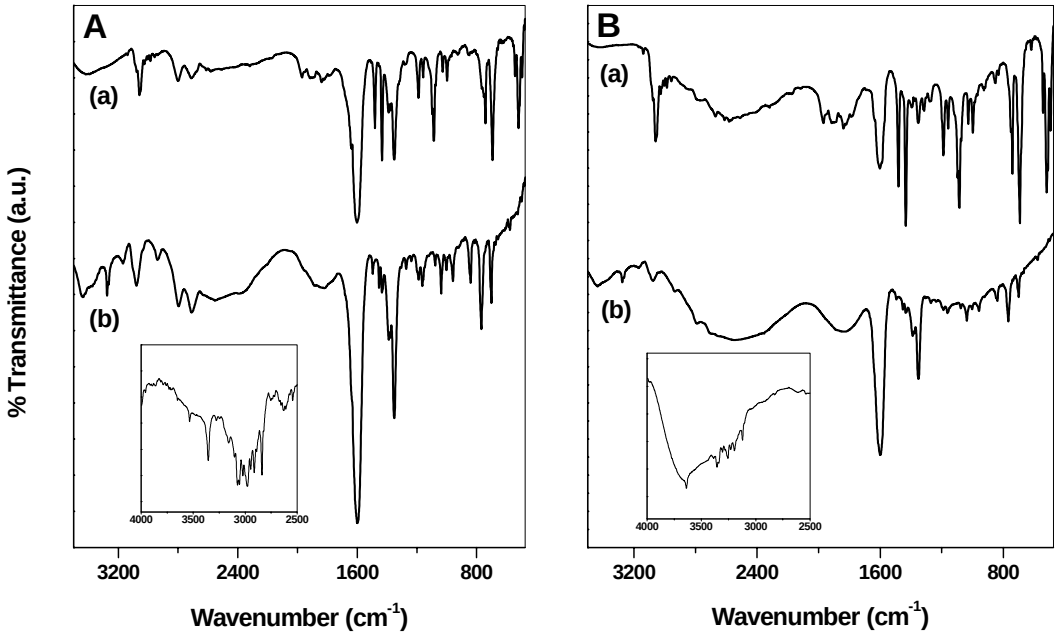

Figure 3.2. FTIR spectra of the (A) (a) RuP-TPEN-MCM-41 and (b) Ru-SB-SDPEN-MCM-41; and (B) (a) RuP-TPEN-MCM-48 and (b) Ru-SB-SDPEN-MCM-48 materials. Insets represent the FTIR spectra of the (A) SDPEN-MCM-41 and (B) SDPEN-MCM-48 materials.

3.3.4. ^{31}P CP MAS NMR Spectra

The $^{1}H–^{31}P$ coupled CP MAS NMR spectra of the (a) RuP-NH_2-MCM-41, (b) RuP-TPEN-MCM-41, (c) Ru-SB-TPEN-MCM-41 and (d) Ru-SB-SDPEN-MCM-41 materials are given in Figure 3.3. The spectrum of the RuP-NH_2-MCM-41 material reveals two major ^{31}P peaks at δ = 35 and 76 ppm, each split by J-coupling to other ^{31}P nuclei (Fig. 3.3, curve a). The integrated intensity for these major signals is in the ratio of 2:1. The $RuCl_2(PPh_3)_3$ molecule has a distorted square pyramidal structure, with the equatorial positions occupied by two PPh_3 groups trans to each other, and two –Cl ligands trans to each other. Another PPh_3 group occupies the axial position (Scheme 3.1). This makes the central Ru nuclei

coordinatively unsaturated. The three phosphorus atoms in $RuCl_2(PPh_3)_3$ may be grouped into (i) one distinct (one PPh_3 group in axial position) and (ii) two equivalent (two PPh_3 groups in equatorial position trans to each other) phosphorus environments (Scheme 3.1). The P–P coupling of the axial P atom with the two equivalent P atoms in equatorial position causes the doublet at δ = 76 ppm. Similarly the two equivalent P atoms at the equatorial position are split into a doublet by the distant P atom, further split by coupling to ruthenium to give a doublet of a doublet. But, since $|J_{P-P} - J_{P-Ru}| < \Delta\nu$ (where $\Delta\nu$ = MAS line width), only a triplet at δ = 35 ppm was observed. This spectrum (Fig. 3.3, curve a) clearly indicates that the N atom of the pendant propylamine group in NH_2-MCM-41 donates its lone electron pair to the Ru^{II} nuclei to form a coordinate bond, which in turn creates an octahedral environment around the central Ru atom, as depicted in Scheme 3.1.

On interaction of $RuCl_2(PPh_3)_3$ with the chelating ethylenediamine ligand of the TPEN-MCM-41 material, one PPh_3 group in the equatorial position leaves the system due to strong trans effect of another PPh_3 group. Thus the bidentate ethylenediamine ligand coordinates with the Ru nuclei through (i) the vacant equatorial position created by the PPh_3 group, and (ii) through the already vacant axial position, thus creating two non-equivalent phosphorus environments (Scheme 3.2). This mechanism depicted in Scheme 3.2 is supported by the spectrum of the RuP-TPEN-MCM-41 material, in which two distinct signals of almost equal intensity at δ = 36 and 69 ppm were observed (Fig. 3.3, curve b), signifying the existence of two non-equivalent phosphorus atoms in the material.

Both the ^{31}P NMR spectra of the Ru-SB-TPEN-MCM-41 and Ru-SB-SDPEN-MCM-41 materials (Fig. 3.3, curves c and d) show two distinct peaks of approximately equal intensity at $\delta \sim 40$ and 71 ppm, which can also be attributed to the presence of two non-equivalent phosphorus atoms of the BINAP ligand inside the material. The inclusion of the TPEN and SDPEN moieties on the mesoporous silica surface and their coordination

with Ru^{II} nuclei lead to two non-equivalent phosphorus environments inside the Ru-SB-TPEN-MCM-41 (Scheme 3.3) and Ru-SB-SDPEN-MCM-41 (Scheme 3.4) materials, respectively, which accounts for the two strong ^{31}P signals.

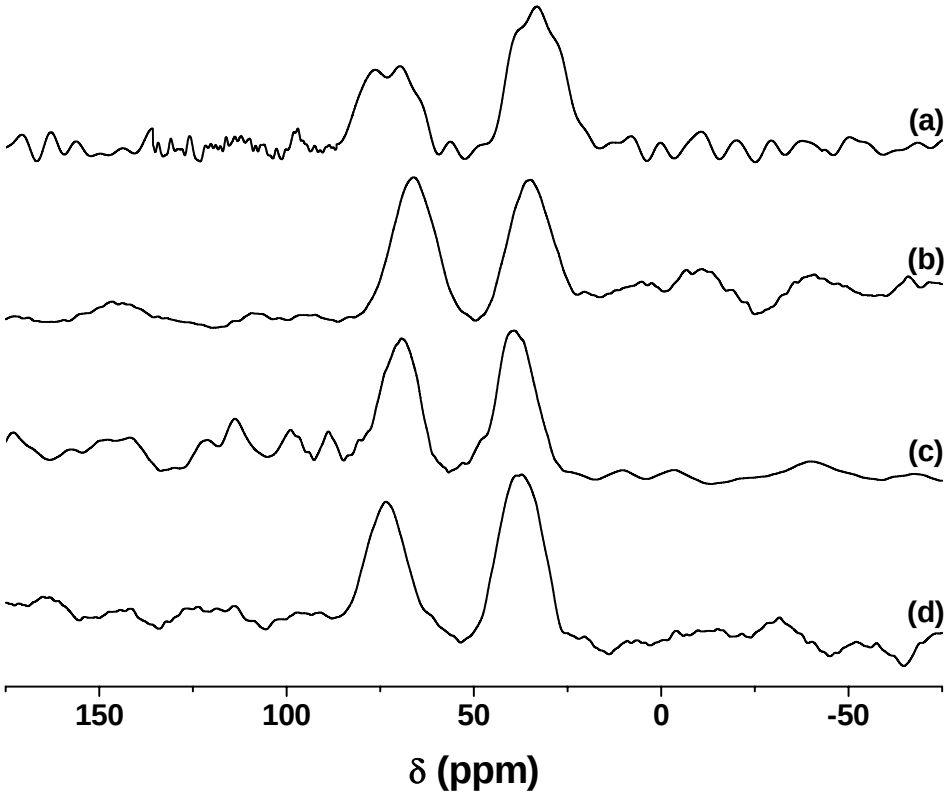

Figure 3.3. The ^{1}H–^{31}P coupled CP MAS NMR spectra of the (a) RuP-NH_2-MCM-41, (b) RuP-TPEN-MCM-41, (c) Ru-SB-TPEN-MCM-41 and (d) Ru-SB-SDPEN-MCM-41 materials.

3.3.5. X-Ray Photoelectron Spectra

Additional support for the anchoring of the Ru^{II}-complexes onto the solid mesoporous materials was obtained by X-ray photoelectron spectroscopic (XPS) analyses. Table 3.2 represents the Ru $3d_{5/2}$, Ru $3p_{3/2}$, N 1s, Si 2p and P 2p core level binding energies (BE) obtained from XPS analyses of the NH_2-MCM-41/48, TPEN-MCM-41/48 and SDPEN-MCM-41/48 materials before and after anchoring of $RuCl_2(PPh_3)_3$ and Ru-(*S*)-BINAP complexes, and of the Ru-complex–fumed silica composite materials. From the Ru

$3d_{5/2}$ and $3p_{3/2}$ BE values at *ca*. 280 eV and *ca*. 465 eV respectively, it is evident that all ruthenium in the catalysts are present as Ru^{II} species.[33] The P 2p BE values are also consistent with those obtained from Ru^{II}-phosphine complexes.[33] This further showed that the integrity of the $RuCl_2(PPh_3)_3$ and Ru-(*S*)-BINAP complexes was retained when anchored into the supports, with no beam damage suffered by the supports.

Table 3.2. Core level binding energies (in eV) of various elements[a] present in the catalyst precursors and the anchored catalysts

Materials	Ru $3d_{5/2}$	Ru $3p_{3/2}$	N 1s	Si 2p	P 2p
NH_2-MCM-41	-	-	399.3	103.4	-
RuP-NH_2-MCM-41	280.5	464.8	399.9	103.4	131.3
TPEN-MCM-41	-	-	399.4	103.4	-
RuP-TPEN-MCM-41	280.5	464.8	400.1	103.4	131.3
Ru-SB-TPEN-MCM-41	280.8	465.0	400.2	103.4	131.5
SDPEN-MCM-41	-	-	400.1	103.4	-
Ru-SB-SDPEN-MCM-41	280.8	465.0	400.7	103.4	131.6
NH_2-MCM-48	-	-	399.4	103.4	-
RuP-NH_2-MCM-48	280.4	464.9	400.0	103.4	131.3
TPEN-MCM-48	-	-	399.5	103.4	-
RuP-TPEN-MCM-48	280.5	464.9	400.2	103.4	131.3
Ru-SB-TPEN-MCM-48	280.7	465.0	400.3	103.4	131.4
SDPEN-MCM-48	-	-	400.0	103.4	-
Ru-SB-SDPEN-MCM-48	280.7	465.0	400.6	103.4	131.5
RuP-NH_2-SiO_2	280.6	464.8	400.2	103.3	131.4
RuP-TPEN-SiO_2	280.6	464.8	400.3	103.3	131.4
Ru-SB-TPEN-SiO_2	280.8	464.9	400.3	103.3	131.5
Ru-SB-SDPEN-SiO_2	280.8	464.9	400.5	103.3	131.6

[a]The core level binding energies were aligned with respect to the C 1s binding energy of 285 eV using adventitious carbon.

The N 1s BE values in the NH_2-MCM-41/48, TPEN-MCM-41/48 and SDPEN-MCM-41/48 materials indeed confirm successful grafting of amine moieties inside the

mesopores, previously inferred from FTIR spectra (insets of Fig. 3.2). However, an increase in N 1s BE values by *ca*. 0.6–0.7 eV was observed after loading of the Ru-complexes in each material, which can be attributed to coordination of N atoms with the Ru^{II} nuclei. All these results strongly point towards stable anchoring and immobilization of $RuCl_2(PPh_3)_3$ and Ru-(*S*)-BINAP complexes onto the surfaces of MCM-41 and MCM-48 materials.

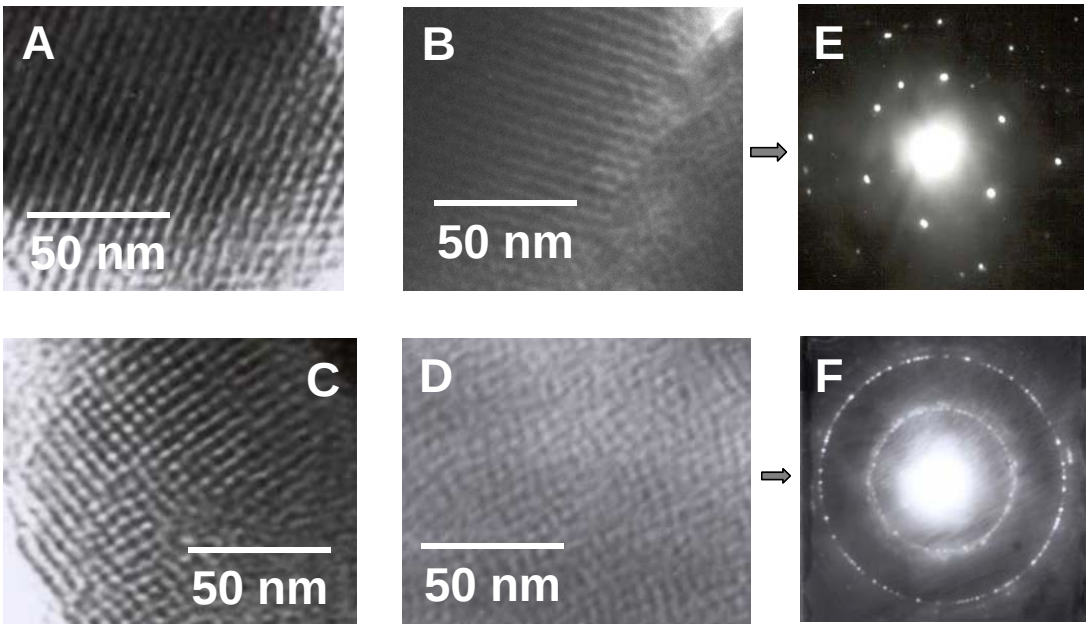

Figure 3.4. TEM images recorded from (A) RuP-TPEN-MCM-41, (B) Ru-SB-SDPEN-MCM-41, (C) RuP-TPEN-MCM-48, and (D) Ru-SB-SDPEN-MCM-48 samples. (E) and (F) show the SAED patterns of the samples shown in (B) and (D), respectively.

3.3.6. Transmission Electron Microscopy

Transmission electron microscopy (TEM) is used as an indispensable tool for characterization of mesoporous supports.[34] Moreover, TEM has also been applied extensively to envisage 3D structures of the mesoporous solids, imaging metal nanoparticle catalysts inside mesoporous hosts and determine the occluded structure-directing organic species.[35] Figure 3.4 represents TEM images recorded from (A) RuP-TPEN-MCM-41, (B) Ru-SB-SDPEN-MCM-41, (C) RuP-TPEN-MCM-48, and (D) Ru-SB-SDPEN-MCM-48

materials. The selected area electron diffraction (SAED) patterns of the samples shown in Fig. 3.4.B and Fig. 3.4.D are given in Fig. 3.4.E and Fig. 3.4.F, respectively. The TEM images and SAED patterns are well consistent with the regular hexagonal and cubic mesophases of MCM-41 and MCM-48, respectively, with homogeneity in patterns throughout, which indicates the retention of ordered patterns of MCM-41 and MCM-48 even after anchoring of the abovementioned Ru^{II}-phosphine complexes. These results corroborate the XRD results presented earlier (Fig. 3.1).

3.4. CATALYTIC HYDROGENATION OF UNSATURATED HYDROCARBONS

To compare the activity of the heterogeneous catalysts (RuP-NH_2-MCM-41, RuP-NH_2-MCM-48 and RuP-NH_2-SiO_2) with that of the corresponding homogeneous $RuCl_2(PPh_3)_3$ catalyst, the hydrogenation three alkenes, namely 1-hexene, cyclohexene and 1-octene, selected as model substrates, was carried out under identical conditions. The results are summarized in Table 3.3. It can be seen from the table that the heterogeneous catalysts are highly active in the above hydrogenation reactions, where the C=C bond was hydrogenated almost quantitatively. Both the MCM-41 and MCM-48 based catalysts show almost similar activity, possibly due to similar rate of interaction between substrate molecules and catalyst active site.

3.4.1. Influence of Reaction Time over Conversion

The influence of reaction time over the conversion in the hydrogenation of 1-hexene is presented in Figure 3.5. It was manifested that in the case of the MCM-41 and MCM-48 based heterogeneous catalysts, the conversion increases as the reaction proceeds, and reaches a maxima (99%) at *ca*. 2 h time. However, for the homogeneous catalyst, the

substrate was almost quantitatively hydrogenated at *ca*. 1 h time. Thus the TOF of the homogeneous reaction is nearly double than that of the reactions in heterogeneous phase. This might have occurred due to restricted orientation of the metal complex resulted from anchoring inside porous supports. The TOF was calculated on the basis of the time required for 90% conversion of the substrate.

Table 3.3. Catalytic hydrogenation[a] of unsaturated hydrocarbons by homogeneous and heterogenized $RuCl_2(PPh_3)_3$ complex

Catalyst	Substrate	Conv. (mol. %)	TON[b]	TOF (h^{-1})[c]
RuP-NH_2-MCM-41	1-hexene	>99	4626	2595
RuP-NH_2-MCM-48	1-hexene	>99	4699	2794
RuP-NH_2-SiO_2	1-hexene	>99	4550	2275
$RuCl_2(PPh_3)_3$[d]	1-hexene	>99	4950	5060
RuP-NH_2-MCM-41	Cyclohexene	>99	4626	2572
RuP-NH_2-MCM-48	Cyclohexene	>99	4699	2763
$RuCl_2(PPh_3)_3$[d]	Cyclohexene	>99	4950	5057
RuP-NH_2-MCM-41	1-octene	>99	4626	2565
RuP-NH_2-MCM-48	1-octene	>99	4699	2754
$RuCl_2(PPh_3)_3$[d]	1-octene	>99	4950	5039

[a]Reaction conditions: Catalyst = 100 mg; Substrate = 15 mmol; Substrate: Base = 100: 1, Ru: Substrate = 1: 4673 (RuP-NH_2-MCM-41), 1: 4747 (RuP-NH_2-MCM-48), 1: 5000 [$RuCl_2(PPh_3)_3$]; Temperature = 100 °C; H_2 pressure = 1.38 MPa; Stirring speed = 500 rpm; Duration = 2 h (heterogeneous), 1 h (homogeneous).

[b]TON = (mmol of alkene converted to alkane) × $(\text{mmol of Ru})^{-1}$.

[c]TOF = TON × Time^{-1} (in h). TOF is calculated on the basis of the time required to achieve minimum 90% conversion of each substrate (See Figure 3.5)

[d]Reaction under homogeneous conditions.

3.4.2. Influence of Temperature over Conversion

A critical temperature of 100 °C is required to acquire the activation energy for hydrogenation by the chosen heterogeneous and homogeneous catalyst system, as has been

evidenced from Figure 3.6. At this temperature, the C=C bond of 1-hexene was hydrogenated nearly quantitatively (Fig. 3.6) by both of the homogeneous and heterogeneous catalysts. By increasing the temperature beyond 100 °C (upto 120 °C), no further change in reaction rate was observed.

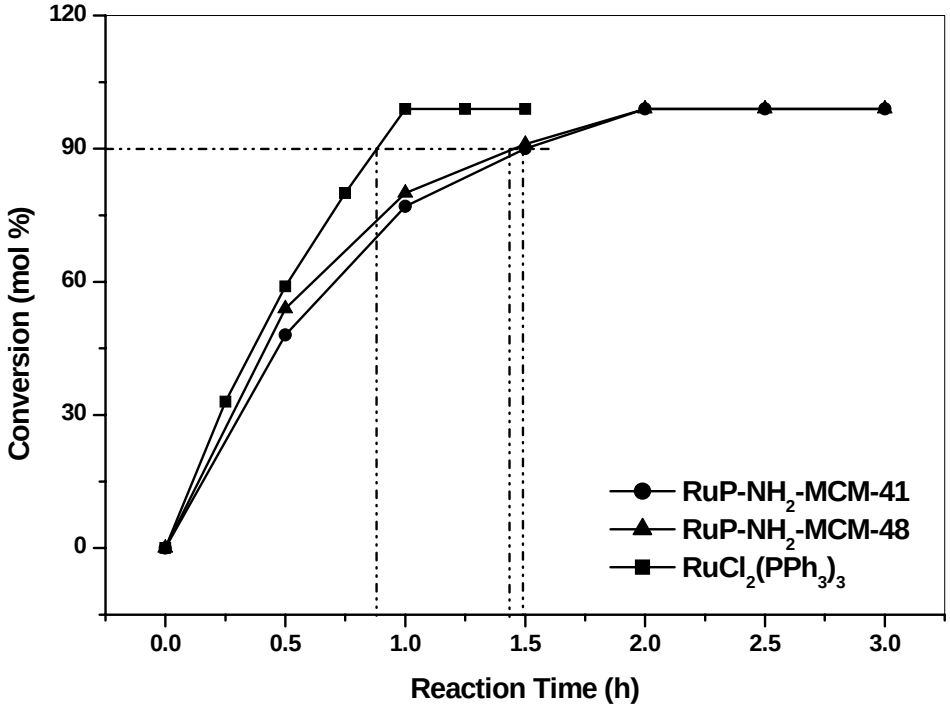

Figure 3.5. Influence of reaction time on conversion in the hydrogenation of 1-hexene. Reaction conditions: Temperature = 100 °C, H_2 pressure = 1.38 MPa, Stirring speed = 500 rpm.

3.4.3. Influence of H_2 Pressure over Conversion

The pressure of molecular dihydrogen inside the reaction vessel has pronounced effect over the conversion. As represented in Figure 3.7, conversion of 1-hexene markedly increases with H_2 pressure. However, a minimum pressure of 1.38 MPa was required to achieve almost quantitative conversion of the olefins (Figure 3.7). Beyond this pressure, no further change in reaction rate was observed.

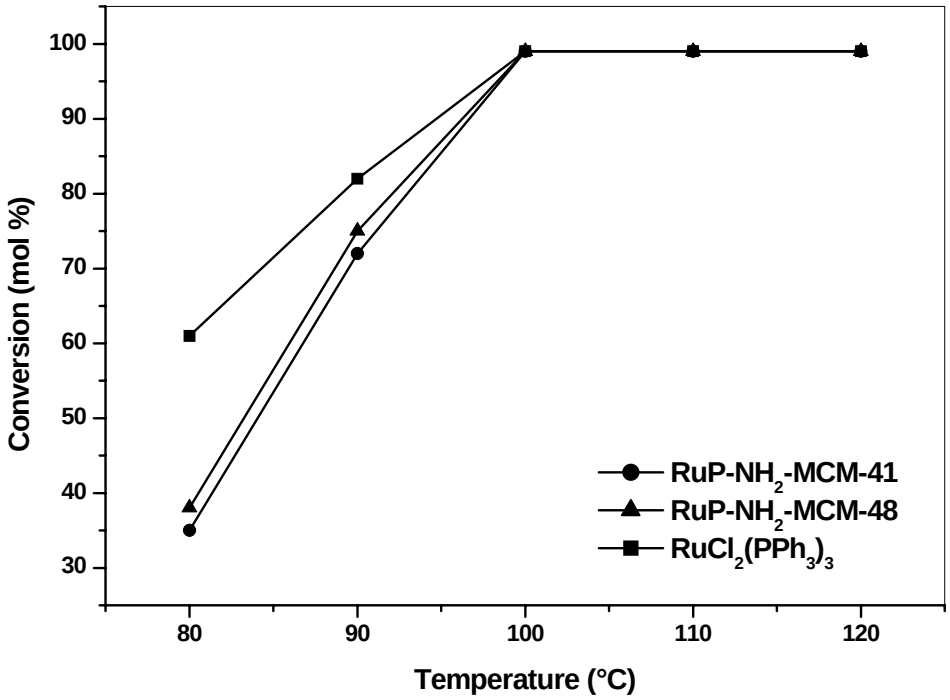

Figure 3.6. Influence of temperature on conversion in the hydrogenation of 1-hexene. Reaction conditions: Duration = 2 h, H_2 pressure = 1.38 MPa, Stirring speed = 500 rpm.

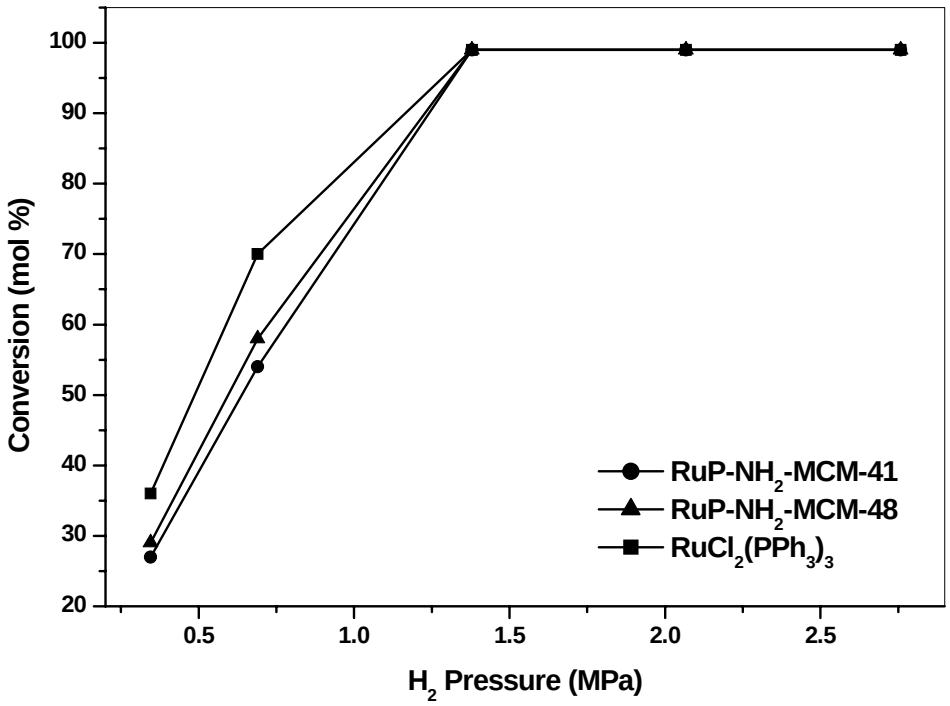

Figure 3.7. Influence of H_2 pressure on conversion in the hydrogenation of 1-hexene. Reaction conditions: Duration = 2 h, Temperature = 100 °C, Stirring speed = 500 rpm.

3.4.4. Recycle Studies

To assess the stability of the heterogeneous catalysts, those were recovered from the hot reaction mixtures by filtration, and the filtrates were analyzed for Ru content by ICP-AES. In the case of RuP-NH_2-MCM-41 and RuP-NH_2-MCM-48 catalysts, the Ru contents in the filtrate were found to be *ca*. 6.7×10^{-4}% of the total Ru present in the catalysts, indicating inconsiderable leaching of the metal to the organic phase. In addition, both the MCM-41 and MCM-48 based catalysts were successfully recycled four times for hydrogenation of 1-hexene without any considerable decline in activity (Table 3.4). In contrast to these, the catalyst prepared by anchoring the $RuCl_2(PPh_3)_3$ complex onto amine-functionalized fumed silica showed considerable amount of leaching of Ru metal (*ca*. 16% of the total Ru present in the catalyst used) during reaction in the first cycle, which also leads to significant decrease in catalytic activity after four recycles (Table 3.4).

Table 3.4. Recycle studies of the heterogeneous catalysts for hydrogenation of 1-hexene

No. of Recycles	RuP-NH_2-SiO_2 Conv. (mol. %)	RuP-NH_2-MCM-41 Conv. (mol. %)	RuP-NH_2-MCM-48 Conv. (mol. %)
1	79.0	>99.0	>99.0
2	64.3	99.0	99.0
3	51.6	98.7	98.8
4	33.2	98.9	98.5

3.5. CHEMOSELECTIVE HYDROGENATION OF α,β-UNSATURATED ALDEHYDES

The RuP-TPEN-MCM-41, RuP-TPEN-MCM-48, RuP-TPEN-SiO_2 and RuP-NH_2-MCM-41 catalysts were examined for the chemoselective hydrogenation of α,β-unsaturated aldehydes, and the activity and chemoselectivity of these heterogeneous catalysts was

compared with those of the $RuCl_2(PPh_3)_3$–ethylenediamine (EN) composite system under homogeneous condition. The results are summarized in Table 3.5. Under our experimental conditions, hydrogenation of either C=C bond or C=O bond was observed, resulted in formation of either saturated aldehyde or unsaturated (allylic) alcohol, respectively. Formation of saturated alcohol by simultaneous hydrogenation of both C=C and C=O bonds was not at all observed.

From Table 3.5, it is evident that the RuP-TPEN-MCM-41, RuP-TPEN-MCM-48 and RuP-TPEN-SiO_2 catalysts are highly active in the hydrogenation reactions, with conversion upto 85% and chemoselectivity upto 79%. The selectivity towards hydrogenation of C=O bond to form unsaturated alcohol was observed to increase with increasing substitution on the terminal carbon atom of the C=C group, *i.e.*, the β-carbon atom. But increasing the substitution on the α-carbon atom does not affect the chemoselectivity to a large extent. The rate of the reaction involving the corresponding homogeneous catalyst [$RuCl_2(PPh_3)_3$–ethylenediamine composite system] is higher than that concerning the heterogeneous catalysts, as envisioned from the high TOF values. This is obviously due to restricted interaction of the metal complex with the substrate molecules in heterogeneous reaction conditions compared to that in homogeneous conditions. However, both the MCM-41 and MCM-48 based catalysts show almost similar activity and chemoselectivity, possibly due to similar rate of interaction between substrate molecules and catalyst active site.

It was also observed from the table that the RuP-NH_2-MCM-41 catalyst is not very active in the hydrogenation of α,β-unsaturated aldehydes. Further, hydrogenation of only C=C bond was occurred with this catalyst, that too with only 45% conversion. The presence of the electron-withdrawing C=O group conjugated to the C=C group accounts for this lower reaction rate, as compared with hydrogenation of simple olefins (Table 3.3). These

results strongly point towards the necessity of an ethylenediamine moiety in the catalyst system, since the reactions are supposed to proceed through the "*Metal-ligand bifunctional catalysis*" mechanism.[14,15]

Table 3.5. Chemoselective hydrogenation[a] of α,β-unsaturated aldehydes

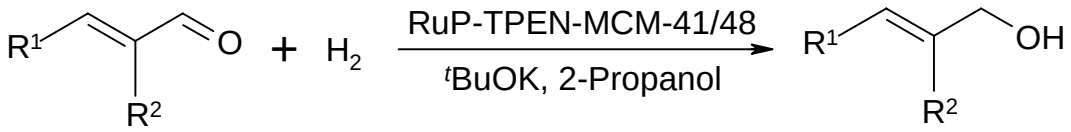

Catalyst	Substrate	Conv. (mol. %)	TON[b]	TOF (h^{-1})[c]	>C=O Selectivity (%)[e]
RuP-TPEN-MCM-41	R^1 = H, R^2 = H	85	2475	619	44
RuP-TPEN-MCM-48	R^1 = H, R^2 = H	87	2454	613	46
RuP-TPEN-MCM-41	R^1 = CH_3, R^2 = H	81	2359	590	63
RuP-TPEN-MCM-48	R^1 = CH_3, R^2 = H	82	2313	578	67
RuP-TPEN-MCM-41	R^1 = Ph, R^2 = H	74	2155	539	76
RuP-TPEN-MCM-48	R^1 = Ph, R^2 = H	76	2143	536	79
RuP-TPEN-SiO_2	R^1 = Ph, R^2 = H	72	2160	540	76
$RuCl_2(PPh_3)_3$–EN[e]	R^1 = Ph, R^2 = H	85	2550	1275	82
RuP-NH_2-MCM-41	R^1 = Ph, R^2 = H	45	1261	315	0
RuP-TPEN-MCM-41	R^1 = Ph, R^2 = CH_3	67	1951	489	74
RuP-TPEN-MCM-48	R^1 = Ph, R^2 = CH_3	69	1946	486	75

[a]Reaction conditions: Catalyst = 100 mg; Substrate = 9 mmol; Substrate: Base = 100: 1; Ru: Substrate = 1: 2912 (RuP-TPEN-MCM-41), 1: 2821 (RuP-TPEN-MCM-48), 1: 3000 ($RuCl_2(PPh_3)_3$–EN); Temperature = 100 °C; H_2 pressure = 1.38 MPa; Stirring speed = 500 rpm; Duration = 4 h (heterogeneous), 2 h (homogeneous).

[b]TON = (Total mmol of unsaturated aldehyde hydrogenated) × $(\text{mmol of Ru})^{-1}$.

[c]TOF = TON × Time^{-1} (in h).

[d]>C=O Selectivity (%) = (mmol of >C=O hydrogenated) × (total mmol of >C=O and >C=C< hydrogenated)$^{-1}$ × 100.

[e]Reaction under homogeneous conditions.

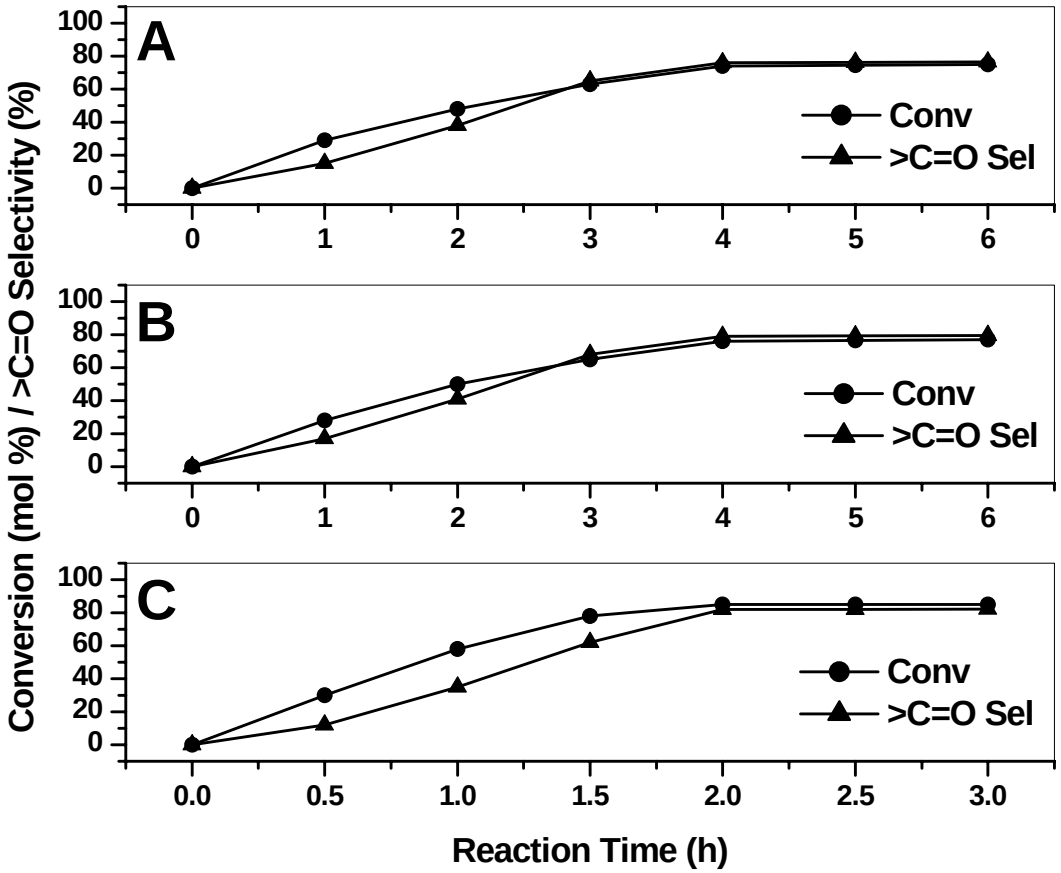

Figure 3.8. Influence of reaction time over conversion and chemoselectivity in the hydrogenation of cinnamaldehyde by (A) RuP-TPEN-MCM-41, (B) RuP-TPEN-MCM-48, and (C) homogeneous $RuCl_2(PPh_3)_3$–ethylenediamine catalysts. Reaction conditions: Temperature = 100 °C, H_2 pressure = 1.38 MPa, Stirring speed = 500 rpm.

3.5.1. Influence of Reaction Time over Conversion and Chemoselectivity

The influence of reaction time over the conversion and chemoselectivity in the hydrogenation of cinnamaldehyde is presented in Figure 3.8. It was noticed that in the case of the heterogeneous catalysts, both the conversion and selectivity towards hydrogenation of C=O bond increases as the reaction proceeds, and reaches a maxima at *ca*. 4 h time. The saturated alcohol formed from the hydrogenation of C=C bond is the kinetically controlled product (KCP), which predominates during the initial stages of the reaction. However, the unsaturated alcohol formed from the hydrogenation of C=O bond being the

thermodynamically controlled product (TCP), becomes the major product as the reaction progresses further (at *ca*. 4 h time). However, in the case of the homogeneous catalyst, the unsaturated alcohol becomes the major product before 2 h time.

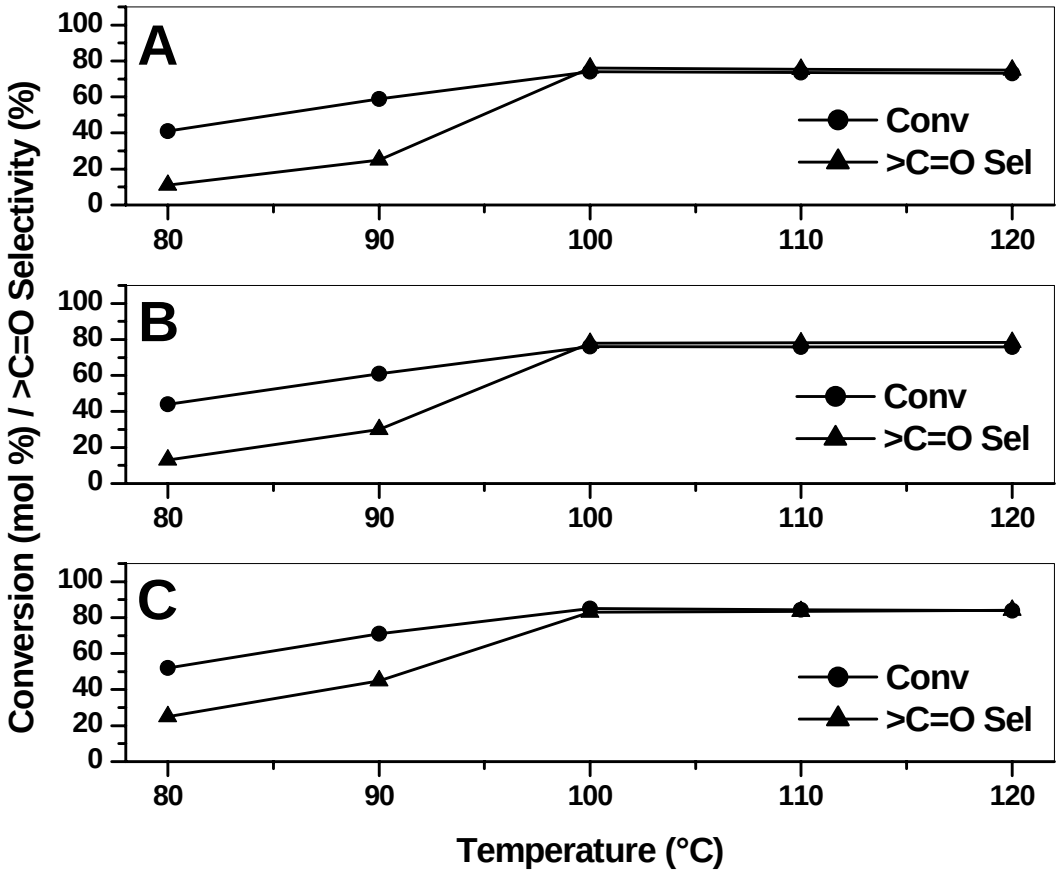

Figure 3.9. Influence of temperature over conversion and chemoselectivity in the hydrogenation of cinnamaldehyde by (A) RuP-TPEN-MCM-41, (B) RuP-TPEN-MCM-48, and (C) homogeneous $RuCl_2(PPh_3)_3$–ethylenediamine catalysts. Reaction conditions: Duration = 4 h, H_2 pressure = 1.38 MPa, Stirring speed = 500 rpm.

3.5.2. Influence of Temperature over Conversion and Chemoselectivity

A minimum temperature of 100 °C is required to attain the maximum conversion and chemoselectivity in the hydrogenation of cinnamaldehyde by both the homogeneous and heterogeneous catalysts, as has been evidenced from Figure 3.9. Moreover the KCP (saturated aldehyde) was formed predominantly at lower temperature regime (80–90 °C),

while the TCP (unsaturated alcohol) was the major product at temperatures at and beyond 100 °C.

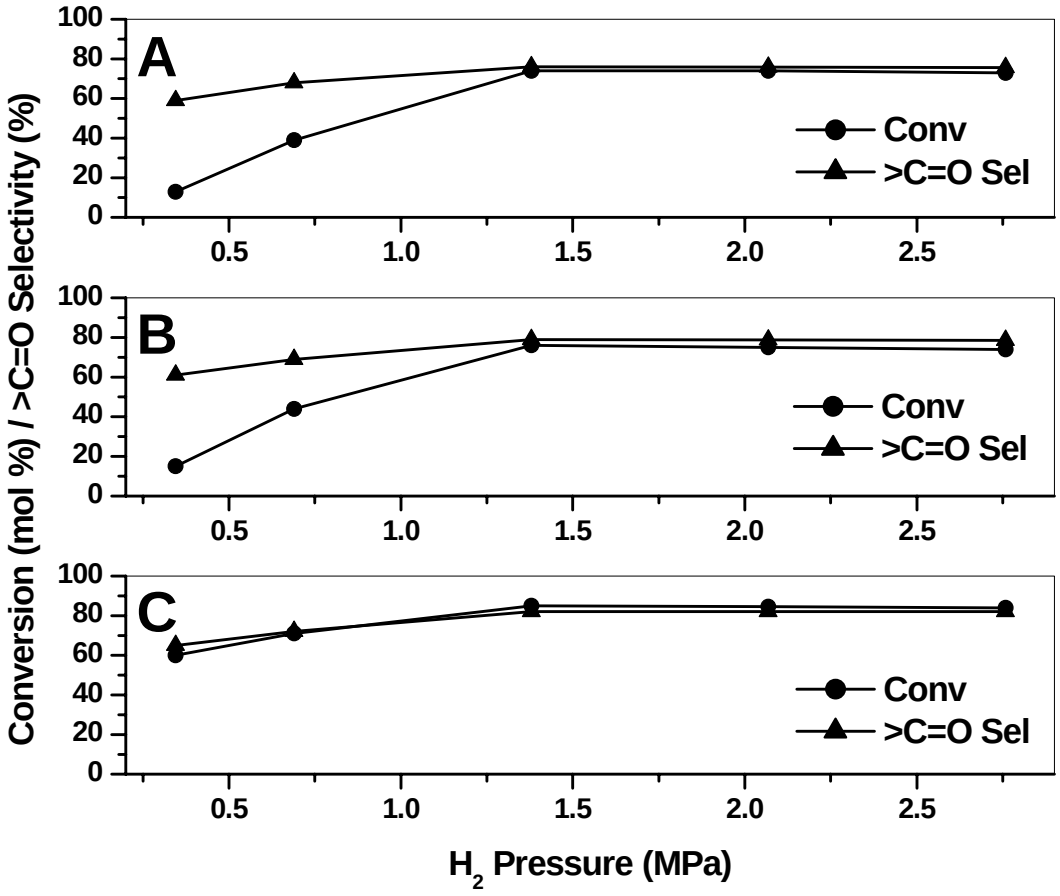

Figure 3.10. Influence of H_2 pressure over conversion and chemoselectivity in the hydrogenation of cinnamaldehyde by (A) RuP-TPEN-MCM-41, (B) RuP-TPEN-MCM-48, and (C) homogeneous $RuCl_2(PPh_3)_3$–ethylenediamine catalysts. Reaction conditions: Duration = 4 h, Temperature = 100 °C, Stirring speed = 500 rpm.

3.5.3. Influence of H_2 Pressure over Conversion and Chemoselectivity

The effect of H_2 pressure over the conversion and chemoselectivity in the hydrogenation of cinnamaldehyde is presented in Figure 3.10. It was envisaged that a minimum pressure of 1.38 MPa was required for maximum conversion of the substrate by both the heterogeneous RuP-TPEN-MCM-41/48 and homogeneous $RuCl_2(PPh_3)_3$–ethylenediamine catalysts. Beyond this pressure no further enhancement in reaction rate was

observed. But the selectivity towards hydrogenation of C=O bond is very high even at lower H_2 pressure (0.35–0.7 MPa).

3.5.4. Recycle Studies

The stability of the heterogeneous catalysts was evaluated by analyzing the filtrates from the reaction mixtures by ICP-AES. In the case of RuP-TPEN-MCM-41 and RuP-TPEN-MCM-48 catalysts, the Ru contents of the filtrate were found to be *ca*. 8.9×10^{-4}% of the total Ru present in the catalysts, signifying negligible leaching of Ru from the mesoporous hosts to the liquid phase during reactions. Furthermore, both of these catalysts were successfully recycled four times for hydrogenation of cinnamaldehyde without any considerable decrease in activity and chemoselectivity (Table 3.6). On the contrary, the catalyst prepared by anchoring the $RuCl_2(PPh_3)_3$ complex onto ethylenediamine-functionalized fumed silica (RuP-TPEN-SiO_2) material showed substantial amount of leaching of Ru metal (*ca*. 22% of the total Ru present in the catalyst used) during reaction in the first cycle, which also leads to significant decrease in catalytic activity and selectivity after four recycles (Table 3.6).

Table 3.6. Recycle studies of the heterogeneous catalysts for hydrogenation of cinnamaldehyde

No. of Recycles	RuP-TPEN-SiO_2		RuP-TPEN-MCM-41		RuP-TPEN-MCM-48	
	Conv. (mol. %)	>C=O Sel. (%)	Conv. (mol. %)	>C=O Sel. (%)	Conv. (mol. %)	>C=O Sel. (%)
1	61	72	73	74	75	77
2	43	69	75	75	74	76
3	31	56	73	74	75	75
4	15	47	76	74	72	77

3.6. ENANTIOSELECTIVE HYDROGENATION OF PROCHIRAL KETONES

All the heterogeneous catalysts prepared in this study were exploited in the enantioselective hydrogenation of prochiral aliphatic, alicyclic and aromatic ketones, and the results are summarized in Tables 3.7 (for aliphatic and alicyclic ketones) and 3.8 (for aromatic ketones). Similar reactions were also performed with the pure Ru-SB-SDPEN complex[13] under homogeneous conditions for comparative purpose.

From the tables, it is evident that all the substrates were hydrogenated with very high conversion (upto 99%) and high enantiomeric excess (upto 99%) by the Ru-SB-SDPEN-MCM-41 and Ru-SB-SDPEN-MCM-48 catalysts. Although, the RuP-TPEN-MCM-41/48 and Ru-SB-TPEN-MCM-41/48 catalysts also show similar catalytic activity, they exhibit poor enantioselectivity [ee < 25% (for RuP-TPEN-MCM-41/48) and < 40% (for Ru-SB-TPEN-MCM-41/48)]. Moreover, the RuP-NH_2-MCM-41 catalyst is not all catalytically active in the hydrogenation of prochiral ketones. Similar phenomena was also observed in the case of hydrogenation of α,β-unsaturated aldehydes by the RuP-NH_2-MCM-41 catalyst, where hydrogenation of C=O bond had not occurred at all (Table 3.5). From these results the it is evident that (i) the presence of one ethylenediamine moiety is essential for hydrogenation of carbonyl groups by Ru^{II}-phosphine complexes, since the reactions are expected to proceed through the "*Metal-ligand bifunctional catalysis*" mechanism,[14,15] and (ii) both the biphosphine and diamine ligands around the central Ru^{II} ion necessarily have to be chiral for maximum enantioselection, in agreement with the observations of Noyori *et al.*[14,15] Almost comparable activity and enantioselectivity of MCM-41 and MCM-48 based catalysts show that the reaction rate does not essentially depend upon whether the support is MCM-41 or MCM-48, possibly due to similar rate of interaction between substrate molecules and catalyst active site.

Table 3.7. Enantioselective hydrogenation[a] of prochiral aliphatic and alicyclic ketones

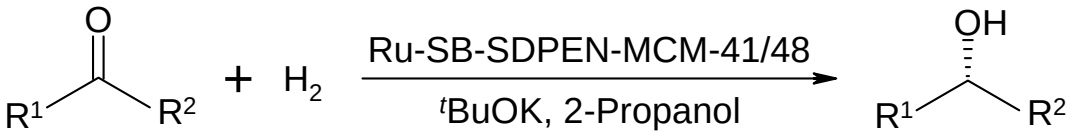

Catalyst	Substrate	Conv. (mol. %)[b]	TON[c]	TOF (h^{-1})[d]	ee (%)
RuP-NH_2-MCM-41	$R^1 = C_2H_5$, $R^2 = CH_3$	4	87	22	0
RuP-TPEN-MCM-41	$R^1 = C_2H_5$, $R^2 = CH_3$	91	2061	515	16
Ru-SB-TPEN-MCM-41	$R^1 = C_2H_5$, $R^2 = CH_3$	93	1979	495	28
Ru-SB-SDPEN-MCM-41	$R^1 = C_2H_5$, $R^2 = CH_3$	96	1930	483	99
RuP-TPEN-MCM-48	$R^1 = C_2H_5$, $R^2 = CH_3$	90	1975	494	14
Ru-SB-TPEN-MCM-48	$R^1 = C_2H_5$, $R^2 = CH_3$	94	1874	469	29
Ru-SB-SDPEN-MCM-48	$R^1 = C_2H_5$, $R^2 = CH_3$	97	2026	507	99
Ru-SB-SDPEN-SiO_2	$R^1 = C_2H_5$, $R^2 = CH_3$	91	1820	455	90
Ru-SB-SDPEN[e]	$R^1 = C_2H_5$, $R^2 = CH_3$	>99	1880	940	>99
Ru-SB-SDPEN-MCM-41	R^1 = Cyclohexyl, $R^2 = CH_3$	72	1448	362	91
Ru-SB-SDPEN-MCM-48	R^1 = Cyclohexyl, $R^2 = CH_3$	79	1575	394	94

[a]Reaction conditions: Catalyst = 100 mg; Substrate = 7 mmol; Substrate: Base = 100: 1; Ru: Substrate = 1: 2265 (RuP-TPEN-MCM-41), 1: 2194 (RuP-TPEN-MCM-48), 1: 2128 (Ru-SB-TPEN-MCM-41), 1: 1994 (Ru-SB-TPEN-MCM-48), 1: 2011 (Ru-SB-SDPEN-MCM-41), 1: 2089 (Ru-SB-SDPEN-MCM-48), 1: 2000 (Ru-SB-SDPEN); Temperature = 100 °C; H_2 pressure = 1.38 MPa; Stirring speed = 500 rpm; Duration = 4 h (heterogeneous), 2 h (homogeneous).

[b]Absolute configuration of all the reaction products is (*S*).

[c]TON = (mmol of ketone converted to alcohol) × $(\text{mmol of Ru})^{-1}$.

[d]TOF = TON × Time^{-1} (in h).

[e]Reaction under homogeneous conditions.

Table 3.8. Enantioselective hydrogenation[a] of prochiral aromatic ketones

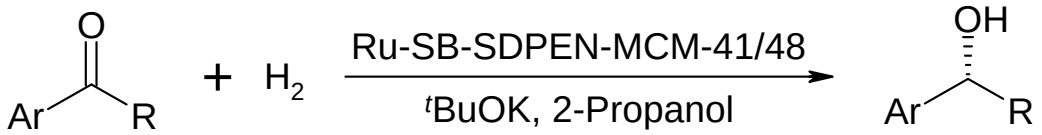

Catalyst	Substrate	Conv. (mol. %)[b]	TON[c]	TOF (h^{-1})[d]	ee (%)
RuP-TPEN-MCM-41	Ar = Ph, R = Me	89	2016	504	18
Ru-SB-TPEN-MCM-41	Ar = Ph, R = Me	92	1958	489	31
Ru-SB-SDPEN-MCM-41	Ar = Ph, R = Me	94	1890	472	93
RuP-TPEN-MCM-48	Ar = Ph, R = Me	86	1887	472	22
Ru-SB-TPEN-MCM-48	Ar = Ph, R = Me	91	1814	454	39
Ru-SB-SDPEN-MCM-48	Ar = Ph, R = Me	96	2005	501	95
Ru-SB-SDPEN-SiO_2	Ar = Ph, R = Me	92	1840	460	94
Ru-SB-SDPEN[e]	Ar = Ph, R = Me	>99	1980	990	>99
Ru-SB-SDPEN-MCM-41	Ar = 4'-Me-Ph, R = Me	95	1910	478	94
Ru-SB-SDPEN-MCM-48	Ar = 4'-Me-Ph, R = Me	97	2026	507	96
Ru-SB-SDPEN-MCM-41	Ar = 4'-Cl-Ph, R = Me	98	1971	493	96
Ru-SB-SDPEN-MCM-48	Ar = 4'-Cl-Ph, R = Me	99	2068	517	98
Ru-SB-SDPEN-MCM-41	Ar = Ph, R = Et	95	1910	478	91
Ru-SB-SDPEN-MCM-48	Ar = Ph, R = Et	96	2005	501	93
Ru-SB-SDPEN-MCM-41	Ar = 4'-MeO-Ph, R = Me	88	1770	442	95
Ru-SB-SDPEN-MCM-48	Ar = 4'-MeO-Ph, R = Me	91	1901	475	96
Ru-SB-SDPEN-MCM-41	Ar = Ph, R = Cyclobutyl	75	1508	377	91
Ru-SB-SDPEN-MCM-48	Ar = Ph, R = Cyclobutyl	79	1650	413	93

[a]Reaction conditions: Catalyst = 100 mg; Substrate = 7 mmol; Substrate: Base = 100: 1; Ru: Substrate = 1: 2265 (RuP-TPEN-MCM-41), 1: 2194 (RuP-TPEN-MCM-48), 1: 2128 (Ru-SB-TPEN-MCM-41), 1: 1994 (Ru-SB-TPEN-MCM-48), 1: 2011 (Ru-SB-SDPEN-MCM-41), 1: 2089 (Ru-SB-SDPEN-MCM-48), 1: 2000 (Ru-SB-SDPEN); Temperature = 100 °C; H_2 pressure = 1.38 MPa; Stirring speed = 500 rpm; Duration = 4 h (heterogeneous), 2 h (homogeneous).
[b]Absolute configuration of all the reaction products is (*S*).
[c]TON = (mmol of ketone converted to alcohol) × $(\text{mmol of Ru})^{-1}$.
[d]TOF = TON × Time^{-1} (in h).
[e]Reaction under homogeneous conditions.

Control experiments with the homogeneous Ru-SB-SDPEN complex show that the reaction is *ca*. twice faster in the homogeneous system *vis-à-vis* the same complex anchored in MCM-41 or MCM-48. This could be due to slower rate of interaction between the substrate and the catalyst active site in the heterogeneous solid-liquid system compared to that in the homogeneous liquid system.

In the case of acyclic ethylmethylketone, while the conversion is higher *vis-à-vis* cyclohexylmethylketone (Table 3.7), as expected due to relative bulkiness of the substituent group in the vicinity of the carbonyl group, the ee in the case of both the substrates was comparable. A similar trend was also observed in the case of acetophenone and cyclobutylphenylketone (Table 3.8). However, there was insignificant effect of substitution in the aromatic ring of acetophenone on the conversion as well as ee (Table 3.8), in agreement with the results obtained by Hu *et al*.[18]

3.6.1. Influence of Reaction Time over Conversion and Enantioselectivity

The influence of reaction time over the conversion and enantioselectivity in the hydrogenation of acetophenone is presented in Figure 3.11, which illustrates that the conversion increases with time, as expected, and reaches an optimum value (> 90%) before 4 h in the case of the heterogeneous catalysts, and before 2 h in the case of the homogeneous catalyst. This accounts for the high TOF values in the case of the homogeneous catalyst compared to its heterogeneous counterparts (Tables 3.7 and 3.8), expectedly due to restricted interaction between substrate molecules and catalyst active site under heterogeneous reaction conditions compared to that in homogeneous conditions, as mentioned above. The enantiomeric excess values, however, attain a maximum from the very beginning of the reactions.

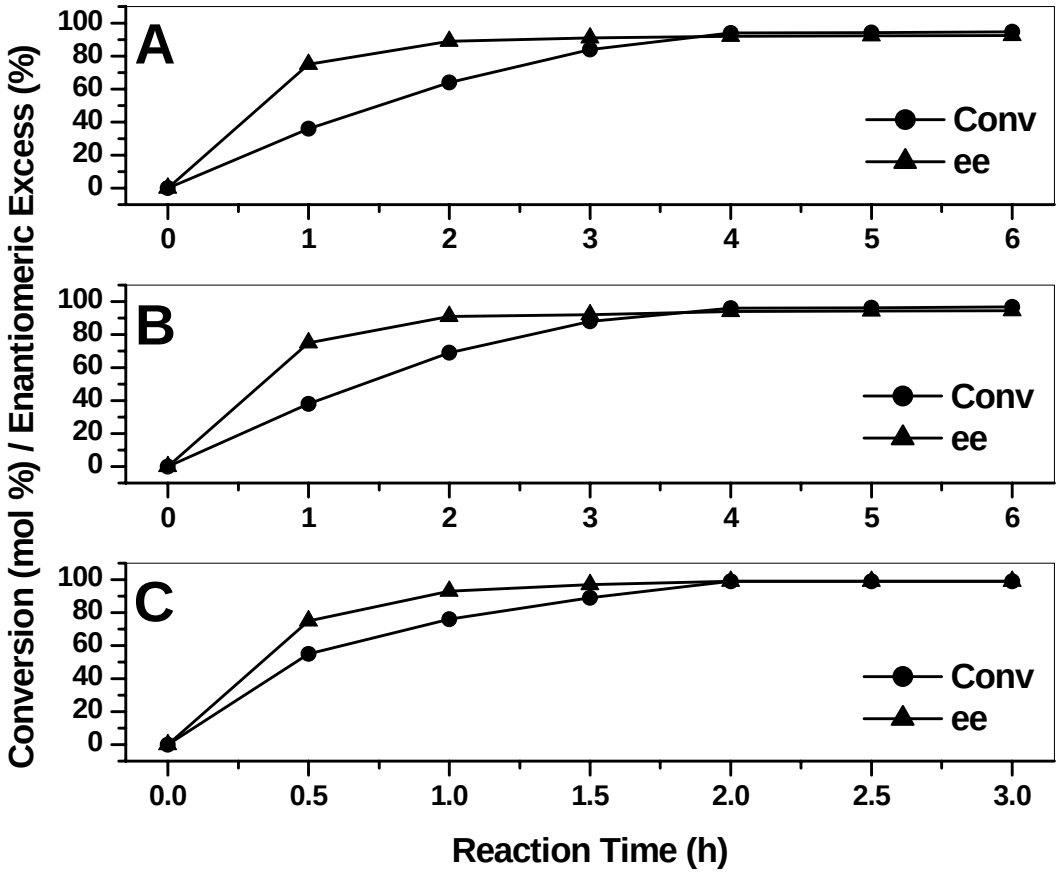

Figure 3.11. Influence of reaction time over conversion and enantioselectivity in the hydrogenation of acetophenone by (A) Ru-SB-SDPEN-MCM-41, (B) Ru-SB-SDPEN-MCM-48, and (C) homogeneous Ru-SB-SDPEN catalysts. Reaction conditions: Temperature = 100 °C, H_2 pressure = 1.38 MPa, Stirring speed = 500 rpm.

3.6.2. Influence of Temperature over Conversion and Enantioselectivity

As experienced earlier from the hydrogenation studies of olefins and α,β-unsaturated aldehydes, an optimum temperature of 100 °C is required to attain the maximum conversion by the heterogeneous Ru-SB-SDPEN-MCM-41/48 and homogeneous Ru-SB-SDPEN catalyst systems (Figure 3.12). By increasing the temperature upto 120 °C, no further change in reaction rate was observed. The best ee was obtained at 100 °C, below which the ee was slightly less.

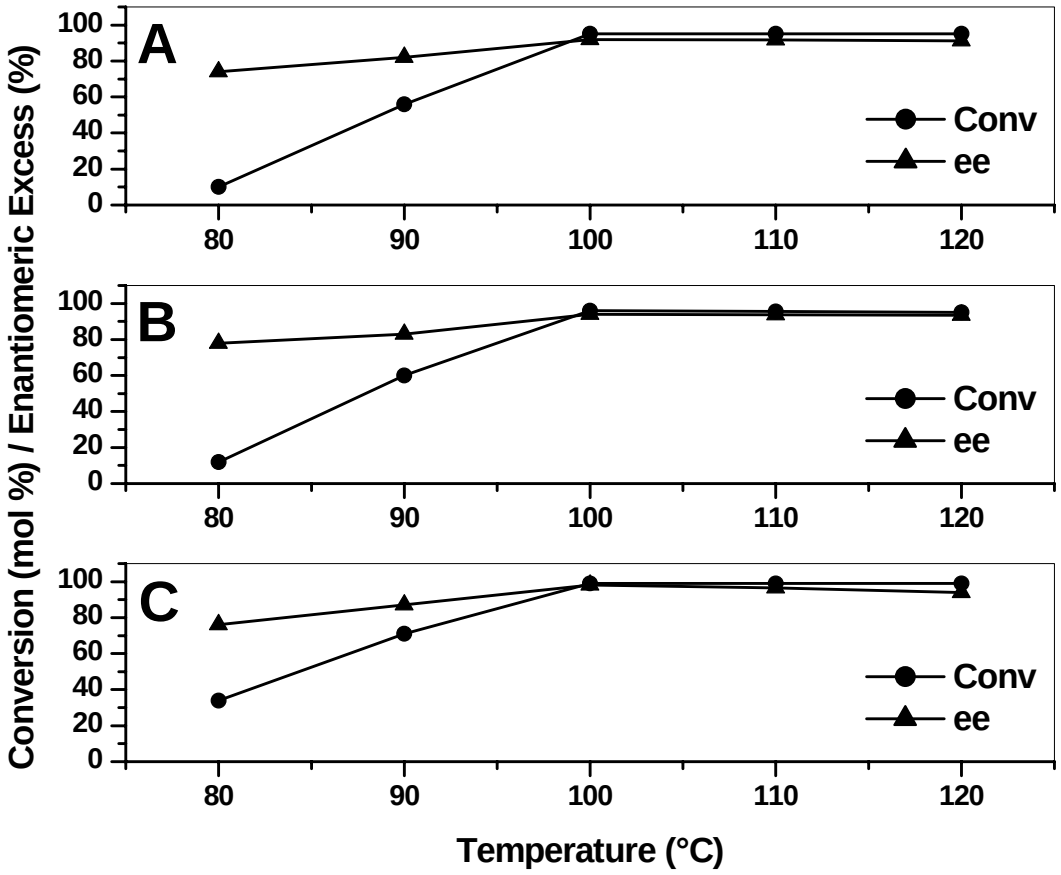

Figure 3.12. Influence of temperature over conversion and enantioselectivity in the hydrogenation of acetophenone by (A) Ru-SB-SDPEN-MCM-41, (B) Ru-SB-SDPEN-MCM-48, and (C) homogeneous Ru-SB-SDPEN catalysts. Reaction conditions: Duration = 4 h, H_2 pressure = 1.38 MPa, Stirring speed = 500 rpm.

3.6.3. Influence of H_2 Pressure over Conversion and Enantioselectivity

The effect of H_2 pressure over the conversion and enantioselectivity in the hydrogenation of acetophenone is presented in Figure 3.13. It was envisaged that the maximum conversion of the substrate and ee were achieved at 1.38 MPa pressure, beyond which no further enhancement in reaction rate as well as in ee was experienced. But the enantioselectivity of the catalyst system (Ru-SB-SDPEN-MCM-41/48) is very high even at lower H_2 pressure (0.35–0.7 MPa).

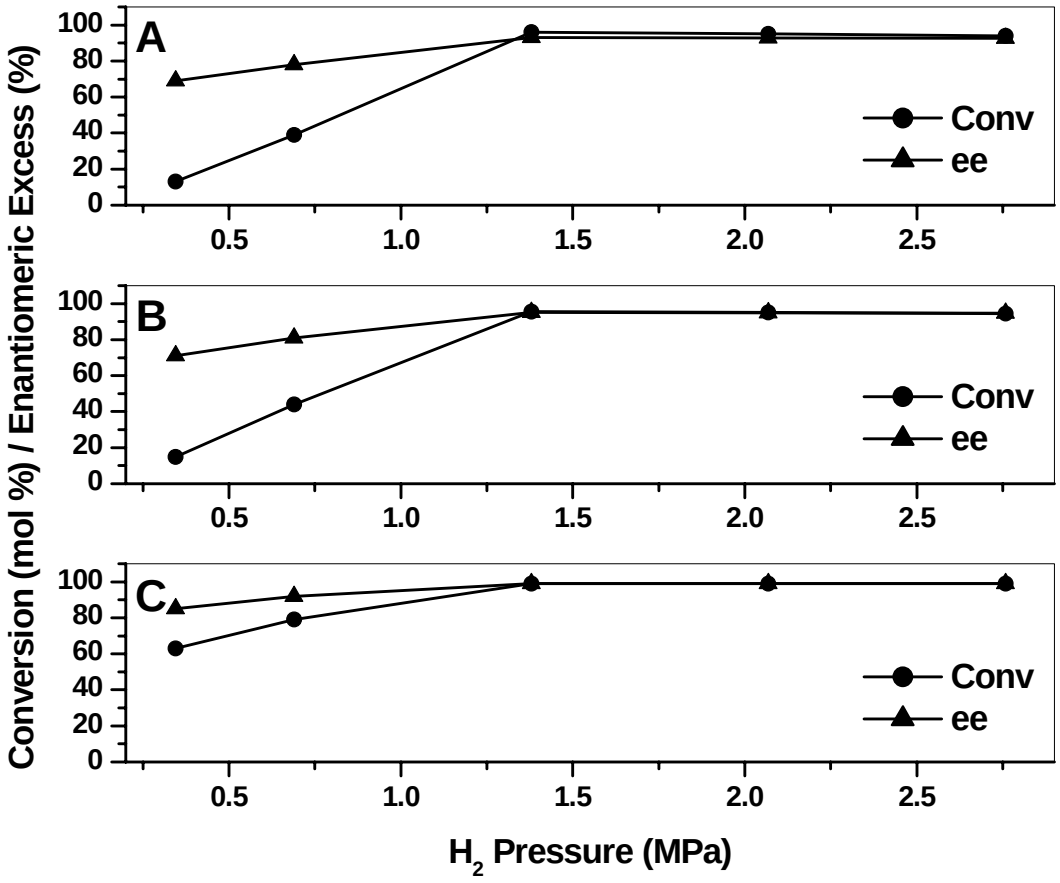

Figure 3.13. Influence of H_2 pressure over conversion and enantioselectivity in the hydrogenation of acetophenone by (A) Ru-SB-SDPEN-MCM-41, (B) Ru-SB-SDPEN-MCM-48, and (C) homogeneous Ru-SB-SDPEN catalysts. Reaction conditions: Duration = 4 h, Temperature = 100 °C, Stirring speed = 500 rpm.

3.6.4. Recycle Studies

The stability of the heterogeneous catalysts was evaluated by recovering them from the hot reaction mixtures by filtration, and analyzing the filtrates for Ru content by ICP-AES. In the case of Ru-SB-SDPEN-MCM-41/48 catalysts, the Ru contents in the total filtrate were found to be *ca*. 9.3×10^{-4}% of the total Ru present in the catalyst, indicating insignificant leaching of the metal and therefore metal complex. Besides, both of these catalysts were effectively recycled four times for hydrogenation of acetophenone without any significant decline in activity and enantioselectivity (Table 3.9). Whereas, the catalyst

prepared by anchoring the Ru-(*S*)-BINAP complex onto SDPEN-functionalized fumed silica (Ru-SB-SDPEN-SiO_2 material) showed substantial amount of leaching of Ru metal (*ca*. 26.5% of the total Ru present in the catalyst used) during reaction in the first cycle, which also leads to major decrease in catalytic activity and selectivity after four recycles (Table 3.9).

Table 3.9. Recycle studies of the heterogeneous catalysts for hydrogenation of acetophenone

No. of Recycles	Ru-SB-SDPEN-SiO_2		Ru-SB-SDPEN-MCM-41		Ru-SB-SDPEN-MCM-48	
	Conv. (mol. %)	ee (%)	Conv. (mol. %)	ee (%)	Conv. (mol. %)	ee (%)
1	78.3	84	93.7	93	95.9	95
2	58.9	72	93.8	93	95.7	95
3	42.3	71	93.5	93	95.8	95
4	20.6	70	93.3	93	95.4	95

The stability of the heterogeneous catalysts after hydrogenation reactions was also supported from XPS analyses of the filtered catalysts. The core level BE of the elements in the recycled MCM-41 and MCM-48 catalysts are presented Table 3.10.

Table 3.10. Core level binding energies (in eV) of various elements[a] in the heterogeneous catalysts after hydrogenation of different substrates

Catalysts	Substrates Studied	Ru $3d_{5/2}$	Ru $3p_{3/2}$	N 1s	Si 2p	P 2p
RuP-NH_2-MCM-41	1-hexene	280.5	464.8	399.9	103.4	131.3
RuP-NH_2-MCM-48	1-hexene	280.4	464.9	400.0	103.4	131.3
RuP-TPEN-MCM-41	Cinnamaldehyde	280.5	464.8	400.1	103.4	131.3
RuP-TPEN-MCM-48	Cinnamaldehyde	280.5	464.9	400.2	103.4	131.3
Ru-SB-SDPEN-MCM-41	Acetophenone	280.8	465.0	400.7	103.4	131.6
Ru-SB-SDPEN-MCM-48	Acetophenone	280.7	465.0	400.6	103.4	131.5

[a]The core level binding energies were aligned with respect to the C 1s binding energy of 285 eV using adventitious carbon.

From the table, it was manifested that the Ru $3d_{5/2}$, Ru $3p_{3/2}$, N 1s and P 2p core level binding energies are matching exactly with those in the parent materials before reaction (Table 3.2), indicating that neither the metal nor the ligands changed their chemical environment during reactions.

In conclusion, few efficient heterogeneous catalyst systems, involving anchoring of various Ru^{II}-phosphine-diamine complexes on the inner surfaces of organo-functionalized MCM-41 and MCM-48 molecular sieves, for chemoselective hydrogenation of α,β-unsaturated aldehydes and enantioselective hydrogenation of prochiral ketones, were designed. Detailed characterization of these new catalyst systems strongly point towards stable immobilization of the Ru-complexes inside the mesoporous matrices. These newer catalyst systems show promising activity and selectivity in the aforesaid hydrogenation reactions, and can be recycled effectively and reused several times without any loss in activity and selectivity.

3.7. REFERENCES

1. *Chirality in Industry: The Commercial Manufacture and Applications of Optically Active Compounds*, Eds: A. N. Collins, G. N. Sheldrake, J. Crosby, Wiley, New York, **1997**.
2. R. A. Sheldon, *Chirotechnology*, Marcel Dekker Inc., New York, **1993**.
3. I. Ojima (Ed), *Catalytic Asymmetric Synthesis*, *2nd ed.*, Wiley, New York, **2000**.
4. R. Noyori, (Nobel Lecture 2001) *Adv. Synth. Catal.* **2003**, *345*, 15.
5. J. Halpern, *Science* **1982**, *217*, 401.
6. R. Noyori, *Asymmetric Catalysis in Organic Synthesis*, Wiley, New York, **1994**, Chapter 2, pp. 17–94.
7. T. Ohkuma, R. Noyori, in: *Comprehensive Asymmetric Catalysis*, *Vol. 1*, Eds: E. N. Jacobsen, A. Pfaltz, H. Yamamoto, Springer, Berlin, **1999**, pp. 199–246.
8. R. L. Augustine, *Heterogeneous Catalysts in Organic Synthesis*, Dekker, New York, **1995**.
9. P. Claus, *Top. Catal.* **1998**, *5*, 51.
10. P. Gallezot, D. Richard, *Catal. Rev. -Sci. Eng.* **1998**, *40*, 81.
11. V. Ponec, *Appl. Catal. A: Gen.* **1997**, *149*, 27.
12. T. Ohkuma, H. Ooka, S. Hashiguchi, T. Ikariya, R. Noyori, *J. Am. Chem. Soc.* **1995**, *117*, 2675.
13. T. Ohkuma, H. Ooka, T. Ikariya, R. Noyori, *J. Am. Chem. Soc.* **1995**, *117*, 10417.
14. R. Noyori, T. Ohkuma, *Angew. Chem. Int. Ed.* **2001**, *40*, 40.
15. R. Noyori, M. Yamakawa, S. Hashiguchi, *J. Org. Chem.* **2001**, *66*, 7931.
16. R. Noyori, S. Hashiguchi, *Acc. Chem. Res.* **1997**, *30*, 97.
17. D. E. De Vos, M. Dams, B. F. Sels, P. A. Jacobs, *Chem Rev.* **2002**, *102*, 3615.
18. P. N. Liu, P. M. Gu, F. Wang, Y. Q. Tu, *Org. Lett.* **2004**, *6*, 169.

19. T. Ohkuma, H. Takeno, Y. Honda, R. Noyori, *Adv. Synth. Catal.* **2001**, *343*, 369.

20. C. E. Song, S. Lee, *Chem. Rev.* **2002**, *102*, 3495.

21. A. Hu, H. L. Ngo, W. Lin, *Angew. Chem. Int. Ed.* **2003**, *42*, 6000.

22. A. Hu, H. L. Ngo, W. Lin., *J. Am. Chem. Soc.* **2003**, *125*, 11490.

23. A. Zsigmond, K. Bogar, F. Nothiesz, *J. Catal.* **2003**, *213*, 103.

24. P. McMorn, G. J. Hutchings, *Chem. Soc. Rev.* **2004**, *33*, 108.

25. R. Raja, J. M. Thomas, M. D. Jones, B. F. G. Johnson, D. E. W. Vaughan, *J. Am. Chem. Soc.* **2003**, *125*, 14982.

26. M. D. Jones, R. Raja, J. M. Thomas, B. F. G. Johnson, D. W. Lewis, J. Rouzaud, K. D. M. Harris, *Angew. Chem. Int. Ed.* **2003**, *42*, 4326.

27. A. Ghosh, R. Kumar, *J. Catal.* **2004**, (in press).

28. F. H. Jardine, *Prog. Inorg. Chem.* **1984**, *31*, 265.

29. M. A. Bennett, A. K. Smith, *J. Chem. Soc., Dalton Trans.* **1974**, 233.

30. H. C. Brown, B. T. Cho, W. S. Park, *J. Org. Chem.* **1988**, *53*, 1231;

31. K. Nakamura, T. Matsuda, *J. Org. Chem.* **1998**, *63*, 8957.

32. D. Venegas-Yazigi, M. Campos-Vallette, A. B. P. Lever, J. Costamagna, R. O. Latorre, W. Hernandez G., *J. Chil. Chem. Soc.* **2003**, *48*, 79.

33. *Practical Handbook of Spectroscopy*, Ed: J. W. Robinson, CRC Press, Florida, **1991**, pp. 183–418.

34. D. S. Shephard, W. Zhou, T. Maschmeyer, J. M. Matters, C. L. Roper, S. Parsons, B. F. G. Johnson, M. J. Duer, *Angew. Chem. Int. Ed.* **1998**, *37*, 2719.

35. J. M. Thomas, O. Terasaki, P. L. Gai, W. Zhou, J. Gonzalez-Calbet, *Acc. Chem. Res.* **2001**, *34*, 583.

4.1. INTRODUCTION

During the past few decades or so, much efforts have been directed towards understanding the size-dependent physicochemical properties of nanoparticles because of their immense importance in a variety of applications such as in catalysis,[1] optoelectronics,[2] as novel templates in biomineralization,[3] in medicine (diagnostics and therapeutics)[4,5] *etc*. Generally surfactant molecules containing polar head groups like thiol (–SH), amine ($–NH_2$) *etc*. are used to stabilize the nanoparticles and to prevent their agglomeration to get the quantum dots.[6,7] The propylamine and propylthiol functionalized MCM-41 materials are particularly important in the sense that they have the polar head groups generally required to stabilize the nanoparticles. Further, they provide a solid support of well-defined pores to the entrapped nanoclusters. Therefore, these nanocomposites can be envisaged as a three-layered entity, where the outer sphere is the inorganic support, the second sphere is the organic moiety attached to the surface of MCM-41 and protruding inside the pores, and the third sphere consists of the nanoparticles hooked to the polar head groups of the organic moiety present inside the pores. These three-layered nanocomposites may lead to some interesting non-linear optical properties for future optoelectronic applications,[8] and they are excellent materials for studying host-guest interactions.[9] The stabilization of nanoparticles inside the well-defined pores of MCM-41 materials may lead to the formation of nanowires, which are the building units of future nanoelectronic circuits.[2]

Among the transition metals, gold hitherto had the reputation of being the least catalytically active. Hammer *et al*. had explained theoretically why the smooth surface of gold is noble in the dissociative adsorption of molecular hydrogen.[10] However, a substantial amount of work done by Haruta *et al*. has established that nanosized gold particles when deposited on certain oxides exhibits surprisingly high catalytic activity in oxidation of carbon monoxide at or below ambient temperatures.[11] The catalytic potential of supported

gold nanoparticles in partial and complete oxidation of hydrocarbons, hydrogenation of carbon monoxide, nitric oxide and unsaturated hydrocarbons has also been reported.[12]

The remarkably high catalytic activity of gold arises from formation of very small particles. It is known that the bulk metal and larger metallic particles cannot chemisorb most of the reactant molecules; chemisorption occurs only when a satisfactory number of low-coordination number surface atoms are present, preferably on smaller particles lacking complete metallic character. Recent literature on supported gold catalysts shows that the principal factors for attaining high catalytic activity are (i) smaller particle size (<4 nm) and (ii) support.[13] In most cases, cations of the first transition series elements, and a few pre- or post-transition series elements, capable of forming hydroxides or hydrated oxides in presence of an alkali, were used as precursors for the supports.

Preparation of supported gold catalysts can be achieved by the following different traditional routes; (i) impregnation of a preformed support with a solution of chloroauric acid followed by drying and reduction,[14] (ii) cation exchange with the support by cationic gold complexes followed by washing, drying and reduction,[15] (iii) coprecipitation of hydroxides of both support and gold followed by drying, calcination and reduction,[16] (iv) deposition-precipitation of gold hydroxide to a suspension of the support followed by drying, calcination and reduction,[17] and (v) chemical vapor deposition of a volatile compound of gold to a high area support through an inert gas.[18]

However, in all the methods stated above, and in most of the reports on the formation and stabilization of metallic nanoparticles, barring those of Esumi *et al*.[19] using sugar balls and Mukherjee *et al*.[20] using microorganisms, the hosts are usually passive and do not participate actively in the reduction of metal ions to form nanoparticles followed by their entrapment in host matrix. Some external methods, as stated above, have to be employed for the formation of nanoparticles prior to their stabilization.

Realizing the immense importance of nanocomposites in various applications, we have developed a novel method for the synthesis of gold nanoparticles by *in situ* reduction of aqueous chloroaurate ions ($AuCl_4^-$) *via* silanol groups present in inner surfaces of organo-functionalized MCM-41 or on the surface of amorphous silica (Scheme 4.1).[21-23] Employing this method, we can avoid the use of any external reducing environment other than the host matrix.

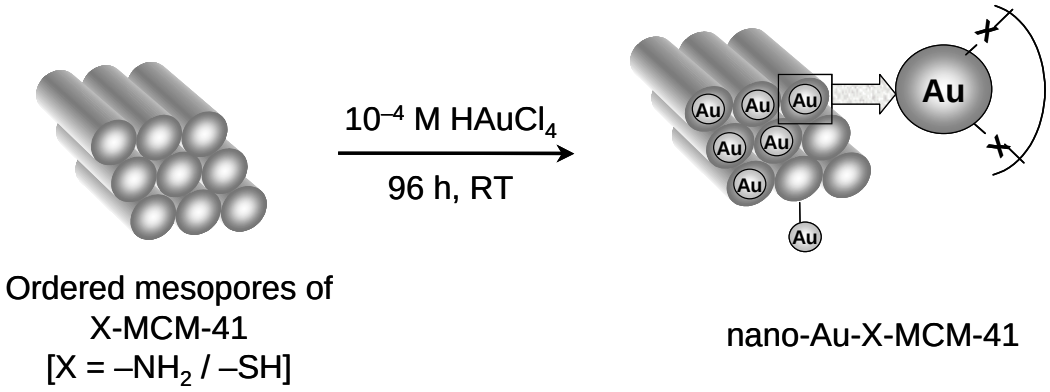

Scheme 4.1. The probable structure of the organo-functionalized MCM-41 material before and after immersion in $HAuCl_4$ solution. The magnified view of the cross-section shows the entrapped gold nanoparticles formed by spontaneous reduction of $AuCl_4^-$ ions by the MCM-41 material.

In this chapter, the detailed studies on the synthesis of gold nanoparticles of controlled and uniform size by *in situ* reduction of Au^{III} to Au^0, and their simultaneous stabilization using propylamine-MCM-41 (NH_2-MCM-41) and propylthiol-MCM-41 (SH-MCM-41) in a single step will be demonstrated. The organic functional groups act as anchors for the nanoparticles by binding them through covalent interactions, thereby avoiding the requirement of external capping agents like alkylamines or alkylthiols for particle size control.[6,7,22] A possible pathway for the formation of gold nanoparticles will be proposed by similar experiments with amorphous (fumed) silica. The catalytic potential of these Au-MCM-41 nanocomposites will be exploited in preferential oxidation of carbon

monoxide (CO) in hydrogen-rich reformates used for polymer electrolyte membrane fuel cells (PEMFC), and in the hydrogenation of unsaturated hydrocarbons.

4.2. EXPERIMENTAL

4.2.1. Materials

Tetraethyl orthosilicate (TEOS), 3-aminopropyltrimethoxy silane (APTS), 3-mercaptopropyltrimethoxy silane (MPTS), fumed silica (SiO_2), n-octadecylamine (ODA), 1-hexene and 1-octene were purchased from Aldrich; cetyltrimethylammonium bromide (CTABr), chloroauric acid ($HAuCl_4$), cyclohexene, n-octylamine (NOA), and dodecylamine (DDA) were purchased from SD Fine Chem, India, and were used as received without further purification.

4.2.2. Preparation of Nanogold-MCM-41 Hybrid Materials

All the organo-functionalized MCM-41 materials were synthesized by "one-pot co-condensation" method, as described in Chapter 2. In the synthesis gel, the XPTS/TEOS ratios (XPTS = APTS or MPTS) were varied from 0.17–0.4 to estimate the influence of organic functional groups in the reduction of $AuCl_4^-$. However, the samples prepared with XPTS : TEOS = 0.4:1 were used in majority of the experiments. The surfactant from the NH_2-MCM-41 and SH-MCM-41 materials was removed by a solvent extraction method, as demonstrated in Chapter 2.

Synthesis of Si-MCM-41 was carried out using the following ratio in the initial gel mixture: SiO_2–0.32NaOH–0.2CTABr–125H_2O, as described in Chapter 2. The surfactant from the as-synthesized sample was burnt off by calcination at 540 °C for 10 h.

The formation of nano-Au-MCM-41 hybrid materials by *in situ* reduction of $AuCl_4^-$ ions were achieved by treating 1.0 g of each of the Si-MCM-41, NH_2-MCM-41 and SH-

MCM-41 materials with 100 mL of 10^{-4} M $HAuCl_4$ solution for 96 h at ambient conditions. Further, 0.5 g of each of the nano-Au-Si-MCM-41, nano-Au-NH_2-MCM-41 and nano-Au-SH-MCM-41 materials were separately stirred with 50 mL of distilled water for 12 h. The materials thus obtained after aqueous treatment (designated as Au-Si-MCM-41-w, Au-NH_2-MCM-41-w and Au-SH-MCM-41-w respectively) were filtered, washed with water and dried under vacuum.

4.2.3. Preparation of Nanogold–Fumed Silica Composite Materials

Fumed silica samples with different concentrations of surface hydroxyl groups were prepared by reacting 0.5 g of fumed silica with 50 mL of 5% HCl for 0, 1, 6, 12 and 24 h at room temperature. These samples were then filtered, washed thoroughly with copious amounts of water and dried. The sample numbers are given as 1, 2, 3, 4 and 5 respectively.

The concentration of surface silanol groups in the different fumed silica samples was determined by a modified Fripiat and Uytterhoeven method,[24] where different fumed silica samples were treated with methyl magnesium iodide in dibutylether under nitrogen atmosphere, and the evolved methane gas was measured quantitatively.

The "*autoreduction*" of $AuCl_4^-$ ions by the fumed silica samples with different silanol concentration was carried out by treating 0.5 g of each of the fumed silica samples 1–5 with 50 mL of 10^{-4} M $HAuCl_4$ solution for 40 h at room temperature. The samples are designated as SiAu1–5 respectively. Similar experiments were performed with fumed silica sample 5 and 10^{-4} M aqueous $HAuCl_4$ solution in presence of following concentrations of dodecylamine (DDA) molecules: (i) 10^{-1} M, (ii) 10^{-3} M, (iii) 10^{-6} M; and in presence of 10^{-3} M solutions of (iv) n-octylamine (NOA), and (v) octadecylamine (ODA). The amine molecules were solubilized in the $AuCl_4^-$ ion solution using minimum volume of ethanol. After 40 h of stirring, the samples were filtered, washed repeatedly with distilled water and

dried under vacuum at ambient temperature. The samples are designated as SiAuDDA1, SiAuDDA3, SiAuDDA6, SiAuNOA3 and SiAuODA3 respectively. A small amount of the autoreduced gold sample 5 (SiAu5) was heated at 400 °C for 1 h to study the effect of heating on the size of the gold nanoparticles and their packing density on the silica surface (designated as SiAu400).

4.2.4. Instruments for Characterization

Low angle X-ray diffraction patterns of the siliceous as well as organo-functionalized MCM-41 materials before and after entrapment of gold nanoparticles were recorded on a Rigaku MiniFlex instrument using Cu K_α radiation (λ = 1.5404 Å) in the 2θ range of 1.5–10° at a scan rate of 1°/min. Further, XRD patterns of the nano-Au-MCM-41 and nano-Au–fumed silica samples were recorded on a Philips PW 1830 instrument operating at 40 kV and a current of 30 mA with Cu K_α radiation (λ = 1.5404 Å) between the 2θ range of 30° and 45° with a scan rate of 1°/min. From the broadening of the Au(111) reflection at 2θ = 38.2°, the average size of the gold nanoparticles was evaluated applying the Debye-Scherrer equation.[25]

The specific surface areas of all the mesoporous samples were determined by the BET method[26] from N_2 adsorption isotherms at 77 K using an Omnisorb CX-100 Coulter instrument. Prior to the adsorption experiments, the samples were activated at 150 °C for 6 h at 1.3×10^{-2} Pa. Pore size distribution of the samples was computed by Barrett-Joyner-Halenda (BJH) model.[27]

The UV-Vis spectra of the nano-Au-MCM-41 and nano-Au–fumed silica samples were recorded on a Shimadzu UV-2102 PC spectrophotometer operating at the reflectance mode at a resolution of 2 nm using barium sulphate as a standard for background correction.

Further, UV-Vis spectra of the different filtrates were recorded on the same instrument using distilled water as a standard for background correction.

The NH_2-MCM-41 and SH-MCM-41 materials with and without the entrapped gold nanoparticles was subjected to thermogravimetric (TGA) and differential thermal analysis (DTA) performed on a Seiko Instruments model TG/DTA 32 at a heating rate of 10 °C/min.

Elemental analyses of NH_2-MCM-41 and SH-MCM-41 materials after template removal were carried out on a Carlo Erba EA 1108 elemental analyzer. X-ray fluorescence (XRF) measurements of nano-Au-MCM-41 and nano-Au–fumed silica composite materials (for weight percentage of gold) were performed on a Rigaku 3070 sequential wavelength dispersive spectrophotometer, with a rhodium target energized at 50 kV and 40 mA.

The X-ray photoelectron spectra (XPS) of the nano-Au-NH_2-MCM-41 and nano-Au-SH-MCM-41 materials were recorded on a VG Microtech ESCA 3000 instrument at a pressure better than 1.3×10^{-7} Pa. The general scan and C 1s, S 2p, N 1s, Si 2p and Au 4f core level spectra were recorded with unmonochromatized Mg K_α radiation (photon energy = 1253.6 eV) at pass energy of 50 eV and an electron takeoff angle (angle between electron emission direction and surface plane) of 60°. The overall resolution of the measurements was approximately 1 eV for the XPS measurements. The core level spectra were background-corrected using the Shirley algorithm[28] and the chemically distinct species resolved using a nonlinear least squares procedure. The core level binding energies were aligned with respect to the Au $4f_{7/2}$ binding energy of 84 eV.

The nano-Au-MCM-41 and nano-Au–fumed silica samples were dispersed on Holey carbon grids and transmission electron microscopic (TEM) images were scanned on a Jeol Model 1200 EX instrument operated at an accelerating voltage of 100 kV.

4.2.5. Preferential Oxidation of CO in H_2 Rich Reformates

The preferential oxidation of CO was carried out in a fixed bed, down flow, glass reactor (internal diameter = 15 mm) using 0.5 g of each of the catalysts. The catalyst sample was made into pellets without any binder, crushed and sized (10–20 mesh). It was then activated at 300 °C for 3 h in flowing hydrogen and then cooled to 130–200 °C. A synthetic feed gas mixture of volume composition H_2 (74.17%) + CO (0.49%) + CO_2 (23.26%) + CH_4 (2.08%) was passed through a mass flow controller at a specific flow rate (GHSV = 5000 h^{-1}), along with the required amount of oxygen in air (O_2/CO = 0.5–1.5). The composition of the products at different reaction conditions were analyzed online using a Chemito 8610 gas chromatograph equipped with a methanator, and containing a Spherocarb column (3.175 mm diameter × 2.44 m length). A calibrated gas mixture was used as a reference to quantify the composition of the outlet gas mixture.

4.2.6. Catalytic Hydrogenation by Supported Gold Nanoparticles

All the hydrogenation reactions were carried out in a 100 mL high-pressure autoclave at temperatures ranging from 100–150 °C and H_2 pressures ranging from 1.4–5.5 MPa for 1–8 h at 500 rpm. In each case, 10 mmol of the substrate, 200 mg of the catalyst and 30 mL of toluene solvent were used. The reaction mixtures were analyzed by a Shimadzu 17A series gas chromatograph containing capillary column (10% permethylated β-cyclodextrin, 30 m × 0.32 mm × 0.25 μm film thickness) and flame ionization detector.

4.3. CHARACTERIZATION

4.3.1. N_2 Adsorption and Desorption

The specific surface areas of the nano-Au-Si-MCM-41, nano-Au-SH-MCM-41 and nano-Au-NH_2-MCM-41 materials before and after incorporation of gold nanoparticles were determined from N_2 adsorption isotherms. Figure 4.1 shows the typical N_2 adsorption-

desorption isotherms and the corresponding pore size distribution curves for the nano-Au-NH_2-MCM-41 and nano-Au-SH-MCM-41 samples. All the samples showed isotherms of type IV in the IUPAC classification,[29] with inflection points around P/P_0 = 0.3–0.45, which is characteristic of M41S type ordered mesoporous materials.[30] The samples exhibit complementary textural and framework-confined mesoporosity, as evidenced by the presence of two separate, well-defined hysteresis loops. One is in the P/P_0 = 0.3–0.45 region indicating framework-confined mesopores, and the other one occurs at $P/P_0 \geq 0.8$ corresponding to capillary condensation in the interparticle pores.[31] The position of the inflection point in the P/P_0 = 0.3–0.45 region depends on the diameter of the mesopores, and its sharpness indicates the uniformity of the narrow pore size distribution.

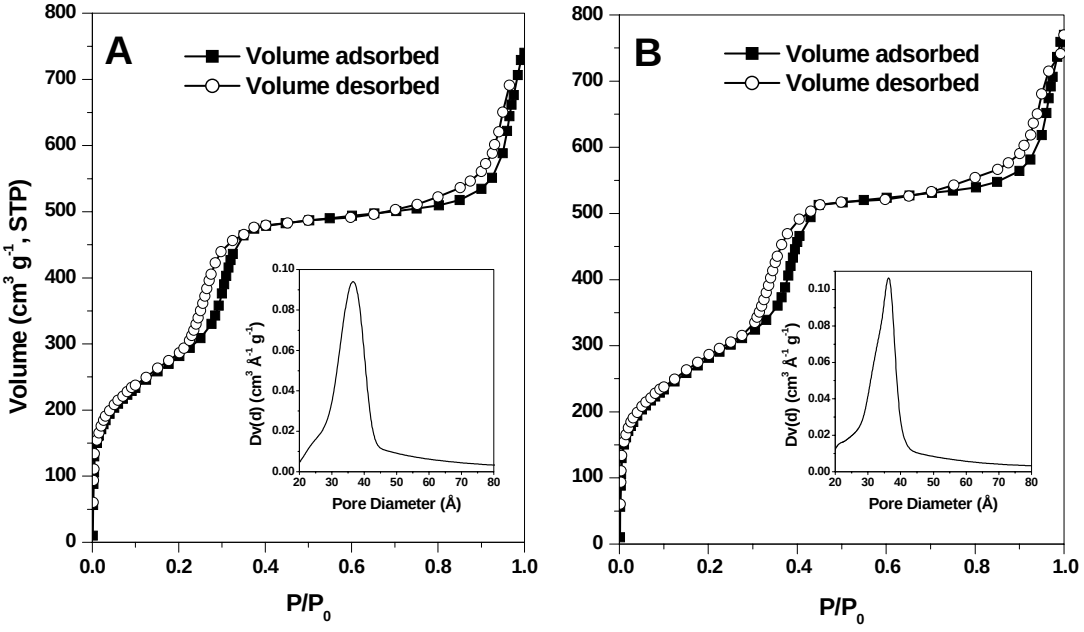

Figure 4.1. N_2 adsorption-desorption isotherms and corresponding pore size distribution curves (insets) for (A) nano-Au-NH_2-MCM-41 and (B) nano-Au-SH-MCM-41 samples.

The specific BET surface areas, pore volumes and mean pore diameters calculated from the N_2 adsorption isotherms using the BJH model are summarized in Table 4.1. After *in situ* reduction of the $AuCl_4^-$ ions by the mesoporous samples, it was observed that the

surface areas of the Si-MCM-41, NH_2-MCM-41 and SH-MCM-41 materials were decreased by *ca.* 9%, 20% and 22%, respectively, and pore volumes were decreased by *ca*. 8%, 18% and 22%, respectively. However, the mean pore diameters of the materials after entrapment of gold nanoparticles did not alter considerably, indicating partial filling of the mesopores by Au nanoparticles keeping the mesoporous structure intact.

Table 4.1. Mean pore diameter (PD), pore volume (PV), specific surface area (SA), d_{100} spacing, unit cell parameter (a_0), framework thickness (FWT) and mean diameter of Au nanoparticles (D) in different MCM-41 samples

Sample	PD (Å)	PV ($cm^3\ g^{-1}$)	SA ($m^2\ g^{-1}$)	d_{100} (Å)	a_0 (Å)	FWT[a] (Å)	D (Å)
Si-MCM-41	39.61	1.19	1322	42.64	49.24	9.63	-
nano-Au-Si-MCM-41	39.57	1.12	1203	42.42	49.03	9.46	n. d.[b]
NH_2-MCM-41	38.77	1.06	947	42.03	48.53	9.76	-
nano-Au-NH_2-MCM-41	38.71	0.91	758	41.81	48.32	9.61	34.1
SH-MCM-41	36.79	1.01	883	40.11	46.31	9.52	-
nano-Au-SH-MCM-41	36.62	0.83	689	39.94	46.12	9.50	32.3

[a]FWT = a_0 – PD.

[b]n. d. = Not determined.

4.3.2. Powder X-Ray Diffraction

Figure 4.2 shows the low angle XRD patterns of (a) Si-MCM-41, (b) nano-Au-Si-MCM-41, (c) SH-MCM-41, (d) nano-Au-SH-MCM-41, (e) NH_2-MCM-41 and (f) nano-Au-NH_2-MCM-41. The strong (100) Bragg reflection is visible in all the materials along with the weak (110), (200) and (210) reflections, indicating high degree of ordered hexagonal mesopores even after anchoring of functional groups, removal of surfactant, and *in situ* formation of gold nanoparticles within the cavities. In fact, the mesopores are only partially filled with gold nanoparticles (as evident from Table 4.1), which did not alter the ordered structure to a considerable extent. The d_{100} values along with the corresponding unit cell

parameter (a_0) of the different MCM-41 samples are given in Table 4.1. The a_0 values were calculated by the equation $a_0 = 2d_{100}/\sqrt{3}$. The average diameter of the gold nanoparticles in the nano-Au-NH_2-MCM-41 and nano-Au-SH-MCM-41 materials was evaluated from the diffraction patterns in the region of the Au(111) Bragg reflection at $2\theta = 38.2°$, which are shown in inset of Fig. 4.2. The solid lines are the Lorentzian fits to the respective curves. Under the experimental conditions of the XRD measurements (small slit width and monochromatized Cu K_α radiation), it was felt that the XRD line-shape would be better approximated by a Lorentzian than a Gaussian. Indeed, poorer chi-square error values (which denote the goodness of fit) were observed while fitting the (111) Bragg reflection of gold to a Gaussian line-shape.

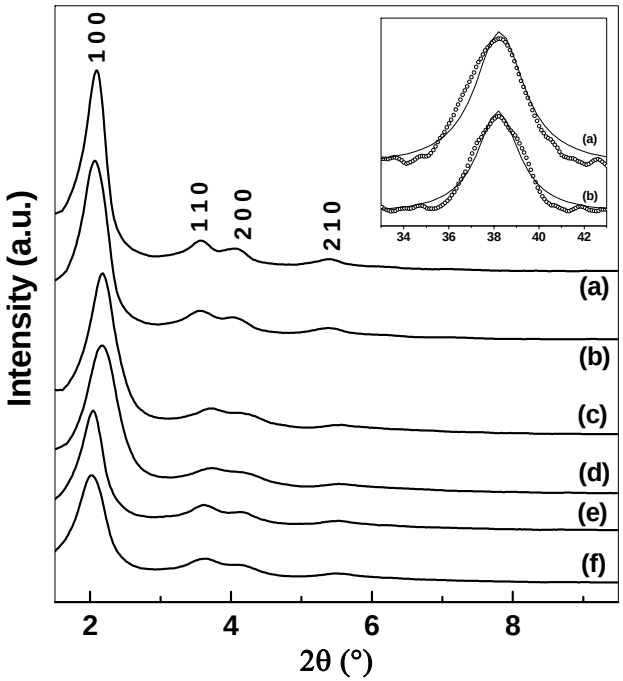

Figure 4.2. Powder XRD patterns of (a) Si-MCM-41, (b) nano-Au-Si-MCM-41, (c) SH-MCM-41, (d) nano-Au-SH-MCM-41, (e) NH_2-MCM-41, and (f) nano-Au-NH_2-MCM-41. Inset shows the diffraction patterns of (a) nano-Au-SH-MCM-41 and (b) nano-Au-NH_2-MCM-41 in the region of the Au(111) Bragg reflection at $2\theta = 38.2°$, the solid lines being the Lorentzian fits to the respective curves.

The mean diameter of the gold nanoparticles was estimated from the broadening of the (111) peak using the Debye-Scherrer equation,[25] which yielded the values of *ca*. 3.4 ± 0.5 nm for nano-Au-NH_2-MCM-41 (inset of Fig. 4.2, curve b) and *ca*. 3.2 ± 0.5 nm for nano-Au-SH-MCM-41 (inset of Fig. 4.2, curve a). These values are in good agreement with the maximum possible particle size that can be accommodated within the pores of the NH_2-MCM-41 and SH-MCM-41 materials, the mean pore diameters of which, as we recollect, are 3.9 and 3.7 nm, respectively.

4.3.3. UV-Vis Experiments

After treatment of the Si-MCM-41, NH_2-MCM-41 and SH-MCM-41 materials individually with $AuCl_4^-$ ions for 96 h, it was observed that all of the materials had attained a deep pink color, evidently due to the presence of Au nanoparticles in the cavities of the silicate matrix. Au nanoparticles have a characteristic absorption band in the visible region of the electromagnetic spectrum at around 520–550 nm due to surface plasmon vibrations, which is responsible for the striking violet to pink range of colors depending upon particle size.[32,33] Figure 4.3.A shows the UV-Vis spectra recorded from the (a) parent Si-MCM-41, (b) nano-Au-Si-MCM-41, (c) Au-Si-MCM-41-w, (d) the filtrate obtained from the Si-MCM-41 material after treatment with $HAuCl_4$, and (e) the filtrate obtained from the nano-Au-Si-MCM-41 material after treatment with distilled water. Figures 4.3.B and 4.3.C represent similar UV-Vis spectra obtained from NH_2-MCM-41 and SH-MCM-41 materials, respectively. A strong absorption at *ca.* 540 nm was observed for all the mesoporous materials after treatment with $HAuCl_4$ solution and is a clear indication of reduction of the $AuCl_4^-$ ions by all the three materials, *viz*., Si-MCM-41 (Fig. 4.3.A, curve b), NH_2-MCM-41 (Fig. 4.3.B, curve b), and SH-MCM-41 (Fig. 4.3.C, curve b). This resonance is clearly

absent in the parent Si-MCM-41 (Fig. 4.3.A, curve a), NH_2-MCM-41 (Fig. 4.3.B, curve a) and SH-MCM-41 (Fig. 4.3.C, curve a) materials as expected.

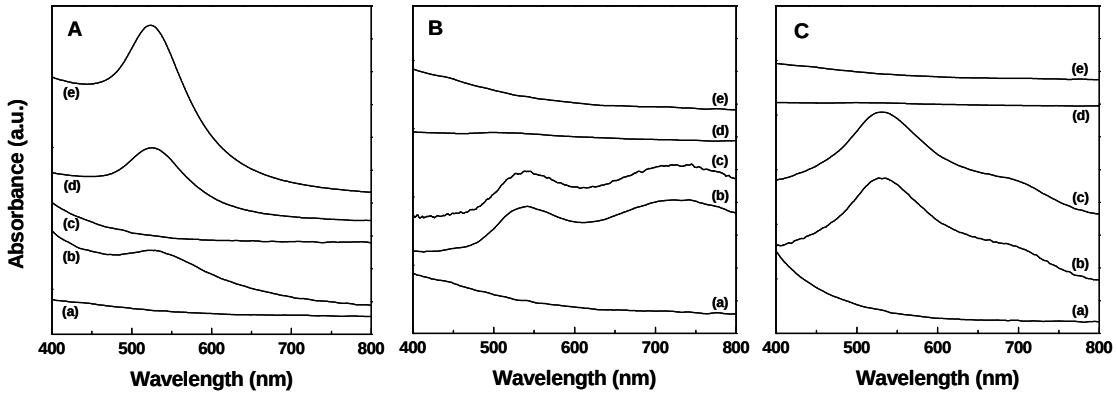

Figure 4.3. UV-Vis spectra recorded from (A) (a) Si-MCM-41, (b) nano-Au-Si-MCM-41, (c) Au-Si-MCM-41-w, (d) filtrate obtained from Si-MCM-41 after treatment with $AuCl_4^-$, and (e) filtrate obtained from nano-Au-Si-MCM-41 after aqueous treatment; (B) (a) NH_2-MCM-41, (b) nano-Au-NH_2-MCM-41, (c) Au-NH_2-MCM-41-w, (d) filtrate obtained from NH_2-MCM-41 after treatment with $AuCl_4^-$, and (e) filtrate obtained from nano-Au-NH_2-MCM-41 after aqueous treatment; and (C) (a) SH-MCM-41, (b) nano-Au-SH-MCM-41, (c) Au-SH-MCM-41-w, (d) filtrate obtained from SH-MCM-41 after treatment with $AuCl_4^-$, and (e) filtrate obtained from nano-Au-SH-MCM-41 after aqueous treatment.

An interesting observation is the presence of additional resonances at *ca*. 725 nm and at *ca.* 710 nm in the case of the nano-Au-NH_2-MCM-41 (Fig. 4.3.B, curve b) and nano-Au-SH-MCM-41 (Fig. 4.3.C, curve b) materials, respectively. This feature arises due to excitation of longitudinal surface plasmon vibrations due to close packing of the gold nanoparticles[34,35] within the mesoporous channels, which resulted from anchoring of the gold nanoparticles to the inner surfaces of siliceous matrices by the amine or thiol groups. It is known that primary amines and thiols covalently bind to gold nanoparticles,[6,7,36] and may be the binding mode in our study also.

The mode of stabilization of the gold nanoparticles formed by *in situ* reduction within the MCM-41 matrix was evaluated by treatment of the nano-Au-Si-MCM-41, nano-

Au-NH_2-MCM-41 and nano-Au-SH-MCM-41 materials with distilled water for 12 h. The UV-Vis spectra of the respective samples after aqueous treatment, namely Au-Si-MCM-41-w (curve c), Au-NH_2-MCM-41-w (curve c) and Au-SH-MCM-41-w (curve c) are shown in Figs. 4.3.A, B and C, respectively. The characteristic absorption at *ca.* 540 nm of gold nanoparticles was missing in Au-Si-MCM-41-w (Fig. 4.3.A, curve c), clearly indicating that almost all the gold nanoparticles were leached out into the aqueous phase. But the characteristic absorption of Au nanoparticles was visible in the UV-Vis spectra of the filtrate obtained from the Si-MCM-41 material after treatment with $HAuCl_4$ (Fig. 4.3.A, curve d) and that of the filtrate obtained from the nano-Au-Si-MCM-41 material after treatment with distilled water (Fig. 4.3.A, curve e). Comparing the UV-Vis spectra of the nano-Au-Si-MCM-41 material (Fig. 4.3.A, curves b and c), it can be inferred that the stabilization of the gold nanoparticles in the cavities of Si-MCM-41 was not achieved at all. However, the UV-Vis spectra of the filtrates obtained from the NH_2-MCM-41 (Fig. 4.3.B, curve d) and SH-MCM-41 (Fig. 4.3.C, curve d) materials after treatment with $HAuCl_4$, and those of the filtrates obtained from the nano-Au-NH_2-MCM-41 (Fig. 4.3.B, curve e) and nano-Au-SH-MCM-41 (Fig. 4.3.C, curve e) materials after aqueous treatment did not show any absorbance in this visible region, clearly indicating that there is no leaching of Au nanoparticles in the case of NH_2-MCM-41 and SH-MCM-41 materials. Further, the UV-Vis spectra of the Au-NH_2-MCM-41-w (Fig. 4.3.B, curve c) and Au-SH-MCM-41-w (Fig. 4.3.C, curve c) materials, which are almost similar to those of the nano-Au-NH_2-MCM-41 (Fig. 4.3.B, curve b) and nano-Au-SH-MCM-41 (Fig. 4.3.C, curve b) materials, respectively, including the respective additional absorbances at *ca.* 725 nm and *ca.* 710 nm, indicate the stabilization of the close-packing of gold nanoparticles in open, string-like networks within NH_2-MCM-41 and SH-MCM-41. These results clearly indicate the crucial

role played by the pendant organic functional groups in binding the Au nanoparticles to the mesoporous framework, thereby stabilizing them.

Since all the organo-functionalized MCM-41 materials were synthesized by the "one-pot co-condensation" method, which leads to grafting of all the organic functional groups on the inner surfaces of the mesopores,[37] quite obviously the Au nanoparticles would be stabilized within the mesopores only, and not on the outer surface, as there is no binding moiety present on the outer surface. So we can conclusively say that the Au nanoparticles are present inside the pores of the organo-functionalized MCM-41 materials, which was previously inferred from decrease in surface area and pore volume of the materials.

Table 4.2. Results of chemical analyses, and mean diameter (D) of Au nanoparticles in different nano-Au-MCM-41 composites

Sample	XPTS[a] : TEOS	N (wt %)	S (wt %)	Au (wt %)	D (nm)[b]
NH_2-MCM-41	0.17	2.33	-	3.1	3.4 ± 0.5
	0.25	3.41	-	3.2	3.4 ± 0.5
	0.4	5.52	-	3.1	3.4 ± 0.5
SH-MCM-41	0.17	-	4.91	3.2	3.2 ± 0.5
	0.25	-	7.29	3.5	3.2 ± 0.5
	0.4	-	11.70	3.2	3.2 ± 0.5

[a]XPTS = APTS or MPTS

[b]Calculated from Debye-Scherrer equation.

4.3.4. Chemical Characterization by X-Ray Fluorescence and X-Ray Photoelectron Spectroscopy

Table 4.2 summarizes the results of elemental analyses of different NH_2-MCM-41 and SH-MCM-41 materials synthesized with different XPTS : TEOS ratios, and XRF measurements of the corresponding nano-Au-NH_2-MCM-41 and nano-Au-SH-MCM-41

samples. From the table, it is evident that the concentration of Au in the silicate matrices does not significantly depend upon the population of pendant $–NH_2$ or –SH groups in the inner surfaces of MCM-41.

Figure 4.4 shows the Au 4f and N 1s core level spectra from the nano-Au-NH_2-MCM-41 material (A and B) as well as the Au 4f and S 2p core level spectra recorded from the nano-Au-SH-MCM-41 sample (C and D). Strong signals from the gold nanoparticles entrapped in the mesoporous silica matrix can be seen in both samples (Fig. 4.4.A and C). These core levels could be fit to a single spin-orbit pair indicating no chemical shifts arising due to complexation with $–NH_2$ and –SH groups in the MCM-41 matrix. The S 2p signal from the nano-Au-SH-MCM-41 sample (Fig. 4.4.D) could be satisfactorily fit to a single spin-orbit pair separated by 1.14 eV. It is interesting to note the absence of an additional high binding energy component in the S 2p spectrum at *ca.* 168 eV that is often observed in self-assembled monolayers of alkanethiols on silver alloy surfaces.[38] The fact that this component is not observed indicates that the thiol groups are not oxidized to a sulfonate species and that complexation with gold nanoparticles stabilizes them. The N 1s signal from the nano-Au-NH_2-MCM-41 sample (Fig. 4.4.B) shows the presence of two distinct chemical species having binding energies of 399 and 402.4 eV, respectively. The low binding energy component is assigned to nitrogen in the pendant amine groups directly bound to the entrapped gold nanoparticles, while the higher binding energy component arises due to electron emission from nitrogen in protonated amine pendant groups. Similar binding energies have been observed in earlier studies on Langmuir-Blodgett films of octadecylamine in a partially ionized state.[39] These protonated ammonium groups cannot bind to the gold nanoparticle surface.

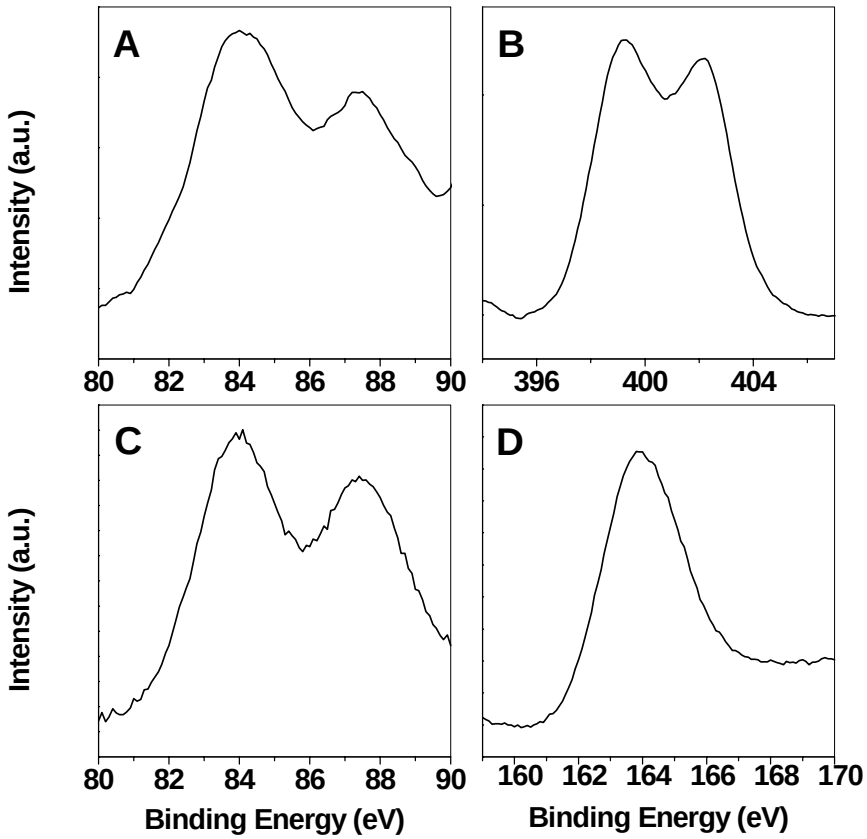

Figure 4.4. (A) Au 4f and (B) N 1s core level spectra recorded from the nano-Au-NH_2-MCM-41 material; (C) Au 4f and (D) S 2p spectra recorded from the nano-Au-SH-MCM-41 material.

4.3.5. Transmission Electron Microscopy

The TEM images of the nano-Au-NH_2-MCM-41 and nano-Au-SH-MCM-41 samples are given in Figure 4.5, inset of Fig. 4.5.A showing a selected area electron diffraction (SAED) pattern of the corresponding sample. The parallel fringes due to side-on view of the long pores of MCM-41 are well visible in the images. These equidistant parallel fringes are characteristic features of separate layers, the addition of which results in the formation of a bunch of layers. The SAED pattern of the sample exhibits well-defined hexagonal maxima, further confirming periodicity of the structure. The entrapped gold nanoparticles are visible in the figures (highlighted by arrows), which shows that the spatial

distribution of the nanoparticles in the perpendicular direction to the channels is consistent with the pore spacing.

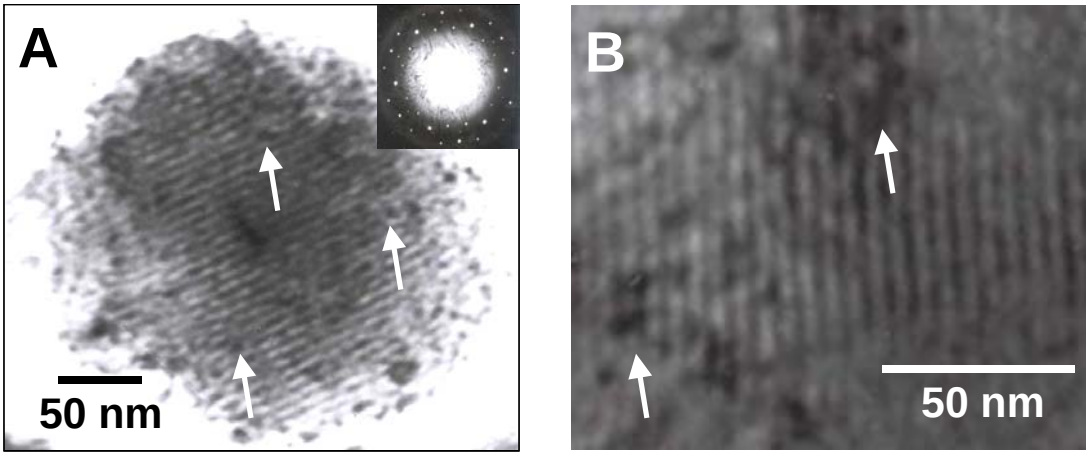

Figure 4.5. Representative TEM images of (A) nano-Au-NH_2-MCM-41 (inset showing the selected area electron diffraction pattern), and (B) nano-Au-SH-MCM-41 samples. The arrows in the figures identify gold nanoparticles within the pores.

4.3.6. Thermal Analyses

Figure 4.6 (left axis) shows the TGA data recorded from (A) the SH-MCM-41 sample after removal of surfactant, (B) the nano-Au-SH-MCM-41 material, (C) the NH_2-MCM-41 sample after removal of surfactant, and (D) the nano-Au-NH_2-MCM-41 material. The principal features in the TGA curves for all the materials are almost similar. The significant weight loss at *ca*. 330 °C in all the cases can be attributed to decomposition of the propylthiol or propylamine groups from the framework. Significant differences are observed in the DTA curves for the parent and gold containing SH-MCM-41 or NH_2-MCM-41 materials in the high temperature region. An exothermic process is observed at *ca*. 440 °C for the nano-Au-SH-MCM-41 (Fig. 4.6.B, right axis) and nano-Au-NH_2-MCM-41 (Fig. 4.6.D, right axis) samples, which is clearly absent in the parent materials (right axes of Figs. 4.6.A and C, respectively).

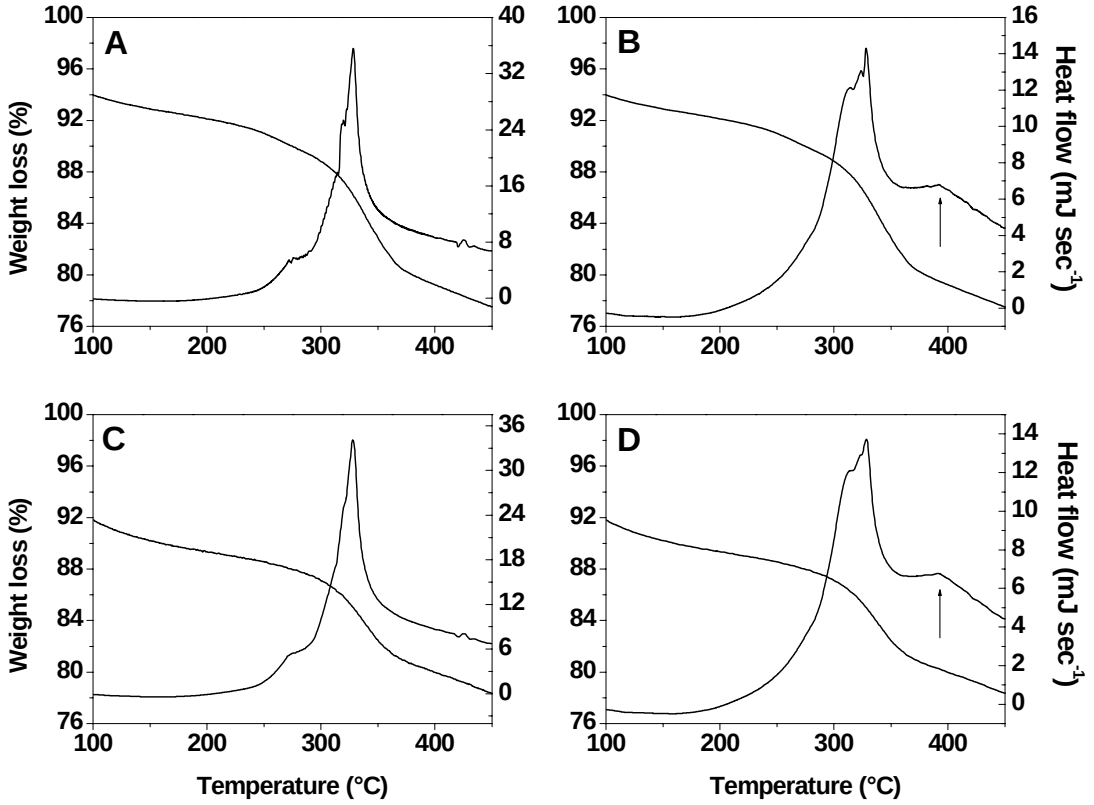

Figure 4.6. TGA curve (left axis) and DTA curve (right axis) for the (A) SH-MCM-41, (B) nano-Au-SH-MCM-41, (C) NH_2-MCM-41, and (D) nano-Au-NH_2-MCM-41 materials.

This exothermic process is not accompanied by a detectable weight loss as evidenced from TGA data. This exothermic reaction occurred due to sintering of the gold nanoparticles within the porous framework. The decomposition of the amine or thiol groups at *ca*. 330 °C facilitates diffusion of the free Au nanoparticles within the porous network and thereafter, sintering. This is clearly indicative of cross-linking of the colloidal gold nanoparticles, which opens a new strategy for the formation of nanoparticle–superstructures with controllable geometry.[40]

4.4. PROBABLE MECHANISM OF NANOPARTICLE FORMATION

It is pertinent to mention here the work of Esumi *et al.*,[19] who have demonstrated that the reduction of chloroaurate ions by sugar balls (sugar persubstituted

poly(amidoamine) dendrimers, containing large amount of hydroxyl groups on the outer surface) occurs *via* the hydroxyl groups in the sugars; the hydroxyl groups being converted to carbonyl groups thereafter. Although, unlike alcoholic group, the silanol groups cannot be oxidized, the reduction of the chloroaurate ions within the pores of the mesoporous material may well occur through silanol groups on the surface of the siliceous materials, followed by stabilization of the gold nanoparticles thus formed by the pendant organic functionality. That the silanol groups are responsible for the reduction process is borne out by the fact that amorphous (fumed) silica can also form surface bound gold nanoparticles in similar conditions, and concentration of gold on silica depends on the number of silanol groups present on the silica surface.[22,23] However, the concentration of gold in the MCM-41 matrices does not depend on the population of pendant organic functional groups, as evidenced from Table 4.2. This clearly indicates that the pendant organic functional groups do not influence the reduction process. Therefore it is worthwhile to consider a probable mechanism as depicted in Scheme 4.2. It seems likely that the reduction of Au^{3+} to Au^0 takes place *via* chloride ions, which in turn may be oxidized to Cl_2. In this section we shall try to prove this contention experimentally.

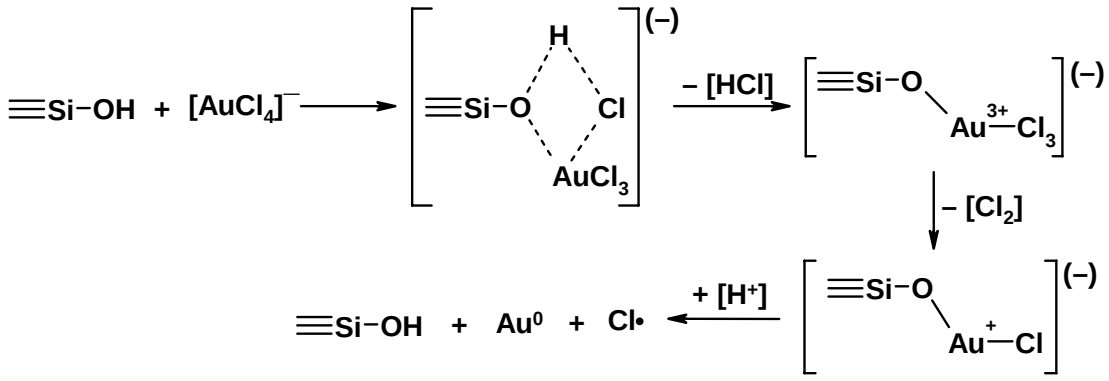

Scheme 4.2. Probable pathway for the formation of surface bound gold nanoparticles.

4.4.1. Formation of Gold Nanoparticles by Amorphous Silica

In this section, formation of gold nanoparticles by *in situ* reduction of aqueous chloroaurate ions by a purely inorganic host matrix will be illustrated. Aqueous chloroaurate ions when treated with fumed silica form gold nanoparticles subsequently bound fairly strongly to the fumed silica surface. The concentration and optical properties of gold nanoparticles are observed to be dependent on surface hydroxyl group concentration. It will also be shown that the size of the nanoparticles thus formed could be controlled by addition of alkylamine molecules, particle size being dependent on concentration of alkylamine and alkyl chain length.

Fumed silica samples with different concentrations of surface hydroxyl groups were prepared by treatment of fumed silica with dilute HCl for different durations (Table 4.3). The concentration of surface silanol groups in the different fumed silica samples was determined by a modified Fripiat and Uytterhoeven method,[24] and the results are summarized in Table 4.3. It is clearly seen from the table that there is a uniform increase in the surface hydroxyl concentration as the time of reaction of fumed silica with HCl increases. The experimental conditions and designation of the samples prepared from autoreduction of $AuCl_4^-$ ions by the fumed silica samples with different silanol concentration in presence or absence of alkylamine molecules are summarized in Table 4.3.

4.4.2. Chemical Analyses by X-Ray Fluorescence

The Au/Si weight ratios of different fumed silica–gold nanocomposites, measured from XRF, are given in Table 4.3. It was manifested that concentration of gold on silica surface increases with increasing concentration of surface hydroxyl groups (Table 4.3, samples SiAu1 to SiAu5). This indeed confirms the active participation of surface silanol groups in the autoreduction of chloroaurate ions to form the Au nanoparticles.

Table 4.3. Concentration of silanol groups, Au content and mean diameter (D) of Au nanoparticles on different fumed silica surfaces

Time of HCl treatment (h)	Surface silanol concentration (mmol g^{-1})	Alkylamine added[a]	Concentration of alkylamine (M)	Sample name	Au/Si (w/w)	D (nm)[c]
0	0.58	-	-	SiAu1	0.03	n. d.[d]
1	0.85	-	-	SiAu2	0.04	n. d.
6	2.96	-	-	SiAu3	0.05	n. d.
12	3.5	-	-	SiAu4	0.07	n. d.
24	4.77	-	-	SiAu5	0.09	17.2
24	-	DDA	10^{-1}	SiAuDDA1	0.09	10.0
24	-	DDA	10^{-3}	SiAuDDA3	0.10	15.9
24	-	DDA	10^{-6}	SiAuDDA6	0.08	18.8
24	-	NOA	10^{-3}	SiAuNOA3	0.09	21.3
24	-	ODA	10^{-3}	SiAuODA3	0.08	10.5
24[b]	-	-	-	SiAu400	0.02	20.6

[a]DDA = dodecylamine, NOA = n-octylamine, ODA = octadecylamine.

[b]Sample SiAu5 heated at 400 °C for 1 h.

[c]Calculated from Debye-Scherrer equation.

[d]n. d. = Not determined.

4.4.3. Optical Properties

The inset of Figure 4.7.A shows pictures of (A) fumed silica sample 5 before immersion in $HAuCl_4$ solution, (B) SiAu5, (C) SiAu400, and (D) SiAuDDA3 samples. It can clearly be seen that while the fumed silica sample is colorless, the other samples are colored, the colors ranging from blue (inset of Fig. 4.7.A, picture B) to a very light pink (inset of Fig. 4.7.A, picture D). These colors are clearly due to the presence of gold nanoparticles on the fumed silica surface and occur as a result of the excitation of surface plasmon vibrations in the gold nanoparticles.[41] Thus, $AuCl_4^-$ ions are spontaneously reduced in the presence of fumed silica resulting in the formation of surface-bound gold

nanoparticles. Colloidal gold solutions are normally ruby-red in color under conditions where the particles are in a dispersed state.[42] When the particles are close enough such that there is overlap of the surface plasmon vibrations between neighboring particles, the optical properties change and the solution turns blue. Such changes in the optical properties of colloidal gold solutions have been used with success in monitoring the biotin-avidin interaction process[43] as well as in the hybridization of DNA.[44] Thus, the blue color in the SiAu5 materials indicate fairly close packing of the gold particles on the silica surface. On heating, the composite turns to a light red color (inset of Fig. 4.7.A, picture C), which is indicative of reduced packing density of the gold particles. This may occur either by aggregation of gold particles leading to an effective increase in the average interparticle distance or by desorption of weakly bound gold nanoparticles on the surface of fumed silica. We strongly believe the latter mechanism is operative since XRF analyses of the concentration of gold on silica after heat treatment yielded a decrease in the Au/Si weight ratio (Table 4.3, samples SiAu5 and SiAu400). The light pink color of the SiAuDDA3 (inset of Fig. 4.7.A, picture D) sample also indicates much smaller, well-dispersed gold nanoparticles on the surface of fumed silica. The separation between the gold nanoparticles in this case is possibly stabilized by a monolayer of dodecylamine molecules bound to the surface of the gold nanoparticles.

More precise changes in the optical properties of the different nano-Au–fumed silica composites were scrutinized by UV-Vis experiments. Figure 4.7.A shows the spectra recorded from samples SiAu1 to SiAu5 (curves 1–5 respectively) and the SiAu5 sample after heat treatment (SiAu400, curve 6). A strong absorbance in the visible region of the electromagnetic radiation (around 520–540 nm, due to excitation of surface plasmon vibrations)[34,45] is observed in all the nano-Au–fumed silica samples and is responsible for pink-blue coloration of the composite materials. While the main features of the spectra of

the samples SiAu1 to SiAu4 are essentially the same (Fig. 4.7.A, curves 1–4), an additional band at *ca*. 820 nm is observed for sample SiAu5 (Fig. 4.7.A, curve 5). On heating the sample SiAu5, this band shifts to the blue to a value of *ca*. 725 nm (curve 6). This can be attributed to excitation of longitudinal surface plasmon vibrations and is a consequence of close packing of the gold nanoparticles in silicate matrix. It is also well known that the red shift in the longitudinal plasmon vibration is an indicator of the extent of aggregation of the nanoparticles.[45] The results indicate that though the concentration of surface hydroxyl groups increases monotonically for samples SiAu1 to SiAu5 (Table 4.3), close packing in terms of overlap of plasmon vibrations in the gold particles occurs only above a critical hydroxyl group concentration, which was achieved in the case of fumed silica sample 5. The shift in the longitudinal plasmon resonance from 820 nm for the SiAu5 material to 725 nm on heating indicates disruption in the close packing of the gold nanoparticles on the fumed silica surface, which certainly arose from desorption of gold nanoparticles from fumed silica surface as evident from XRF measurements (Table 4.3, sample SiAu400).

The inset of Fig. 4.7.B shows the pictures of (A) SiAuDDA1, (B) SiAuDDA3, (C) SiAuDDA6, (D) SiAuNOA3, and (E) SiAuODA3 samples. From the pictures, it is clearly seen that the color gradually changes from purple to light pink, as concentration of dodecylamine is increased from 10^{-6} M to 10^{-1} M, and as alkyl chain length increases from 8 to 18. This variation in color certainly arises from different sizes of the gold nanoparticles. That this is indeed true is borne out by XRF measurements carried out on the gold nanoparticles grown in the presence of alkylamine molecules (Table 4.3, samples SiAuDDA1–3, SiAuNOA3 and SiAuODA3), which show that the Au : Si weight ratio is essentially constant. Therefore, the change in optical properties for these materials must be attributed to size-dependent variation in the electronic structure and not to nanoparticle packing considerations.

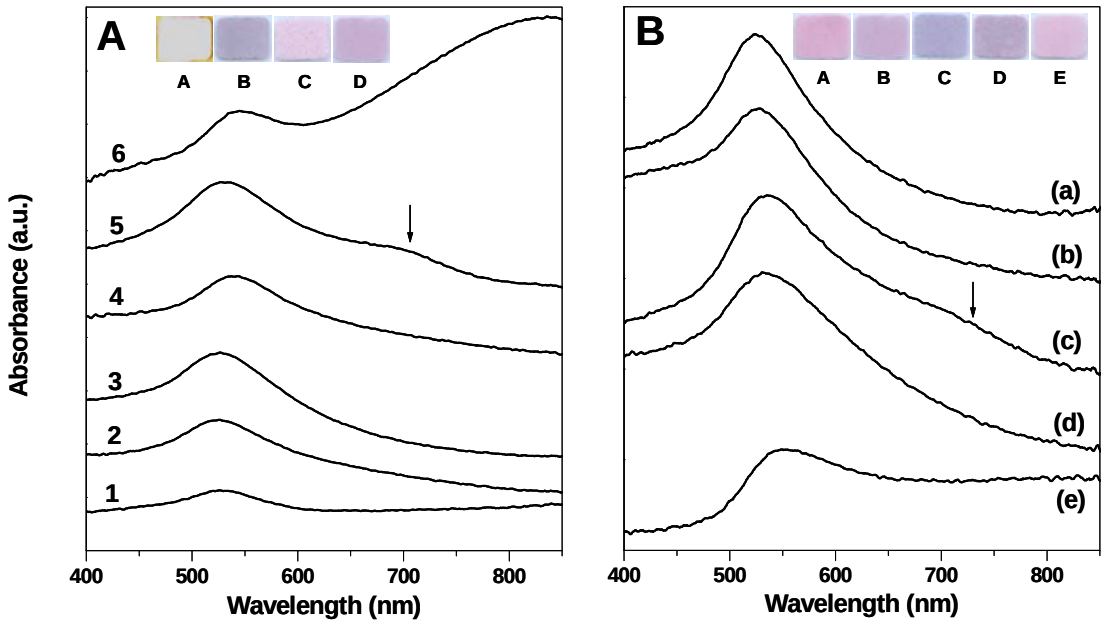

Figure 4.7. (A) UV-vis spectra recorded from fumed silica samples 1–5 after spontaneous reduction of $AuCl_4^-$ ions. The numbers of the samples are indicated next to the respective curves. The spectrum recorded from the SiAu400 material (spectrum 6) is also shown. The inset shows pictures of (A) fumed silica sample 5 before immersion in $HAuCl_4$ solution, (B) SiAu5, (C) SiAu400, and (D) SiAuDDA3 samples. (B) UV-vis spectra recorded from (a) SiAuDDA1, (b) SiAuDDA3, (c) SiAuDDA6, (d) SiAuNOA3, and (e) SiAuODA3 samples. The inset shows pictures of the corresponding samples.

Figure 4.7.B shows the UV-Vis spectra recorded from the (a) SiAuDDA1, (b) SiAuDDA3, (c) SiAuDDA6, (d) SiAuNOA3, and (e) SiAuODA3 materials. A strong absorbance at the region 520–540 nm is observed for these samples also. Further, an additional band at *ca*. 710 nm is observed for the sample SiAuDDA6, which again can be attributed to excitation of longitudinal surface plasmon vibration due to close packing of gold nanoparticles in the siliceous matrix. Previously it was stated that close packing occurs only above a critical hydroxyl group concentration that was achieved in case of SiAu5 sample, for which, we recollect, an additional band at *ca*. 820 nm was observed. The shift in the longitudinal plasmon resonance from 820 nm to 710 nm for the SiAuDDA6 sample

indicates disruption in the close packing, which may be due to formation of self-assembled monolayers of dodecylamine over the surface of gold nanoparticles, and separation of the nanoparticles on the surface of fumed silica.

The UV-Vis results clearly point to the important role played by the hydroxyl groups on the surface of fumed silica samples in the reduction of $AuCl_4^-$ ions. In this regard, we mention that when an oxide such as silica is desired as a support for some metal, the oxide should have a specific surface area ranging from 100–700 $m^2\ g^{-1}$.[46] The fumed silica material used here has a specific surface area of 384 $m^2\ g^{-1}$, which can serve the purpose of a good support for gold nanoparticles excellently. The higher concentration of silanol groups in fumed silica sample 5 leads to a higher density of Au nanoparticles on the fumed silica surface and to important changes in the optical properties of the nanocomposite (Fig. 4.7.A), thereby supporting the contention that the silanol groups are responsible for the reduction of $AuCl_4^-$ ions.

4.4.4. Transmission Electron Microscopy

The size of the gold nanoparticles formed on the surface of SiAu5 sample before heating as well as the nano-Au–fumed silica samples grown in the presence of dodecylamine molecules was estimated by transmission electron microscopy. Figure 4.8.A shows the TEM image recorded from the SiAu5 sample. A number of gold nanoparticles can clearly be seen ranging in size from 2–30 nm. The size of the nanoparticles was analyzed from this picture and the particle size histogram is plotted in Figure 4.8.B. It was observed that the particle size distribution was broad with some indication of bimodality. The smaller sized particles were found to have an average size of *ca*. 7 nm while the bigger particles were of *ca*. 16 nm dimensions. Fairly dense packing of the gold nanoparticles can be seen thus supporting the UV-Vis results presented earlier (Fig. 4.7.A, spectrum 5).

Selected area electron diffraction patterns (not shown) clearly indicated the formation of nanocrystalline gold particles on the surface of fumed silica.

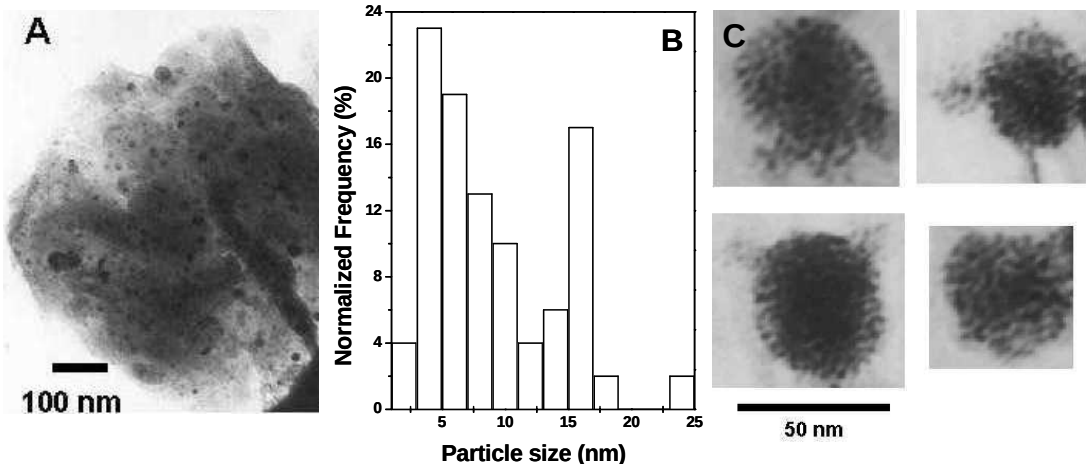

Figure 4.8. (A) TEM image of the SiAu5 sample. (B) Particle size histogram from an analysis of the gold nanoparticles shown in (A). (C) Series of four TEM images recorded from the SiAuDDA3 sample.

Figure 4.8.C shows a series of four magnified TEM images recorded from the SiAuDDA3 sample. In contrast with the TEM image recorded from the nanocomposite grown without any alkylamine molecules (Fig. 4.8.A), it is seen that the nanoparticles grown in the presence of amine molecules are smaller. An average gold nanoparticle diameter of *ca.* 3.7 ± 0.5 nm was estimated from an analysis of the TEM images shown in Fig. 4.8.C. It is obvious that the DDA molecules present in solution during the reduction of the $AuCl_4^-$ ions by fumed silica significantly reduce the size of the nanoparticles formed and lead to more monodisperse particle size distribution. This presumably occurs by formation of a self-assembled monolayer of the amine molecules on the surface of the gold nanoparticles during the initial nucleation and growth stage of the nanoparticles. The dodecylamine monolayer thus limits the growth of the nanoparticles and stabilizes the particle size distribution and is an important result of this investigation.

4.4.5. Powder X-Ray Diffraction

The size of the gold nanoparticles was also estimated from the X-ray diffraction line width broadening of the (111) Bragg reflection of gold by applying the Debye-Scherrer equation.[25] Figure 4.9.A shows the XRD patterns recorded from the samples (a) SiAuDDA1, (b) SiAuDDA3, (c) SiAuDDA6, (d) SiAu5, and (e) SiAu400, in the 2θ range of 36–40°. Figure 4.9.B shows the XRD patterns recorded from the samples (a) SiAuNOA3, (b) SiAuDDA3, and (c) SiAuODA3, the solid lines being the Lorentzian fits to the respective curves. Under the experimental conditions of the XRD measurements (small slit-width and monochromatized Cu K_α radiation) it was felt that the XRD line-shape would be better approximated by a Lorentzian than a Gaussian. Indeed, poorer chi-square error values, which denote goodness of the fit, were observed while fitting the (111) Bragg reflection of Au to a Gaussian line-shape. The (111) Bragg reflection from the gold nanoparticles at $2\theta = 38.2°$ is clearly observed in all the samples. From the broadening of the (111) reflection in the XRD patterns, the size of the gold particles was estimated (listed in Table 4.3). It is observed that the width of the Bragg reflection is considerably reduced after the heat treatment (compare curves d and e, Fig. 4.9.A). This indicates sintering of the gold nanoparticles on heating at 400 °C, which could not be inferred from UV-Vis experiments alone, which only indicated a reduction in the density of the gold nanoparticles on the fumed silica surface after the annealing process. Comparing the broadening of the curves a, b and c in Fig. 4.9.A, and that of the curves a, b and c in Fig. 4.9.B, it can be inferred that diameter of the gold particles depend on concentration and alkyl chain length of the alkylamines.

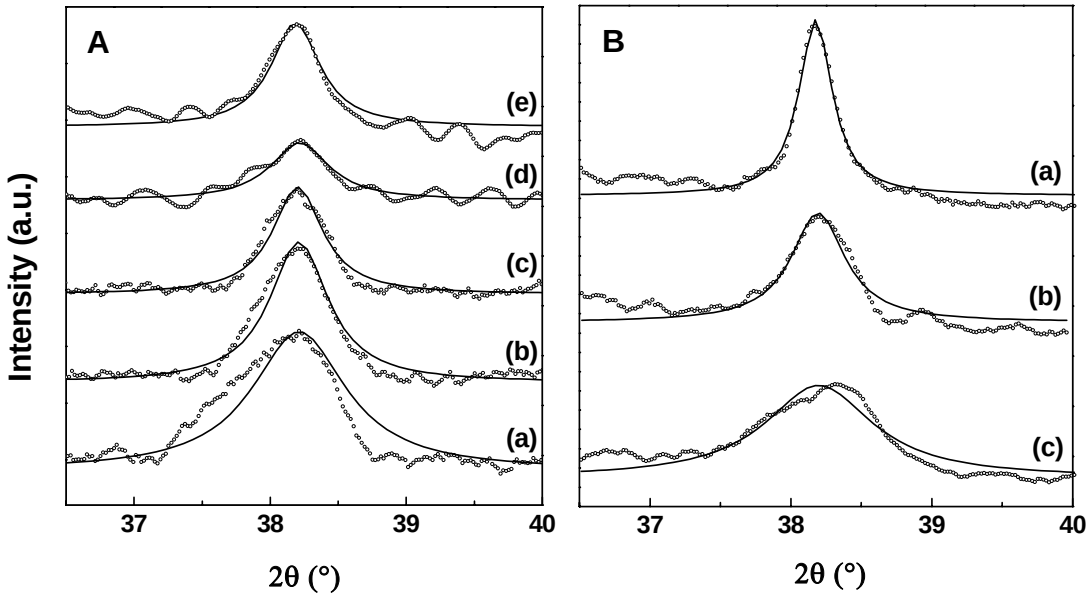

Figure 4.9. Powder XRD patterns recorded from (A) (a) SiAuDDA1, (b) SiAuDDA3, (c) SiAuDDA6, (d) SiAu5, and (e) SiAu400; (B) (a) SiAuNOA3, (b) SiAuDDA3, and (c) SiAuODA3 samples. Solid lines indicate Lorentzian fits to the respective curves.

4.5. CATALYTIC ACTIVITIES OF SUPPORTED GOLD NANOPARTICLES

It is pertinent to mention here that the size of the supported gold nanoparticles is consistent with the size range where gold nanoparticles show excellent catalytic activity in a variety of reactions as reviewed by Bond and Thompson.[12] Hence, our approach for the preparation of supported gold nanoparticles on siliceous matrices offers distinct advantages in exploiting the catalytic potential of these materials, as will be demonstrated in this section.

4.5.1. Preferential Oxidation of CO in H_2 Rich Reformates

In present day catalytic research, selective removal of CO from streams containing an excess of H_2 and significant amounts of CO_2 and H_2O is a potential challenge, especially for preparation of H_2 feeds that are suitable for polymer electrolyte membrane fuel cells

(PEMFC).[47,48] H_2 is usually generated from hydrocarbons or alcohols by steam reforming followed by water-gas shift reaction.[49] Typical effluents from such a process contain about 0.3–1.0% of CO in a large excess of H_2 (40–75%) and about 20–25% CO_2. CO levels, however, have to be reduced to below 100 ppm and preferably, below 10 ppm for use in PEMFC.[47] Preferential oxidation (PROX) of CO to CO_2 without simultaneous oxidation of H_2 to H_2O is one of the solutions.[50] However, the latter reaction is more exothermic and hence, favored at higher temperatures. Therefore, selective catalysts that are active at lower temperature for CO oxidation are required for this purpose.

It was established that gold nanoparticles (of *ca*. 3–4 nm size) supported on certain oxides exhibit surprisingly high catalytic activity in oxidation of CO at or below ambient temperatures.[11,13] The Au-MCM-41 nanocomposites synthesized by the *in situ* reduction method, therefore, were our automatic choice for the PROX reaction. The catalytic activity of the SiAu5 sample was also tested for comparison.

The summary of the results of preferential oxidation of CO by the Au-MCM-41 and Au-SiO_2 nanocomposites is presented in Table 4.4. PROX selectivity is defined as (O_2 consumed in oxidation of CO) × (total O_2 consumed in oxidation of CO and H_2)$^{-1}$ × 100. Under our reaction conditions oxidation of CH_4 was not observed. From the table, it is evident that the Au-SiO_2 nanocomposite (sample SiAu5) is least catalytically active in CO oxidation, obviously due to larger sizes of Au nanoparticles on silica surfaces. Smaller sized particles can allow more number of reactant molecules to become chemisorbed per unit surface area.

The influence of temperature on the catalytic activity and selectivity of the nano-Au-MCM-41 and SiAu5 materials is presented in Figure 4.10. It was observed that the nano-Au-NH_2-MCM-41 and nano-Au-SH-MCM-41 catalysts have comparable catalytic activity

in CO oxidation, probably due to equivalent sizes of gold nanoparticles in both the materials. And the activity of the SiAu5 catalyst is very low, as expected.

Table 4.4. Preferential oxidation of CO[a] over Au-MCM-41 and Au–fumed silica nanocomposites

Catalyst	Conversion of CO (%)	Conversion of H_2 (%)	CO Selectivity (%)[b]
nano-Au-NH_2-MCM-41	50.6	1.0	38.85
nano-Au-SH-MCM-41	43.6	1.0	38.66
SiAu5	19.7	1.0	37.17

[a]Reaction conditions: Catalyst = 0.5 g. Feed = H_2 (74.17%) + CO (0.49%) + CO_2 (23.26%) + CH_4 (2.08%). Temperature = 200 °C. O_2/CO = 1.25. GHSV = 5000 h^{-1}. Run time = 5 h.
[b]CO selectivity = (O_2 consumed in oxidation of CO) × (total O_2 consumed in oxidation of CO and H_2)$^{-1}$ × 100.

The catalytic activity of the nano-Au-MCM-41 samples increases with temperature and approaches a maximum at 175–200 °C. Beyond 200 °C temperature, the activity for CO oxidation decreases. This may be due to either of the two reasons: (i) the rate of oxidation of H_2 increases at higher temperatures, since this reaction is more exothermic; or (ii) sintering of Au nanoparticles occurs at and above 200 °C. However, the selectivity for CO oxidation remains essentially the same in the entire temperature range.

The effect of time on stream on the conversion and selectivity of CO oxidation by the nano-Au-MCM-41 catalysts was given in Figure 4.11. It was observed that the activity of the catalysts for CO oxidation increases markedly with an increase in time on stream and reached a maximum beyond 5 h reaction time. However, the selectivity of CO oxidation remains almost constant with increase in time on stream.

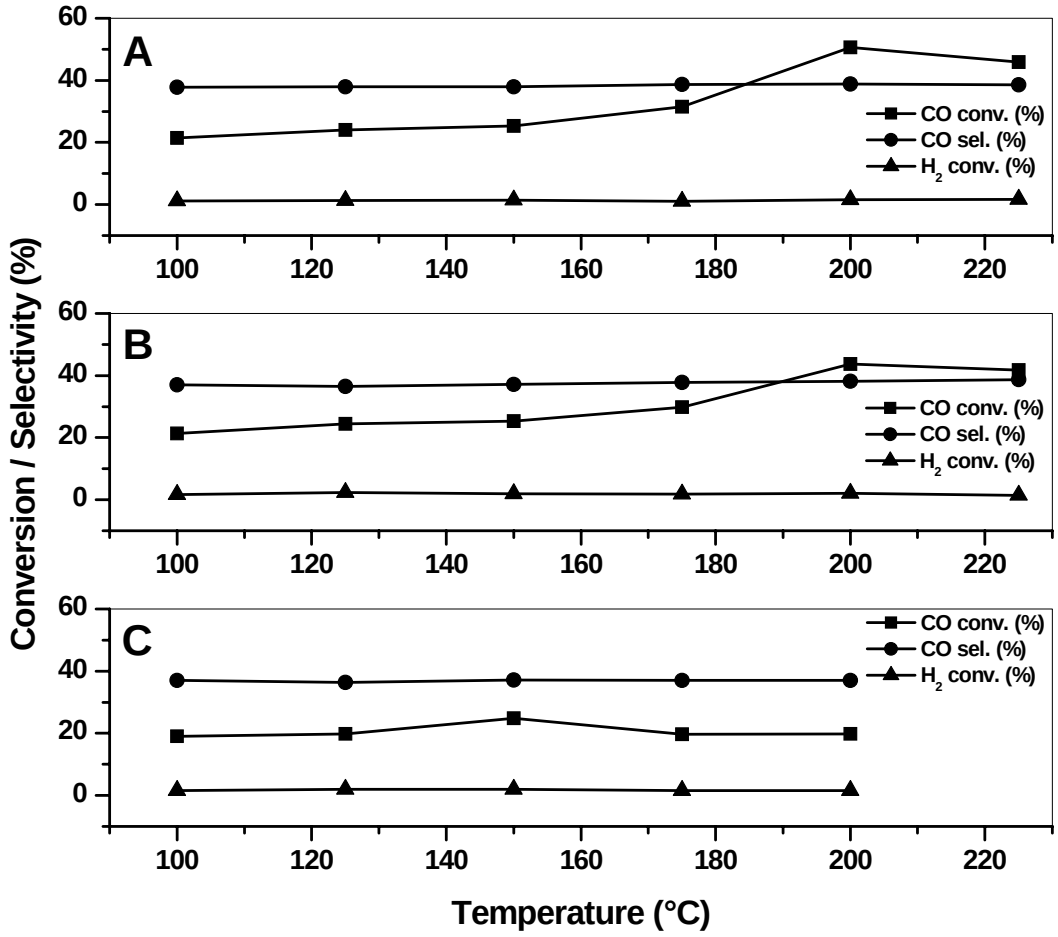

Figure 4.10. Influence of temperature on conversion and selectivity in oxidation of CO by (A) nano-Au-NH_2-MCM-41, (B) nano-Au-SH-MCM-41, and (C) SiAu5 composites. Reaction conditions: Catalyst = 0.5 g. Feed = H_2 (74.17%) + CO (0.49%) + CO_2 (23.26%) + CH_4 (2.08%). O_2/CO = 1.25. GHSV = 5000 h^{-1}. Run time = 5 h.

Figure 4.12 represents the influence of O_2/CO ratio on the conversion and selectivity in CO oxidation by the (A) nano-Au-NH_2-MCM-41 and (B) nano-Au-SH-MCM-41 materials. It was experienced that the activity of the catalysts for CO oxidation increases with an increase in O_2/CO ratio and reached an optimum value at O_2/CO = 2. The selectivity towards CO oxidation is very high (*ca*. 93%) at O_2/CO = 0.5. However, the selectivity decreases radically with an increase in O_2/CO ratio.

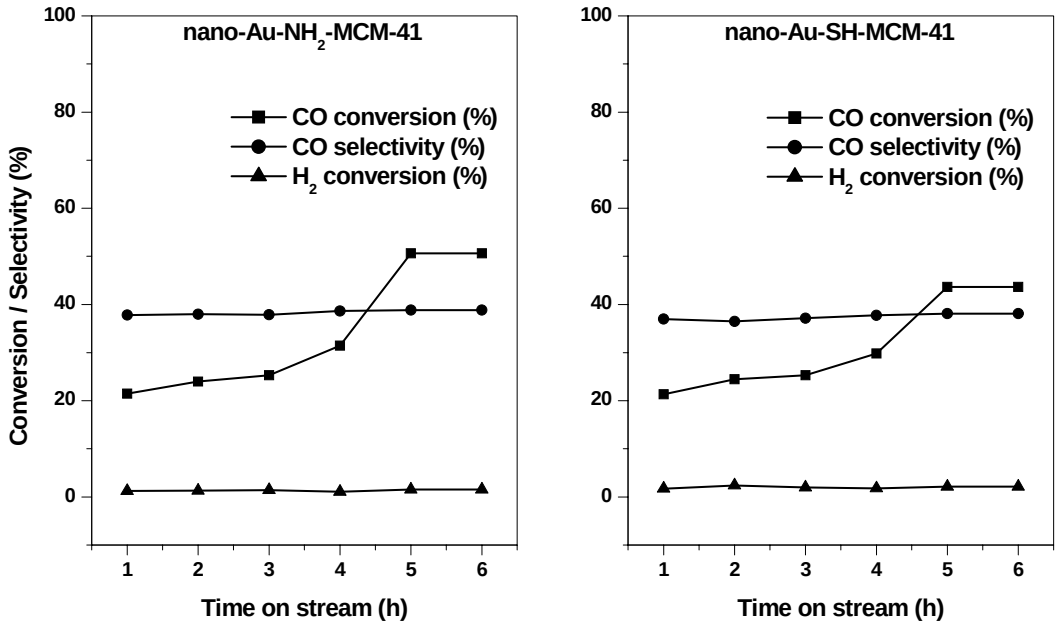

Figure 4.11. Influence of time on stream on PROX activity and selectivity by the nano-Au-NH_2-MCM-41 and nano-Au-SH-MCM-41 catalysts. Reaction conditions: Catalyst = 0.5 g. Feed = H_2 (74.17%) + CO (0.49%) + CO_2 (23.26%) + CH_4 (2.08%). Temperature = 200 °C. O_2/CO = 1.25. GHSV = 5000 h^{-1}.

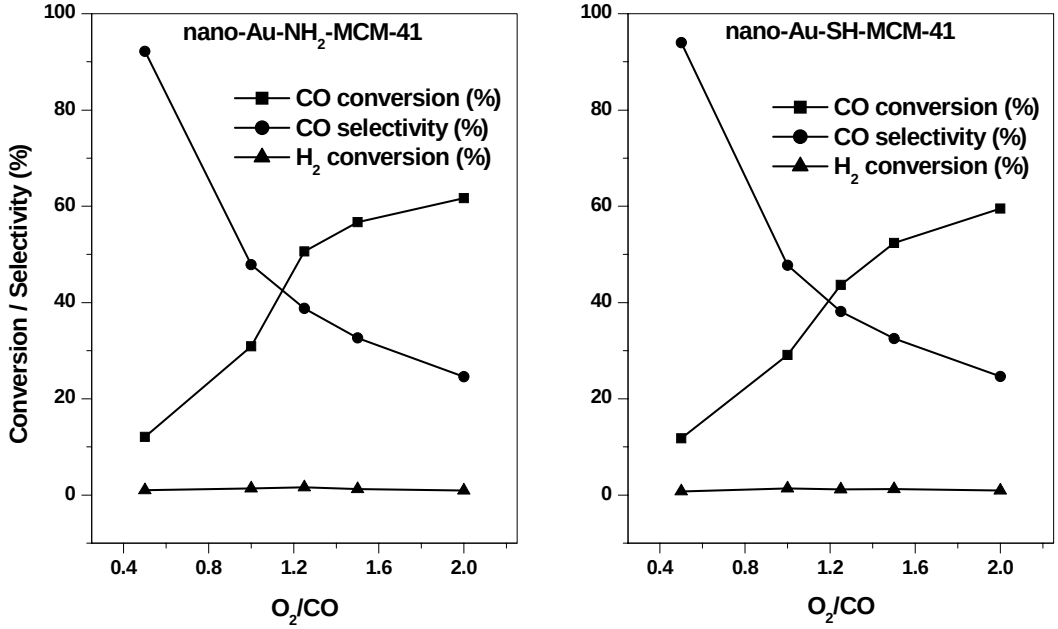

Figure 4.12. Effect of O_2/CO ratio on conversion of CO and H_2 and selectivity towards CO oxidation by the nano-Au-NH_2-MCM-41 and nano-Au-SH-MCM-41 hybrid materials. Reaction conditions: Catalyst = 0.5 g. Feed = H_2 (74.17%) + CO (0.49%) + CO_2 (23.26%) + CH_4 (2.08%). Temperature = 200 °C. GHSV = 5000 h^{-1}. Run time = 5 h.

4.5.2. Hydrogenation of Unsaturated Hydrocarbons

There are ample references in the literature where hydrogenation of linear alkenes has been reported to occur on gold nanoparticles supported on silica[51-53] and alumina[51] at moderate temperature, catalytic activity depending on particle size and nature of support. The supported nanosized gold particles synthesized by *in situ* reduction of aqueous chloroaurate ions were employed in the catalytic hydrogenation of different unsaturated hydrocarbons at different reaction conditions. The results are given in Tables 4.5 and 4.6.

The conversion of 1-hexene in the final reaction mixture, and mean diameter of gold nanoparticles in different supports are summarized in Table 4.5. It was observed that the nano-Au-NH_2-MCM-41 and nano-Au-SH-MCM-41 materials have similar catalytic activity, certainly due to the comparable sizes of Au nanoparticles in the materials. All these three materials have far better activity than the fumed silica–nano-Au composites, obviously due to the greater Au nanoparticle sizes in the fumed silica matrices, since smaller sized particles have more available space for the reactant molecules to get adsorbed onto the surface. The effect of reaction time on conversion is shown in Figure 4.13.A, from which it was observed that conversion of 1-hexene increases with time and reaches an optimum value thereafter. The reactions were carried out at 150 °C under 5.5 MPa pressure of H_2.

The influence of temperature on catalytic activity of nano-Au-MCM-41 hybrid materials is presented in Figure 4.13.B. The reactions were carried out under 5.5 MPa H_2 pressure for 6 h. The temperature has a marked effect on the conversion of 1-hexene, and as expected, conversion increases with temperature.

Figure 4.13.C shows the influence of H_2 pressure on the conversion of 1-hexene. The reactions were carried out at 150 °C for 6 h. It was observed that conversion markedly increases with pressure.

Table 4.5. Hydrogenation of 1-hexene on different supported gold catalysts[a]

Catalysts	Mean diameter of Au nanoparticles (nm)	Conversion of 1-hexene (mol. %)
nano-Au-NH_2-MCM-41	3.4 ± 0.5	18.5
nano-Au-SH-MCM-41	3.2 ± 0.5	18.7
SiAu5	17.2 ± 0.5	6.8
SiAu400	20.6 ± 0.5	7.2
SiAuDDA1	10.0 ± 0.5	8.7
SiAuDDA3	15.9 ± 0.5	7.6
SiAuDDA6	18.8 ± 0.5	9.6
SiAuNOA3	21.3 ± 0.5	5.1
SiAuODA3	10.5 ± 0.5	8.3

[a]Reaction conditions: Substrate = 10 mmol; Catalyst = 200 mg; Solvent = Toluene, 30 mL; Temperature = 150 °C; H_2 pressure = 5.5 Mpa; Duration = 6 h.

Table 4.6. Results of catalytic hydrogenation of different olefinic substrates[a] by nano-Au-MCM-41 materials

Catalyst	Substrate	Conversion (mol. %)	Selectivity (%)[b]
nano-Au-NH_2-MCM-41	Cyclohexene	8.9	100
	1-Hexene	18.5	100
	1-Octene	13.5	100
nano-Au-SH-MCM-41	Cyclohexene	9.7	100
	1-Hexene	18.7	100
	1-Octene	12.9	100

[a]Reaction conditions: Substrate = 10 mmol; Catalyst = 200 mg; Solvent = Toluene, 30 mL; Temperature = 150°C; H_2 pressure = 5.5 MPa; Duration = 6 h.

[b]Selectivity for cyclohexane, n-hexane and n-octane respectively.

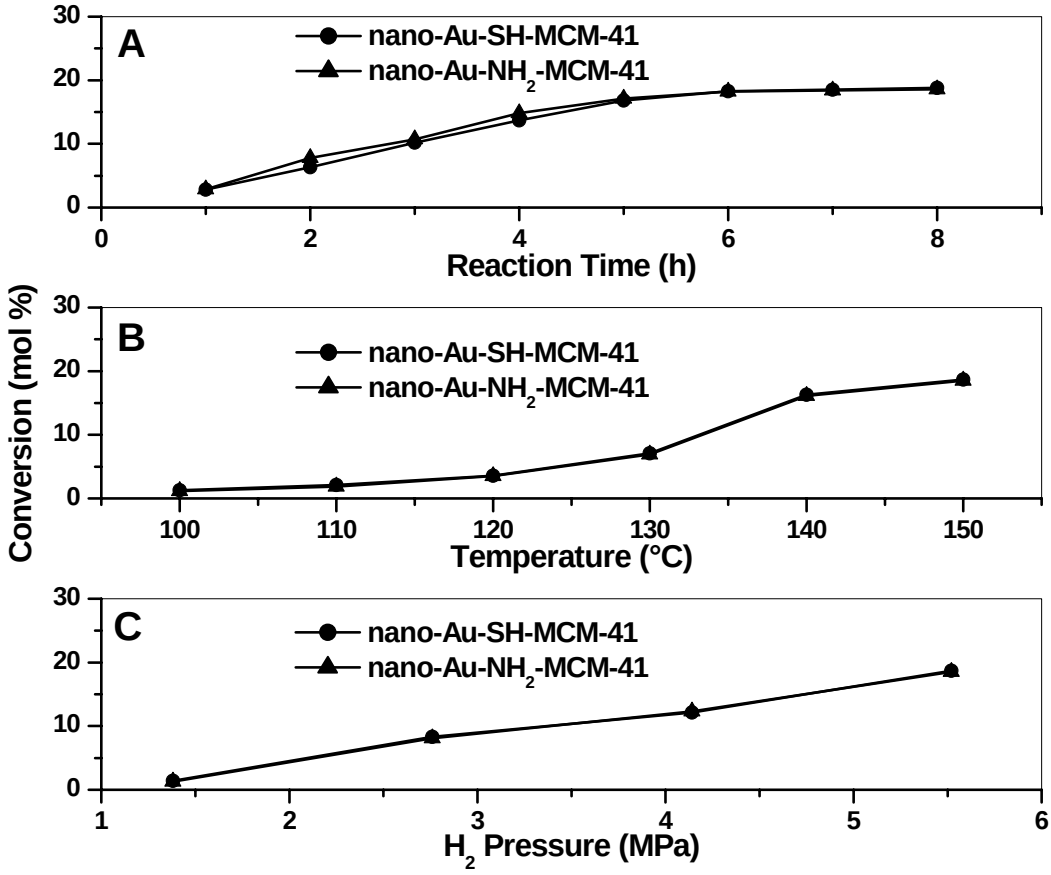

Figure 4.13. Hydrogenation of 1-hexene over nano-Au-MCM-41: (A) Influence of reaction time, (B) influence of temperature, and (C) influence of H_2 pressure over conversion.

From the results, it can be concluded that gold nanoparticles can be conveniently synthesized and stabilized in siliceous matrices, ordered mesoporous or amorphous, by a new *in situ* reduction method. The silanol groups present on the surface of host matrices are responsible for the formation of the nanoparticles. The gold nanoparticles supported on surface modified mesoporous silica exhibit better catalytic activity in oxidation of CO and in hydrogenation of unsaturated hydrocarbons than the gold–fumed silica nanocomposites. This makes the nano-Au-MCM-41 materials budding systems for future applications in catalysis.

4.6. REFERENCES

1. M. Valden, X. Lai, D. W. Goodman, *Science* **1998**, *281*, 1647.
2. G. Markovich, C. P. Collier, S. E. Henrichs, F. Remacle, R. D. Levine, J. R. Heath, *Acc. Chem. Res.* **1999**, *32*, 415.
3. J. Kunther, R. Seshadri, G. Nelles, W. Assenmacher, H. -J. Butt, W. Mader, W. Tremel, *Chem. Mater.* **1999**, ***11***, 1317.
4. G. W. Hacker, C. Hauser-Kronberger, I. Zehbe, H. Su, A. Schiechl, O. Dietze, R. Tubbs, *Cell Vision* **1997**, *4*, 54.
5. C. M. Niemeyer, *Angew Chem. Int. Ed.* **2001**, *40*, 4128.
6. M. Brust, M. Walker, D. Bethell, D. J. Schiffrin, R. Whyman, *J. Chem. Soc., Chem. Commun.* **1994**, 801.
7. D. V. Leff, L. Brandt, J. R. Heath, *Langmuir* **1996**, *12*, 4723.
8. D. H. Gracias, J. Tien, T. L. Breen, C. Hsu, G. M. Whitesides, *Science* **2000**, *289*, 1170.
9. K. Moller, T. Bein, *Chem. Mater.* **1998**, *10*, 2950.
10. B. Hammer, J. Norskov, *Nature* **1995**, *376*, 238.
11. M. Haruta, *Catal. Today* **1997**, *36*, 153.
12. G. C. Bond, D. T. Thompson, *Catal. Rev. -Sci. Eng.* **1999**, *41*, 319.
13. M. Haruta, M. Date, *Appl. Catal. A: General* **2001**, *222*, 423.
14. S. Galvagno, G. Parravano, *J. Catal.* **1978**, *55*, 178.
15. D. Guillemot, V. Y. Borovkov, V. B. Kazansky, M. Polisset-Thfoin, J. Fraissard, *J. Chem. Soc., Faraday Trans.* **1997**, *93*, 3587.
16. M. Haruta, N. Yamada, T. Kobayashi, S. Ijima, *J. Catal.* **1989**, *115*, 301.
17. M. Haruta, S. Tsubota, T. Kobayashi, H. Kageyama, M. J. Genet, B. Delmon, *J. Catal.* **1993**, *144*, 175.
18. R. V. Parish, *Gold Bull.* **1998**, *31*, 14.

19. K. Esumi, T. Hosoya, A. Suzuki, K. Torigoe, *Langmuir* **2000**, *16*, 2978.

20. P. Mukherjee, A. Ahmad, D. Mandal, S. Senapati, S. R. Sainkar, M. I. Khan, R. Ramani, R. Pasricha, P. V. Ajayakumar, M. Alam, M. Sastry, R. Kumar, *Angew. Chem. Int. Ed.* **2001**, *40*, 3585.

21. A. Ghosh, C. R. Patra, P. Mukherjee, M. Sastry, R. Kumar, *Microporous Mesoporous Mater.* **2003**, *58*, 201.

22. P. Mukherjee, C. R. Patra, A. Ghosh, R. Kumar, M. Sastry, *Chem. Mater.* **2002**, *14*, 1678.

23. R. Kumar, A. Ghosh, C. R. Patra, P. Mukherjee, M. Sastry, in: *Nanotechnology in Catalysis*, *Vol. 1*, Eds: B. Zhou, S. Hermans, G. A. Somorjai, Kluwer Academic/Plenum Publishers, New York, **2004**, Chapter 6, pp. 111–136.

24. J. J. Fripiat, J. Uytterhoeven, *J. Phys. Chem.* **1962**, *66*, 800.

25. R. C. Rau, in: *Advances in X-ray Analysis*, *Vol. 5*, Ed: W. M. Mueller, Sir Isaac Pitman & Sons Ltd., London, **1962**, pp. 104–116.

26. S. Brunauer, P. H. Emmett, E. Teller, *J. Am. Chem. Soc.* **1938**, *60*, 309.

27. E. P. Barrett, L. G. Joyner, P. P. Halenda, *J. Am. Chem. Soc.* **1951**, *73*, 373.

28. D. A. Shirley, *Phys. Rev. B* **1972**, *5*, 4709.

29. S. J. Gregg, K. S. W. Sing, *Adsorption, Surface Area and Porosity*, Academic Press, London, **1967**, Chapter 3, pp. 121–194.

30. C. -Y. Chen, H. -X. Li, M. E. Davis, *Microporous Mater.* **1993**, *2*, 17.

31. X. Chen, L. Huang, Q. Li, *J. Phys. Chem. B* **1999**, *103*, 4212.

32. S. Underwood, P. Mulvaney, *Langmuir* **1994**, *10*, 3427.

33. S. Link, M. A. El-Sayed, *J. Phys. Chem. B* **1999**, *103*, 4212.

34. C. G. Blatchford, J. R. Campbell, J. A. Creighton, *Surf. Sci.* **1982**, *120*, 435.

35. K. S. Mayya, V. Patil, M. Sastry, *Langmuir* **1997**, *13*, 3944.

36. M. D. Porter, T. B. Bright, D. L. Allara, C. E. D. Chidsey, *J. Am. Chem. Soc.* **1987**, *109*, 3559.

37. S. L. Burkett, S. D. Sims, S. Mann, *Chem. Commun.* **1996**, 1367.

38. K. Bandyopadhyay, K. S. Mayya, K. Vijayamohanan, M. Sastry, *J. Electron Spectrosc. Relat. Phenom.* **1997**, *87*, 101.

39. P. Ganguly, D. V. Paranjape, M. Sastry, *J. Am. Chem. Soc.* **1993**, *115*, 793.

40. S. M. Marinakos, L. C. Brousseau, III, A. Jones, D. L. Feldheim, *Chem. Mater.* **1998**, *10*, 1214.

41. J. J. Storhoff, A. A. Lazarides, R. C. Mucic, C. A. Mirkin, R. L. Letsinger, G. C. Schatz, *J. Am. Chem. Soc.* **2000**, *122*, 4640.

42. R. R. Reynolds III, C. A. Mirkin, R. L. Letsinger, *J. Am. Chem. Soc.* **2000**, *122*, 3795.

43. M. Sastry, N. Lala, V. Patil, S. P. Chavan, A. G. Chittiboyina, *Langmuir* **1998**, *14*, 4138.

44. R. Elghanian, J. J. Storhoff, R. C. Mucic, R. L. Letsinger, C. A. Mirkin, *Science* **1997**, *277*, 1078.

45. U. Kreibig, L. Genzel, *Surf. Sci.* **1985**, *156*, 678.

46. G. C. Bond, in: *Handbook of Heterogeneous Catalysis*, *Vol. 2*, Eds: G. Ertl, H. Knozinger, J. Weitkamp, Wiley-VCH, Weinheim, **1997**, Section 3, pp. 752–770.

47. D. L. Trimm, Z. Ilsen Onsan, *Catal. Rev. -Sci. Eng.* **2001**, *43*, 31.

48. T. V. Choudhary, D. W. Goodman, *Catal. Today* **2002**, *77*, 65.

49. J. R. Rostrup-Nielson, T. Rostrup-Nielson, *Cattech* **2002**, *6*, 150.

50. P. Ratnasamy, D. Srinivas, C. V. V. Satyanarayana, P. Manikandan, R. S. Senthil Kumaran, M. Sachin, V. N. Shetti, *J. Catal.* **2004**, *221*, 455.

51. P. A. Sermon, G. C. Bond, P. B. Wells, *J. Chem. Soc., Faraday Trans. I* **1979**, *75*, 385.

52. S. Naito, M. Tanimoto, *J. Chem. Soc., Chem. Commun.* **1988**, 832.

53. S. Naito, M. Tanimoto, *J. Chem. Soc., Faraday Trans.* **1988**, *84*, 4115.

5.1. SUMMARY

The present thesis gives an account of (i) the syntheses of inorganic–organic hybrid mesoporous materials by immobilization of several ruthenium complexes and gold nanoparticles on organically modified M41S type molecular sieves, (ii) in-depth characterization of these composite materials, and (iii) application of these materials as catalysts in selective hydrogenation and oxidation reactions.

Chapter 1 presents a general introduction about various physicochemical aspects of mesoporous materials with particular emphasis to different synthesis routes, mechanisms proposed for their formation, and different approaches for their surface modification. Application of these materials as supports for different catalytically active transition metal complexes and nanoparticles, and characterization techniques of these composite materials are also discussed in brief. Based on the literature survey, the scope and objectives of the present work have been summarized at the end of the chapter.

Chapter 2 provides experimental results on synthesis of siliceous MCM-41 and MCM-48 materials and their surface modification by reactive organic functional groups by two different methods; (i) post-synthesis grafting and (ii) "one-pot" co-condensation. The significance of these processes by various spectroscopic (XRD, CP MAS NMR and elemental microanalyses), microscopic (SEM and TEM), volumetric (N_2 adsorption and surface area analysis) and thermogravimetric (TG-DTA) techniques have been highlighted.

Chapter 3 deals with a novel heterogeneous catalyst system containing immobilized Ru-biphosphine-diamine complexes on surface modified MCM-41 and MCM-48 for chemoselective hydrogenation of α,β-unsaturated aldehydes and enantioselective hydrogenation of prochiral ketones. The chapter describes the synthesis methods for immobilization, and characterization of these heterogeneous catalysts by XRD, FTIR, CP MAS NMR, N_2 adsorption, TEM and XPS. The catalytic potential of these heterogeneous

catalysts in hydrogenation of a number of olefins, chemoselective hydrogenation of α,β-unsaturated aldehydes and enantioselective hydrogenation of prochiral ketones under various reaction conditions have been demonstrated. The recycle studies of the catalysts have also been presented to emphasize the heterogeneous nature of the same.

Chapter 4 focuses on a novel method for the synthesis and simultaneous stabilization of gold nanoparticles formed by *in situ* reduction of aqueous $AuCl_4^-$ ions by organo-functionalized MCM-41 materials. The probable mechanism of the formation of gold nanoparticles has been supported by similar experiments with amorphous silica. These nanocomposites have been extensively characterized by UV-Vis, XRD, N_2 adsorption, XRF, XPS, TEM and TG-DTA. The catalytic activity of these supported gold catalysts in preferential oxidation of carbon monoxide in hydrogen rich reformates, and in hydrogenation of unsaturated hydrocarbons under different reaction conditions has been discussed in detail.

5.2. CONCLUSIONS

5.2.1. Surface Modification and Characterization of Mesoporous Silica

- In the post-synthesis grafting process at room temperature, dichloromethane was found to be the best solvent.
- In the grafting process, the siliceous MCM-41 or MCM-48 materials were first treated with Ph_2SiCl_2 to ensure that the anchoring of the desired organic functional groups occurs primarily within the channels. The samples synthesized without treatment with Ph_2SiCl_2 are of poorer quality as revealed from powder XRD patterns.
- Organo-functionalized MCM-48 materials could not be synthesized by co-condensation method. Instead, structures resembling hexagonal mesoporous silica (HMS) were obtained, as envisaged from XRD, SEM and TEM experiments.

- Solid state NMR spectra show that in the samples prepared by co-condensation, the organic functional groups are more tightly bound to the inner walls, than in the case of post-synthesis grafting.
- The pore diameter of the surface-functionalized MCM-41 samples synthesized by co-condensation is somewhat larger than those prepared by grafting. Therefore, these materials can be selectively used to host different chemical species having different dimensions.

5.2.2. Immobilization of Transition Metal Complexes

- An efficient heterogeneous catalyst system for chemoselective and stereoselective hydrogenation of carbonyl compounds was synthesized by a simple and easier approach, involving anchoring of various achiral and chiral Ru^{II}-phosphine-diamine complexes on the inner surfaces of organo-functionalized MCM-41 and MCM-48 materials.
- Powder XRD patterns and TEM images reveal highly ordered hexagonal and cubic patterns of the organo-functionalized MCM-41 and MCM-48 materials, respectively, even after incorporation of Ru-complexes. The integrity of the Ru-complexes was retained after anchoring into the mesoporous hosts, which was supported from FTIR, ^{31}P CP MAS NMR and XPS analyses.
- This catalyst shows promising activity and selectivity in the chemoselective hydrogenation of α,β-unsaturated aldehydes and enantioselective hydrogenation of prochiral ketones. As high as 95–99% ee in the hydrogenation of prochiral ketones and *ca*. 75–79% chemoselectivity towards the hydrogenation of carbonyl group in unsaturated aldehydes could be obtained using these solid catalysts under heterogeneous reaction conditions.

- The presence of both phosphine and ethylenediamine moieties are essential for hydrogenation of carbonyl group in the unsaturated aldehydes or prochiral ketones.
- Both the biphosphine and diamine ligands have to be chiral to achieve maximum enantioselectivity in the hydrogenation of prochiral ketones.
- The anchored solid catalysts can be recycled effectively and reused several times without any decrease in activity and selectivity.

5.2.3. Formation and Stabilization of Metal Nanoparticles

- Gold nanoparticles were synthesized conveniently and simultaneously stabilized in siliceous matrices, ordered or amorphous.
- The application of any external reducing atmosphere for the reduction of the metal ions to form the nanoparticles is not required at all. The silanol groups present on the surface of host matrices participate in the reduction of aqueous chloroaurate ions to form the nanoparticles, which are subsequently bound fairly strongly to the host matrix.
- Powder XRD patterns and TEM images reveal highly ordered hexagonal patterns of the organo-functionalized MCM-41 materials, even after incorporation of Au nanoparticles.
- When amorphous silica was used as the host, size of the nanoparticles could be controlled by external addition of alkylamine molecules. The alkylamine molecules form self-assembled monolayers on the surface of the gold nanoparticles during the initial nucleation period, and thus prevent further growth. Particle size is dependent on concentration and alkyl chain length of the alkylamine molecules.
- When organo-functionalized MCM-41 was used as the host, the addition of alkylamine molecules was not at all necessary. The presence of pendant $–NH_2$ or –SH functional groups inside the mesopores serves the same purpose by entrapping the gold nanoparticles through covalent interactions just after their formation.

- The gold nanoparticles supported on organo-functionalized MCM-41 materials exhibit promising catalytic activity in the preferential oxidation of CO in H_2 rich reformates, and in hydrogenation of olefinic substrates. In fact, these materials show better catalytic activity than the fumed silica–gold nanocomposites, obviously due to smaller particle sizes.

5.3. FUTURE OUTLOOK

The possibilities of chemoselective and enantioselective hydrogenation by different coordination compounds of Ru^{II} with cheaper ligands, such as phenanthroline, bipyridyl, substituted ethylenediamine *etc*., anchored on mesoporous silica, could be explored. Further, to achieve 100% chemoselectivity towards hydrogenation of C=O bond in α,β-unsaturated aldehydes, *i.e.*, quantitative conversion of α,β-unsaturated aldehyde to allylic alcohol, could be a potential challenge.

In this thesis, enantioselective hydrogenation of prochiral aliphatic, alicyclic and aromatic ketones have been studied. However, there is ample opportunity to study enantioselective hydrogenation of different types of functionalized ketones, *e.g.*, heteroaromatic ketones, amino ketones, β-ketoesters *etc*. employing the present heterogeneous catalyst system. These substrates are commercially applied as chiral synthons in the synthesis of vitamins, fragrances, pheromones, pharmaceuticals *etc*.

Gold nanoparticles supported on metal oxides can catalyze partial and complete oxidation of hydrocarbons. The nano-Au-MCM-41 composites prepared in this study can also be exploited in selective oxidation of hydrocarbons. Immediate challenges are oxidation of olefinic substrates to epoxides, and oxidation of cyclohexane to adipic acid.

List of Publications

1. Characterization and catalytic activity of gold nanoparticles synthesized by auto-reduction of aqueous chloroaurate ions with fumed silica

   Priyabrata Mukherjee, Chitta Ranjan Patra, **Anirban Ghosh**, Rajiv Kumar and Murali Sastry

   Chemistry of Materials **2002**, *14*, 1678–1684

2. Formation and stabilization of gold nanoparticles in organo-functionalized MCM-41 mesoporous materials and their catalytic applications

   Chitta Ranjan Patra, **Anirban Ghosh**, Priyabrata Mukherjee, Murali Sastry and Rajiv Kumar

   in: *Nanoporous Materials III*, Eds: A. Sayari, M. Jaroniec, *Studies in Surface Science and Catalysis*, Elsevier, Amsterdam, **2002**, *Vol. 141*, pp. 641–646

3. Entrapment and stabilization of cadmium sulphide (CdS) nanoclusters formed inside propylthiol functionalized MCM-41 mesoporous materials

   Anirban Ghosh, Chitta Ranjan Patra, Priyabrata Mukherjee, Murali Sastry and Rajiv Kumar

   in: *Nanoporous Materials III*, Eds: A. Sayari, M. Jaroniec, *Studies in Surface Science and Catalysis*, Elsevier, Amsterdam, **2002**, *Vol. 141*, pp. 647–652

4. Heteropolyacids aided rapid and convenient synthesis of highly ordered MCM-41 and MCM-48: Exploring the accelerated process by ^{29}Si MAS NMR and powder X-ray diffraction studies

   Kausik Mukhopadhyay, **Anirban Ghosh** and Rajiv Kumar

   Chemical Communications **2002**, 2404–2405

5. Preparation and stabilization of gold nanoparticles formed by *in situ* reduction of aqueous chloroaurate ions within surface modified mesoporous silica

   Anirban Ghosh, Chitta Ranjan Patra, Priyabrata Mukherjee, Murali Sastry and Rajiv Kumar

   Microporous and Mesoporous Materials **2003**, *58*, 201–211

6. Gold nanoparticles formed within ordered mesoporous silica and on amorphous silica

   Rajiv Kumar, **Anirban Ghosh**, Chitta Ranjan Patra, Priyabrata Mukherjee and Murali Sastry

   in: *Nanotechnology in Catalysis*, Eds: B. Zhou, S. Hermans, G. A. Somorjai, Kluwer Academic/Plenum Publishers, New York, **2004**, *Vol. 1*, Chapter 6, pp. 111–136

7. Formation of gold nanoparticles within surface-functionalized ordered mesoporous molecular sieves

   Anirban Ghosh, Chitta Ranjan Patra, Murali Sastry and Rajiv Kumar

   Indian Journal of Physics **2004**, *78A*, 75–79

8. Keggin anions promoted synthesis of zeolites and mesoporous materials

   Kausik Mukhopadhyay, **Anirban Ghosh** and Rajiv Kumar

   in: *Proceedings of the 14th International Zeolite Conference*, Eds: E. Van Steen, L. Callanan, M. Claeys, Catalysis Society of South Africa, Cape Town, **2004**, pp. 461–467.

9. An efficient heterogeneous catalytic system for enantioselective hydrogenation of prochiral carbonyl compounds

   Anirban Ghosh and Rajiv Kumar

   Journal of Catalysis **2004**, (in press)

List of Manuscripts Communicated

1. An efficient heterogeneous catalytic system for chemoselective hydrogenation of α,β-unsaturated carbonyl compounds

   Anirban Ghosh and Rajiv Kumar

   Applied Catalysis A: General (communicated)

Contributions to National/International Symposia/Conferences

1. Formation of gold nanoparticles by spontaneous reduction of aqueous chloroaurate ions with amorphous silica: A novel approach to gold nanoparticle synthesis

   Anirban Ghosh, Chitta Ranjan Patra, Priyabrata Mukherjee, Murali Sastry and Rajiv Kumar

   International Conference on Progress in Disperse Systems, Organized by "Department of Chemistry, University of Calcutta" and "Indian Society for Surface Science and Technology"

   16–18th January 2002, University College of Science and Technology, University of Calcutta, Kolkata, India (***Poster presentation***)

2. Formation and stabilization of gold nanoparticles in organo-functionalized MCM-41 mesoporous materials and their catalytic applications

   Chitta Ranjan Patra, **Anirban Ghosh**, Priyabrata Mukherjee, Murali Sastry and Rajiv Kumar

   3rd International Symposium on Nanoporous Materials, Organized by "Center for Catalysis Research and Innovation, University of Ottawa"

   12–15th June 2002, University of Ottawa, Ottawa, Canada (***Poster presentation***)

3. Entrapment and stabilization of cadmium sulphide (CdS) nanoclusters formed inside propylthiol functionalized MCM-41 mesoporous materials

   Anirban Ghosh, Chitta Ranjan Patra, Priyabrata Mukherjee, Murali Sastry and Rajiv Kumar

   3rd International Symposium on Nanoporous Materials, Organized by "Center for Catalysis Research and Innovation, University of Ottawa"

   12–15th June 2002, University of Ottawa, Ottawa, Canada (***Poster presentation***)

4. Selective isopropylation of ethylbenzene over zeolites

   Chitta Ranjan Patra, Mahesh D. Kadgaonkar, **Anirban Ghosh** and Rajiv Kumar

   Catalysis: Concepts to Practice, Organized by "NCL Research Foundation"

   26-27th June 2002, National Chemical Laboratory, Pune, India (***Poster presentation***)

5. Formation of gold nanoparticles within surface-functionalized ordered mesoporous molecular sieves

   Anirban Ghosh, Chitta Ranjan Patra, Murali Sastry and Rajiv Kumar

   National Seminar on Science and Technology of Nanomaterials, Organized by "Materials Research Society of India" and "Physical Sciences Section, West Bengal Academy of Science of Technology"

   6–7th March 2003, Central Glass and Ceramic Research Institute, Kolkata, India (***Poster Presentation***)

6. Keggin anions promoted synthesis of zeolites and mesoporous materials

   Kausik Mukhopadhyay, **Anirban Ghosh** and Rajiv Kumar

   14th International Zeolite Conference, Organized by "International Zeolite Association" and "Catalysis Society of South Africa"

   25–30th April 2004, Cape Town International Conventional Center, Cape Town, South Africa (***Poster presentation***)

7. A new mesoporous organo-inorganic hybrid catalytic system for chemoselective hydrogenation of α,β-unsaturated aldehydes

   Anirban Ghosh and Rajiv Kumar

   4th International Mesostructured Materials Symposium, Organized by "International Mesostructured Materials Association"

   1st–4th May 2004, Golden Tulip Lord Charles Hotel, Cape Town, South Africa (***Poster presentation***)

8. Heterogenization of transition metal complexes for selective reduction of carbonyl compounds

   Anirban Ghosh and Rajiv Kumar

   7th National Symposium in Chemistry, Organized by "Chemical Research Society of India"

   4th–6th February 2005, Indian Association for the Cultivation of Science, Kolkata, India (***Poster Presentation***)

9. Preferential oxidation of carbon monoxide by gold nanoparticles stabilized on organo-functionalized mesoporous silica

   Anirban Ghosh, Sachin S. Malwadkar, C. V. V. Satyanarayana and Rajiv Kumar

   7th National Symposium in Chemistry, Organized by "Chemical Research Society of India"

   4th–6th February 2005, Indian Association for the Cultivation of Science, Kolkata, India (***Poster Presentation***)